



**HAL**  
open science

## Co-localized AFM/Raman characterization of multiphase polymer systems

Joao Paulo Cosas Fernandes

► **To cite this version:**

Joao Paulo Cosas Fernandes. Co-localized AFM/Raman characterization of multiphase polymer systems. Polymers. Université Grenoble Alpes, 2017. English. NNT : 2017GREAI081 . tel-01725368

**HAL Id: tel-01725368**

**<https://theses.hal.science/tel-01725368>**

Submitted on 7 Mar 2018

**HAL** is a multi-disciplinary open access archive for the deposit and dissemination of scientific research documents, whether they are published or not. The documents may come from teaching and research institutions in France or abroad, or from public or private research centers.

L'archive ouverte pluridisciplinaire **HAL**, est destinée au dépôt et à la diffusion de documents scientifiques de niveau recherche, publiés ou non, émanant des établissements d'enseignement et de recherche français ou étrangers, des laboratoires publics ou privés.

## THÈSE

Pour obtenir le grade de

### **DOCTEUR DE LA COMMUNAUTE UNIVERSITE GRENOBLE ALPES**

Spécialité : **Matériaux, Mécanique, Génie Civil, Electrochimie**  
Arrêté ministériel : 25 mai 2016

Présentée par

**João Paulo COSAS FERNANDES**

Thèse dirigée par **Laurent GONON** et  
codirigée par **Vincent MAREAU**

préparée au sein du **Laboratoire Systèmes Moléculaires et  
nanoMatériaux pour l'Energie et la Santé / Polymères Conducteurs  
Ioniques**  
dans l'**École Doctorale Ingénierie-Matériaux, Mécanique  
Énergétique, Environnement, Procédés, Production (I-MEP<sup>2</sup>)**

## **Co-localisation AFM/Raman : Caractérisation de systèmes polymères multiphasés**

Thèse soutenue publiquement le **16 novembre 2017**,  
devant le jury composé de :

### **DR Didier R. LONG**

Directeur adjoint Laboratoire Polymères et Matériaux Avancés LPMA de Lyon  
(UMR5268), CNRS – Président

### **Pr. Isabelle ROYAUD**

Département Science et Ingénierie des Matériaux et Métallurgie (SI2M) de  
l'Institut Jean Lamour (UMR 7198), Université de Lorraine - Rapporteur

### **Pr. Odile FICHET**

Co-directrice du Laboratoire de Physicochimie des Polymères et des Interfaces  
(EA2528), Université de Cergy Pontoise - Rapporteur

### **DR Deborah JONES**

Directrice associée de l'Institut Charles Gerhardt de Montpellier, CNRS - Membre

### **Delphine TAVERNIER-LOHR**

Responsable R&D Groupe Serge Ferrari, La Tour du Pin - Membre







# **Co-localized AFM/Raman characterization of multiphase polymer systems**

**João Paulo Cosas Fernandes**

This dissertation is submitted for the degree of Doctor of Philosophy  
16 November 2017

Even Diamonds start as Coal  
Just give it Time  
The Fire feels Divine

- Incubus



# Acknowledgements

---

First I would like to thank my thesis directors Laurent Gonon and Vincent Mareau, for believing in me and giving me the means to fulfill my goals, inside the lab and outside as well. Laurent was always pushing me to go beyond the expectations, always scientifically rigorous and critical, but also a good listener to my ideas and opinions. Vincent is a master of experimentation in the lab, with whom I learned a lot about putting ideas into practice. Our scientific discussions have always been a challenge for me, but also made me go further into any subject we worked on together. I hope the best for you !

To my friends from the lab, Ph.D. students, post-docs, senior researchers, professors, staff... You were part of my daily life for the past 3 years and I thank you a lot for the good times we spent together. Lucille, Katya, Natacha, Nicolas, Coraline, Tao, Rémi, Laurent, Christopher, thank you for the daily laughs and for the great support until the very end ! Hakima, you are a great person, mother and researcher. You have always been there for me when I needed answers, with your enthusiasm and kindness. Emilie, Charly and Joëlle, thanks for being my support in the daily life of the lab, from experiments to the bureaucracy of a foreign student, you were always very helpful and kind. Jojo, may you continue to enlighten peoples' life with your great sense of humor !

Outside the lab, I had the pleasure of meeting incredible people, each of one battling to achieve their best selves. I thank the people that kindly welcomed me back in Grenoble, Figueira, Julianny, Drieli and Marina, and all the BRAFITECs that came into my life and made it more joyful. Volta, Lorena, Ebert, Contin, Raíssa, Juliana, Luciane, Thibault.. Thanks for the shared moments. I thank the CrazyVosDent volleyball team for the two and a half years of partnership, victories, defeats and *apéros* after each match. Les Ducs du Tranqui ! Certainly the best friends I had the pleasure of meeting and living together for the past 2 years. Tuxo and Xaxa, thanks for the good moments, discussions, laughs, travels and snowboarding weekends. I am truly grateful for the daily support and I hope the best for your future ! A special thanks to Julie Grande, for being by my side until the end, for caring for my back's health and for teaching me more than she can imagine.

I thank my family, my aunts, uncles and cousins, for the support you gave me at each step of my education and for the warmest welcomes each time I come back home.

At last, but not least, I thank my parents Sonia and Mauricio. You have always been there for me, you gave me all the conditions and opportunities to be who I am today. Even when my decisions made me go so far away from home, you gave me strength. For you both, I will keep trying my best. I love you.







# Contents

---

<b>INTRODUCTION</b>	<b>xiii</b>
<b>CHAPTER 1</b>	
<b>MOTIVATION</b>	
<b>PROLOGUE</b>	<b>1</b>
1. Heterogeneous and multi-phase complex polymer materials	2
1.1. Polymer Blends	2
1.2. Multilayer Polymeric Materials	3
1.3. Fiber Reinforced Polymer Composites	6
1.3.1. Polymer Nanocomposites	8
1.4. Block-copolymers	10
2. Bulk vs Surface Properties	11
2.1. Characterization of both the Surface and Bulk of Polymer Materials	13
2.2. Sample Preparation Techniques for Bulk Direct Observations	14
3. Polymer membranes	15
4. Manuscript Structure	16
<b>CHAPTER 2</b>	
<b>Co-Localized AFM/Raman and Complementary Analyses</b>	
<b>PROLOGUE</b>	<b>19</b>
1. Fundamentals of Atomic Force Microscopy	20
1.1. Fundamentals of PeakForce Quantitative NanoMechanics (QNM)	21
1.2. System Calibration for Quantitative Nano-Mechanical Measurements	24
1.3. Nanomechanical Models for Quantitative Measurements	25
1.4. Absolute vs Relative Calibration Method	27
2. Fundamentals of Raman Spectroscopy	28
2.1. Raman Principle	28
2.2. Raman Mapping and Spatial Resolution	29
3. AFM-Confocal Raman Coupling	32
3.1. Commercially available AFM-Raman coupling systems	32
4. Sample Preparation Techniques	35
4.1. Cryo-Fracture	35
4.2. Cryo-Ultramicrotomy	36

---

4.3.	Focused Ion Beam (FIB) cross-sectioning	39
4.4.	Summary Table of Sample Preparation Techniques	41
5.	Complementary Analyses	43
5.1.	Optical Microscopy (OM)	43
5.2.	Electron Microscopies	43
5.2.1.	Scanning Electron Microscopy (SEM)	44
5.2.2.	Transmission and Scanning Transmission Electron Microscopy (TEM/STEM)	47
5.3.	Fourier Transform Infrared Spectroscopy (FTIR)	49
5.4.	Summary Table of Characterization Techniques	51
6.	Conclusions of Chapter 2	53
6.1.	Difficulties related to sample preparation by Cryo-Ultramicrotomy	53
6.2.	Difficulties related to the co-localization of AFM/Raman analyses	53
7.	Conclusions du Chapitre 2 en Français	54
7.1.	Difficultés liées à la préparation des échantillons par Cryo-Ultramicrotomie	54
7.2.	Difficultés liées à la co-localisation des analyses AFM/Raman	54

## CHAPTER 3

### Experimental Methods and Developments

PROLOGUE	57
1. Sample preparation by Cryo-Ultramicrotomy	57
1.1. Sectioning of injection molded specimens	58
1.2. Sectioning of polymer membranes	59
1.3. Cryo-ultramicrotomy parameters	59
1.4. Avoiding frost melting water-diffusion onto the sample's surface	60
2. AFM/Raman Co-localization Setup	60
2.1. Atomic Force Microscope (AFM)	61
2.1.1. AFM Calibration Method	61
2.2. Raman Spectrometer	67
2.2.1. Raman Calibration Method	67
3. Co-localization Methods	68
3.1. Co-localization with the Co-localized Raman Microscope	68
3.2. Co-localization with the Regular Raman Microscope - Shuttle Stage	69
4. Complementary Analyses	71
4.1. Scanning Electron Microscopy (SEM)	71
4.2. Transmission and Scanning Transmission Electron Microscopy (TEM/STEM)	71

4.3. $\mu$ -ATR-FTIR imaging	71
5. Conclusions of Chapter 3	73
6. Conclusions du Chapitre 3 en Français	74

## CHAPTER 4

### Compatibilization of Polymer Blends based on PA6/ABS

PROLOGUE	77
1. Theoretical Background and Motivation	78
1.1. Polyamide 6 (PA6)	78
1.2. Acrylonitrile-Butadiene-Styrene (ABS)	79
1.3. Mixing and compatibilization of polymer blends	80
1.4. Objectives of work	81
2. Study of compatibilization of PA6/ABS blends with SAN-MA	82
2.1. Materials used	82
2.2. Blending protocols	82
2.3. Phase identification of the reference sample by Raman and AFM analyses	83
2.4. Effect of blending protocol on morphology	85
2.5. Effect of the morphology on the rheological behavior	87
2.5.1. Discussions of the effect of blending protocol on morphology and rheological properties	88
2.6. Effect of SAN-MA compatibilizer on PA6 structure	89
2.6.1. PA6 polymorphs quantification by Differential Scanning Calorimetry (DSC )	90
2.6.2. Distribution of PA6 polymorphs studied by co-localized AFM-Raman analyses	91
2.6.3. Discussions of the effect of SAN-MA compatibilizer on PA6 structure	94
3. Conclusions of Chapter 4	95
3.1. Summary of conclusions of Chapter 4	96
4. Conclusions du Chapitre 4 en Français	97
4.1. Résumé des conclusions du Chapitre 4 en Français	98

## CHAPTER 5

### Hybrid Membranes for Fuel Cell

PROLOGUE	101
1. Theoretical Background and Motivation	102
1.1. Hydrogen Fuel Cells Fundamentals	102
1.2. Polymer Membrane Electrolytes	103
1.2.1. Sulfonated Polyether-etherketone (sPEEK)	104

---

1.3. Sol-Gel method	105
1.4. Objectives of work	106
2. Study of hybrid membranes based on dimethoxysilane (SHDi) precursors	107
2.1. Materials used	107
2.2. Micro-scale distribution of the SG along the membrane's cross-section	108
2.3. Impact of the processing steps on the hybrid membrane's morphology	110
2.4. Impact of the processing steps on the hybrid membrane's nanomechanical properties and SG uptake	112
2.5. Insights on the SG condensation process thanks to the water trapped at the ultramicrotomed surfaces	112
2.6. Morphological evolution over time	114
2.7. Nano-manipulation and nanomechanical characterization of growing crystals	115
2.7.1. Co-localized AFM/Raman analysis on the crystals	116
2.8. Morphological Analysis by Scanning Electron Microscopy (SEM)	117
2.9. Discussion of the characterization of hybrid membranes based on SHDi precursor	118
2.10. Complementary $\mu$ -ATR-FTIR analysis – Feasibility and preliminary results	120
2.11. Conclusions of the Study of Hybrid membranes based on SHDi precursor	122
3. Study of hybrid membranes based on trimethoxysilane (SHTriM) precursors	123
3.1. Materials used	123
3.2. Effect of the thermal treatments on the membrane's morphology	124
3.2.1. Effect of the SG uptake on the morphology	125
3.3. Complementarity between AFM and SANS	126
3.3.1. Fundamentals of Small Angle Neutron Scattering	126
3.3.2. SANS experiments	127
3.4. Co-localized AFM/Raman cross-section analysis	129
3.5. Conclusions of the Study of Hybrid Membranes based on SHTriM precursors	131
4. Summary of Conclusions of Chapter 5	132
5. Résumé des Conclusions du Chapitre 5 en Français	134

## CHAPTER 6

### Copolymer Electrolytes for Lithium Batteries

PROLOGUE	137
1. Theoretical Background and Motivation	138
1.1. Lithium Batteries Fundamentals	138
1.2. Polymer Electrolytes based on PEO	139
1.3. Copolymers as Electrolytes	140

1.4.	Morphological Analysis of Polymer Electrolytes	142
1.5.	Objectives of work	143
2.	Study PS-PEO-PS copolymers doped with lithium salt	144
2.1.	Materials used	144
2.2.	Sample preparation for cross-section analysis	145
2.3.	Morphological study of PS-PEO-PS copolymers	146
2.3.1.	Effect of the Lithium salt on the morphology	146
2.4.	Effect of reticulation on PS-PCi-PS copolymers morphologies	150
3.	Study of “single ion” copolymer electrolyte	152
3.1.	Material used	152
3.2.	Morphology of PSTFSiLi-PEO-PSTFSiLi copolymer	153
3.3.	Surface morphology and properties evolution with hydration degree	156
4.	Conclusions of Chapter 6	161
4.1.	Summary of Conclusions of Chapter 6	162
5.	Conclusions du Chapitre 6 en Français	163
5.1.	Résumé des Conclusions du Chapitre 6 en Français	164
<b>CONCLUSIONS</b>		<b>166</b>
<b>ANNEXES</b>		<b>186</b>
Annex 1.	Annexes of Chapter 4: Compatibilization of compatibilized blends based on PA6/ABS	187
Annex 1.1	Blending procedure	187
Annex 1.2	Raman band assignment of the blend components	187
Annex 1.3	Rheological Measurements	189
Annex 1.4	Differential Scanning Calorimetry (DSC)	189
Annex 1.5	Fabrication and analysis of the reference PA6 polymorphs	189
Annex 1.6	Co-localized AFM-Raman analyses of the compatibilized blends	191
Annex 1.7	Raman analysis of characteristic PA6 $\gamma$ -phase band at $960\text{ cm}^{-1}$	193
Annex 2.	Annexes of Chapter 5: Hybrid Membranes for Fuel Cell	193
Annex 2.1	Fabrication process of the hybrid membranes based on SHDi precursor	193
Annex 2.2	Thermogravimetric Analysis (TGA) of hybrid membranes based on SHDi precursors	194
Annex 2.3	Raman assignment of the sPEEK and SG phase chemical signatures	194
Annex 2.4	Fabrication process of the hybrid membranes based on SHTriM precursor	196

Annex 2.5 Effect of trapped water on the surface of Polyethylene terephthalate (PET) membranes	196
<b>List of Tables</b>	<b>201</b>
<b>List of Figures</b>	<b>202</b>
<b>BIBLIOGRAPHY</b>	<b>210</b>

# Abbreviations

---

<b>ABS</b>	Acrylonitrile-Butadiene-Styrene.	<b>k</b>	Spring Constant.
<b>ATR</b>	Attenuated Total Reflection.	<b>LB</b>	Lithium Batteries.
<b>ATR-FTIR</b>	Attenuated Total Reflection Fourier Transform Infrared Spectroscopy.	<b>LDPE</b>	Low Density Polyethylene.
<b>BSE</b>	Backscattered Electrons.	<b>LEPMI</b>	Laboratoire d'Electrochimie et de Physico-chimie des Matériaux et des Interfaces. ,
<b>D</b>	Deflection.	<b>LiTFSI</b>	Lithium bis(trifluorosulfone)imide.
<b>DMA</b>	Dynamic Mechanical Analysis.	<b>LMP</b>	Lithium Metal Polymer.
<b>DSC</b>	Differential Scanning Calorimetry.	<b>MA</b>	Maleic Anhydride.
<b>E</b>	Modulus.	<b>MEA</b>	Membrane Electrode Assembly.
<b>EDS</b>	Energy Dispersive X-ray Spectroscopy.	<b>MMA-MA</b>	Methyl Methacrylate-Maleic Anhydride.
<b>EELS</b>	Electron Energy Loss Spectroscopy.	<b>MPP</b>	Maleic anhydride grafted Polypropylene.
<b>EOC</b>	Ethylene Octene Copolymer.	$\eta^*$	Complex Viscosity
<b>EPDM</b>	Ethylene Propylene Diene Terpolymer.	<b>NR</b>	Natural Rubber.
<b>F</b>	Force.	<b>OM</b>	Optical Microscopy
<b>FIB</b>	Focused Ion Beam.	<b>OsO<sub>4</sub></b>	Osmium tetroxide
<b>FT-IR</b>	Fourier transform Infrared Spectroscopy.	<b>PA6</b>	Polyamide 6
<b>G'</b>	Storage Modulus.	<b>PB</b>	Polybutadiene.
<b>GF</b>	Glass Fiber.	<b>PC</b>	Polycarbonate.
<b>GFc</b>	non-treated commercial glass fiber.		Post-condensation.
<b>Gff</b>	Glass Fiber with film former.	<b>PCL</b>	Poly- $\epsilon$ -caprolactone.
<b>HDPE-g-MAH</b>	Polyethylene-graft-Maleic Anhydride.	<b>PEMFC</b>	Proton Exchange Membrane Fuel Cells.
<b>HT</b>	HydroThermal.	<b>PEMWE</b>	Proton Exchange Membrane Water Electrolyzer.
<b>iPP</b>	isotactic Polypropylene.	<b>PEO</b>	Polyethylene Oxide.
<b>IR</b>	Infrared Spectroscopy.	<b>PET</b>	Polyethylene terephthalate.

<b>PLA</b>	Poly(lactic acid).	(3-mercaptopropyl)-methyldimethoxysilane.
<b>PLLA</b>	Poly(L-lactic acid).	<b>SHTriM</b>
<b>PMMA</b>	Poly(methyl methacrylate).	(3-mercaptopropyl)-trimethoxysilane.
<b>POE</b>	Polyolefin Elastomer.	<b>sPEEK</b>
<b>PP</b>	Polypropylene.	sulfonated Polyether-etherketone. ,
<b>PS</b>	Polystyrene.	<b>SPEs</b>
<b>PSTFSILI</b>	Polystyrene-grafted-Lithium bis(trifluorosulfone)imide.	Solid Polymer Electrolytes.
<b>QNM</b>	Quantitative NanoMechanics.	<b>STEM</b>
<b>R</b>	Tip radius	Scanning Transmission Electron
<b>R-PA6</b>	Recycled-Polyamide 6.	Microscope.
<b>RuO<sub>4</sub></b>	Ruthenium tetroxide.	<b>TEM</b>
<b>s.</b>		Transmission Electron Microscope.
<b>SAN-MA</b>	Styrene-Acrylonitrile grafted with Maleic Anhydride.	Transmission Electron Microscopy.
<b>SANS</b>	Small Angle Neutron Scattering.	<b>Tg</b>
<b>SAXS</b>	Small Angle X-Ray Scattering.	Glass Transition Temperature.
<b>SBC</b>	Styrene-Butadiene Copolymer.	<b>TGA</b>
<b>SE</b>	Secondary Electrons.	Thermogravimetric Analysis.
<b>SEM</b>	Scanning Electron Microscopy.	<b>Tm</b>
<b>SG</b>	Sol-Gel.	Melting Temperature
<b>SHDi</b>		<b>UFSCar</b>
		Federal University of São Carlos.
		<b>UHMWPE</b>
		Ultrahigh Molecular Weight Polyethylene
		<b>V</b>
		Deflection Voltage
		<b>WAXD</b>
		Wide Angle X-Ray Diffraction.
		<b>WVP</b>
		Water Vapor Permeability
		<b>XANES</b>
		X-ray Absorption Near Edge Structure.
		<b>XPS</b>
		X-ray Photoelectron Spectroscopy.
		<b>Z</b>
		Z-Position
		<b>δ</b>
		Indentation
		<b>ν</b>
		Poisson ratio



# INTRODUCTION

---

In this thesis, we present the development of an innovative approach for the characterization of polymer systems, especially membranes, that couples co-localized Atomic Force Microscopy (AFM) and Confocal Raman microspectroscopy with electron microscopies (STEM and SEM) and other complementary techniques. We present here an experimental approach giving access to topographic, nanomechanical and chemical co-localized analyses after cross-sectioning of polymer membranes using cryo-ultramicrotomy without epoxy embedding. Obtaining co-localized information is the key element to study the process-structure-properties relationship of a variety of heterogeneous or multiphase polymer systems, like blends, nanocomposites, hybrids, multilayers and aged materials. The project was carried out in the Laboratory of Molecular Systems and Nanomaterials for Energy and Health (SyMMES), under the guidance of Laurent Gonon and Vincent Mareau.

Our objective was to develop an experimental methodology of characterization capable of providing multiples information at multiple scales, analyzing a single sample specially prepared to be suitable for complementary analyses. A substantial effort was done in order to apply this strategy to the characterization of thin polymer membranes (thickness below 100  $\mu\text{m}$ ). We demonstrated that the co-localization of information is essential for the elucidation of the process-structure-properties interplays, for various systems like compatibilized polymeric blends, hybrid polymer membranes for Fuel Cell, and also copolymer electrolyte membranes for lithium batteries.

## French Introduction

Dans cette thèse, nous présentons le développement d'une approche innovante pour la caractérisation des systèmes polymères, en particulier des membranes, qui couple la Microscopie de Force Atomique (AFM) avec la microspectroscopie confocale Raman avec des microscopes électroniques (STEM et SEM) et d'autres techniques complémentaires. Nous présentons ici une approche expérimentale donnant accès à des analyses topographiques, mécaniques et chimiques co-localisées après coupe transversale des membranes polymères à l'aide de cryo-ultramicrotomie sans enrobage d'époxy. L'obtention d'informations co-localisées est l'élément clé dans l'étude de la relation structure-structure-structure d'une variété de systèmes polymères hétérogènes ou polyphasés, tels que des mélanges, des nanocomposites, des hybrides, des multicouches et des matériaux vieilliss. Le projet a été réalisé dans le laboratoire des Systèmes Moléculaires et des nanoMatériaux pour l'Energie et la Santé (SyMMES) sous la direction de Laurent Gonon et Vincent Mareau.

Notre objectif était de développer une méthodologie de caractérisation expérimentale capable de fournir des multiples informations sur plusieurs échelles, en analysant un échantillon unique spécialement préparé pour être adapté aux analyses complémentaires. Des efforts considérables ont été faits pour appliquer cette stratégie à la caractérisation de membranes polymères fines (épaisseur inférieure à 100  $\mu\text{m}$ ). Nous avons démontré que la co-localisation de l'information est essentielle pour l'élucidation des interactions mise en œuvre-structure-propriété, pour divers systèmes tels que les mélanges de polymères compatibilisés, les membranes polymères hybrides pour les piles à combustible et les membranes polymères pour les batteries au lithium.





# CHAPTER 1

---

## MOTIVATION

## PROLOGUE

This chapter will illustrate the complexity of different polymeric systems, such as polymer blends, multilayers, (nano)-composites and copolymers. For each system, we will present studies where the understanding of their intrinsic complex characteristics and interactions was important and challenging for the development of new engineering solutions. We will see, among other examples, how the morphology of immiscible polymer blends affects their mechanical properties, and how their performances can be optimized; the effect of a compatibilization strategy on the performance of polymer composites reinforced with glass fibers and its effect on the matrix morphology, and finally the importance of the control of copolymer morphologies or crystalline polymorphs on the functional properties of gas separation membranes.

The last part of this chapter will be focusing on the necessity to characterize both the surface and the bulk of materials. For the sake of clarity, we will consider the term “bulk” as being a synonym of “core”, i.e., relative to the interior of the volume or thickness of the material, excluding the external surface. We will show that the proper characterization of the whole material (bulk + surface) makes possible the understanding of degradation processes or the optimization of material properties by tuning both bulk and surface morphologies and chemistries. Finally, a particular attention will be given to thin polymeric materials like films and membranes, for which additional technical challenges are associated to achieve co-localized information, and to separate bulk and surface contributions.

### French Prologue

Ce chapitre illustrera la complexité des différents systèmes polymères, tels que les mélanges de polymères, les multicouches, les (nano)-composites et les copolymères. Pour chaque système, nous présenterons des études où la compréhension de leurs caractéristiques et interactions complexes intrinsèques était importante et difficile pour le développement de nouvelles solutions d'ingénierie. Nous verrons, entre autres exemples, comment la morphologie des mélanges de polymères immiscibles affecte leurs propriétés mécaniques et leur performance optimale; l'effet d'une stratégie de compatibilité sur la performance des composites polymères renforcés avec des fibres de verre et leurs effets sur la morphologie de la matrice, et enfin l'importance du contrôle des morphologies du copolymère ou des polymorphes cristallins sur les propriétés fonctionnelles des membranes de séparation des gaz.

La dernière partie de ce chapitre sera axée sur la nécessité de caractériser à la fois la surface et l'intérieur des matériaux. Par souci de clarté, nous considérerons le terme «masse» comme synonyme de «noyau», c'est-à-dire par rapport à l'intérieur du volume ou de l'épaisseur du matériau, à l'exclusion de la surface externe. Nous montrerons que la caractérisation appropriée de tout le matériau (masse + surface) permet de comprendre le processus de dégradation ou l'optimisation des propriétés du matériau en accordant à la fois les morphologies et les chimies de masse et de surface. Enfin, l'attention particulière sera accordée aux matériaux polymères minces comme les films et les membranes, pour lesquels des défis techniques supplémentaires sont associés à la acquisition d'informations co-localisées et à séparer les contributions de la masse et de la surface.

## 1. Heterogeneous and multi-phase complex polymer materials

### 1.1. Polymer Blends

A polymer blend is a mixture of two or more polymers to create a new material with specific physical properties.<sup>1</sup> This strategy is widely used since the development of a polymer blend is less time and money consuming than the synthesis of a new polymer for a specific application. However, it requires a systematic study of the process-structure-properties relationships of the blend material. Polymer blends are a typical example of how important the developed morphology is for the final properties of the material. For entropic reasons, most polymers are immiscible<sup>2</sup> and the blends show a phase-segregated morphology, as illustrated in Figure 1.1. The properties of these phases separated materials are roughly the average of the properties of each component alone. For example, Ruckdäschel *et al.*<sup>3,4</sup> have studied immiscible poly(2,6-dimethyl-1,4-phenylene ether) (PPE) and poly(styrene-co-acrylonitrile) (SAN) blends. SAN is a rather rigid material with a modulus of  $3.80 \pm 0.12$  GPa, presenting low deformation at rupture and fracture energy ( $2.93 \pm 0.06$  % and  $27 \pm 1$  kJ/m<sup>2</sup>). Compared to SAN, PPE presents a lower modulus of  $2.50 \pm 0.09$  GPa but much higher deformation at rupture of  $69.8 \pm 39$  % and fracture energy ( $710 \pm 443$  kJ/m<sup>2</sup>). The authors have shown, for example, that for a 60/40 composition (wt%), a PPE/SAN blend verifies the rule of averaged properties: a modulus of  $3.08 \pm 0.15$  GPa, a deformation at rupture and fracture energy of  $40.2 \pm 24.5$  % and  $418 \pm 252$  kJ/m<sup>2</sup> respectively. Transmission Electron Microscopy (TEM) image on Figure 1.1 shows the continuous nature of the SAN (bright phase) while the PPE (dark phase) tends to form particles. The proper control of the morphology, considering size and distribution of the domains, interface interactions and adhesion between the components, is mandatory to obtain improved synergic properties.

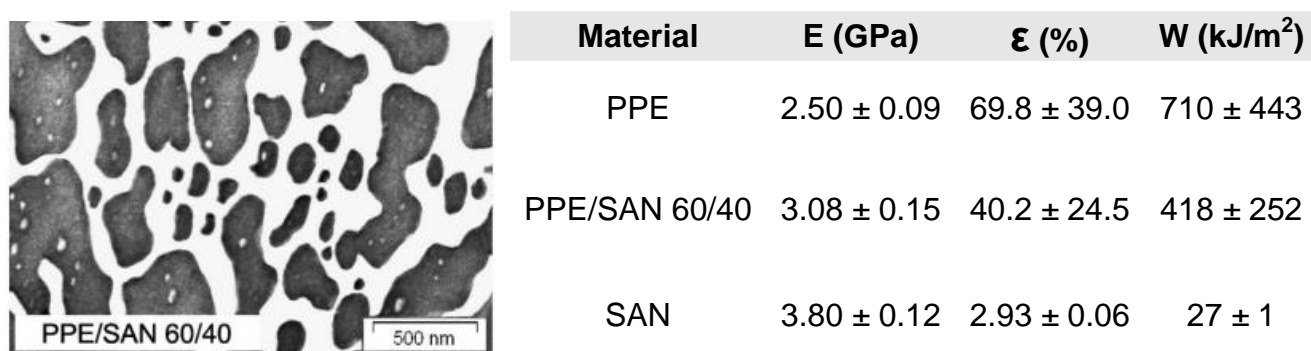


**Figure 1.1.** TEM micrograph of an immiscible PPE/SAN 60/40 wt% blend and table of mechanical properties of PPE, SAN and 60/40 PPE/SAN blend.<sup>3,4</sup>

Improvement of modulus is only attained on polymer blends when the adhesion of the materials at the interfaces is sufficient. If not the case, the incompatibility between the components can lead to the formation of defects at the interface and therefore to brittle characteristics.<sup>3</sup> One of the most mature strategies to improve the miscibility of polymer blends is compatibilization. Compatibilizing agents are chemically modified copolymers capable of interacting with one or both components of the blend, acting like surfactants to modify the interfacial tension between phases, improving the phases' dispersion. The final morphology developed in the presence of these compatibilizers corresponds to smaller droplets of the minority phase dispersed into the main component. Ruckdäschel *et al.*<sup>3,4</sup> have used this strategy to improve the miscibility of PPE/SAN blends using compatibilizers based on polystyrene-polybutadiene-poly(methyl methacrylate) triblock terpolymers (SBM). Figure 1.2 shows TEM images of the morphological evolution of the

PPE/SAN blend with the increasing amount of SBM and the mechanical properties of each composition. They observed that the addition of 5 wt% of SBM led to no significant morphological change, but almost doubled the deformation at rupture and the fracture energy (from  $40.2 \pm 24.5\%$  to  $76.4 \pm 14.6\%$  and from  $418 \pm 252 \text{ kJ/m}^2$  to  $817 \pm 156 \text{ kJ/m}^2$ , respectively). These improvements were attributed to the presence of the compatibilizer at the interphase, confirmed by TEM by the irregularly contrasted regions at the phases' boundaries (Figure 1.2 (b)). Increasing SBM compatibilizer's ratio up to 10%, the morphology of the blend was modified, becoming co-continuous, which improved the deformation at rupture and the fracture energy of the blend up to  $97.9 \pm 3.0\%$  and  $1022 \pm 32 \text{ kJ/m}^2$  respectively. On the other hand, the Young's modulus keep on dropping from  $3.08 \pm 0.09 \text{ GPa}$  for the uncompatibilized blend to  $3.01 \pm 0.09 \text{ GPa}$  for 5% SBM and  $2.84 \pm 0.07 \text{ GPa}$  for 10% SBM. Further addition of SBM to 20 wt% turned back the morphology to a dispersed PPE phase into a SAN matrix. However, the average droplet size of the PPE phase was reduced in comparison to the previous compositions. The good deformation at rupture and the fracture energy properties were maintained ( $96.8 \pm 12.7\%$  and  $944 \pm 127 \text{ kJ/m}^2$ ) but it caused a more pronounced drop of the modulus ( $2.57 \pm 0.06 \text{ GPa}$ ).<sup>3,4</sup> This example evidences the need to understand the impact of the compatibilizer on both the morphology and the mechanical properties of the compatibilized blends in order to optimize their resulting properties

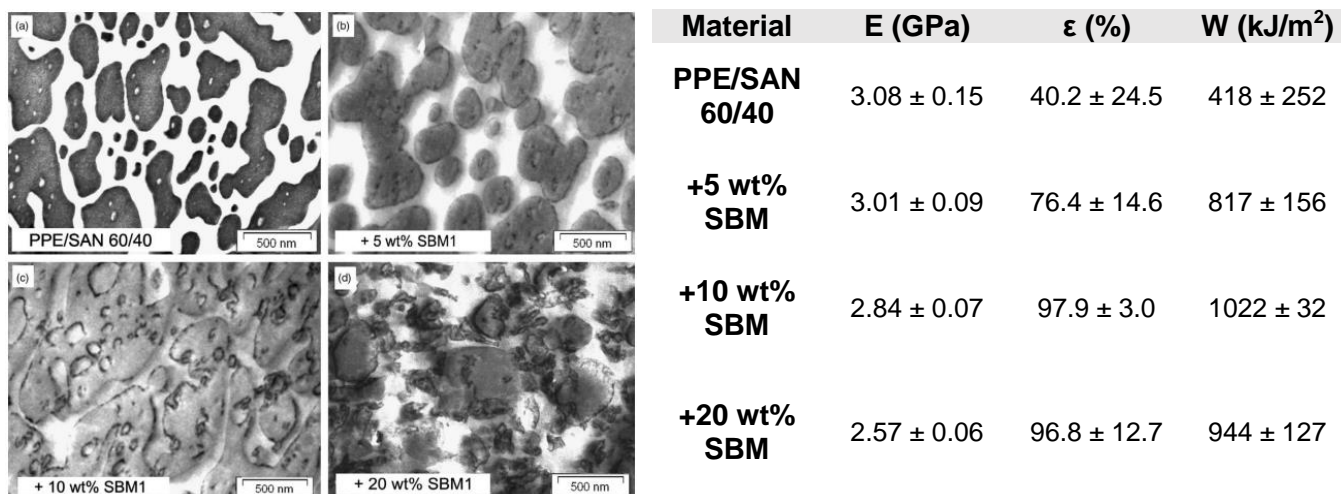


**Figure 1.2.** TEM micrographs showing different morphologies developed for increasing amount of SBM compatibilizer into PPE/SAN blends. The table presents the corresponding mechanical properties.<sup>3,4</sup>

## 1.2. Multilayer Polymeric Materials

Another approach used to combine properties of different polymers in a material is to produce multilayer films, with each layer consisting of a polymer with specific properties. These materials are widely used in the food industry. To guarantee the integrity and safety of the food, packaging films must have the following properties: strength (resistance to puncture, impact and tear), sealing and preservation against moisture (barrier to the transmission of water vapor in or out), oxygen (to reduce microbial activity), light (prevent light-induced changes in flavor or nutritional quality) and chemicals (prevent the food from absorbing unwanted substances from the environment). The use of a single material with all those properties is highly improbable. Hence the development of multilayer materials is of prime importance.<sup>5,6</sup> Figure 1.3 shows an example of multilayer material which is mainly composed of an outer layer of Nylon, responsible for the mechanical strength and scuff resistance, a layer of Ethylene vinyl alcohol (EVOH), which is an excellent gas barrier, and a layer of Low Density Polyethylene (LDPE), an inert polymer good for

food-contact. In order to ensure that the layers stick to each other, an adhesive layer called “tie layer” is often used.

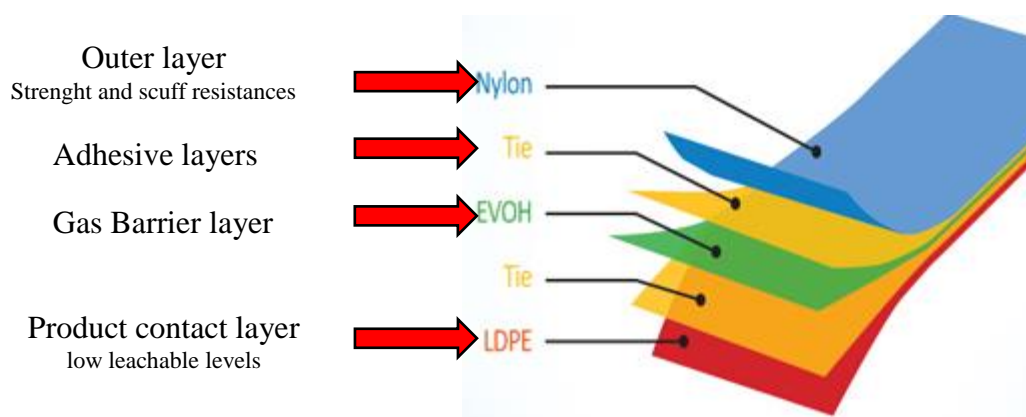


**Figure 1.3.** Example of multilayer polymer material composed of an outer layer of nylon, a gas barrier layer of EVOH and the contact layer of LDPE intercalated with adhesive layers

Multilayer processing creates interfaces between different materials and the adhesion between them is critical for the mechanical and barrier properties. To overcome this problem, it was necessary to develop adhesives layers, or “tie layers”, which are used between each different polymeric layer to enhance surface compatibility and to seal up any voids and defects. Common adhesives used on multilayers are based on reactive polyurethane chemistry, i.e, the reaction of an isocyanate with a hydroxyl group to form a urethane linkage. The isocyanate pre-polymer will always contain a portion of free diisocyanate monomer, which is consumed within the adhesive layer during the curing reaction. The major issue of this adhesive layer consists on the migration of unreacted diisocyanate through the layers into the food, in which it can react with water, forming amines. Some aromatic amines are potential carcinogens, thus, it is very important to study the nature of the materials used as adhesives and the efficiency of the curing process, in order to ensure the safety of the material for food application.<sup>5-9</sup> However these investigations are challenging due to the complexity of the final product and the low thickness of each phase.

For some other applications, the ability of selected additives to migrate through the layers can also be used to improve the multilayer properties. For example, Gherardi and coworkers<sup>7</sup> developed a procedure to incorporate antimicrobial agents in a multilayer material, based on a commercial packaging with a polyurethane adhesive free of isocyanate. They have studied the antimicrobial activity of the new films and the release of the active compounds. Mass spectrometric results showed that the compounds were released from the adhesive layer, crossing the material and reaching the food for antimicrobial action. On the other hand, the researchers claimed that a deeper research was necessary to study the correlation between their release rates and the thickness, chemical composition and structure of the adhesive layer. The characterization of the chemical profile throughout the cross-section of the multilayer film, for example with spectroscopy techniques, could have given insights on the specific layer limiting or controlling the release rate of the antimicrobial agents. The challenge for this kind of sample is to be able to properly open the membrane, if possible without an embedding, to avoid a chemical contamination of the material by diffusion of the embedding medium.

The gas barrier properties, often required for multilayer polymer materials (not only for food packaging), will depend on the nature of the gas and the properties of the polymers, such as the degree of crystallinity, cross-linking, polymer chemistry, glass transition temperature (Tg). The gas



barrier properties are highly affected by crystallization and orientation of the lamellae, as the chains packing affects the free volume available for gas transportation.<sup>10-15</sup> Cocca and coworkers<sup>16</sup> have studied the effect of crystal polymorphism on the mechanical and barrier properties of Poly(L-lactic acid) (PLLA). They have shown how the degree of crystallinity (crystal fraction) and the nature of the polymorph ( $\alpha$  or  $\alpha'$ ) affected the Young's modulus and elongation at break (Figure 1.4(a) and (b), respectively). The authors discussed how the transition from the  $\alpha'$  to the  $\alpha$  polymorph (higher chain packing and interchain interaction for the  $\alpha$  form) affected the mechanical properties of the material, improving Young's modulus but decreasing elongation at rupture. This transition from  $\alpha'$  to  $\alpha$  form corresponds also to the abrupt decrease of the water vapor permeability (WVP), shown on Figure 1.4(d), with somehow the same degree of crystallinity (very small increase of the crystal fraction). Correlation between optical microscopy and Wide Angle X-Ray Diffraction (WAXD) analysis was used to estimate the polymorphic composition of the PLLA samples, however, no quantitative determination was possible due to the very similar WAXD profiles of the two polymorphs.<sup>16</sup> This problem could be addressed by the co-localization of microscopies and spectroscopy techniques, which could have provided direct morphological and chemical information for the quantitative analysis of the nature of the phases in the samples.<sup>17</sup> Furthermore, the analysis of the distribution of polymorphs and the size of the crystallite in the samples could have explained the drop on the elongation at break and WVP for samples with almost the same degree of crystallinity (Figure 1.4 (c)).

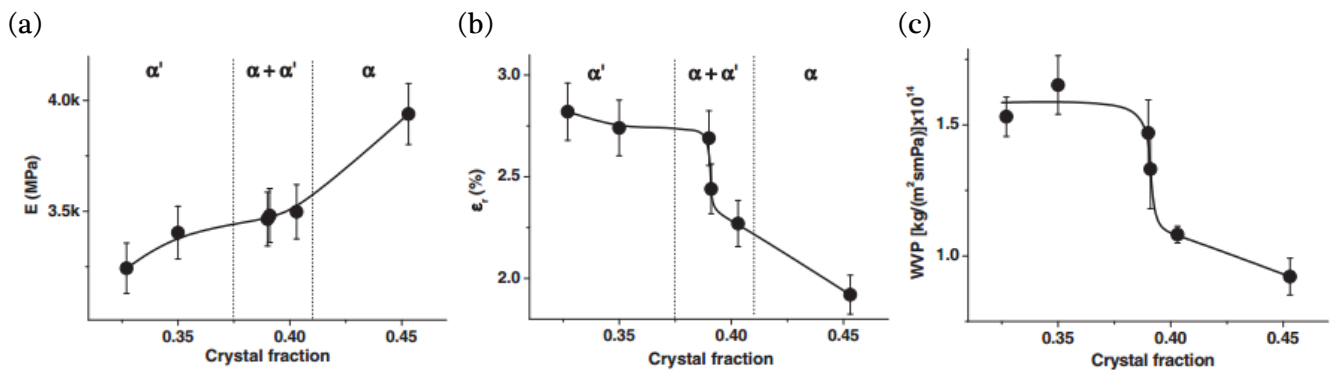


**Figure 1.4.** Different properties of PLLA films as function of the degree of crystallinity: (a) Young's modulus, (b) elongation at break and (c) permeability to water vapor (WVP). The crystal polymorphs are indicated for each degree of crystallinity.<sup>16</sup>

### 1.3. Fiber Reinforced Polymer Composites

A composite is a structured material that consists of two or more constituents which are combined at a macroscopic level and are not soluble in each other.<sup>18</sup> The matrix of the composite, generally continuous, can be a metal, a ceramic, carbon or a polymer. Embedded inside the matrix, the second constituent is the reinforcing phase, which can be of different natures (ceramic clays, polymers/ natural fibers, inorganic fillers...) and have a variety of forms and shapes, such as fibers, particles or flakes. The nature and shape of the secondary phase is mainly determined by the application or the properties that one wants to improve.

The most common use of the polymer composite strategy is for the enhancement of mechanical properties of the polymer itself. For this mean, fibers are generally used due to their high aspect ratio, i.e., the ratio between their length and diameter ( $l/d$ ). The performance of a polymer/fiber composite will be determined by the interactions between the matrix and the reinforcement. Indeed, the mechanical properties of the composite are mainly ensured by the fibers and a good charge transfer from the matrix to the fibers is necessary to reach the best performances. This load transfer is only effective if the fibers are well dispersed in the matrix and if the adhesion of the matrix on the fiber is good. Therefore the quality of the interface can be problematic when hydrophobic polymer matrices like Polyethylene are used with hydrophilic fibers like glass fibers for example. The incompatibility between the components leads to poor wettability during processing, creating discontinuities and voids at the interface, which are ineffective for load transfer and actually act like stress-concentration points, hampering the mechanical performance of the composite.

In order to improve and guarantee the interface bonding, a common strategy is based on the chemical modification of the fiber's surface using a sizing to improve their wettability by the matrix, and the creation of chemical bonds between the fiber's surface and the polymer matrix. For example, a sizing containing a coupling agent is commonly applied on glass fibers. The most common kind of coupling agents used are organometallic or organosilanes.<sup>19-23</sup> Organosilane precursors are molecules that contain two types of reactive functional groups (Figure 1.5): one capable of forming chemical bonds with inorganic materials and one capable of interacting with organic materials. The hydrolysis of the ethoxy or methoxy groups (O-X) in contact with water leads to the formation of silanol groups, which engender the creation of oligomers by partial condensation. The silanol dimers hydrogen bond to the surface of the fiber and then, through water condensation, chemical bonds are created between the coupling agent and the surface of the glass fibers. The reactive group R bore by the coupling agent (vinyl groups, epoxy, amino, mercapto, etc) is available to physico-chemical interactions with the chain of the polymer matrix, improving wettability, miscibility and forming chemical bonds or hydrogen bonds with polar matrices.

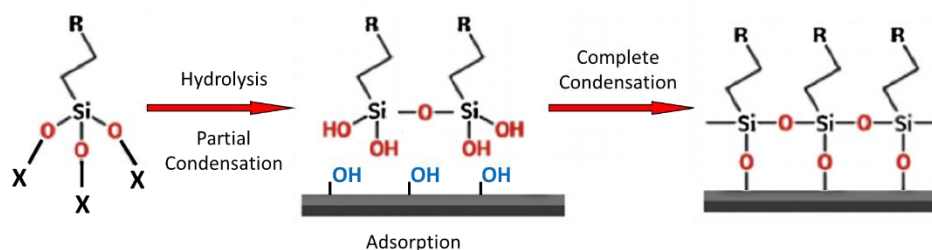


**Figure 1.5.** Scheme of reaction of hydrolysis and condensation of a silane coupling agent for surface modification of fibers. R: vinyl groups, epoxy, amino, mercapto; X: methyl or ethyl groups.

Other alternatives to the use of silane coupling agents have been developed with the use of reactive copolymers like Maleic Anhydride grafted on polyolefines.<sup>24-26</sup> For example, Guojun Luo *et al*<sup>24</sup> studied a polypropylene/glass fiber (PP/GF) composites prepared by treating GF with a film former (GFf) containing maleic anhydride grafted polypropylene (MPP) and a  $\beta$ -nucleating agent. The interfacial adhesion and the crystal morphology between GF and PP were observed by scanning electron microscopy (SEM) (shown on Figure 1.6) and the tensile and impact strength were measured (Table 1.1). The composite prepared with the non-treated commercial fiber (GFc) presented poor interfacial adhesion and a smooth GF surface was observed after debonding (Figure 1.6 (a)). This caused poor mechanical properties, i.e., no substantial improvement on tensile strength (from 27.1 MPa for PP alone to 31.3 MPa for the composite) and especially the impact strength, which dropped from 10.4 to 5.1 kJ/m<sup>2</sup>, as shown on Table 1.1. The interfacial adhesion was improved by the presence of the coating film. SEM images showed a layer of remnant polymer on the surface of the GFf after debonding (Figure 1.6(b)) and the tensile strength attained 61.8 MPa. With the addition of 2 wt% MPP, the covering polymer layer on the GF surface appeared thicker and with a roughen fracture surface. The fact that the impact strength attained 14.2 kJ/m<sup>2</sup> (roughly the double from the composite without MPP) evidenced the better adhesion interface. The authors verified that when the content of MPP was increased to 3 wt% and 10 wt%, the interface microstructures appeared nearly identical, with fibers completely covered (Figure 1.6 (c), (d) and (e)). On the other hand, the tensile strength of the composites increased from 61.6 MPa (3 wt% MPP) to 67.3MPa (10 wt% MPP), even though the interface microstructure was unchanged.

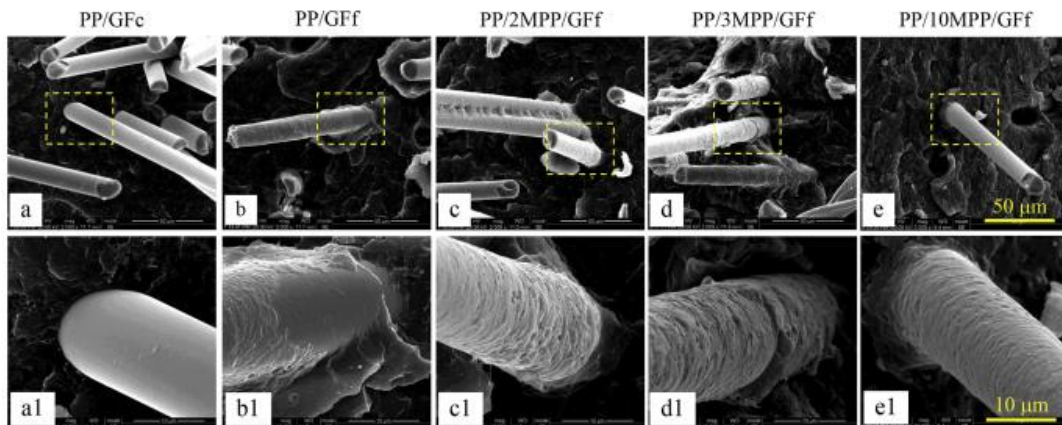


**Figure 1.6.** SEM micrographs representing the interfacial adhesion between GF and PP matrix for PP/GFc (a, a1), PP/GFf (b, b1), PP/2MPP/GFf (c, c1), PP/3MPP/GFf (d, d1) PP/10MPP/GFf (e, e1). (a1), (b1), (c1), (d1) and (e1) are enlarged areas marked by the dashed yellow squares in (a), (b), (c), (d) and (e) respectively.<sup>24</sup>

**Table 1.1.** Tensile and Impact strength of the PP composites<sup>24</sup>

Sample codes	Tensile strength (MPa)	Impact strength (kJ/m <sup>2</sup> )
PP	27.1	10.4
PP/GFc	31.3	5.1
PP/GFf	61.8	7.4
PP/2MPP/GFf	59.6	14.2
PP/3MPP/GFf	61.6	12.8
PP/10MPP/GFf	67.3	10.2

To understand the impact of the GF coating film on the crystallization process, the researchers monitored the isothermal crystallization by optical microscopy. On the one side, for PP/GFc sample, PP crystals nucleated randomly and grew into large spherulites, as shown on Figure

1.7(a). On the other side, in PP/Gff sample, nuclei were found concentrated near the surface of Gff, and after 600 s a layer of oriented crystalline lamellae was found surrounding the Gff. A SEM image of the etched fractured surface of this sample showed structures in the form of spikes grown perpendicular to the fibers, which were attributed to  $\beta$ -transcrystals. The very good adhesion of these crystals to the Gff surface (intimate contact between the two materials) is thus suspected to be responsible for the efficient stress transfer between the PP matrix and the GF. Structural, chemical and morphological analyses of these structures (by Confocal Raman for example) could have provided an unambiguous attribution of the crystals nature. In addition, nano-mechanical properties, such as adhesion and modulus profiles at the fiber-matrix interface could have been accessed by AFM in order to characterize the quality, integrity and continuity of the interface.

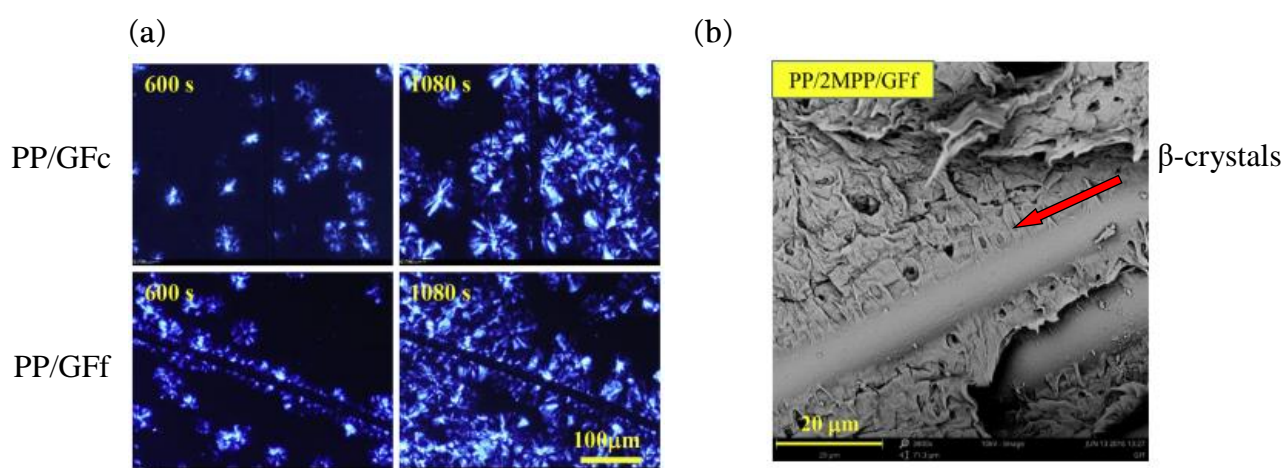


**Figure 1.7.** (a) Polarized optical micrographs during an isothermal PP crystallization at 135°C around a single fiber (GFc or Gff) (b) SEM micrograph of the etched fracture surface for PP/2%MPP/Gff injection molded sample. Adapted from <sup>24</sup>

The impact of the coupling agent at the fiber-polymer interface has to be studied at a local scale to be able to optimize the material's performances. Therefore the development of characterization methods that can provide direct probing of morphological, mechanical and chemical properties of the polymer-fiber interface/interphase could accelerate the progress in the field.

### 1.3.1. Polymer Nanocomposites

The complexity of composite materials increases when one of the fillers has at least one of its dimensions in the nano-range, turning it into a nanocomposite material. Usually nanocomposite materials have enhanced properties when compared to their non-nano composite equivalent.<sup>27-33</sup> Inorganic additives, like calcium carbonate, glass beads, talc and clay for example, were often used as fillers on polymer materials to reduce cost and enhance the mechanical properties, but the use of the corresponding nano-fillers has given them a much more functional interest.

As for the reinforcement fibers, the interface between the nanoclay and the polymer is determinant in the effectiveness of load transfer from the polymer matrix to nanofillers. As most polymers are hydrophobic, they are not compatible with hydrophilic nanoclays for example. This means that a simple mixing of the components would create agglomerates of nanoclay, which would lose their nano-dimensions. An exfoliation of the nanoclay and their perfect embedding by the polymer matrix is required to reach optimal performances. Figure 1.8 shows TEM images of an

agglomerated and an exfoliated nanocomposite.<sup>29</sup> The exfoliation and uniform dispersion of nanofillers in the polymer matrix can be achieved by means of surface modification of clays, like grafting and chemical treatments, solution induced intercalation process, in situ polymerization and melting process.<sup>27,29,34–37</sup> Pramoda and coworkers<sup>38</sup> studied how the mechanical and thermal properties of polyamide 6/clay nanocomposite are influenced by the exfoliation degree of the clay particles. They suggest that exfoliated nanocomposites exhibit higher onset temperature for degradation than those with agglomerated clay particles. Chan *et al.*<sup>30</sup> have used morphological characterization to tune their fabrication process in order to produce uniformly-dispersed samples. Thanks to the better dispersion, even when small amounts of nanoparticles from 1 to 10 wt% were incorporated in the polymer matrix, a substantial improvement of mechanical properties was achieved, e.g., up to 57% increase in Young's Modulus using 7 wt% of nanoclay inside an epoxy matrix. Improvements were also observed for exfoliated nanocomposites on their barrier properties, chemical resistance, reduced solvent uptake and flame retardancy: the exfoliated nanofillers making the diffusion pathway through the nanocomposite much more intricate.<sup>36,39–44</sup> Therefore nanocomposites require lower amounts of fillers than regular composites to reach comparable performances.<sup>29</sup>

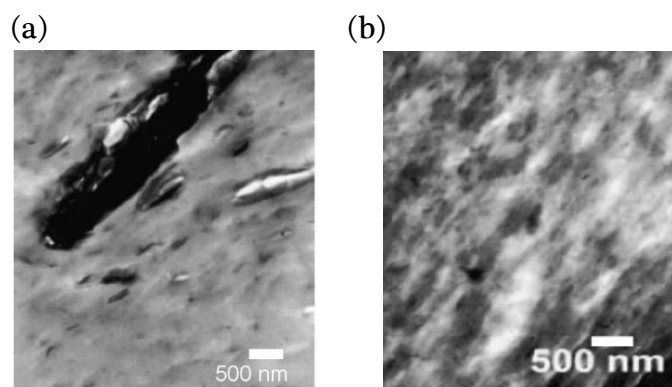


**Figure 1.8.** SEM image characteristic of nanoclay morphology in a 95/5 wt% Polyamide6-Montmorillonite nanocomposite: (a) agglomerated and (b) exfoliated.<sup>29</sup>

Inorganic nanoparticles can also have an impact on the crystallization of the polymer matrix by acting as heterogeneous nucleation sites. Smith and Vasanthan<sup>45</sup> have studied the effect of nanoclay on the crystallization kinetics and spherulitic morphology of poly(trimethylene terephthalate) (PTT)/nanoclay films. They have shown by polarized light microscopy (PLM) that the addition of 10 wt% of nanoclay had great impact on the size and distribution of the spherulites, as shown on Figure 1.9. The conformational changes induced were monitored by Infrared spectroscopy, indicating that nanoclay accelerates the polymer chain conformational transition from trans to gauche. Differences on crystallinity and/or on the crystal structure (polymorphism) have been shown to greatly impact the mechanical and thermal properties of composites.<sup>45–51</sup> The association of optical microscopy with spectroscopy techniques could have directly provided not only information about the conformational transition but also the distribution of the different polymorphic crystals induced by the presence of the clay, by probing the chemical structure of each crystal seen on the optical image.

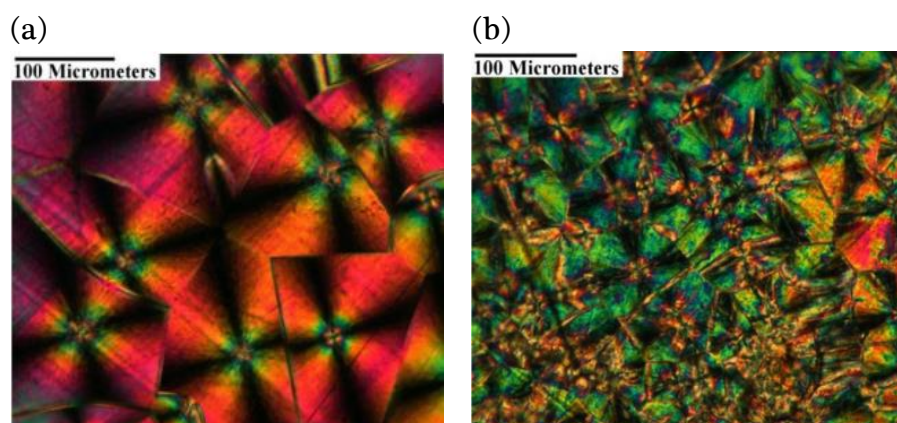


Figure 1.9. PLM photographs of (a) neat PTT and (b) PTT nanocomposite with 10wt% of clay. Adapted from<sup>45</sup>

#### 1.4. Block-copolymers

Block-copolymers, contrary to polymer blends, present covalent links between different polymeric materials usually immiscible, which gives very specific properties due to the resulting nanophase separation (self-assembly). The challenge on the development of these materials lies on the precise control of the nanostructure morphology. This can be achieved by tuning the molecular weight, monomer chemistry and processing temperatures, for example. When composed by two immiscible blocks, nanodomains dimensions can range from 5 nm to more than 100 nm, and the developed morphology can exhibit a big variety of symmetries, resulting into, for example, lamellae, cylinders, bicontinuous gyroids and even body-centered cubic arrays of spheres, as illustrated on Figure 1.10.<sup>52-54</sup>

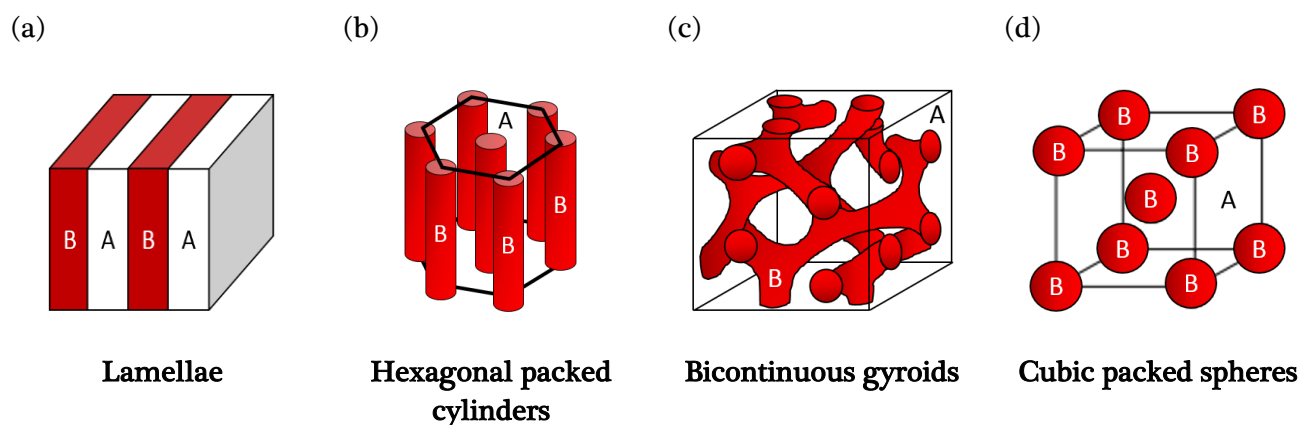
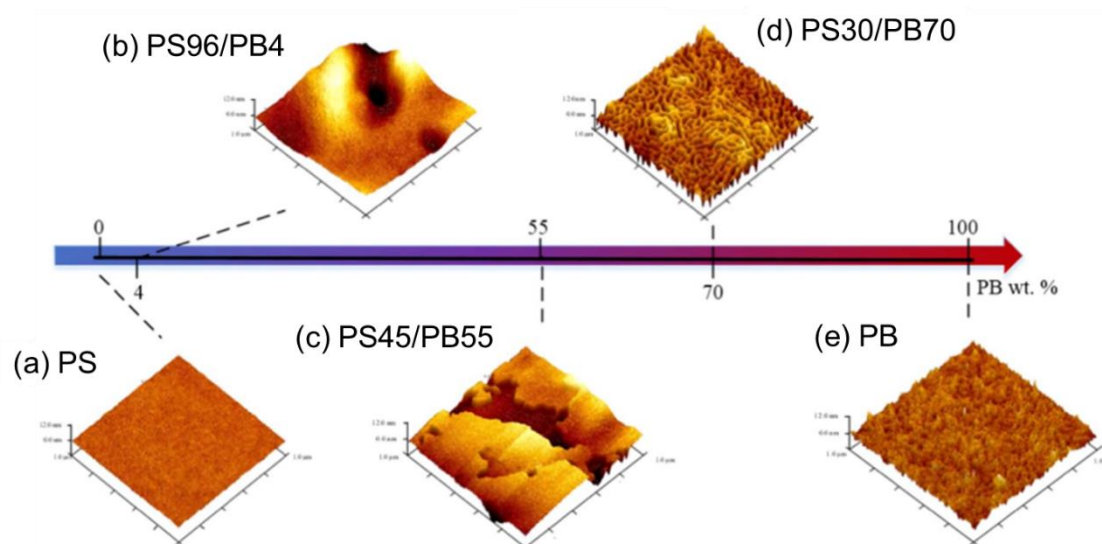


Figure 1.10. Example of copolymer morphologies: (a) lamellae (b) hexagonal packed cylinders (c) bicontinuous gyroids and (d) cubic packed spheres. Adapted from<sup>52-54</sup>

A good example of the impact of the copolymer morphology on its properties is given by Zhuang et al.<sup>55</sup> who studied for styrene-butadiene copolymer (SBC) membranes the impact of the polystyrene/polybutadiene (PS/PB) ratios on both the gas separation ( $\text{CO}_2/\text{N}_2$ ) performance and the ageing properties. They have detected different nanophase-separated structures by AFM at the surface of the copolymer membranes depending on the PS/PB ratios as illustrated on Figure 1.11. Three different morphologies were obtained: cubic lattice spheres of PB in a continuous PS matrix (4 wt% PB), PS and PB lamellae parallel to the membrane surface (55 wt% PB) and cylinders of PS in a continuous PB matrix (70 wt% PB). Crystalline regions inside the PS domain were observed in both samples rich in PB, which affected the gas transport due to the stable and regular molecular

structure of the PS domain. According to the authors, the synergism between the lamellar morphology and the presence of  $\alpha$  crystals in the PS phase increased the diffusion pathway for  $\text{CO}_2$  and simultaneously enhanced the  $\text{CO}_2/\text{N}_2$  selectivity. A similar result was obtained for the cylindrical structure, which presented  $\gamma$  crystals in the PS phase. The different spacing within the crystal lattice restricts the  $\text{N}_2$  transport but do not significantly affect the  $\text{CO}_2$  permeability. This leads to an even higher  $\text{CO}_2/\text{N}_2$  selectivity for the PS30/PB70 membrane. Furthermore, the researchers have shown that the cylindrical micro-structure of the PS30/PB70 membrane exhibited high ageing resistance under operation conditions, due to the morphological stability of the cylindrical micro-structure. The authors prepared these membranes by spin-coating, leading to a membrane thickness of about 10  $\mu\text{m}$ . For such thickness, the morphological analysis of the surface by AFM might be insufficient for the correlation of properties with the morphology, i.e., the development of the morphology through the membrane thickness may be considerably different from what observed at the surface. A cross-section analysis (after cryo-ultramicrotomy for example) would therefore be appropriate to get a deeper understanding of the obtained morphologies. In addition, co-localized confocal Raman spectroscopy may offer a mapping of the PS  $\alpha/\gamma$  crystals distribution and ageing effects on the bulk of the membranes.



**Figure 1.11.** AFM topographic images on the membrane's surface of (a) PS, (b) PS96/PB4, (c) PS45/PB55, (d) PS30/PB70 and (e) PB. Adapted from <sup>55</sup>

## 2. Bulk vs Surface Properties

As discussed on the previous sections, the properties of polymeric materials depend on their nanostructure, the proper control of phase separation, the dispersion and distribution of charges and the quality of interfaces, all of these parameters being potentially variable through the material thickness. The resulting heterogeneities of properties can be induced by the processing methods, or tailored intentionally to achieve specific distinct properties for the surface and the bulk. In addition, after ageing, materials become generally heterogeneous in terms of chemistry, morphology and mechanical properties, due to the inhomogeneous degradation process through the material (surface/bulk).

Processing of thermoplastic polymers is mainly related to the application of shear to the molten material at high temperature followed by high thermomechanical stresses due to the rapid cooling of the material at the end of the process. Therefore, the thermomechanical history may not

be homogeneous throughout the whole thickness of the material, inducing differences in the local order of the polymer chains and the distribution of additives. This can result in different morphologies in terms of molecular orientation, lamellar thickness, crystal structure, shape and dimensions, crystallinity degree, orientation of the amorphous phase, dispersion state of a blended polymer, length and orientation of reinforcing fibers and crystalline texture (skin-bulk structure), since the kinetics and morphology of crystallization are intrinsically related to the flow and cooling regimes.<sup>56</sup> In injection molding, for example, the surface morphology is highly affected by the thermomechanical stresses induced by the rapid cooling of the chains when in contact with the cold mold and the orientation of the chains caused by shear stress. Liparoti and coworkers<sup>57</sup> performed a multiscale mechanical characterization of isotactic polypropylene (iPP) injection molded samples. The developed morphologies were characterized by polarized optical microscopy and AFM, as shown on Figure 1.12.

They revealed a complex multilayer morphology composed of globular elements, fibrils and spherulites, from the surface to the bulk of the sample. The thickness of the different layers was correlated to the injection molding conditions (packing pressures and mold temperatures). The authors also evidenced a correlation between the local mechanical properties and the different morphologies formed along the sample thickness. At the sample's surface, the cooling rate is the highest, which does not allow the crystallization of the macromolecules, therefore low modulus is found. Further from the surface, as the cooling rate decreases, the macromolecules can align themselves and, due to the stress induced by the flow, form compact structures characterized by higher moduli in the shear layer. As the bulk of the material takes more time for cooling and is less affected by the shear, the polymer chains have more time to crystallize, forming spherulites. Thus, flow and thermomechanical stresses will cause a gradient of different morphologies from the surface to the bulk.

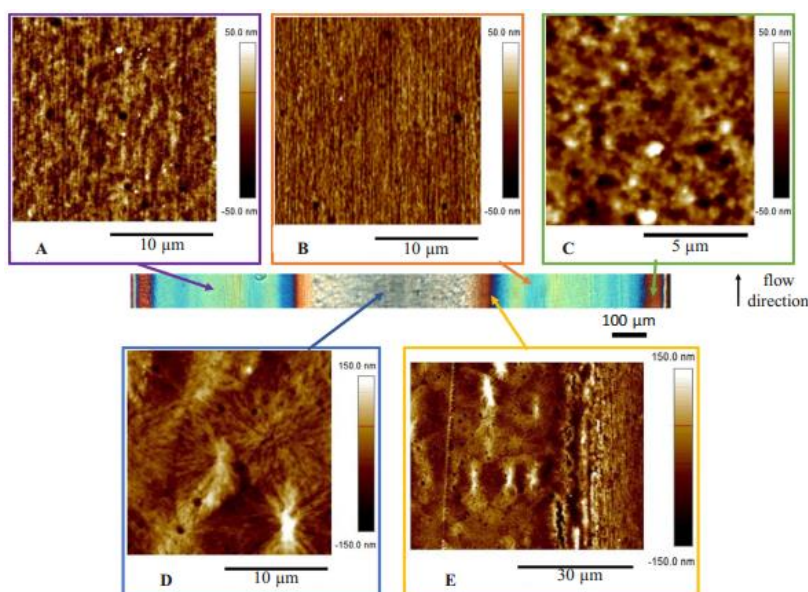


**Figure 1.12.** Morphology profile through the material thickness detected by optical microscopy (central micrograph) and by AFM height maps. The positions where the analyses were performed are indicated by arrows pointing on the cross section optical micrograph.<sup>57</sup>

Important material properties such as optical, chemical, electrical and ionic transport can be tuned by adjusting the material's morphology or gradient of morphologies. For example, the properties of polymeric materials used as membranes for filtration, or separation of gases and



liquids, will depend on both the surface and the bulk properties. On the one hand, the selective sorption of molecules on the membrane's surface is controlled by the morphology, roughness and chemical properties at the surface (hydrophilicity/hydrophobicity, chemical affinity, etc.) and on the other hand, the diffusion of these absorbed molecules through the thickness of the material is controlled by the bulk morphology, dispersion of charges, cross-linking degree, etc.<sup>58-63</sup> Wei Zhang and coworkers<sup>63</sup> have studied the pervaporation performance of polymeric chitosan membranes by simultaneously changing their surface and bulk structures. To adjust the degree of crystallinity of the membrane's bulk they tuned the pre-drying processing step (the shorter this step the lower the degree of crystallinity of the bulk). A lower crystallinity implied that the transport of the permeation molecules was faster, i.e., a membrane with a less compact structure exhibited a higher flux, however it had a lower separation factor. In order to improve selectivity they functionalized the membrane's surface with maleic anhydride. After modifying both the bulk and the surface of the membranes the authors improved by 400% the separation factor and by 60% the flux. They concluded that the combination of bulk modification by pre-drying treatments and surface functionalization was an effective method to simultaneously improve both the permeability and permselectivity of polymeric membranes, but they claim that further research needs to be done in order to understand the relationship between the membrane's bulk characteristics and the pervaporation process. The clear and direct characterization of both the membrane's bulk and surface remains therefore the main technical challenge to be solved.

Ageing is another source of surface/bulk heterogeneity. It results of complex physical and chemical interactions, such as physical creep and relaxation, chemical degradation by oxidation, chain scission and hydrolysis, induced from the operating conditions: high mechanical stresses, mechanical and thermal cycling, attack by chemical agents or UV light exposition, for example. These complex interactions affect the surface and the bulk of the material in different ways. For example, during the thermal ageing of polymers, the bulk can be affected by structural and morphological changes caused by temperature-induced transitions, while the surface is mainly affected by thermo-oxidative degradation, which is limited to a thin surface layer up to a few tens of micrometers, depending on the kinetic of oxidation of the material. The surface contamination of the material by fuels, lubricants and chemicals can diffuse through the thickness of the material over time. Reciprocally, additives such as plasticizers or stabilizers can migrate from the bulk to the surface of the material over time. These diffusion processes and the chemical reactions involved in the ageing mechanism are affected by the nature of the material (selective sorption of molecules on the surface), the state of order and morphology in polymer blends, multilayers and composites, as well as the nature, size and dispersion of charges, and porosity distribution. Thus, during ageing, a gradient profile is formed inside the material. Therefore, the understanding of the mechanisms and kinetics of diffusion and degradation from the surface to the bulk, and of the effects of morphological and chemical changes on the material properties offer a chance to develop ageing mitigation strategies.<sup>64,65</sup>

## 2.1. Characterization of both the Surface and Bulk of Polymer Materials

This section will focus on the experimental techniques classically used for chemical and morphological characterization of both the surface and bulk of polymer materials.

The characterization techniques used for probing the chemical properties of surfaces are based on vibrational spectroscopies and backscattered radiation. The most common vibrational spectroscopies used are Fourier Transform Infrared Spectroscopy (FT-IR) and Raman spectroscopy. These techniques use the frequency-dependent absorption or emission of radiation from chemical bonds and structures, in order to identify and quantify components or chemical groups in the

structure. For IR spectroscopy, Diffuse Reflectance FTIR (DRIFTS) and Specular Reflection FTIR are used for the characterization of rough surfaces (powders) and smooth surfaces, respectively. Attenuated Total Reflection Fourier Transform Infrared Spectroscopy (ATR-FTIR) is the most popular technique for surface analysis due to the short penetration depth (~1 to 5  $\mu\text{m}$  depending on the crystal used and the wavenumber), allowing the characterization of a large area (~1  $\text{mm}^2$ ) of the top layer of the material. Raman spectroscopy is a complementary technique to IR spectroscopy, because some vibration modes are inactive in IR and active in Raman, and vice-versa, allowing the complete chemical characterization of the material. Energy Dispersive X-ray Spectroscopy (EDS or EDX) is a technique based on the interaction of the material with an electron beam, and is used for identifying, quantifying and mapping elements on the surface of the material. X-ray photoelectron spectroscopy (XPS) has a lateral resolution from 1 mm to 10  $\mu\text{m}$ , but a depth resolution of tens of nanometer, being particularly suitable for elementary analysis of modified surfaces, such as plasma-treated or oxidized surfaces, thin coatings or grafted polymers on the surface.

The characterization of the physical properties of the surface include the morphology, topography, crystallization, microphase separation, as well as size, shape, distribution and orientation of charges which can be analyzed by direct observation, e.g., using optical or electron microscopies.<sup>66</sup> Optical Microscopy is a low-resolution (classical resolution roughly about 0,5-1  $\mu\text{m}$ ) and low-magnification technique (from 2x up to ~2000x) used to provide a first look at the surface, due to its easy sample preparation, low cost and simple principles of operation. Scanning Electron Microscopy (SEM) is widely used for the characterization of surfaces with high magnification (up to 500000x) and high resolution (5~10 nm) and can provide additional interesting information depending on the interactions of the electron beam and the specimen used to obtain the image. Using separate detectors for Backscattered Electrons (BSE/ sensitive to electronic density) and Secondary Electrons (SE/ sensitive to surface topography), compositional and topographic images of the same area may be produced. Finally, Atomic Force Microscopy (AFM) is an advanced technique for surface analysis based on the interaction of a scanning probe with the sample's surface. Three dimensional topographic images are obtained, giving access to morphological measurements, including roughness. The lateral resolution will depend mainly on the tip radius of the probe (typically ~5-10 nm). The substantial developments of the past years have enabled different modes of operation, allowing probing the mechanical, thermal, electrical and magnetic properties of the material's surface with a high spatial resolution.

The characterization of the bulk properties is usually performed using techniques that probe the material as a whole, averaging the response of the surface and the bulk. For example, Differential Scanning Calorimetry (DSC) and Dynamic Mechanical Analysis (DMA) are used to evaluate the thermomechanical behavior of the material, providing insights on phase transitions, miscibility of components, crystallinity and degree of crosslinking. However in order to do a direct observation and probe the bulk of the material (without surfaces), special techniques are required to open the sample for optical/electron microscopies, AFM imaging (topography, mechanical, etc.) and chemical mapping (Raman,  $\mu$ -ATR-FTIR), which will be discussed in the next section.

## 2.2. Sample Preparation Techniques for Bulk Direct Observations

The most used and simple technique to access the bulk of a material is the cryo-fracture, in which the polymer is cooled in liquid nitrogen (-196°C), in order to induce afterward a brittle fracture in the rigidified material at its glassy state. The sample is then installed or glued to a support and the surface is imaged using a microscope (generally SEM). Although easy to prepare, the surface is not always representative of the inner morphology of the membrane. The

unpredictable brittle fracture creates irregular rough surface which can follow the material heterogeneities, like particles or phases with different mechanical properties, making difficult to understand the real morphology of the material. Other advanced techniques used to provide better cross-sections are Cryo-Ultramicrotomy and Focused Ion Beam (FIB). Cryo-ultramicrotomy is based on the use of a diamond knife operating at cryo temperature to cut ultrathin slices (down to 50 nm) of the material's surface with controlled cutting speed, angle and depth. FIB cross-sectioning uses a high energy (~30 kV) ionic beam, typically gallium, of 10 nm to 1  $\mu\text{m}$  in diameter to cut the sample surface with controlled parameters. Both techniques can provide surfaced samples with very flat surfaces and minimum artifacts for direct observation by Optical Microscopy, Scanning Electron Microscopy (SEM), Atomic Force Microscopy (AFM) and can also provide thin sections (~50 nm) for complementary morphological analysis using Transmission Electron Microscopy (TEM).<sup>67-69</sup> An advanced discussion of these sample preparation techniques will be presented on Chapter 2.

### 3. Polymer membranes

For polymer films/membranes, the need to distinguish the surface from the bulk of the material becomes even more crucial than it can be for massive polymer products. Indeed the properties gradients that can be found from the surface to the bulk of the membranes can develop at length scales comparable with the membrane's thickness. A polymer film is a continuous planar material which is flexible and "free-standing", with thickness ranging from a few hundreds to tenths of micrometers, in opposition to ultrathin films (thickness at nanometer scale) coated on a substrate.<sup>70</sup> Polymer films can be made of a single material or multiphase systems (blends, composites, multilayers) and are commonly used as barriers for separation of two mediums, like in packaging, or electrical insulators for wires and cables. The term membrane is often used to designate polymer films with specific functionalities of technological interest, i.e., it can be considered as an interphase between two mediums acting as a selective barrier, responsible for the regulation of gas transport, diffusion of liquids or ions between each side of the membrane.<sup>71</sup> Due to these functionalities, membranes are widely used for technical applications, such as desalination of water through reverse osmosis, nanofiltration, dialysis, separation of molecules, liquids or gases, and ion exchange electrolytes for fuel cells and electrolyzers. Due to their technological importance, this section will focus on membranes rather than polymer films.

Membranes can be manufactured by a variety of processes, such as extrusion of the polymer melt, hot pressing, polymerization on substrates and casting by solvent evaporation. Each method induces different morphologies (orientation, asymmetries) on the surface and through the thickness of the membrane, which can deeply affect their functional properties. Figure 1.13 represents the different questions of interest on the surface and the bulk of polymer membranes. However, distinguishing the chemical and physical contributions from the surface and the bulk on these low thickness materials can be difficult due to the experimental issues on accessing, probing and differentiating properties and morphologies.

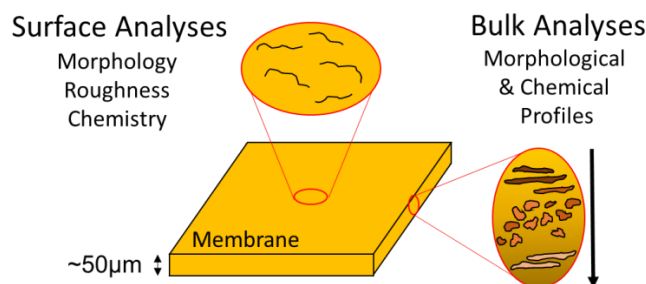


**Figure 1.13.** Schematic representation of the different properties to be characterized on the surface and the bulk of membranes

For this purpose, the use of multiple characterization techniques is at the same time essential and challenging, each technique imposing their own particularities in terms of cost, resolution, sensitivity and dimensions of the probed area.<sup>72</sup> Therefore, this thesis focused on the development of new methodologies and strategies for sample preparation and characterization, allying morphological, physical and chemical information, to contribute to the advance study of the process-structure-properties relationships of a variety of heterogeneous or multiphase polymeric systems, especially when processed into membranes.

#### 4. Manuscript Structure

This manuscript will be composed by the following chapters:

##### **Chapter 2: Co-localized AFM/Raman and Complementary Analyses**

In the second chapter, we will present an introduction to the fundamentals of each technique used to study complex polymer systems. Special attention will be given to AFM and Confocal Raman spectroscopy, being the techniques chosen to be the basis of our multiscale characterization approach for co-localized chemical, nanomechanical and morphological analysis. The techniques most suitable for sample preparation will be presented, as well as the specific technical challenges associated to the characterization of polymer membranes.

##### **Chapter 3: Experimental Methods and Developments**

The third chapter will be focused on the methodology used and experimental developments done for sample preparation by cryo-ultramicrotomy, as well for the co-localized AFM/Raman analyses and complementary techniques (SEM, STEM and  $\mu$ -ATR-FTIR). A specific technique of co-localization has been developed in order to ensure the acquisition of physical, morphological and chemical data on the same area.

##### **Chapter 4: Compatibilization of Polymer Blends based on PA6/ABS**

The co-localized methodology will be used to study the compatibilization of PA6/ABS polymer blends. The interest, accuracy and complementarity of co-localized AFM and Raman analysis will be demonstrated by elucidating the effect of the compatibilizer and blending protocol on the blend's morphology and on the PA6 crystallization's polymorphism ( $\alpha$  and  $\gamma$  phase amount and distribution in the blends).

### **Chapter 5: Hybrid Membranes for Fuel Cell**

This chapter will be dedicated to the study done on alternative membranes for Fuel Cell operation, based on the hybridization of a sulfonated polyether-etherketone (sPEEK) membrane with an active network by sol-gel chemistry. Thanks to the technical developments specific for membrane characterization presented on Chapter 3, we will demonstrate the impact of each step of fabrication on the membrane's morphology, nanomechanical properties and stability over time of two different hybrid membranes.

### **Chapter 6: Copolymer Electrolytes for Lithium Batteries**

At last, chapter 6 will focus on the study of the bulk morphology of new Lithium batteries electrolytes made of Polyethylene Oxide (PEO) based copolymers with different structures. Challenges lay in sample preparation due to the high hydrophilicity of the materials, which implied special development for proper sample characterization without modification induced by water adsorption. The effect of the copolymer structure on the morphologies will be shown by AFM and compared to previously done Small Angle X-Ray Scattering (SAXS) experiments, providing a clear morphological determination and evaluation of nanomechanical properties.

# CHAPTER 2

---

## Co-Localized AFM/Raman and Complementary Analyses

## PROLOGUE

Complementary characterization techniques must be used for the complete understanding of the process-structure-properties relationship of materials and this implies a full knowledge of the physical, morphological and chemical properties through the material thickness. Our strategy is based on the co-localization of morphological, nanomechanical and chemical information acquired from AFM/Raman but also by complementary techniques like Optical Microscopy, Electron Microscopies ( Scanning Electron Microscopy (SEM) and Scanning Transmission Electron Microscopy (STEM)) and finally by micro-Infrared Spectroscopy ( $\mu$ -ATR-FTIR).

In this chapter, the fundamentals of AFM and Raman micro-spectroscopy will be presented and the accessed information, resolution and limitations of each will be discussed in order to define the best way to perform efficient co-localized analyses. As a key step is the sample preparation, the techniques giving access to the bulk of the material as Cryo-fracture, Cryo-ultramicrotomy and Focused Ion Beam milling will be described. A brief introduction to each technique will be presented, discussing the methods, limitations and potential artifacts.

### French Prologue

Une compréhension complète de la relation mise en œuvre-structure-propriétés d'un matériau implique une connaissance approfondie de ses propriétés physiques, morphologiques et chimiques dans tout son volume et implique donc l'utilisation de techniques complémentaires. La stratégie développée est basée sur la co-localisation des informations morphologiques, nanomécaniques et chimiques acquises par AFM et par Raman, mais aussi par des techniques complémentaires comme la microscopie (optique, électronique à balayage (SEM) et à transmission (STEM)) ou la spectroscopie micro-infrarouge ( $\mu$ -ATR-FTIR).

Dans ce chapitre, les fondements de la micro-spectroscopie AFM et Raman seront présentés et les informations acquises, la résolution et les limites de chaque technique seront discutées afin de définir la stratégie la plus efficace pour réaliser des analyses co-localisées de la même zone d'intérêt. Une étape clé étant la préparation d'échantillon, les différentes techniques permettant d'ouvrir le matériau telles que Cryo-fracture, Cryo-ultramicrotomie et découpe par un faisceau d'ions (FIB) seront présentées. Une brève introduction à chaque technique sera présentée, en discutant les méthodes, les limites et les artefacts potentiels.

## 1. Fundamentals of Atomic Force Microscopy

AFM is a high-resolution method based on the use of a very sharp probe installed on a cantilever to scan the sample surface. A laser beam is constantly reflected from the top of the cantilever towards a position-sensitive photodetector, which detects the deflection of the cantilever and calculates its Z position (Figure 2.1). In contact mode, for example, an electronic feedback loop is used to keep the cantilever deflection constant during scanning, i.e., the feedback adjusts the height of the probe support along the Z axis so that the deflection is kept constant to a user-defined value (setpoint). In this situation, the feedback output equals the sample surface topography to within a small error. The image is then built by scanning the sample's surface line by line at a constant frequency rate using a xyz piezoelectric scanner. Thanks to this scanning probe microscopy (SPM) imaging technique, the resolution is not limited by diffraction, but depends on the size and shape of the probe, generally a tip radius of curvature of less than 5 nm is used for accurate surface analysis.

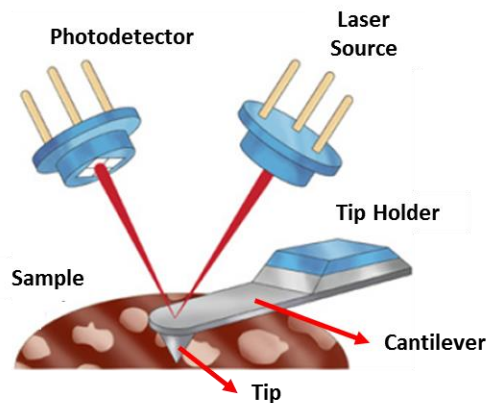


**Figure 2.1.** Basic setup for AFM analysis showing the reflection of the laser on the cantilever surface towards the photodetector. Adapted from <sup>73</sup>

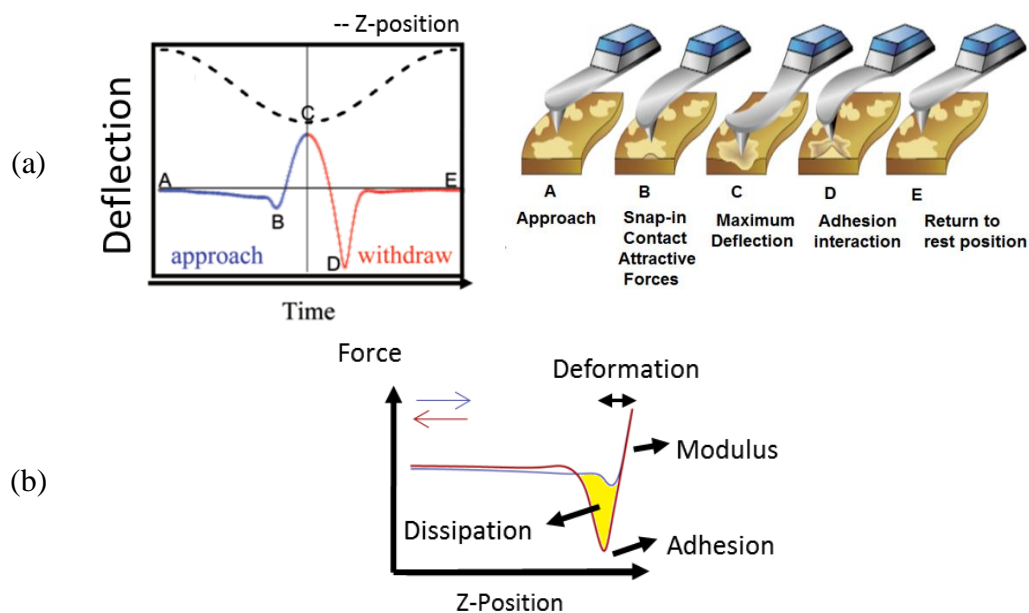
Since the introduction of the Atomic Force Microscopy by Binnig in 1986<sup>74</sup>, a substantial development of the system capabilities has been done. Different modes of tip-sample interaction can be used to image the sample. The most basic one is the Contact Mode, in which a piezoelectric ceramic raises or lowers the cantilever in order to maintain a constant deflection (cantilever motion on the Z direction) and therefore a constant contact force, as it scans the imaged area.<sup>75,76</sup> In order to overcome the drawbacks of the Contact Mode, like the high lateral friction forces, researchers have developed the Tapping Mode in 1993. In Tapping operating mode in air, a piezoelectric ceramic installed in the tip holder makes the cantilever oscillates a little bit below its resonance frequency. The tip oscillates vertically and touches or "taps" the sample's surface at a constant frequency during the scan. Due to the intermittent contact with the sample, the lateral friction forces between the tip and the material are minimized, thus minimizing damage to the sample and improving the durability of the probe. The feedback loop adjusts the height of the scanner to keep a constant oscillation amplitude of the cantilever (setpoint), therefore, topographic information are collected.<sup>77</sup> The mechanical interactions between the probe and each component of the material can engender a shift between the phase of the imposed oscillation by the piezoelectric ceramic and the phase measured by the photodiode. Especially for adhesive and viscoelastic samples, it allows the formation of a "phase image" consisting of an overlap of properties (modulus, adhesion, etc.). In 2008 an operation mode called Harmonix was released, allowing the reconstruction of the force-distance curves from the lateral deflection signal, and the extraction of quantitative mechanical



data. However, it required special asymmetric probes and the operation and interpretation of the results was difficult. To overcome these difficulties, the PeakForce QNM (Quantitative NanoMechanics) mode was introduced in 2012, with a relatively simple operation process possible to use with any kind of probes. An oscillation of the cantilever in the Z-direction at 2 kHz is imposed by the piezoelectric scanner, which also controls the xyz displacements. 2 kHz is a much lower frequency than the resonant frequency of typical probes (50 – 300 kHz). This mode of operation allows for acquiring force-distance curves in real time (2000 per second), as well as their analysis, meaning the simultaneous mapping of mechanical information like Young's modulus, adhesion, deformation and dissipation along with the classical topography image. These mapping therefore have the same nanometric lateral resolution as the topography image.<sup>78,79</sup> The fundamentals of PeakForce QNM will be presented in the next section.

### 1.1. Fundamentals of PeakForce Quantitative NanoMechanics (QNM)

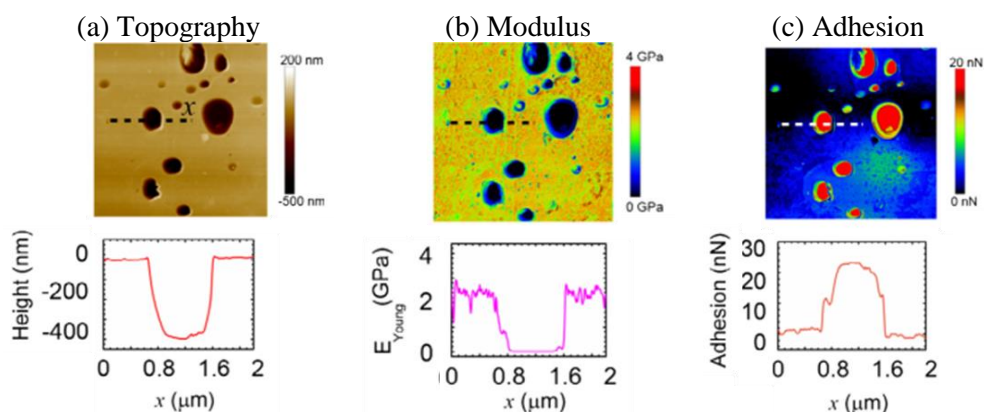
The PeakForce QNM is based on the control of the cantilever deflection. A feedback-loop imposes a setpoint to the maximal value of the deflection, and therefore the maximum force applied on the sample, called the Peak Force. In order to understand how the imaging control is done, one should first analyze the dynamics of the tip-sample interaction. Figure 2.2 represents the Z position of the cantilever (dashed line) over time as the piezoelectric system approaches the tip, touches the surface and retracts to the original position. At the same time, the deflection of the cantilever is followed on the approach and withdraw motions, represented by the blue and red lines respectively. From point A to point B, the figure represents the approach of the cantilever. As the tip gets closer to the sample, attractive forces (Van der Waals force, dipole-dipole interactions and electrostatic forces) overcome the cantilever stiffness and pull the tip over the surface (point B), causing a downward deflection of the cantilever called the “snap-on”. The tip stays in contact with the surface and the deflection increases until the Z position of the modulation reaches its bottom limit position (maximum deflection) at point C. While the probe is retracted from the surface, the deflection decreases accordingly. Adhesion interactions, usually capillary meniscus between tip and surface prevent the probe from retracting from the surface, causing a downwards deflection, characterized by a minimum peak on the curve (point D). Finally, the cantilever deflection goes back to zero when the adhesion forces are overcome, and then damped oscillations are usually observed for low spring constant cantilevers (not represented here) up to the zero deflection position (point E).



**Figure 2.2.** (a) Schematic representation of the tip-sample interaction dynamics<sup>79</sup> (b) Force-distance curve obtained from the tip-surface contact with the approach in blue and the retraction in red. Different mechanical properties are extracted from the curves: Modulus from the slope of the linear part, Adhesion from the minimum force of the retraction curve, Deformation calculated from the distance in separation from the point of contact to the maximum load on the approach curve, and Dissipation of energy as the area between the approach and retraction curves (yellow area).

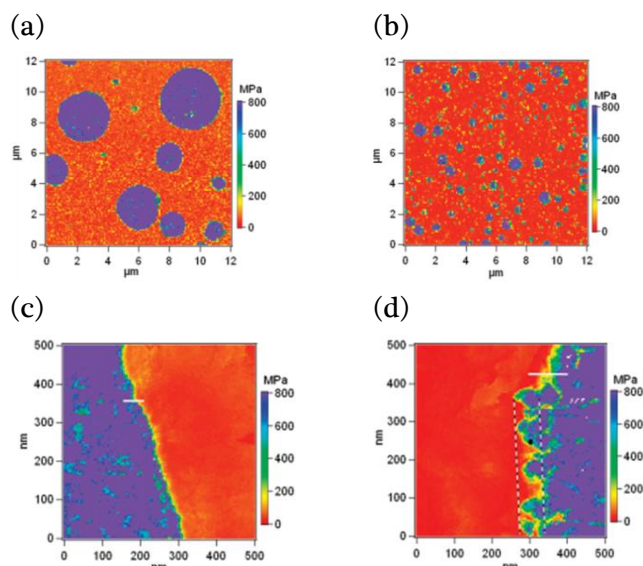
From the determination of the cantilever spring constant, one can transform the previous diagram of the deflection as a function of time (Figure 2.2(a)) on a force-distance curve, as shown on Figure 2.2(b). When scanning the sample surface, the tip oscillates in the Z-direction with a frequency of 2 kHz (2000 force-distance curves per second). A minimum of 2 force-distance curves is necessarily averaged for each pixel of the image. For typical 512 x 512 pixels images, 2048 force-distance curves are needed to achieve the 512 + 512 pixels of each line (trace and retrace). Therefore the maximum scan frequency is then 0.977 Hz for such a resolution. The change in Z-position used as the distance between the tip and the sample must be corrected considering the deflection of the cantilever. The corrected distance, called separation, is then calculated by subtracting the cantilever deflection from the Z-position. The real-time analysis of half a million force-distance curves per image allows the acquisition of mechanical mappings: modulus (from the slope of the linear part of the retracting curve), adhesion (minimum force of the retracting curve), deformation (calculated from the distance in separation from the point where the force is zero to the maximum load on the approach curve) and energy dissipation (area between approach and retraction curves).

Figure 2.3 shows an example of the application of the technique to a polylactic acid (PLA)/natural rubber (NR) blend by Martínez-Tong and coworkers.<sup>80</sup> Topography, elastic modulus and adhesion maps were obtained simultaneously, revealing the morphology of the blend on an area of  $5 \times 5 \mu\text{m}^2$  (Figure 2.3 (a), (b) and (c), respectively). The PLA matrix appeared with a Young's modulus of about 2.4 GPa and an adhesion close to zero. NR appeared like droplets with diameters ranging from 50 to 1000 nm, a mean modulus value of 12 MPa and high adhesion (near 20 nN). This was attributed to the rubbery characteristic of NR ( $T_g = -73^\circ\text{C}$ ) in comparison to that of PLA ( $T_g = 58^\circ\text{C}$ ).



**Figure 2.3.**  $5 \times 5 \mu\text{m}^2$  AFM PF-QNM images of (a) topography, (b) Young's modulus and (c) adhesion force presented with their corresponding profiles, along the dashed line indicated in the corresponding image. Adapted from <sup>80</sup>

As another example, Dong Wang and coworkers<sup>81</sup> were interested on the morphology of blends based on polyolefin elastomer (POE)/polyamide (PA6) compatibilized with POE grafted maleic anhydride (POE-g-MA). They have used nanomechanical mappings to reveal morphological differences on the distribution of the PA6 domains dispersed in the POE matrix and the POE/PA6 interface of the blends. Figure 2.4 (a) shows characteristic image of a non-compatible blend with droplets of PA6 of high modulus (2.5GPa – purple on the image) with sizes ranging from 2 to 4  $\mu\text{m}$ , dispersed in the low modulus POE matrix (23.5 MPa/red). The compatibilized blend (Figure 2.4 (b)) presented a homogeneous and fine dispersion of the PA6 phase with sizes of less than 1  $\mu\text{m}$ . Figure 2.4 (c) and (d) show the mapping of the mechanical properties at the interface of the uncompatibilized and compatibilized blends, respectively. The uncompatibilized interface appears with a neat phase separation, whereas the compatibilized interface is much rougher, due to the increased interdiffusion of the phases. Other recent studies probing nanomechanical properties of compatibilized blends and hybrid films can be found in the literature.<sup>82–84</sup>



**Figure 2.4.** AFM modulus images of (a) uncompatibilized POE/PA6 and (b) reactive compatibilized POE-g-MA/PA6 blends. Interfacial roughening observed with nanomechanical mapping: (c) POE/PA6 and (d) POE-g-MA/PA6 blends.

## 1.2. System Calibration for Quantitative Nano-Mechanical Measurements

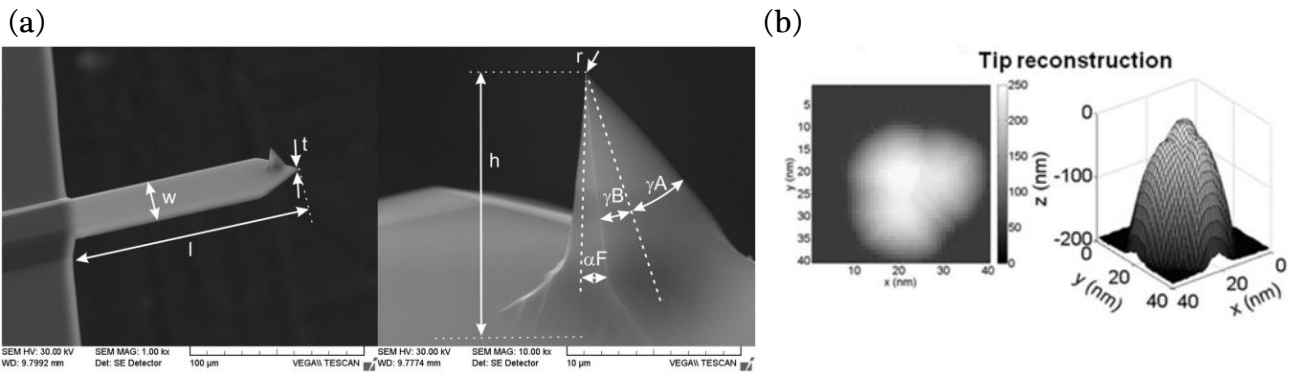
To measure quantitative mechanical properties one needs to control the calibration procedure, as well as the operating conditions. First of all, calibration should take into account mainly three aspects:

- Cantilever/Photodetector's deflection sensitivity;
- Cantilever's spring constant;
- Dimensions and shape of the tip.

The deflection sensitivity of the cantilever/photodetector provides a relationship between cantilever deflection (nm) and the potential change across the photodetector (V), which is the main parameter used for feedback control. This parameter depends on the properties of the probe, the laser alignment and the quality of the laser reflection on the cantilever. The deflection sensitivity is often measured by doing an indentation ramp on a hard sample like sapphire or fused silica (non-deformable). The downward motion of the probe on the sapphire's surface is recorded (Z-direction) and directly correlated to the potential change of the photodetector, since there is no sample deformation.

The spring constant of the cantilever can be determined by different methods, the usual one being the measurement of the Thermal Tune noise and the Sader methods. An interlaboratory study evidenced that the determination of the cantilever's spring constant is a crucial step, as the simple use of the nominal spring constant given by the manufacturer can result into errors up to 125%.<sup>85</sup> The Thermal Tune noise method is based on the acquisition of the thermal amplitude fluctuations versus frequency from which the spring constant of the cantilever can be calculated. The Sader method extracts the cantilever spring constant in the fundamental resonance mode from the dimensions of the cantilever as well as its resonant frequency, the density of the surrounding medium (usually air), and the local Reynolds' number. This method has been shown to work well for cantilevers with a rectangular section, over a wide range of spring constants. However, precise measurements of the cantilever dimensions, fluid density and the fluid Reynolds' number are essential for this model, and therefore limit its practical use. Therefore, the Thermal Tune method is used, as this procedure is universal (independent of the material and geometry of the cantilever and of the environment) and less time consuming. This method is considered to have a better accuracy than the Sader method, with error of less than 8%.<sup>86-89</sup>

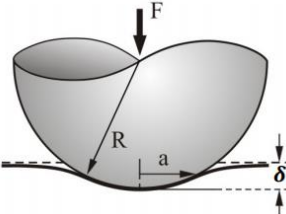
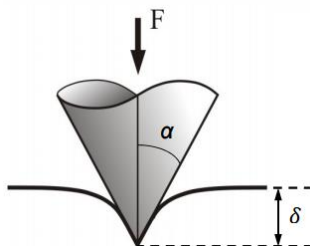
The accurate evaluation of the tip shape and size is also very important, since the tip-sample contact area defines the mechanical stresses imposed on the material (therefore on the cantilever) affecting the mechanical measurements. This can be achieved by direct observation of the tip shape by SEM (Figure 2.5 (a)) or even by blind tip reconstruction techniques, i.e., deconvolution of the tip geometry from a topographic image of a rough sample (Figure 2.5(b)).<sup>90-92</sup> Indeed, when imaging a rough sample with very sharp features, the image shows the tip geometry (the sharpest feature takes an image of the biggest one). However, imaging rough samples can cause tip abrasion, loss of resolution and therefore the true tip dimensions remain unknown, as they evolve during the calibration step.



**Figure 2.5.** (a) SEM micrographs showing the direct measurement of the cantilever and tip dimensions (b) Blind tip reconstruction for evaluation of tip shape.<sup>90,92</sup>

### 1.3. Nanomechanical Models for Quantitative Measurements

Among the nanomechanical models used for quantitative measurements, the most common in the literature are the Hertz, Derjaguin-Muller-Toporov (DMT), Sneddon and Johnson-Kendall-Roberts (JKR) 's models.<sup>91,93,94</sup> Each model has its own particularities (Figure 2.6) and can be more suitable for the study of different polymer systems (glassy or rubbery). The Hertz model describes the indentation of spherical indenter (the probe tip) on an elastic surface. This model is appropriate when the indentation depth is significantly less than the radius of curvature of the probe. The Sneddon model considers a conical indenter and is more suitable when the indentation depth exceeds the radius of curvature of the probe. Like the Hertz model, Sneddon model neglects the adhesion forces between the tip and the sample, hence, it can only be applied when the sample exhibits adhesion forces much smaller than the load force.<sup>95,96</sup> The DMT and JKR models are a modification of the Hertz model that take into account the adhesive forces outside and inside the contact area between the tip and the surface, respectively.

Indenter	Models
<p><b>Spherical</b></p> 	<p><b>Hertz</b></p> $F = \frac{4}{3} \frac{E}{(1-\nu^2)} \sqrt{R} \delta^{\frac{3}{2}}$ <p><b>DMT</b></p> $F = \frac{4}{3} \frac{E}{(1-\nu^2)} \sqrt{R} \delta^{\frac{3}{2}} - 2\pi R \gamma$ <p><b>JKR</b></p> $F = \frac{9}{3} \frac{E}{(1-\nu^2)} \sqrt{R} \delta^{\frac{3}{2}} \Delta \gamma$
<p><b>Conical</b></p> 	<p><b>Sneddon</b></p> $F = \frac{2}{\pi} \frac{E}{(1-\nu^2)} \tan \alpha \delta^2$

**Figure 2.6.** Schematic representation of two different kinds of indenters and the mechanical models used to describe the tip-sample interaction.  $F$  is the applied force (from force curve),  $E$  is the Young's modulus (fit parameter),  $\nu$  is Poisson's ratio (typically 0.2-0.5 for polymer materials),  $R$  is the radius of curvature of the indenter (tip),  $\delta$  is indentation depth,  $\gamma$  the work of adhesion and  $\alpha$  is the half angle of the indenter.<sup>96,97</sup>

It is still a difficult task to get quantitative mechanical properties at the nanoscale. Modulus measurements with AFM are based on a surface analysis and dependent on the theoretical models used for calculation. The measured modulus is then the average of thousands of measurements on the probed surface. Macroscopic modulus measurements however are based on a volumetric measurement, not only the surface, which means it can be influenced by the morphology of the phases, properties of the interphases and imperfections inside the material.<sup>98</sup>

Dokukin *et al.*<sup>99</sup> estimated the Young's modulus of polymers using different nanomechanical models and tip shapes for comparison with macroscopic measurement done by Dynamic Mechanical Analysis (DMA). Table 2.1 presents the results of the measured modulus of Polyurethane (PU) and Polystyrene (PS) samples. They showed that, by AFM, there can be an overestimation of the Young's modulus by an order of 2.5 to 3.5 compared to the macroscopic modulus measured by DMA. It is commonly assumed that the AFM modulus measurements are done within the linearity limits of the stress-strain relation, however, the use of extreme sharp probes can lead to high stresses that exceed the linearity limits, which causes plastic deformation and bias to the results. Dokukin used dull probes with tip radius of more than 200 nm and different nanomechanical models (depending on the sample) to achieve a better agreement with the macroscopic value of Young's modulus, with a rather high resolution up to 50 nm. However, the use of dull probes is more likely to produce topographic artifacts.

**Table 2.1.** Comparison of PU and PS modulus measured with different techniques and nanomechanical models<sup>99</sup>

	$E_{PU}$ (GPa)	$E_{PS}$ (GPa)	Contact Diameter (nm)	Depth (nm)
<b>Macro DMA</b>	$0.63 \pm 0.15$	$2.68 \pm 0.23$	$\sim 5 \times 10^6$	n/a
<b>Nanoindenter</b>	$0.91 \pm 0.02$	$< 3.4$	$> 8000$	$> 300$
<b>AFM PeakForce QNM (Sharp probe, DMT model)</b>	$2.2 \pm 0.3$	$3.7 \pm 0.6$	5-10	1-3
<b>AFM PeakForce QNM (Dull probe, DMT model)</b>	$0.66 \pm 0.07$	$1.6 \pm 0.4$	35-70	2-10
<b>AFM PeakForce QNM (Dull probe, JKR model)</b>	$0.98 \pm 0.22$	$2.7 \pm 0.5$	$\sim 50$	$\sim 3$

#### 1.4. Absolute vs Relative Calibration Method

Different methods have been used to achieve reliable calibration for AFM mechanical measurements, which can be divided in two: the Absolute Calibration and the Relative Calibration.

The Absolute Calibration Method requires the correct determination of the tip radius corresponding to the indentation depth used when imaging the sample (either by direct observation or by tip reconstruction). The tip radius is then used on nanomechanical models to calculate the Young's Modulus of the material. The Absolute Method is time consuming and rather difficult to implement due to the tip evaluation. The tip shape is rarely an ideal sphere, which leads to errors in the measurements. Furthermore, there may be lateral and buckling movements of the AFM tip which engenders shear forces that are not taken into account by nanomechanical models.<sup>97</sup>

The alternative approach used is the Relative Calibration Method, which relies on the use of a standard sample with known modulus to estimate the tip radius corresponding to a certain deformation depth. This method avoids the need to determine the exact shape of the tip by the estimation of an "effective" tip radius used to correct the measured modulus on a reference sample, avoiding errors in the measurement of the tip radius and considering the effective tip-surface area of contact. This method is less time consuming but implies a careful control on the deformation depth while probing the sample, to keep it identical to the one used during the calibration step.

In conclusion, the power of AFM relies on its high lateral resolution ( $\sim 5-10$  nm), very high vertical resolution (better than 1 nm), the possibility to operate in air or in liquid, the possibility to measure any type of materials (conductive and non-conductive), and finally AFM is a non-destructive technique (surface deformation of few nanometers). For conventional surface analysis, the sample does not need any special treatment and it can be characterized in its pristine state. To access to the bulk properties of the materials, fracturing or sectioning are necessary, taking great care to preserve the original morphology and produce a flat surface. Indeed, excessively rough surfaces can engender artifacts, since the topographic and mechanical information derived from the tip-sample interaction are greatly affected by the topology of the material.<sup>99</sup> Techniques for sample preparation will be discussed later on this chapter.

## 2. Fundamentals of Raman Spectroscopy

### 2.1. Raman Principle

In Raman spectroscopy, the sample is irradiated with light from a laser source and consequently the molecules are excited from their ground state to an unstable virtual state. Immediately after excitation, the molecules return to either their original vibration level (elastic Rayleigh scattering) or to other energy levels, as illustrated on Figure 2.7. The difference in energy between the elastically scattered photons and the Raman shifted photons is caused by the excitation (Stokes Raman scattering) or annihilation (Anti-Stokes Raman scattering) of a specific molecular vibration.

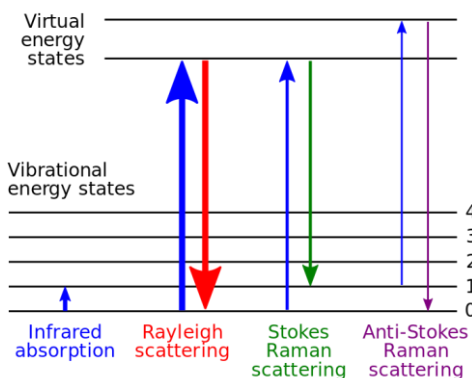


**Figure 2.7.** Energy level diagram showing the states involved in Raman signal

The intensity of the Raman emission comes from changes in the polarization of vibrations, thus, symmetric or nonpolar vibrations are strongly active in Raman. Generally, Raman active bands tend to be weak or inactive in Infrared spectroscopy (IR), and vice versa, both techniques are therefore very complementary. The vibrational frequency of functional groups scatter the radiation at characteristic frequencies, giving therefore a fingerprint for the type and coordination of the molecules involved in the scattering process. Figure 2.8 (a) shows an example of a characteristic Raman spectrum of Polystyrene. These specific interactions allow for qualitative and quantitative analyses of the material's composition, such as its chemistry (the structural units, type and degree of branching, end groups and additives), conformation order (physical arrangement of the polymer chain), its state of order (crystalline, mesomorphous and amorphous phases) and orientation (type and degree of polymer chain and side group alignment in anisotropic materials), as summarized on Figure 2.8 (b).<sup>100-103</sup>

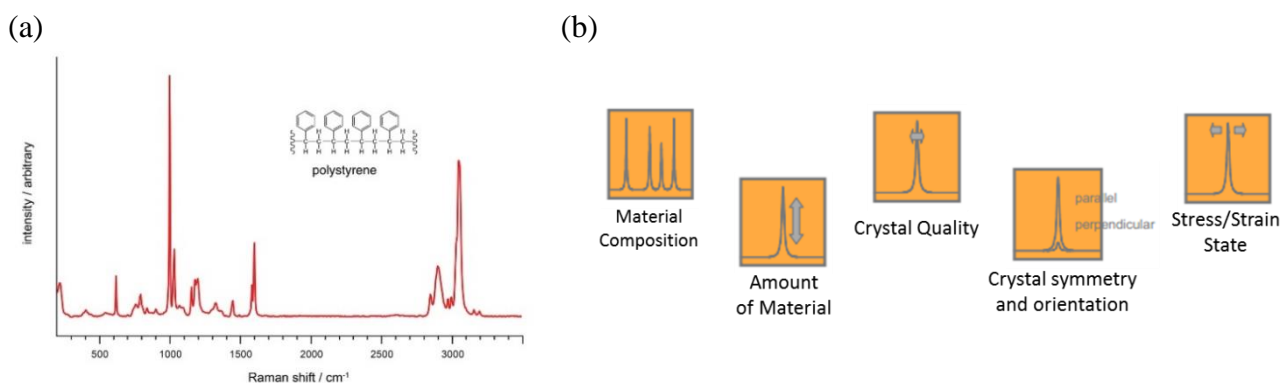


**Figure 2.8.** (a) Raman spectrum of Polystyrene (b) schematic representation of different chemical and structural information issued from the interpretation of Raman spectra.



## 2.2. Raman Mapping and Spatial Resolution

To obtain local information on the material chemistry/composition, Raman analysis must be performed in confocal mode.

The basic Confocal Raman setup is composed by a laser source, objective lenses, filters, confocal aperture, slit, grating monochromators and a CCD detector, as illustrated on Figure 2.9. Grating monochromators and the slit width determine the spectral resolution of a spectrometer. The more grooves per millimeter, the better is the dispersion, and the greater is the resolution. Shortening the slit width can also improve the spectral resolution, at the cost of signal intensity loss and increasing analysis time.<sup>104</sup>

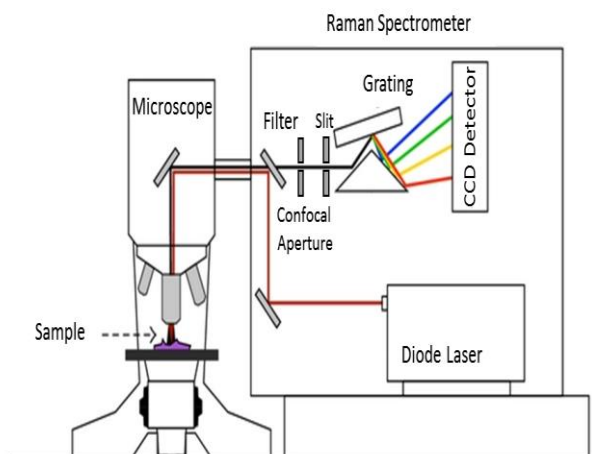


**Figure 2.9.** Schematic representation of a Confocal Raman spectrometer. Adapted from <sup>104,105</sup>

An example of Raman mapping is given by the work of Luckachan and Mittal, who characterized the crystallinity variations and phase distribution in polymer blends based on poly-L-lactide (PLA), poly- $\epsilon$ -caprolactone (PCL) and thermoplastic starch (TPS).<sup>106</sup> Carbonyl carbon bands centred at 1768 and 1723  $\text{cm}^{-1}$  correspond to crystalline bands of PLA and PCL respectively. Figure 2.10 shows the chemical mappings of an area of  $25 \times 25 \mu\text{m}^2$  from the binary PLA/PCL blends and a ternary PLA<sub>50</sub>/TPS<sub>30</sub>/PCL<sub>20</sub> blend. The binary blend (Figure 2.10(a)) presented small domains of PLA phase confined between large clusters of PCL phase. The analysis of the Raman spectra indicated that the PLA was in an amorphous state, which was confirmed by X-ray diffraction. The addition of TPS (Figure 2.10 (b)) improved the dispersion of both PLA and PCL components and resulted in enhanced crystallinity of PLA. The study demonstrated the potential of Raman mapping to evaluate the phase distribution and crystallinity of individual components in polymer blends. The co-localization of this chemical information with nanomechanical information from AFM could, on the one hand, provide the study of the blends morphology with a better resolution (nanometric for AFM rather than micrometric for Raman) and, on the other hand, allow the acquisition of complementary nanomechanical properties of the polymer phases to study the interface between the components.

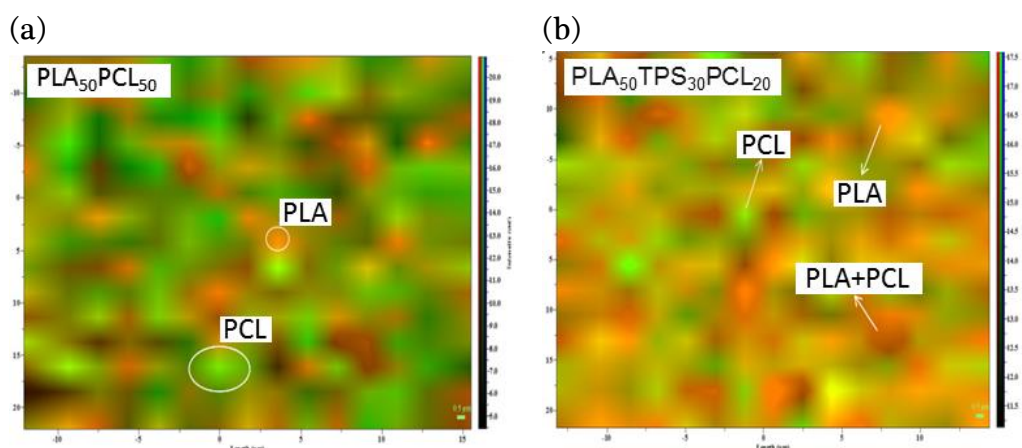


**Figure 2.10.** Raman mapping images of (a) PLA/PCL binary blend and (b) PLA50/TPS30/PCL20 ternary blend plotted from the combination of intensity maps of the bands centered at  $1768\text{ cm}^{-1}$  (PLA) and  $1723\text{ cm}^{-1}$  (PCL).<sup>106</sup>

To analyze the internal chemical structure and composition through the thickness of the material, mainly two approaches can be used with Raman microscopy. The first is the depth profiling of the sample with the confocal microscopy mode and the second involves real sample sectioning.

For the first approach, the scattered light from the illuminated spot is collected and collimated by the same objective and focused in a detector, passing through a pinhole aperture, as illustrated in Figure 2.11(a), where only light from a selected spot C can reach the detector, while the emitted radiation from spots A and B are excluded. The limited aperture improves the lateral and axial spatial resolution of the microscope, allowing nondestructive depth profiling, i.e., the confocal microscope focus is moved incrementally deeper into the sample to act like a depth selector. Figure 2.11 (b) is an example of depth profiling on a Polyethylene terephthalate (PET) sample coated with a  $15\text{ }\mu\text{m}$  layer of Polyethylene (PE). Spectra were taken from  $10\text{ }\mu\text{m}$  away from the surface to  $20\text{ }\mu\text{m}$  deep in the material.

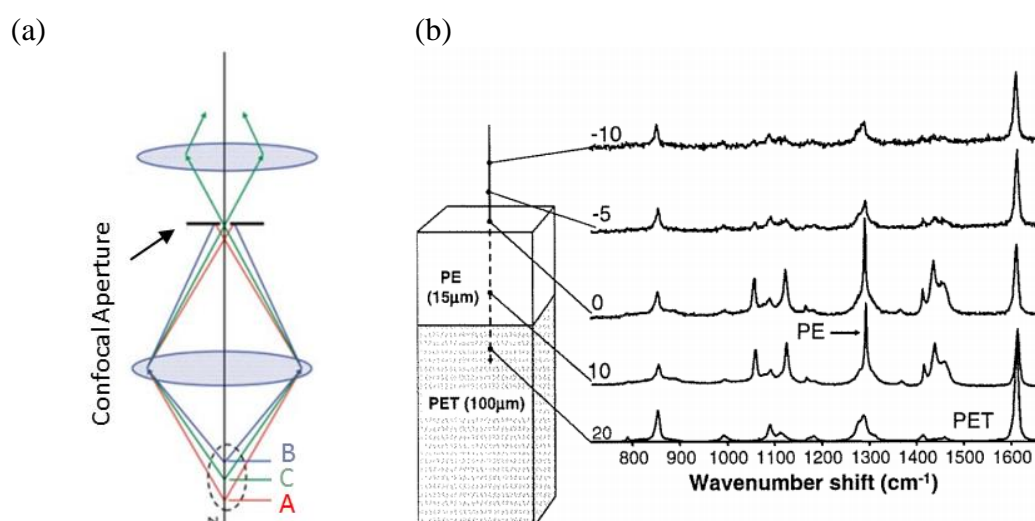


**Figure 2.11.** (a) Schematic representation of the confocal aperture used for depth profiling (b) Confocal depth profiling scan through a  $15\text{ }\mu\text{m}$  coating of PE on PET. Adapted from <sup>107,108</sup>

The combination of the high chemical sensitivity of Raman spectroscopy with the spatial resolution of confocal microscopy is currently said to be able to provide information from very small sample volumes, down to  $1 \mu\text{m}^3$ , depending on the wavelength used (better resolution for shorter wavelengths). But great care must be taken when obtaining Raman confocal depth profiles, lateral lines and maps, since artifacts can be created by the fact that the focused laser beam generates an extended illumination volume within the sample. The contribution of out-of-focus sample regions has been shown to be very pronounced when doing confocal Raman depth profiles in polymers, causing miscalculations of phase thickness and misinterpretation of chemical composition due to data superposition. As illustrated on Figure 2.11 (b), Neil J. Everall has shown that when probing a  $15 \mu\text{m}$  PE coating on a PET substrate by depth profiling, PET signal could be detected even  $10 \mu\text{m}$  away from the surface.<sup>107,109</sup>

The second approach to perform analyses through the thickness is to mechanically open the material perpendicular to the surface and then do a confocal Raman mapping of the exposed section, by lateral scanning rather than depth profiling. However, even for this approach, out-of-focus effects can be a problem, as signals from materials outside of the intended focus can contribute to the collected light. Everall showed that when moving the laser laterally from the PET/PE interface towards the PE/air interface (Figure 2.12 (a)), the PET signal fell monotonically, as expected, but when the laser focus was positioned  $1 \mu\text{m}$  outside the PE layer, in the air (yellow spectrum), the PE signal almost disappeared but the PET signal increased by an order of magnitude, the global intensity dropping again when moving away from the layer. He explained this phenomenon by the excitation of waveguide modes by the focused photons, observed for systems with a coating layer ( $15 \mu\text{m}$  in this case), which induces diffraction at the coating/air interface (illustrated on Figure 2.12 (b)). The author concluded that the interpretation of data when focusing near a surface, either in depth profiling or lateral scanning, is difficult, especially when working with multilayers or coated materials.<sup>108</sup>

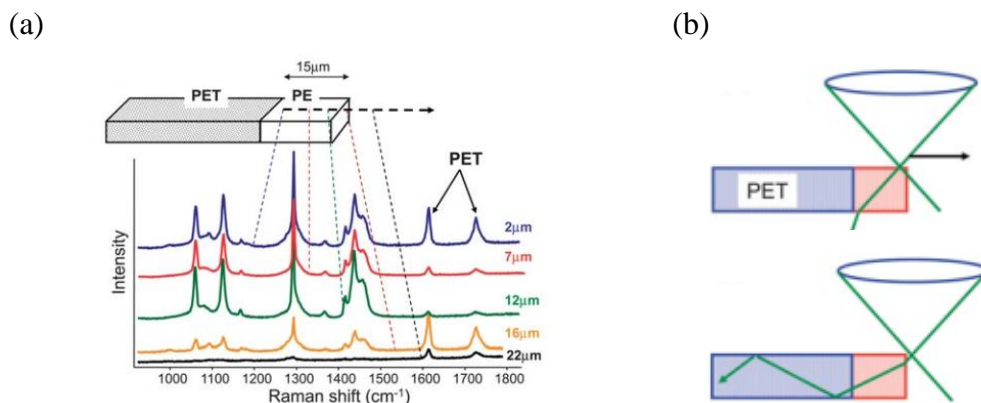


**Figure 2.12.** (a) Lateral scan on the cross-section of PET/PE laminate showing spectra at each distance from the PET/PE interface (b) schematic representation of the effect of the excited waveguide modes which increase the observed PET signals outside the sample.<sup>108</sup>

Therefore, despite the artifact observed for multilayer samples even for lateral scanning, the method of mechanically sectioning the material is still considered to be more accurate than the depth profiling. Naturally, sample preparation is more time consuming and requires special tools and knowledge, in order to preserve the internal structure for reliable chemical analysis.<sup>109</sup> This issue will be discussed in Section 4 dedicated to sample preparation techniques.

In addition, limitations of Raman spectroscopy lie on the fact that some materials fluoresce under light irradiation, which can mask the Raman bands. To decrease fluorescence, two solutions are often used: illuminating the sample for a certain time before the spectra acquisition in order to

quench the fluorescence, and/or to use monochromatic laser source with higher wavelength, which however degrades the resolution. Moreover, the focused monochromatic laser beam may cause local heating and/or photodecomposition of sensible samples, requiring the use of low power (filters). Finally the collection of data from such a small volume ( $\sim 1 \mu\text{m}^3$ ) can be difficult when probing a rough surface, causing loss of focus during imaging. This problem may be addressed by the use of auto-focus system to automatically find and correct potential drifts. However, use of auto-focus considerably increases the acquisition time for mappings.

### 3. AFM-Confocal Raman Coupling

Studies of the chemical composition and structure of polymers used in a variety of applications have been done using Raman spectroscopy. This goes from composites for engineering, nanocomposites, polymer blends, to membranes for electro dialysis and fuel cell application as examples among others.<sup>110-113</sup> It has been reported as well in the literature the capabilities of the technique on the study of chemical and structural changes induced by ageing effects, with very localized information.<sup>114-117</sup> Nanocomposites and polymer blends have also been studied by AFM, demonstrating its capacity for the identification of the different phases thanks to morphological and mechanical characterization at nanoscale.<sup>118-123</sup> The independent studies already done show that these techniques, if used together in a co-localized way, have a huge potential in the characterization and development of new materials, as they provide qualitative and quantitative complementary information in high resolution to understand the process-structure-properties interplays. Some authors have already tried to couple AFM and Raman information for surface and bulk analyses.<sup>124,125</sup> Roigé and coworkers<sup>125</sup> have performed non co-localized AFM and Raman spectroscopy measurements during heating of thin films for organic photovoltaics (OPVs) and were able to characterize different crystallization transitions at the surface (probed with AFM) and at the bulk (probed by depth profiling with Raman). Based on each of the analysis done separately, the authors supposed that there may be morphological and/or molecular mobility gradient along the film thickness. A direct observation and co-localized AFM/Raman analysis of the material's bulk would clear any doubts about morphological profiles on the cross-section.

Different strategies are proposed in order to combine AFM and Raman microscopes. This combination can be done using two separate instruments or with a dedicated instrument.

#### 3.1. Commercially available AFM-Raman coupling systems

One example of combination of separate instruments is the setup proposed by Bruker and Horiba Jobin Yvon, leading companies on the production of AFM and Raman instruments, respectively. The setup is composed of a Dimension Icon AFM with a modified LabRam Confocal Raman Spectrometer equipped with two microscopes, as shown on Figure 2.13 (a). One in a classic configuration for Raman analysis and another one installed laterally and specially dedicated for AFM-Raman co-localized analysis. The two systems are coupled by using the AFM stage to move the sample from below the AFM head to below the Raman objective (Figure 2.13 (b) and (c)). First, the AFM analysis is done, then the co-localization is achieved by the motorized stage and finally the Raman analysis is performed. The setup is designed to permit co-localization of data and at the same time to ensure the high performance of both systems. Each instrument can also be used independently and simultaneously for conventional AFM and Raman analyses.

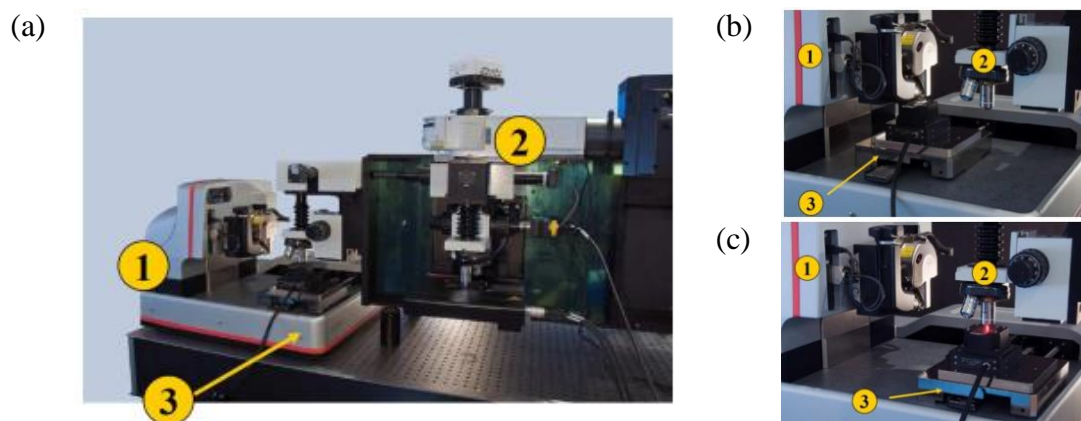


**Figure 2.13.** (a) Bruker/Horiba Jobin Yvon AFM-Raman setup composed of (1) AFM Dimension Icon; (2) Modified Raman LabRam HR; (3) Motorized stage from Icon equipped with a second piezoelectric stage controlled by LabRam for Raman mapping. Co-localization strategy is shown by images (b) with the sample below the AFM head and (c) with the sample below the Raman objective.<sup>126</sup>

The strategy of combining both AFM and Raman analyses in a single instrument is illustrated by the setup proposed by Witec (Figure 2.14(a)). A special designed AFM head is installed on the objective turret of the microscope, as shown in Figure 2.14 (b). The system allows the switching between the imaging techniques by the turn of the objective turret without moving the sample (Figure 2.14 (c)), which permits the co-localization of morphological and chemical data from nanometric to micrometric scale. As for the previous setup shown, each of the measurements is done separately and co-localized by simply turning the turret, which guaranties the accuracy of the co-localization. On the other hand, the setup does not allow independent and simultaneous AFM and Raman analyses. In addition the AFM performances are lower than with a dedicated AFM.

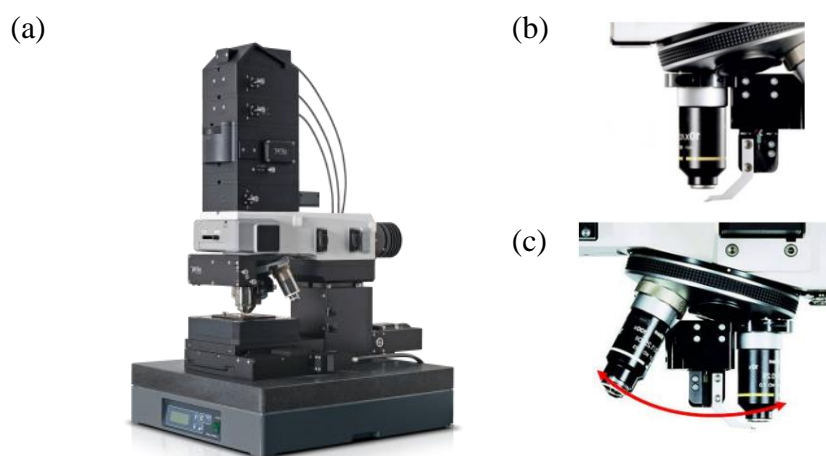


**Figure 2.14.** (a) Witec setup allying AFM-Raman in a single instrument. (b) AFM head installed on the objective turret (c) Co-localization strategy based on the turning of the objective turret to switch between AFM and Raman analyses.

The last example of a dedicated combination of AFM and Raman in a single instrument is given by the strategy of Tip Enhanced Raman Spectroscopy (TERS). The instrument proposed by Horiba Jobin Yvon takes advantage that the incident laser generates a strong electromagnetic field at the apex of the tip (metal coated), which acts like an antenna to enhance the Raman signal of the molecules near the tip by a factor of  $10^{14-15}$ , overcoming the diffraction limit of conventional Raman spectroscopy. The spatial resolution of such measurement depends upon the tip itself, which has

dimensions typically <50 nm, thus TERS would similarly have a spatial resolution of <50 nm. Topographic and chemical information can be then acquired in high resolution. The technique can be used for transparent (transmission mode) and opaque samples (reflection mode), as illustrated on Figure 2.15 (a) and (b). The company states that the achievement of high spatial resolution (<50 nm) results is not guaranteed, and cannot be expected for every possible sample. Actually, to achieve the TERS enhancements, it is important to control the spectral response of the metallic tip to match the excitation light frequency. The main challenges on the fabrication of TERS probes are: (i) manufacturing reproducible probes with high enhancement factors and high resolution imaging capabilities; (ii) probe lifetime and (iii) probe mass production not involving complicated and poorly reproducible manual procedures. Therefore, due to the lack of reproducibility, the control of the plasmon resonance at the probe apex is still a challenge in TERS developments.<sup>127</sup>

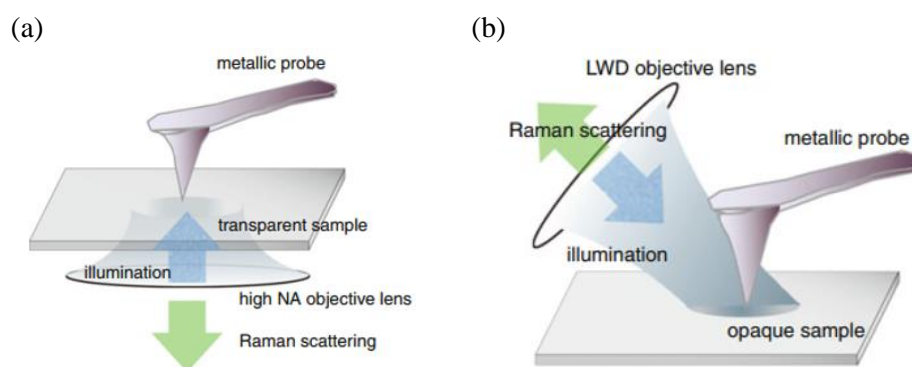


**Figure 2.15.** Schematic representation of Tip-Enhanced Raman Spectroscopy in two configurations: (a) transmission for transparent samples and (b) reflection for opaque samples. Adapted from <sup>127</sup>

The combination of both techniques in a single instrument can be advantageous for the accuracy of the co-localization of morphological and chemical analyses. The TERS technique could provide the best resolution to the analysis, but the poorly reproducible probes remain as the main limiting factor for nano-Raman to become a routine characterization technique. The system using the turning turret for switching between techniques can certainly provide a fast and precise co-localization of information, but does not allow the individual and simultaneous operation of both instruments and have lower performances than dedicated instruments. Therefore, the combination of two separate instruments dedicated for AFM and Raman analyses, respectively, seems to be the most advantageous, benefiting of the best performance of each instrument, as well as an increased productivity as both instruments can also be used simultaneously.

However, when combining an AFM and a Raman, it is important to preserve the performances of each instrument, which requires a good management of the mechanical noises caused by vibrations, cooling fans, thermal drifts, etc., which can strongly affect the quality of repositioning of the co-localized analysis.

The success of the co-localized analysis highly depends on the quality of the sample preparation. Next section will therefore be dedicated to the discussion of the sample preparation techniques used to open samples in order to go beyond the surface.

## 4. Sample Preparation Techniques

Direct observation and probing of the material's bulk requires a proper sample preparation technique, capable of providing a sample compatible with the AFM/Raman analysis requirements (size, shape, thickness, surface conditions, etc.) and if possible representative of the whole material (surface plus bulk). The process of opening a material can involve mechanical and chemical stresses, inherent to the technique used. Artifacts can rarely be avoided, but they must be minimized by the proper choice and control of the sample preparation method.

In this section we will compare the sample preparation techniques providing access to the cross-section of the material, especially of thin membranes (20-300  $\mu\text{m}$ ) : Cryo-fracture, Cryo-ultramicrotomy and Focused Ion Beam (FIB). The techniques were chosen to be compatible with co-localized AFM/Raman and any complementary techniques, such as Electron Microscopies (SEM/STEM). The three techniques will be briefly described, and their compliance with the following requirements will be discussed:

- Access to the complete cross-section of the material (from the surface to the bulk)
- No mechanical, thermal, chemical, structural or morphological (hydration, oxidation...) modification during preparation

### 4.1. Cryo-Fracture

The Cryo-fracture is a technique to open polymeric materials by a brittle fracture at low temperature. To achieve a brittle fracture the polymer needs to be below its glass transition temperature, therefore it is generally covered with liquid nitrogen ( $-196^\circ\text{C}$ ) before being fractured with tweezers, as schematically represented in Figure 2.16. The brittle fracture path is unpredictable and usually follows the structural details/defects of the sample, such as spherulites in semicrystalline polymers, phase boundaries and interfaces in polymer blends and composites, or any heterogeneity where the local mechanical properties are different, inducing a preferable pathway for crack propagation. This creates a rough surface, not always representative of the initial morphology of the material. Nevertheless, it can reveal the size, shape and distribution of phases.

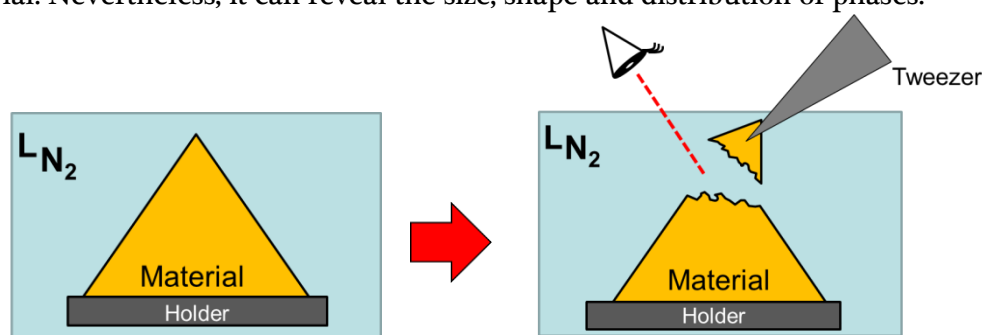


**Figure 2.16.** Schematic representation of the cryo-fracture procedure on a polymer membrane

Especially for AFM and Raman analyses, the technique has another serious drawback as it can induce artifacts due to the achieved surface roughness. The AFM tip is very sensitive to topography variations and artifacts can appear due to the convolution of the tip shape with the topological objects. As illustrated in Figure 2.17, the measured surface will always be a combination of the shape of the tip and the real surface of the sample.<sup>128,129</sup> Therefore, the mechanical properties probed by the tip on the rough surface will present artifacts due to the constant change on the contact point (surface and position of the point of the tip on contact with the sample), which

generates apparent modulus inhomogeneities. Figure 2.17 (b) and (c) show an example of artifacts induced by topography on the modulus measurement of a poly(methyl methacrylate) (PMMA) sample. Although PMMA is amorphous and homogeneous, the image shows a nodular surface and great modulus inhomogeneities. One can see that there is a correlation between the height and the modulus images, which suggests that the nodular morphology is possibly due to convolution artifacts, affecting not only the topography but the measured modulus as well.<sup>99,129</sup>

In addition, a wide rough surface as produced by cryo-fracture would not allow the probing of the entire thickness of the material by AFM, since variations of the order of several microns in the Z direction can occur in a matter of few microns laterally. Such abrupt variations cannot be handled by the tip. The rough surface can also be a problem for the Raman analysis, since it can cause loss of focus from one point to another when mapping the sample. This may be addressed by the use of an autofocus system, but it increases the acquisition time considerably and it is not easy for the system to automatically detect properly the sample's surface.

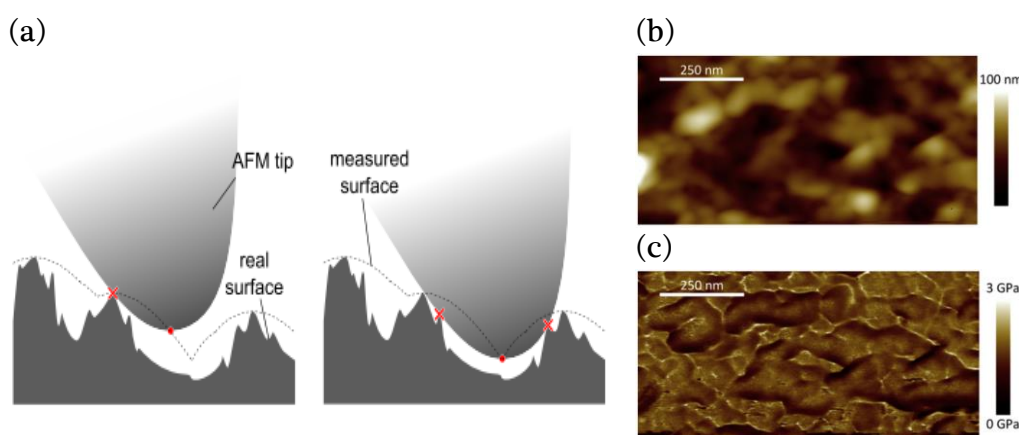


**Figure 2.17.** (a) Schematic representation of tip convolution when probing a rough sample and the differences on the contact point (b) AFM Topography image of a PMMA sample and (c) correspondent AFM Modulus image of the sample showing modulus heterogeneities artifacts induced by sample roughness. Adapted from<sup>129</sup>

At last, another important concern when working with nitrogen cooled materials is the fact that ambient air always contains humidity, which leads to frost deposition on the material's very cold surface.<sup>130</sup> The melting of the ice crystals during warming up to the room temperature can result in morphological changes or even dissolution of the material when working with hydrophilic samples. Thus, it is very important to control the process to avoid morphological modification due to the material swelling or solubilization, in the presence of liquid water.

## 4.2. Cryo-Ultramicrotomy

Cryo-ultramicrotomy is an advanced but usual technique for preparation of thin sections (thickness ~50 nm) for TEM/STEM analysis but can also be used for the production of very flat surfaces for microscopic analysis. The principle of the cryo-ultramicrotome is illustrated on Figure 2.18. A sample is installed in a sample holder, which is moved towards a knife with a given distance and speed in a cyclic motion, the whole system being in cryo temperatures (usually down to -120°C). When the sample goes downward, in contact with the knife, a thin section is cut. Its thickness depends on the cutting depth defined by the forward motion (difference from A to B on Figure 2.18), the cutting angle defined by the inclination of the knife, the type of knife (glass or diamond) and



also the mechanical properties of the material sectioned. The best results are obtained with diamond knives due to their hardness. The flat surfaces of the block after ultramicrotomy can be studied by means of AFM/Raman and the sections produced can be collected on copper grids (Figure 2.18 (b) and (c)) for further TEM/STEM analysis.

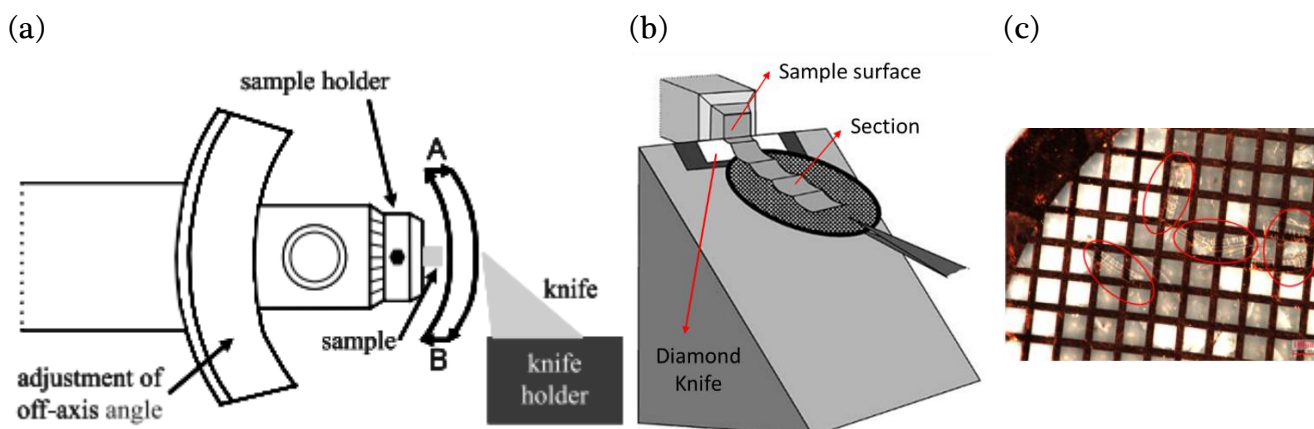


**Figure 2.18.** Schematic representation of Cryo-Ultramicrotomy operation showing: (a) motion of the sample holder during sectioning and (b) the collection of thin sections on a copper grid.<sup>131</sup> (c) Optical microscopy image of a 200 mesh grid with thin transparent samples highlighted by the red circles.<sup>67</sup>

The cryo-ultramicrotome setup allows the control of the temperature and cutting conditions (cutting speed, depth and angle) in order to optimize the process for the preparation according to the sample's properties. Figure 2.19 (a) shows AFM topographic images of a  $5 \times 5 \mu\text{m}^2$  area of a cryo-fractured Poly(lactic acid) sample (A) and a cryo-ultramicrotomed one (B) and their respective profiles. As expected, Martínez-Tong and coworkers<sup>80</sup> showed that the surface of the cryo-ultramicrotomed sample was extremely flat, with roughness of about 10 nm, despite some cutting lines caused by small scratches on the diamond knife, while the surface of the cryo-fractured sample was much rougher. Figure 2.19 (b) and (c) are AFM phase-contrast images (tapping mode) from the work of Tanem *et al.*<sup>132</sup>, which shows how the optimization of the cutting conditions such as temperature and speed, can improve the quality of the obtained surface and therefore of the morphological analysis of heterophasic PP copolymers (PP/Rubber/PE). The non-optimized sample (Figure 2.19 (b)) appears with both matrix and soft rubbery phase heavily deformed. After optimization of the parameters (Figure 2.19 (c)), the interface between the matrix and the rubber phase appears much clearer. Inside the rubbery phase, there are crystalline inclusions, which by itself present islands of soft materials, an information that could not be accessed on the non-optimized sample.

Cryo-ultramicrotomy therefore appears as a better cutting technique than Cryo-fracture for AFM and Raman co-localized analyses. However in both cases, the frost deposition on the surface of the material when warming up to the room temperature can be source of artifacts and therefore must be limited and/or suppressed for water sensitive samples.

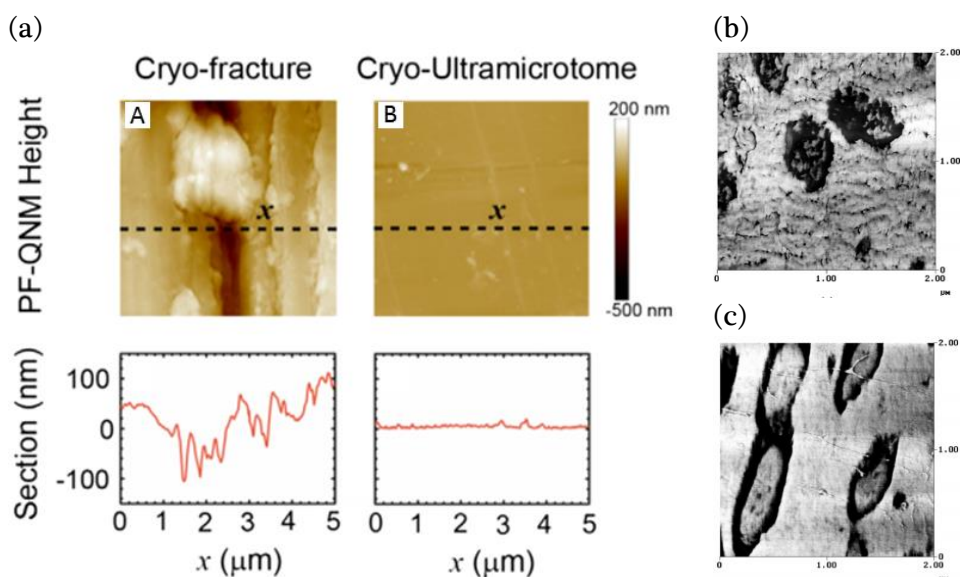


**Figure 2.19.** (a) Comparison of the surface roughness of an area of  $5 \times 5 \mu\text{m}^2$  obtained by cryo-fracture and cryo-ultramicrotomy of a polyurethane sample. Example of an area of  $2 \times 2 \mu\text{m}^2$  a (b) non-optimized and an (c) optimized (cutting temperature and speed) surface of a cryo-ultramicrotomed sample of a heterophasic polypropylene copolymer sample. Adapted from <sup>80,132</sup>

The cryo-ultramicrotomy strategy is usually done on a fragment of the sample mounted or glued to a holder. For thin samples like polymer membranes, which are flexible and cannot be directly glued on the sample holder, a previous step of embedding in a resin is usual. Typical resins are based on epoxy, polyester or methacrylate polymers which are crosslinked by UV radiation or heat, as illustrated on Figure 2.20.

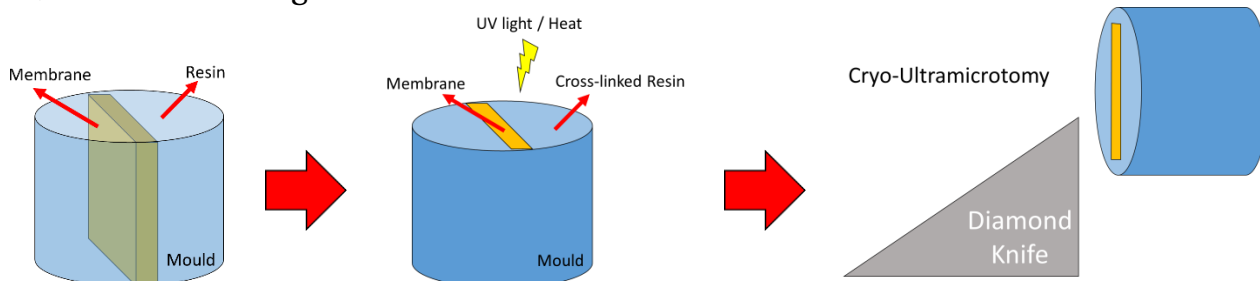


**Figure 2.20.** Schematic representation of the embedding procedure for sectioning of thin materials

The limitations of the embedding technique lie on the interactions between the sample and the resin. Differences on the hardness of the embedding medium and the sample can impose difficulties during the cryo-sectioning (uneven cutting), thus the cross-linking must be well controlled in order to obtain a resin with mechanical properties similar to the sample's ones. Furthermore, the resin used should not chemically interact with the sample or diffuse into it, which could create chemical "pollutant" profiles through its thickness, a critical point when working with thin polymer membranes. The temperature or UV radiation used for polymerization of the resins can also change the sample's morphology and chemistry.<sup>130</sup> Thus, for the application of the cryo-ultramicrotomy technique to thin polymer membranes, an alternative strategy must be developed to avoid using embedding medium. We have used a specially designed sample holder that acts like a vice to hold the sample perpendicular to the knife during sectioning. Details will be given in Chapter 3.

### 4.3. Focused Ion Beam (FIB) cross-sectioning

The operation of the FIB instrument resembles the one of a Scanning Electron Microscope (SEM), but instead of a focused electron beam to image the sample, the FIB uses a focused ion beam capable of imaging, sputtering (surface solid erosion) or milling the sample. The ion beam, usually gallium, is accelerated with energy between 4 and 50 keV. If used in low current ( $\sim 1$  pA) it is capable of providing high resolution imaging (up to 5 nm) and at high current ( $\sim 40$  nA) it can be used for precise ion milling, with nanometric resolution. Some systems ally electron and ion beams in a single instrument (presented schematically on Figure 2.21) to enable SEM imaging during FIB cross-sectioning, and also compositional analysis with energy dispersive systems (EDS, based on the detection and measurement of X-rays).<sup>131,133</sup> For the preparation of cross-sections, the milling is done in multiple steps, first roughly removing material and then smoothly milling using finer beams at each time. Then the sample is tilted and the polished sidewall can be imaged. Cross-sections with depth of a few micrometers and width of 10-15  $\mu\text{m}$  are prepared in a matter of minutes. The technique can also be used (when no other simpler techniques are available) for the preparation of thin sections for TEM analysis, by milling both sides of the area of interest.<sup>134</sup>

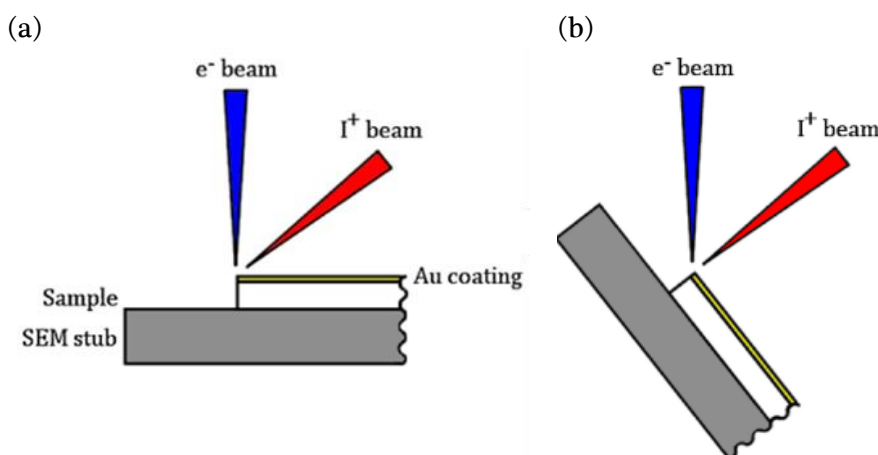


**Figure 2.21.** Schematic representation of a FIB instrument composed by an electron and an ionic beam. (a) Sample is perpendicular to the electron beam for imaging and (b) the sample is tilted for milling with the ionic beam. Adapted from <sup>135</sup>

An example of FIB cross-sectioning is presented on Figure 2.22, showing an image of a graft-copolymer of deproteinized natural rubber and polystyrene (DPNR-graft-PS) prepared by Fukuhara and coworkers.<sup>136</sup> The authors were capable of preparing a very smooth surface throughout several microns of the cross-section, revealing the morphology of the material, with bright domains characteristic of PS and dark domains (OsO<sub>4</sub> stained) of DPNR. This example shows that the technique is suitable for the preparation of cross-sections from blocs, but it can also be adapted for the opening of thin membrane cross-sections for co-localized AFM-Raman analysis, however the opened surface might not be very large (few micrometers).

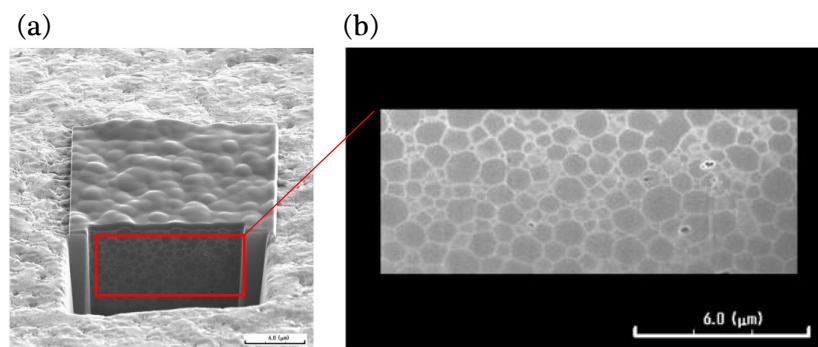


**Figure 2.22.** (a) FIB milling of the cross-section of a DPNR-graft-PS copolymer (b) Inset showing details of the microstructure, PS appearing in bright domains and DPNR in dark.

The greatest limitation of the technique for the preparation of polymer cross-sections is the heating effect induced by the ion beam on the material, which can melt or be partly altered (thermochemical degradation or modification of its crosslinked density/morphology). For example, Polymers known to be sensitive to electron beam damage, such as PMMA, undergo degradation during FIB milling.<sup>80</sup> Bassim and coworkers have studied the effects of electron and ion beam irradiation on the chemistry of polyacrylamide.<sup>137</sup> Figure 2.23 shows an X-ray absorption near edge structure (XANES) spectrum of a ultramicrotomed sample with an intense amide peak (C) characteristic of the polymer, and spectra of FIB-prepared samples showing two additional peaks corresponding to nitrile ( $-C\equiv N$ ) and imine ( $C=N-C$ ). According to the authors, the amide functions are transformed into these other species by the departure of hydrogen atoms or hydroxyl groups. In addition, they have shown that these damages can be amplified by the  $Ga^+$  ions generated during FIB-preparation. For example, Russell J. Bailey *et al.*<sup>135</sup> have shown, by phase contrast AFM mappings, local changes in the elastic modulus of polycarbonate surfaces parallel to a FIB section at varying beam energies. They observed an increase on the elastic modulus of the polymer due to the implantation of  $Ga^+$  ions in the material's surface.

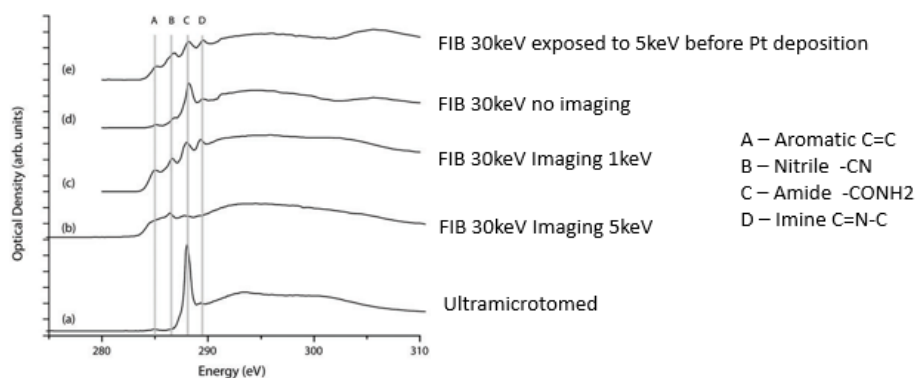


**Figure 2.23.** XANES spectra showing the effect of electron and ion beam on the chemical structure of a polyacrylamide. Adapted from<sup>137</sup>

Different approaches have been proposed to improve the FIB technology to allow a damage free preparation for polymeric samples, which involve the use of in situ low-energy  $Ga^+$  ions (500 eV to 2 keV) or low-energy  $Ar^+$  ions (500 eV to 2.5 keV) at the final milling, or even performing the procedure in cryogenic temperatures.<sup>137</sup> The use of low-energy milling could be a more appropriate technique than embedding and cryo-ultramicrotomy for water sensitive samples, since there is no possibility of frost deposition on the opened sample surface, but the effect of  $Ga^+$  ions implantation in the surface can impact the AFM nanomechanical measurements.

#### 4.4. Summary Table of Sample Preparation Techniques

The advantages and limitations of each sample preparation technique are summarized on Table 2.2.

**Table 2.2.** Summary table of advantages and limitations of the sample preparation methods

Technique	Advantages	Limitations
<b>Cryo-Fracture</b>	Easy sample preparation	High surface roughness not suitable for AFM/Raman analysis
		Not fully representative of materials morphology
		Risk of frost deposition and therefore of liquid water trapped on the opened surface which can induce surface modifications
<b>Cryo-Ultramicrotomy</b>	Surface representative of the inner morphology	Risk of chemical contamination by embedding medium for thin samples
	Low roughness of the opened surface suitable for AFM/Raman analysis	
	Possibility for thin sections collection for additional TEM/STEM analyses	
<b>Focused Ion Beam (FIB)</b>	Surface representative of the inner morphology	Expensive and time consuming technique, not readily available everywhere
	Low roughness of the opened surface suitable for AFM/Raman analysis	Not possible to prepare large surfaces for AFM exploration
	Possibility of thin sections collection for additional TEM/STEM analyses	Electron and Ionic Beam damage can cause chemical and structural changes

Cryo-fracture, although an easy and non-expansive sample preparation method, do not comply with the requirements of surface quality and representability of the original material morphology for further analysis. The rough surface induces measurement artifacts and jeopardizes co-localized AFM/Raman analysis. Cryo-ultramicrotomy and cryo-FIB are both capable of opening materials for bulk analysis and they can provide thin sections for morphological and chemical analysis with TEM/STEM. However, cryo-ultramicrotomy is a much faster process, much cheaper, and able to open much larger surfaces. FIB is therefore usually reserved to impossible or hard to cut samples. The association of techniques can be useful for a better understanding of the polymer structure, allowing the recognition of artifacts that could result in image misinterpretations. However, some limitations still must be addressed for the complete compliance with the requirements.

The FIB electron and ion beam interaction with the material will always be a potential source of damage and artifacts to polymeric materials. These effects are difficult to evaluate and control, and require constant verification by complementary chemical analyses. Cryo-ultramicrotomy has been shown as a technique suitable for opening polymers, but the use of embedding for preparation of thin materials needs to be addressed, once there can be chemical reactions and/or diffusion of the embedding media through the thickness of the polymer. Another important issue is the possibility of frost deposition and subsequent water melt on the opened surface, which could engender chemical and morphological changes.

In conclusion, Cryo-Ultramicrotomy appears as the most promising sample preparation technique for a multiscale and multi characterization approach allowing the combination of co-localized techniques like AFM-Raman setup on the opened surface, as well as Optical and Electron Microscopies (SEM/STEM) for complementary analyses on the opened surface and the ultrathin sections collected. An introduction to the fundamentals of these complementary techniques will be presented in the next section.

## 5. Complementary Analyses

### 5.1. Optical Microscopy (OM)

OM is based on the illumination of the sample with a light source and the collection of the reflected or transmitted light by a system of lenses to form a magnified image of an object. OM provides a rapid overview of the general appearance of a relative large area of the sample with a resolution beyond the limit of the human eye, with magnifications range from 2x to 2000x. For routine analysis, the resolution is of the order of 1  $\mu\text{m}$  but can be pushed to less than 0.5  $\mu\text{m}$  depending on the nature of the sample probed, the objective lens and the wavelength of the light.<sup>71</sup> Sample preparation for OM analysis is simple and no radiation damage occurs during the observation. For these reasons, the use of OM is considered to be a good starting point on the characterization of the morphology of the material or to identify interesting zones for further analyses with other techniques.

In reflection mode, a contrast can be obtained from small differences in the refractive index between dispersed phases, making possible the qualitative and quantitative analysis for morphological characterization (size, shape, orientation, distribution and dispersion of phases, porosity and surface roughness). Several examples from the literature allied OM with different techniques, such as electron microscopies<sup>138–140</sup> and AFM<sup>57,141</sup> for morphological analyses and even Raman spectroscopy for chemical analysis.<sup>142</sup> Thin materials can be observed in transmission mode for quantitative measurement of refractive indices and birefringence. Furthermore, limited chemical information can also be achieved by the assessment of birefringence changes on optically anisotropic samples, as well as color changes occurring during chemical ageing, degradation and crystallization which can be recorded in real time for kinetics studies.<sup>143</sup>

The disadvantages of the technique are related to the limited resolution and the decreasing depth of field with the increasing magnification. The depth of field is the thickness of the sample that appears focused in the image. If the sample is rough due to the sample preparation technique applied, at magnifications of 1000x and higher, it becomes impossible to focus all the surface features at the same time. This problem can basically be solved with the preparation of a flat surface of the material<sup>71,72</sup>, or by the use of specific microscopes equipped with Extended Focal Image (EFI) mode that collect a series of images at different depths, thus obtaining a clear final 2D image over a height greater than that of a conventional optical system. One example is the Opto-digital Microscope DSX500 from Olympus.<sup>144</sup>

### 5.2. Electron Microscopies

The use of a high voltage electron beam instead of light is of prime importance to overcome the limited resolution of OM. The Rayleigh criterion for the diffraction limit to resolution is given by the equation  $\theta = 1.22 \frac{\lambda}{D}$ , where  $\theta$  is the angle the objects are separated by,  $\lambda$  is the wavelength of light and  $D$  is aperture diameter. It states that two objects are just resolvable when the center of the diffraction pattern of one is directly over the first minimum of the diffraction pattern of the other. Practically this usually means that the resolution in microscopy is limited to about  $\frac{1}{2}$  of the wavelength of the illumination source used. The photons used in OM have wavelengths between 400 and 700 nm, electrons, however, present wavelengths of much less than 1 nm (2.5 pm at 200 keV) which can give a sub-nanometric resolution.<sup>71</sup> Electron microscopes can be divided in: Scanning Electron Microscope (SEM), for surface analysis of massive samples, Transmission Electron Microscope (TEM) and Scanning Transmission Electron Microscope (STEM), for bulk analysis of

ultrathin sections. These microscopes are operated in vacuum, in reflection or transmission mode, with acceleration voltage from <math>5\text{ kV}</math> to <math>300\text{ kV}</math>. Furthermore, SEM has a depth of field close to <math>1\ \mu\text{m}</math> which is significantly larger than what is achieved with OM.<sup>145,146</sup> In addition to topographic information (for SEM), these techniques can provide complementary chemical information based on the different interactions of the electron beam with the material, which can emit low-energy electrons, X-rays, optical photons, etc. The detection of these different emissions is useful for chemical and crystallographic analysis at high resolution.<sup>100</sup> A brief description of the fundamentals of the techniques will be discussed.

### 5.2.1. Scanning Electron Microscopy (SEM)

Scanning Electron Microscopy (SEM) is a technique that provides information essentially from the surface of the material, i.e., a few micrometers thick layer, by detecting the electrons emitted after interaction with the primary electron beam. Due to the great depth of field of the technique ( $\sim 1\ \mu\text{m}$ ), images have a three dimensional appearance, even when rough samples are imaged in magnifications of  $1000\times$ .<sup>100,145</sup> For polymers, and non-conductive materials in general, a gold or carbon coating is necessary to avoid charge build up, which distorts the images and can damage the sample's surface.

Images can be formed by collecting different signals emitted from the sample, each of them carrying complementary information. The three most important signals from the specimen are backscattered electrons (BSE), secondary electrons (SE), and X-rays. Figure 2.24 illustrates the interaction volume of the electron beam with the sample and the region from which each signal originates.

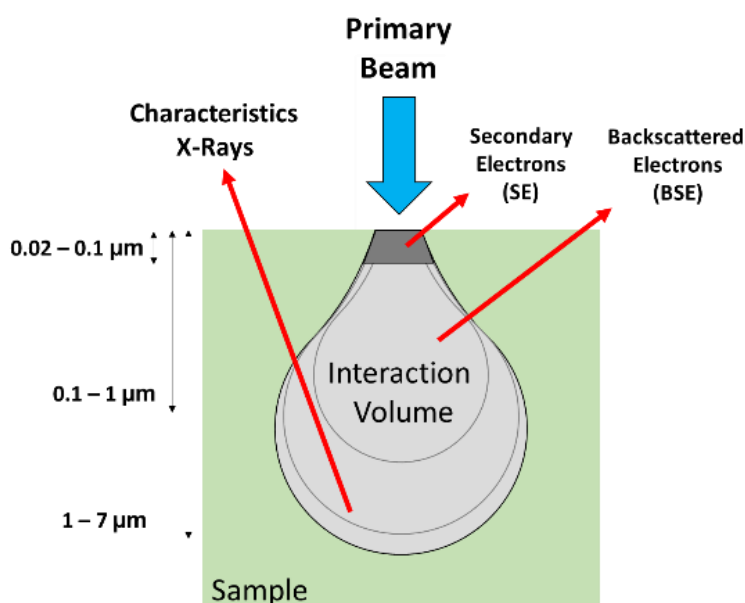


**Figure 2.24.** (a) Schematic representation of the interaction volume of the primary beam with the material showing the regions where the different signals come from.



BSE are formed when the electrons from the beam are scattered by the collision with the atomic nuclei in the sample. Some of the scattered electrons lose their energy and are reflected back from the sample surface, from a depth of 10 nm to more than 1  $\mu\text{m}$  depending on the sample and the beam voltage applied. This energy loss is linked to the atomic number of the material, which means that these electrons give strong compositional contrast in multiphase materials. The lateral resolution of a BSE image can range from 50 to 200 nm, because of the high energy ( $> 50$  eV) and the wide area from which the electrons are ejected. Thus this mode is mainly used to collect images based on atomic distribution. Sample preparation for observation with SEM-BSE is generally simple but since polymers have low atomic number and the scattering of electrons is weak (giving poor contrast), the technique requires the use of staining agents composed by high molecular weight elements, such as osmium tetroxide ( $\text{OsO}_4$ ) and ruthenium tetroxide ( $\text{RuO}_4$ ) for contrast enhancement.

SE are low energy electrons ( $< 50$  eV) that interacted with the superficial layers of the material's surface, and are emitted from a depth of 2 to 10 nm. SE are greatly influenced by the topography of the sample, i.e., if the beam falls on a tilted surface or onto a peak, more of the interaction volume is near to the surface, so more SE will be produced. Therefore steep surfaces and edges tend to be brighter than flat surfaces, valleys or pits, which results in images with a well-defined, three-dimensional appearance. As SE come from an area defined by the beam size, they give very high resolution topographic images (down to about 1 nm). Finally, characteristic X-rays are emitted when the incident electrons are capable of exciting electrons from the nuclei into high energy states, which release energy into X-ray form when decaying back to the low energy state. Each kind of atom has a unique X-ray signature, characteristic of its atomic number, allowing the characterization of the chemical composition of the sample. Energy Dispersive X-ray Spectroscopy (EDS) and Electron Energy Loss Spectroscopy (EELS) are techniques that use this signal for elemental analysis (for elements of atomic number  $Z > 10$ ). However, characteristic X-rays come from depth of 1 to 7  $\mu\text{m}$ , which limits the lateral resolution to several microns.<sup>66,145</sup>

The general spatial resolution depends on the region from which the signal comes from, varying from 1 nm to few micrometers. The interaction volume will depend on the nature of the material being probed and the energy of the primary beam. Low atomic number materials scatter less the electrons from the incident beam, which increases the size of the interaction volume. Increasing the energy of the electron beam has the same effect. Radiation damage can occur if the energy is sufficiently high, causing changes in the structure of polymers, mass and crystallinity loss, dimensional changes and image distortion. Figure 2.25 is an example from the literature showing the effect of a 20 keV electron beam on a poly(methyl methacrylate) sample.<sup>145</sup> Images from (1) to (7) are relative to the application of different etching times to gradually remove the irradiated material, i.e., highly affected material been etched first and less affected material further, revealing an affected zone up to more than 5  $\mu\text{m}$  in depth. Generally, low accelerating voltages and low beam currents are required to avoid radiation damage, under the cost of resolution. Modern SEM systems with a field emission gun can be operated at low beam voltage with high resolution, which reduces the need for metal or carbon coating on the polymer surface.

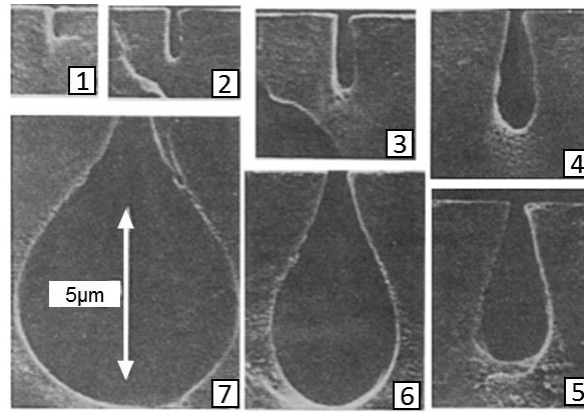


**Figure 2.25.** Example of damage caused by a 20keV electron beam on a polymer sample. Images from (1) to (7) are relative to different etching times applied on the sample to gradually remove the irradiated material and to reveal the damage. Adapted from <sup>145</sup>

An example of the sensitivity of secondary electrons to small topographic features is given by the work of Ming Jin and coworkers<sup>147</sup>, who studied the morphology of ultrahigh molecular weight polyethylene (UHMWPE) and isotactic polypropylene (iPP) blends moulded via micro-injection. Figure 2.26 show SEM-SE images of the morphology of the skin, subskin and core of cryo-ultramicrotomed and then etched injection molded samples. The skin layer (Figure 2.26 (a)) is dominated by abundant shish-kebabs along the flow direction (indicated by the yellow arrow), but a large number of  $\beta$ -cylindrulites appear in the subskin region (Figure 2.26(b)). In the core of the material (Figure 2.26(c)) several oriented bundle-like  $\beta$  crystals were observed aside from randomly distributed  $\beta$  spherulites. The researchers claimed that this study was the first to discover oriented bundle-like  $\beta$  modification in the micro-injected molded parts.

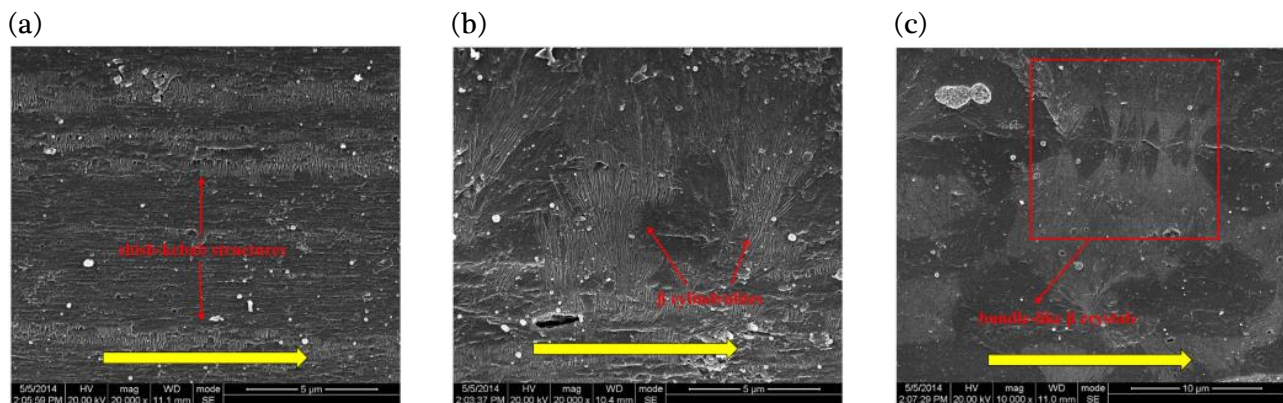


**Figure 2.26.** SEM micrographs of a PP/UHMWPE blend: (a) skin layer showing shish-kebab structures; (b) subskin layer showing  $\beta$ -cylindrulites and (c) core layer showing bundle-like  $\beta$  crystals. The yellow arrow represents the flow direction.<sup>147</sup>

Uthaipan *et al.*<sup>148</sup> used SEM in BSE mode to study the morphologies of ternary blends composed of ethylene propylene diene terpolymer (EPDM), ethylene octene copolymer (EOC) and Polypropylene (PP). The specimens devoted to SEM observation were prepared by cryo-fracture in liquid nitrogen, to form a fresh cross-section surface. The rubber phase was stained with ruthenium tetroxide ( $\text{RuO}_4$ ) vapor to increase the phase contrast in BSE mode. SEM-BSE images on Figure 2.27 show that when the EOC content was increased, the particle size of the dispersed elastomer phases decreased, and coalescence of these dispersed domains was hindered, i.e., the EOC acted as an efficient compatibilizing agent at the EPDM/PP interfaces.

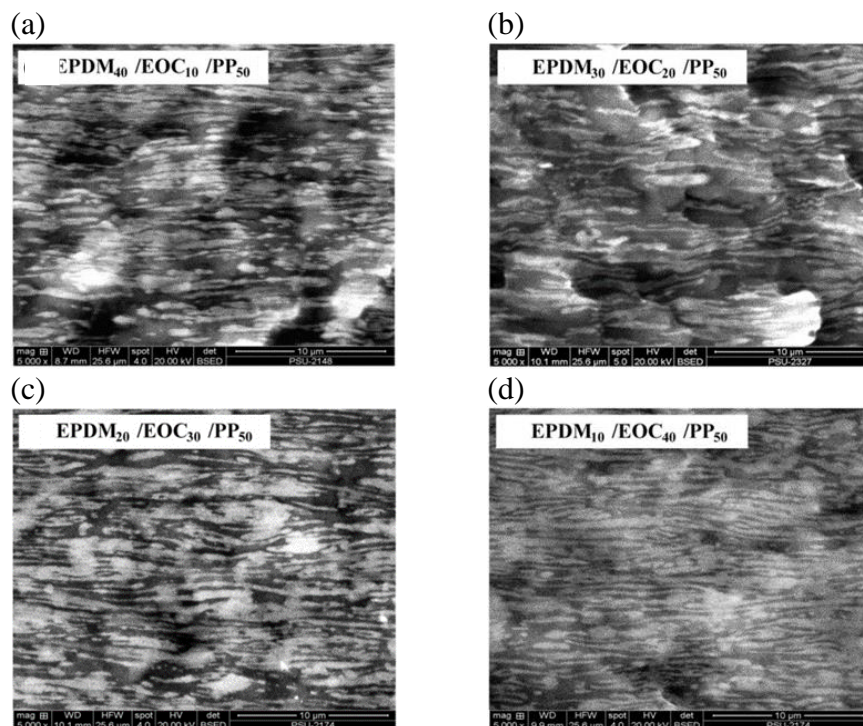


**Figure 2.27.** SEM-BSE images of elastomer phases in PP matrix with different weight compositions: (a) EPDM<sub>40</sub>/EOC<sub>10</sub>/PP<sub>50</sub>, (b) EPDM<sub>30</sub>/EOC<sub>20</sub>/PP<sub>50</sub>, (c) EPDM<sub>20</sub>/EOC<sub>30</sub>/PP<sub>50</sub>, (d) EPDM<sub>10</sub>/EOC<sub>40</sub>/PP<sub>50</sub>.<sup>148</sup>

### 5.2.2. Transmission and Scanning Transmission Electron Microscopy (TEM/STEM)

TEM is operated in transmission mode, which means that the electron beam needs to pass through the thickness of the sample. For that, high accelerating voltages are used, typically 40-120 kV and very thin specimen layers are studied, with thicknesses of the order of 50-150 nm. The detectors collect the electrons scattered by the nuclei of the material. To avoid the scattering of the electrons by air, this technique demands operation in high vacuum.<sup>71</sup>

Sample preparation is a key step for TEM characterization. For bulk sample, thin sections (~50-150 nm) are usually obtained by Cryo-ultramicrotomy or recently by FIB (for hard samples). Like for SEM-BSE, the technique generally requires additional staining steps with osmium tetroxide (OsO<sub>4</sub>) and ruthenium tetroxide (RuO<sub>4</sub>) for contrast enhancement. Image contrast is then achieved from the distribution of the staining elements in the material, i.e., regions with high concentration of the heavier element will scatter more electrons, appearing darker on the image.<sup>100</sup>

Yongjin Li and a coworker<sup>149</sup> studied the morphologies of poly(phenylene oxide)/polyamide 6 (PPO/PA6) blend nanocomposites with organoclay. Sections were stained with OsO<sub>4</sub> for contrast enhancement of the PA6. Figure 2.28 shows TEM images of the composites, PPO appearing as light gray domains and PA6 as dark gray with dark lines inside, relative to the organoclay. The authors observed that the exfoliated clay was located only in the PA6 phase (Figure 2.28 (b)), which they were able to correlate to rheological measurements. They concluded that the selective localization of the exfoliated clay in the PA increased the viscosity of PA6 and impeded the coalescence of the PPO phase. Therefore, the average diameter of the dispersed PPO domains decreased significantly when a small amount of clay was added (1 to 5 %wt).

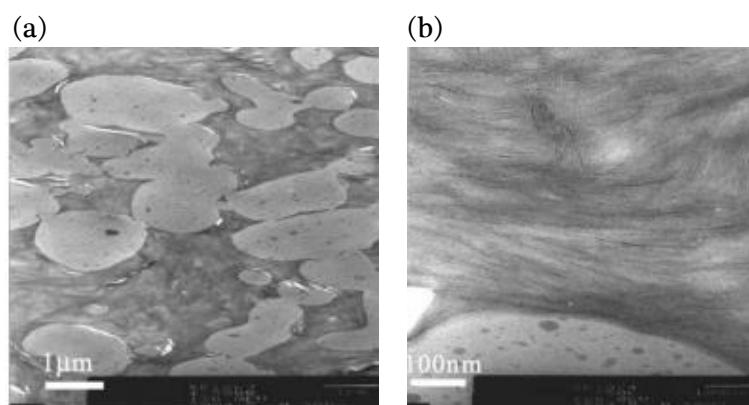


**Figure 2.28.** TEM micrographs of PPO/PA6 nanocomposites at low magnification (a) showing small domains of PPO phase (light gray) in PA6 phase (dark gray) and at higher magnification (b) showing dark lines inside the PA6 phase relative to the organoclay.<sup>149</sup>

A STEM microscope is a combination of a TEM and a SEM. The detectors collect the transmitted electrons scattered by the sample, but the electron beam scans the sample line by line, as in SEM. Advantages of STEM over TEM involve the increase on the thickness of the probed samples (up to a few microns thick at 200 keV, compared to only about 0.5 micron for a TEM at the same energy), the possibility of simultaneously display images using different modes (Bright Field, High Angle Annular Dark Field, Z-contrast), and it can supply more information than the traditional TEM system, like chemical and structural analyses. STEM can collect SE and BSE images in the same way as a standard SEM, allowing to correlate surface information (from SE) with bulk information from the STEM modes, while it offers higher resolution than the SEM system due to the higher accelerating voltages in STEM.<sup>66,150</sup> Chemical analysis from EDS and EELS can be obtained at high resolution (0.1 nm in a dedicated high performance STEM system), allowing the identification of local elemental composition.

Heinzl and coworkers<sup>151</sup> have used a STEM equipped with EDS to study silica reinforced polybenzimidazole membranes. Figure 2.29 (a) show elemental maps (C, O and Si) of the material where it could be seen that the elements Si and O dominated in the bright silica particles. Figure 2.29 (b) shows EDS line scan measurements of the SiO<sub>2</sub> particles, in which a homogeneous elemental composition was observed, free of any kind of contamination, such as enrichment of other elements like P or K (present at the reagents during membrane preparation) at the interface between the particles and the polymer matrix. This example illustrates the power of elemental analysis in high resolution, which could be of interest for the analysis of the interface of chemically modified nanofillers in nanocomposites and hybrid materials.

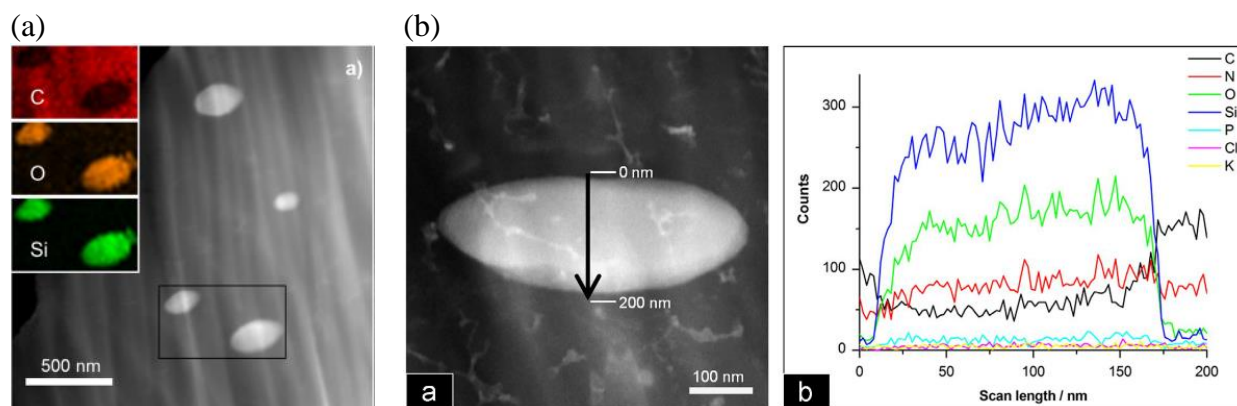


**Figure 2.29.** (a) STEM image of silica reinforced polybenzimidazole membranes with elemental maps for the elements C, O and Si displayed as insets. (b) EDS scan line of a silica particle showing the corresponding elemental distribution.<sup>151</sup>

The major problem with the use of electron microscopy for characterization is the beam-sensitive nature of polymeric materials. The stationary high-energy beam can result in severe radiation damage, causing chemical changes, mass transport, destruction of crystallinity, heating/etching and formation of holes in the thin section. All these changes make the image interpretation difficult during analysis, demanding the preparation of replicate samples, which is time consuming. However, it is a direct complementary technique to AFM for morphological characterization.

### 5.3. Fourier Transform Infrared Spectroscopy (FTIR)

The Infrared spectroscopy technique is based on the absorption of radiation in the infrared frequency range, typically at the mid-IR-region wavenumber from 400 to 4000  $\text{cm}^{-1}$ , due to the molecular vibrations of the functional groups contained in the polymer chain.<sup>152</sup> For the vibration to be detectable in the IR spectra, the absorption must result in a change of dipole moment of the chemical group. Chemical groups with strong dipole moments at the ground state will display strong IR absorptions.<sup>101</sup> On the other hand, certain vibrational modes in symmetric molecules do not show up in IR spectra, due to the absence of dipole moment variation.<sup>71</sup> The vibrational patterns recorded as a function of the wavenumber are characteristic of the internal structure of the material, providing a fingerprint of its molecular structure and composition, allowing the measurement of crystallinity, tacticity and molecular strain.<sup>71</sup>

The acquisition of the vibrational behavior of polymers is usually done in two modes of operation: transmission through the material thickness or attenuated total reflection (ATR) of IR radiation at the surface. Infrared spectroscopy in transmission mode is often used for analysis of thin polymer films from 10 to 30  $\mu\text{m}$  thick, due to the high absorption of the materials. In ATR mode, as illustrated on Figure 2.30, the polymer material is put in contact with a crystal (typically diamond or germanium), in which the beam of infrared light is directed at a certain angle. The infrared will reflect inside the crystal and evanescent waves will penetrate into the surface of the sample, typically from 0.5 to 5  $\mu\text{m}$  depending on the angle of incidence, wavelength of the infrared beam and the type of crystal used.<sup>152</sup> The technique requires a good contact between the sample surface and the crystal for the analysis, which implies the application of a certain pressure that as a drawback is capable of causing damages to the surface.

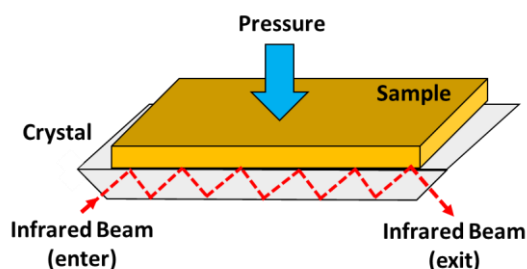


**Figure 2.30.** Schematic representation of the IR spectroscopy in ATR mode

Attenuated total reflection (ATR) has also been combined with a microscope to carry out ATR microspectroscopy. Researchers claim to have attained spatial resolution from 12 down to 2  $\mu\text{m}$ , using a micro-ATR FT-IR objective with germanium crystal.<sup>153–156</sup> Cheng and coworkers<sup>157</sup> have used this technique to study the compatibilization of ultra-high molecular weight poly-ethylene UHMWPE/Recycled-Polyamide 6 (R-PA6) blends with polyethylene-graft-maleic anhydride (HDPE-g-MAH). As show on Figure 2.31, they were able to map the distribution of the components on an area of  $300 \times 300 \mu\text{m}^2$  with resolution down to  $\sim 2 \mu\text{m}$ . Figure 2.31 (a) shows the distribution of R-PA6 in an uncompatibilized UHMWPE/R-PA6 blend with the pink areas relative to R-PA6 domains (obtained using a FTIR spectrum of R-PA6) and the blue areas are for UHMWPE, clearly indicating that these two polymers are incompatible. Figure 2.31 (b) shows the phase distribution of a compatibilized blend with UHMWPE domains with a typical size of 5–40  $\mu\text{m}$  disperses in the R-PA6 phase. Author concluded that adding 8%wt of HDPE-g-MAH to the immiscible UHMWPE/R-PA6 blends significantly improves their miscibility.

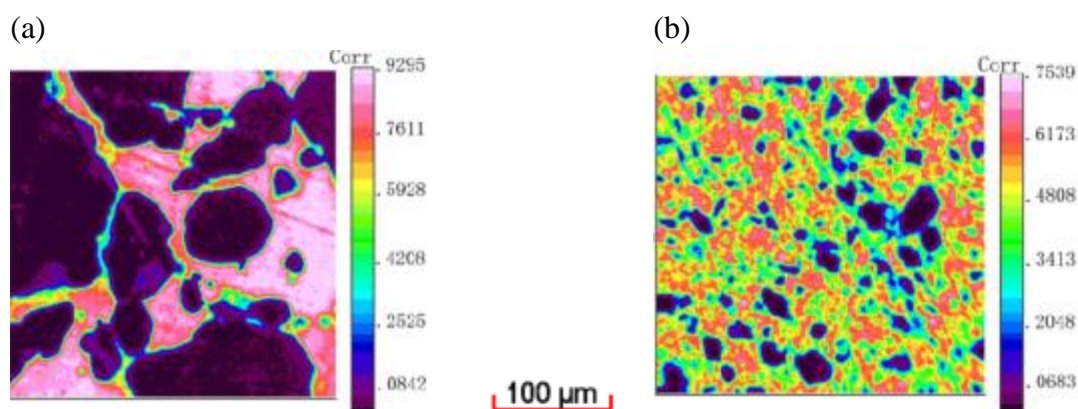


**Figure 2.31.** Micro ATR-FTIR mappings with dimension of  $300 \times 300 \mu\text{m}^2$  representing the distribution of R-PA6 in different UHMWPE/R-PA6 blends. (a) uncompatibilized blend and (b) compatibilized blend with HDPE-g-MAH. Maps were obtained using a FTIR spectrum of R-PA6 as uniquely representative FTIR imaging recognition results.<sup>157</sup>

Like for conventional ATR-FTIR spectroscopy,  $\mu$ -ATR-FTIR requires good contact of the crystal with the sample, which may cause sample damage. The operation must be done several times for the acquisition of a cross-section or a mapping in a large area, which increases the risk of surface damage and transfer of material from one point to another.<sup>157,158</sup> This is critical when probing the cross-section of thin materials, since the high stress imposed can break the sample and make the analysis impossible.

#### 5.4. Summary Table of Characterization Techniques

A summary table of all the characterization techniques is presented below, with the resolution, information acquired and limitations of each technique.

**Table 2.3.** Summary table of techniques used for morphological and chemical characterization of polymers

Technique	Sample Preparation	Resolution	Information	Limits
<b>Atomic Force Microscopy (AFM)</b>	No sample preparation needed for surface analysis	5-20 nm	Topography - 3D images Nano-Mechanical information	Difficult sample preparation for a cross section analysis of a bulk material
<b>Confocal Raman Spectroscopy</b>	Flat surface required to avoid auto-focus system (time consuming)	Spatial resolution down to 1 $\mu\text{m}$	Chemical/structural information Surface and bulk analysis	Slow acquisition for polymers Beam damage for sensible samples
<b>Optical Microscopy (OM)</b>	No sample preparation needed	Micrometric	Rapid view of large area	Low magnification Decreasing depth of field with increasing magnification
<b>Scanning Electron Microscopy (SEM)</b>	Conductive coating for non-conducting samples	1 nm High depth of field	Topography with 3D appearance Chemical Contrast (BSE)	Low beam damage High Vacuum Operation
<b>Transmission Electron Microscopy (TEM)</b>	Thin sections must be prepared Staining for contrast enhancement	< 1 nm	Morphology based on chemical contrast	High beam damage High Vacuum Operation
<b>Scanning Transmission Electron Microscopy (STEM)</b>	Thin sections must be prepared Staining for contrast enhancement	< 1 nm High depth of field (SE mode)	Morphology Chemical analysis (EDS)	High beam damage High Vacuum Operation
<b><math>\mu</math>-ATR-FTIR</b>	No sample preparation needed for surface analysis	Spatial resolution down to 2 $\mu\text{m}$	Chemical/structural information	Difficult sample preparation for bulk analysis Surface damage on contact

Our main objective is to ally complementary techniques capable of providing the best insights into the morphology, mechanical properties and chemical profiles of polymeric materials. The co-localization of information is highly desired for direct correlation between process-structure-properties and morphology. For that, one important issue is the ability to successively characterize the sample with different techniques without any or with very limited sample damage.

The use of Cryo-ultramicrotomy as the sample preparation technique allows for multiple complementary analyses. Electron Microscopies techniques such as SEM and STEM can provide high resolution morphological and chemical analysis complementary to AFM/Raman. To limit any damage on the sample, the analyses must be done in a specific order. OM and AFM, as non-destructive techniques, should be done first. Then, the morphological/nanomechanical information acquired can be co-localized with Raman structural and chemical information by mapping the same area probed by AFM. Punctual Raman analysis can also be done in zones not probed by the AFM. These analyses must be done prior to SEM analysis, as SEM is more destructive for the sample, therefore, being done as the final step of characterization to provide additional morphological analysis with chemical contrast (SE/BSE). In parallel, the thin sections collected during Cryo-ultramicrotomy can be used for complementary bulk analysis for STEM. For complementary chemical analyses, FTIR is able to provide high quality quantitative and qualitative chemical information, but the  $\mu$ -ATR-FTIR technique implies the application of pressure on the surface of the material, which is also source of sample damage. The use of  $\mu$ -ATR-FTIR as complementary technique requires a dedicated sample and special developments to allow the probing of a membrane cross-section. The schematic representation of the characterization strategy is presented on Figure 2.32.

This strategy will make possible quantitative structural/morphological analyses, such as spatial distribution of phases and chemical species, their concentration (or abundance), morphology of the components, mechanical properties and statistical analyses, at scales from tens of nanometers to tens of microns to establish the process-structure-properties relationship of complex polymeric materials.

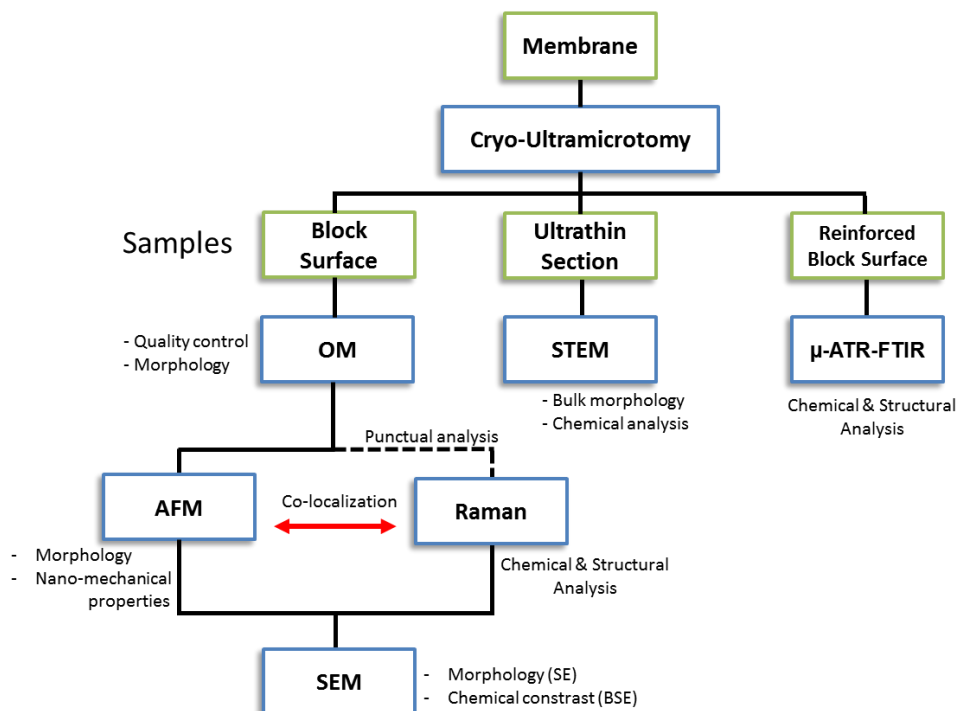


Figure 2.32. Characterization strategy



## 6. Conclusions of Chapter 2

We discussed in this chapter the best strategies for the characterization of the surface and bulk morphology, mechanical properties and chemical composition of polymeric materials. We have described morphological, nanomechanical and chemical characterization techniques: AFM, Raman spectroscopy, Optical Microscopy, SEM, TEM/STEM and  $\mu$ -ATR-FTIR. The sample preparation appear as a key step to combined these different characterization techniques, Cryo-ultramicrotomy being the most promising to properly open the material. From the specificities of each technique, we could define the characterization strategy used in this study. However, some limitations must still be addressed to obtain a surface entirely characteristic of the bulk of the material and to collect co-localized AFM/Raman information without any positioning error:

### 6.1. Difficulties related to sample preparation by Cryo-Ultramicrotomy

In order to produce a well-suited sample for co-localized AFM/Raman analysis, especially for thin polymeric membranes, specific strategies for the following issues must be developed:

- A strategy for the cutting of polymeric thin membranes without embedding to suppress any chemical contamination
- The limitation and/or suppression of frost deposition on the sample surface when warming up to the room temperature in order to avoid any morphological modification due to the sample swelling or solubilizing (water sensitive samples).
- A strategy for the preparation of polymeric thin membranes for  $\mu$ -ATR-FTIR cross-section analysis

### 6.2. Difficulties related to the co-localization of AFM/Raman analyses

Even after a suitable sample preparation, more technical difficulties need to be overcome for a proper co-localization of AFM/Raman information. We have chosen to combine two of the best commercially available instruments but not specifically designed for co-localized analysis. Therefore, noise from mechanical vibrations and operation of the Raman spectrometer can result in instabilities in the feedback loop of the AFM when they are operated simultaneously. Temperature changes in the room will result in the AFM/Raman stage drift, which make it very tough to keep the tip (AFM)/focus (Raman) in the selected field-of-view. Solutions for the following issues must be developed:

- Control of mechanical vibrations and thermal drifts for proper co-localization
- Development of strategies for precise repositioning of the sample

The strategies and developments done in order to address the difficulties in preparing the sample and co-localizing AFM/Raman information will be presented in the next chapter.

## 7. Conclusions du Chapitre 2 en Français

Nous avons discuté dans ce chapitre des meilleures stratégies pour la caractérisation de la morphologie, des propriétés mécaniques et de la composition chimique de la surface et du volume des matériaux polymères. Nous avons décrit les techniques de caractérisation morphologique, nanomécanique et chimique: AFM, spectroscopie Raman, Microscopie optique, SEM, TEM/STEM et  $\mu$ -ATR-FTIR. La préparation de l'échantillon apparaît comme une étape clé pour combiner ces différentes techniques de caractérisation, la Cryo-ultramicrotomie étant la plus prometteuse pour ouvrir correctement le matériau. Cependant, certaines limitations doivent encore être résolues pour obtenir une surface réellement caractéristique de l'intérieur du matériau et garantir une parfaite colocalisation des informations obtenues par AFM et Raman:

### 7.1. Difficultés liées à la préparation des échantillons par Cryo-Ultramicrotomie

Afin de produire un échantillon bien adapté pour les analyses co-localisées AFM/Raman mais aussi TEM/STEM, IR, et ce notamment dans le cas de membranes polymères de faible épaisseur, la technique de préparation des échantillons par cryo-ultramicrotomie doit être adaptée pour permettre:

- La découpe de l'échantillon sans un enrobage pour éviter toute contamination chimique
- La limitation et/ou la suppression du dépôt de givre sur la surface de l'échantillon afin d'éviter une modification de la surface du matériau par l'eau condensée lors du réchauffement de l'échantillon (échantillons sensibles à l'eau)
- La préparation d'une surface compatible pour l'analyse  $\mu$ -ATR-FTIR de la section ouverte.

### 7.2. Difficultés liées à la co-localisation des analyses AFM/Raman

Même après une préparation d'échantillon appropriée, des difficultés techniques supplémentaires doivent être surmontées pour une parfaite co-localisation des informations AFM/Raman. Le bruit provenant des vibrations mécaniques (notamment celles dues au fonctionnement du spectromètre Raman) peut induire des instabilités non compensables par la boucle d'asservissement de l'AFM. De même ; tout changement de température dans la pièce ou d'un des deux instruments peut conduire à la dérive spatiale de l'échantillon, ce qui rend donc problématique toute analyse Raman (perte de focus). Des solutions pour les problèmes suivants doivent être développées :

- Suppression des vibrations mécaniques et limitation des dérives thermiques
- Développement de stratégies pour un repositionnement précis de l'échantillon

Les stratégies et les développements effectués afin de résoudre les difficultés de préparation de l'échantillon et de co-localisation des informations AFM/Raman seront présentés dans le prochain chapitre.



# CHAPTER 3

---

## Experimental Methods and Developments

## PROLOGUE

This chapter will present the experimental methods used and the developments that had to be done in order to (1) achieve cryo-ultramicrotomy of membranes without epoxy embedding and without frost deposition and (2) make possible the co-localized AFM/Raman analysis.

## French Prologue

Ce chapitre présentera les méthodes expérimentales utilisées et les développements qui ont été réalisés pour (1) réaliser une cryo-ultramicrotomie des membranes sans enrobage époxy et sans dépôt de givre et (2) rendre possible l'analyse AFM/Raman co-localisée.

## 1. Sample preparation by Cryo-Ultramicrotomy

Cryo-ultramicrotomy was shown to be the most appropriate to open a sample and to obtain a flat surface well suited for both AFM and Raman analyses, as well as ultrathin sections for complementary TEM/STEM analyses. The cryo-ultramicrotome used is an EM UC7 (Leica Microsystems), presented on Figure 3.1. The system allows the sectioning at room temperature with controlled cutting speed, angle and depth and can be adapted for cryo-sectioning with the installation of a specially designed cryo-chamber (Figure 3.1(b)). The cryo configuration allows the use of two different knives inside the chamber, for trimming and then sectioning (specifications in Section 1.3). An electrostatic discharge and charge system is installed near the sample surface to facilitate handling of the thin sections collected during sectioning. On the side of the knife, tweezers (or clamps) holding a copper grid can be installed collect the sections.

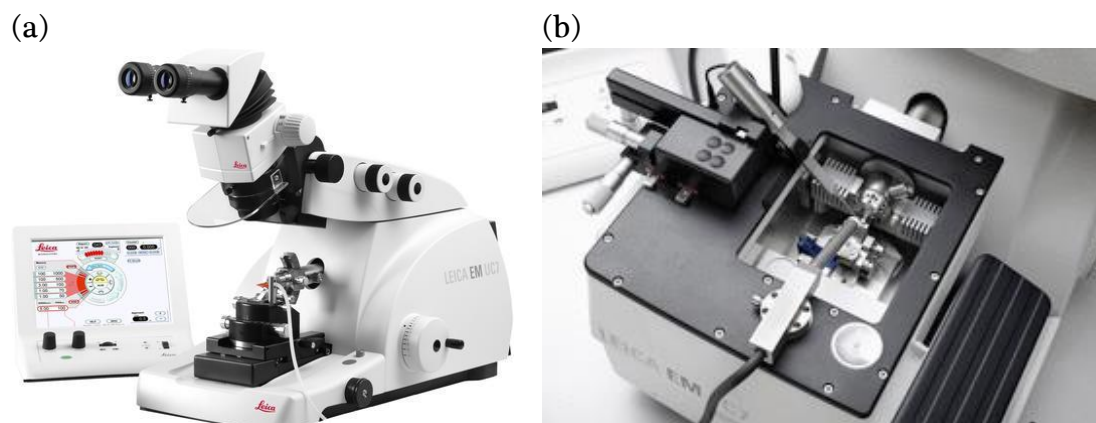


**Figure 3.1.** (a) Ultramicrotome LEICA EM UC7 (RT setup) and (b) cryo-chamber installed for cryo-ultramicrotomy

As discussed in the previous chapter, thin samples like polymer membranes (20-100  $\mu\text{m}$ ) are flexible and cannot be directly glued on a sample holder for cross-sectioning. For such thin samples a previous step of sample embedding in a resin is usually necessary for mechanical support, but can chemically modify the sample. Cutting a thick membrane without embedding or gluing is however classical and can be done using a sample holder from Leica Microsystems (Figure 3.2). The holder is a vice that maintains the sample perpendicular to the knife during sectioning. It can accommodate samples up to 2 mm thick. We adapted this type of sample holder to be able to cut our thin membranes (30-50  $\mu\text{m}$ ) without epoxy embedding very close to the surface of the vice, to avoid any motion of the membrane during AFM measurements (the AFM tip applies a shear stress on the

sample even with PFQNM mode). As a rule of the thumb the sample should not hang out of the vice more than the value of its thickness. For 30  $\mu\text{m}$  thick membranes it implies cutting at 30  $\mu\text{m}$  from the vice's surface, therefore the vice was trimmed and polished to minimize the risk of collision with the diamond knife. The same holder was used to study all the samples: thin and thick membranes, as well as slices from injection molded specimens. The preparation of each kind of sample is presented in the next sections.



**Figure 3.2.** Sample holder used to cut thick membranes (a) classical and (b) modified to minimize the risk of collision when cutting thin membranes close to the surface of the holder.

### 1.1. Sectioning of injection molded specimens

Sections about 1 mm thick were cut with a scroll-saw from the center part of standard injection molded specimens. Then the sections were cut as a triangle with a scalpel and installed in the sample holder, as shown schematically on Figure 3.3 (a). In cryo-ultramicrotomy, the block was first trimmed with the trimmer knife in a trapezoidal shape (Figure 3.3 (b)) and then surfaced perpendicular to the injection direction, first with the trimmer, then with the diamond knife, for perfect surfacing and thin sections' collection on copper grids (Lacey Carbon Support Film 400 mesh).

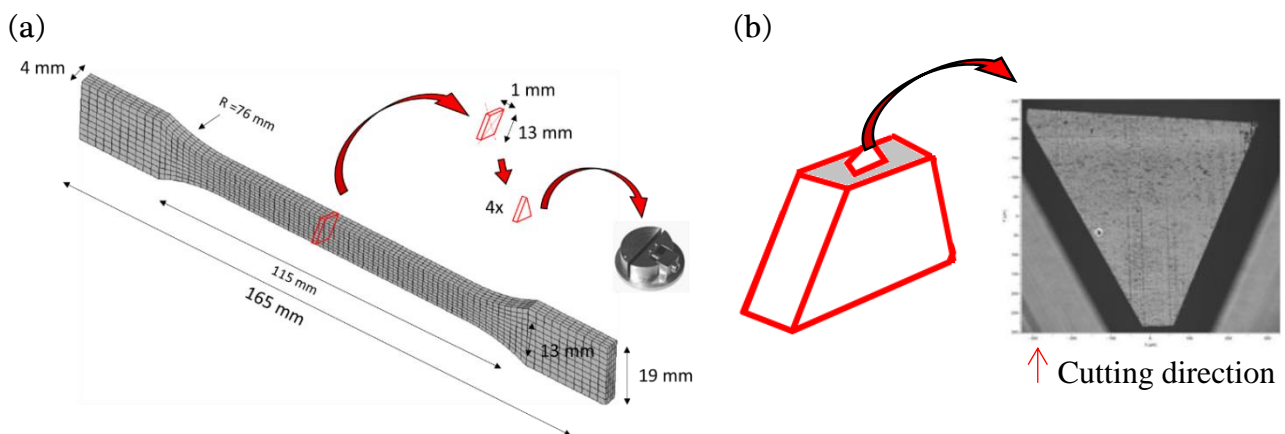


**Figure 3.3.** (a) Schematic representation of sample preparation from standard injection molded specimens (b) Optical micrograph of the trapezoidal shape trimmed at the top of the triangular section, before cryosectioning.

## 1.2. Sectioning of polymer membranes

Polymer membranes with thickness ranging from 20 to 100  $\mu\text{m}$  were first trimmed with a scalpel in a triangular form and then inserted between a folded aluminum foil (Figure 3.4 (a)). Aluminum foil facilitates the sample's handling and makes possible the repositioning of the sample inside the holder (meaning repositioning a sample in the vice for additional characterization after a period of storage out of the vice). The sandwiched membrane was then installed in the holder, protruding about 400  $\mu\text{m}$  from the surface of the vice. The sample was then trimmed and surfaced with a trimmer knife and finally with a diamond knife in the cryo-ultramicrotome. Thin sections were collected onto copper grids for complementary analysis.

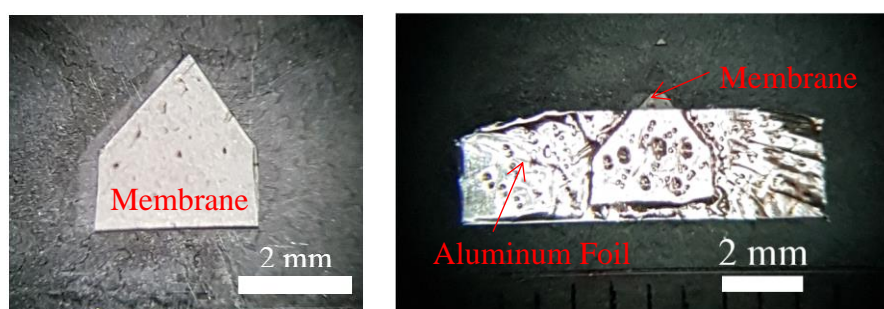


Figure 3.4. Trimmed membrane sandwiched in aluminum foil

## 1.3. Cryo-ultramicrotomy parameters

Two kinds of knife were used, first a Diatome Cryo TRIM 45° for trimming (fast rough cutting) both injection molded specimens (to achieve the trapezoidal shape) and membranes (to trim the membrane's protrusion down to a value close to its thickness: 50-100  $\mu\text{m}$  from the holder), then a Diatome Cryo AFM 35° diamond knife for perfectly surfacing the material for AFM/Raman analyses and for the collection of the ultrathin sections from TEM/STEM analysis. Parameters like cutting temperature, speed and depth (thickness of each slice) were adjusted to the nature of the sample ( $T_g$  of the polymer, thickness of the membrane, etc) in order to produce the smoothest surface and the flattest ultrathin sections. The cutting angle is imposed by the configuration of the knife. Here we have chosen 45° for trimming and 35° for surfacing to limit the compression on the polymer during the last cutting steps. The usual parameter ranges are listed in Table 3.1.

Table 3.1. Cryo-ultramicrotomy parameters used for sample trimming and sectioning

Knife	Temperature (°C)	Cutting Depth (nm)	Speed (mm/s)
Diatome Cryo Trim 45°	-100 to -160	250 - 350	5 - 10
Diatome Cryo AFM 35°	-100 to -160	50 - 100	0.1 - 3

A schematic representation of the installation of the sample on the holder and an optical micrograph of the cryo-ultramicrotomy cutting are shown on Figure 3.5.

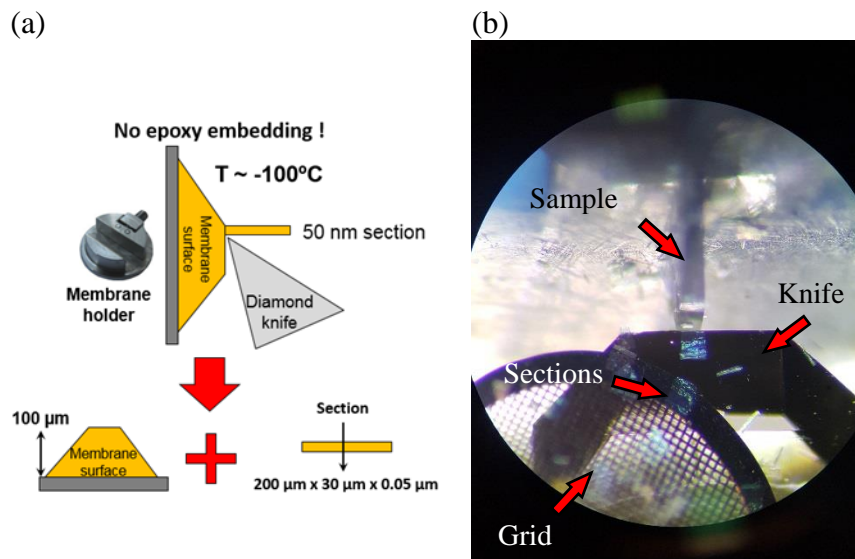


**Figure 3.5.** (a) Schematic representation of the cryo-ultramicrotomy procedure of a polymeric membrane (b) Optical micrograph of the cryo-ultramicrotomy cutting of a thick membrane without embedding

#### 1.4. Avoiding frost melting water-diffusion onto the sample's surface

As discussed in the last chapter, when working with liquid nitrogen cooled materials the presence of humidity in the ambient air is of prime concern, as it gets trapped on cold surfaces (condensation then crystallization) and the subsequent melting of the ice crystals observed during warming-up can seriously impact the sample. In order to limit these effects, we have developed a process to work in a fully controlled environment under a constant flux of dry nitrogen to avoid any contact of the sample (either held by the vice, or sections collected on a copper grid) with the humid air.

## 2. AFM/Raman Co-localization Setup

For the co-localization of AFM and Raman analyses, as explained in the previous chapter, we used a Bruker Dimension Icon AFM microscope co-localized with a Horiba Jobin Yvon LabRam HR Raman spectrometer (Figure 3.6). Each of the two instruments is considered as state of the art. This commercial co-localization system was supposed to allow the co-localization of information and also independent and simultaneous conventional AFM and Raman analyses. However, substantial developments had to be done in order to make it possible. Noise from mechanical vibrations and operation of the Raman spectrometer affected the AFM measurements when both instruments were operated simultaneously, thus a specially designed active piezoelectric table had to be installed under the AFM. Both AFM and Raman microscopes are also installed on an active anti-vibration air table, to filter mechanical vibrations transmitted by the floor. Temperature variations (day/night, despite air conditioning) in the room resulted in a thermal drift of the sample when characterized by the Raman (sample's stage belonging to the AFM). An attempt to limit the thermal drift, consisted to replace the feet of the Raman spectrometer originally made of aluminum by Invar feet (a nickel/iron alloy with low thermal expansion coefficient), however with limited success (for co-localization no longer than 30 minutes), which explains the development of a shuttle stage to solve this issue (details in section 3.2)





**Figure 3.6.** Co-localized AFM/Raman setup installed at the laboratory SyMMES

## 2.1. Atomic Force Microscope (AFM)

The AFM used is a Nanoscope Dimension Icon microscope controlled by the software Nanoscope V, and equipped with the Peak Force QNM mode (PFQNM). AFM measurements were made under ambient conditions (room temperature and relative humidity of about 50%) with a standard cantilever holder for operation in air. For topography measurements, low spring constant ( $k$ ) cantilevers were used with  $k$  ranging from 0.2-0.4 N/m (Bruker ScanAsyst-Air probes) and tip radius of about 10 nm. For nanomechanical analysis using PFQNM, cantilevers with spring constant of about 40 N/m were used (Bruker RTESPA or OTESPA probes), which are suitable for the modulus range of the polymeric materials studied. The tip was oscillated in the  $z$ -direction (travel distance of 150 nm) at 2 kHz (therefore 2000 force-distance curves recorded per second) while scanning the sample line by line at a maximum scan rate of 0.977 Hz, (~9 minutes/image). Images were taken with a resolution of 512x512 pixels. With 2 force-distance curves averaged per pixel, each image corresponds to about half a million force-distance curves. AFM images were analyzed using Nanoscope Analysis version 1.7.

### 2.1.1. AFM Calibration Method

As discussed in Chapter 2, the tip shape is not an ideal sphere and can change due to the mechanical abrasion during calibration and analysis. Thus, the precise determination of the tip radius before calibration is not representative of its real shape when probing the material besides that it is considered as an ideal sphere by the nanomechanical models. In order to avoid these drawbacks, the tip radius was determined by a Relative Calibration method using a dedicated reference samples kit provided by Bruker (Model: PFQNM-SMPKIT-12m). The kit provides different samples with known modulus for cantilever calibration.

#### Theoretical Part

First, using a nanomechanical model we will mathematically deduce the main parameters controlling the measurement of the Young's modulus of the material and the measurements that should be done in reference samples in order to allow further quantitative analysis

Considering the Hertzian model on Equation 3.3, the loading force (F) is given by the reduced Modulus ( $E_*$ ), indentation depth ( $\delta$ ), Poisson ratio ( $\nu$ ) and the tip radius (R).

$$F = \frac{4}{3} E_* \sqrt{R} \delta^{\frac{3}{2}} \quad 3.1$$

The reduced modulus is defined using Equation 3.2, where  $\nu_{probe}$  and  $\nu_{sample}$  are the Poisson's ratio of the probe and the sample, and  $E_{probe}$  and  $E_{sample}$  are the modulus of the probe and the sample.

$$\frac{1}{E_*} = \left( \frac{1 - \nu_{probe}^2}{E_{probe}} \right) + \left( \frac{1 - \nu_{sample}^2}{E_{sample}} \right) \quad 3.2$$

Assuming that  $E_{probe} \gg E_{sample}$ , (since  $E_{probe} \sim 70\text{GPa}$  for silicon) one can neglect the probe contribution and consider the simplification of Equation 3.1, with  $E_{sample}$  and  $\nu_{sample}$  simply as E and  $\nu$  (Equation 3.3).

$$F = \frac{4}{3} \frac{E}{(1 - \nu^2)} \sqrt{R} \delta^{\frac{3}{2}} \quad 3.3$$

The sample Modulus (E) can be then expressed in terms of the applied loading force (F), indentation depth ( $\delta$ ), Poisson ratio ( $\nu$ ) and the tip radius (R) as in Equation 3.4.

$$E = \frac{3}{4} \frac{F}{\sqrt{R} \delta^{\frac{3}{2}}} (1 - \nu^2) \quad 3.4$$

The indentation depth ( $\delta$ ) can be calculated from the subtraction of the deflection (D) from the Z-position (Z). The deflection (D) is by itself calculated from the Sensitivity (S) and the deflection voltage (V) (Equation 3.5). The loading force (F) is related to the spring constant (k) of the cantilever by the deflection (D) as shown in Equation 3.6. Thus, the modulus E can be expressed by Equation 3.7.

$$\delta = (Z - D) = (Z - S \cdot V) \quad 3.5$$

$$F = k \cdot S \cdot V \quad 3.6$$

$$E = \frac{3}{4} \frac{k \cdot S \cdot V}{\sqrt{R} \delta^{\frac{3}{2}}} (1 - \nu^2) \quad 3.7$$

Assuming the analysis of two different materials, the ratio between their moduli is given by:

$$\frac{E_1}{E_2} = \frac{(1 - \nu_1^2)}{(1 - \nu_2^2)} \frac{k_1 \cdot S_1 \cdot V_1}{k_2 \cdot S_2 \cdot V_2} \sqrt{\frac{R_2}{R_1}} \left( \frac{\delta_2}{\delta_1} \right)^{\frac{3}{2}} \quad 3.8$$

If the same cantilever is used to probe both materials ( $k_1=k_2$ ) and the same deflection voltage (V) is applied when imaging each sample individually, the maximum loading force (Peak Force) is the same on both materials. The Z-position (Z) to impose the same deflection voltage depends on the mechanical properties of each material. The modulus ratio is equal to:

$$\frac{E_1}{E_2} = \frac{(1 - \nu_1^2)}{(1 - \nu_2^2)} \sqrt{\frac{R_2}{R_1}} \left(\frac{\delta_2}{\delta_1}\right)^{\frac{3}{2}} = A \cdot \left(\frac{Z_2 - S \cdot V}{Z_1 - S \cdot V}\right)^{\frac{3}{2}} \quad 3.9$$

This means that the modulus ratio will be determined by the value of the deflection sensitivity and the indentation ratio of each phase. If the deflection sensitivity ( $S$ ) is correct, the indentation ratio  $\left(\frac{\delta_2}{\delta_1}\right)$  is correct and hence the modulus ratio  $\left(\frac{E_1}{E_2}\right)$  is correct.

To achieve quantitative force measurements, the rigidity of the cantilever can be measured with the Thermal Tune method. As the procedure of the Thermal Tune method depends on the Deflection Sensitivity, the importance of the proper measurement of the Deflection Sensitivity is evidenced one more time.

Finally, the tip radius must be adjusted according to a certain indentation on a reference sample, to take into account the effective tip-sample area of contact. This can be done by considering the application of Equation 3.9 to compare the measured modulus ( $E_{\text{measured}}$ ) on the reference sample using the Thermal Tuned spring constant ( $k_{\text{Thermal Tuned}}$ ), with the expected value for its modulus ( $E_{\text{reference}}$ ) that should be measured with the actual tip radius, that we call  $R_{\text{estimated}}$ . Since  $\nu$ ,  $k_{\text{Thermal Tuned}}$ ,  $S$ ,  $Z$  and  $V$  are the same, Equation 3.9 can be written as:

$$\frac{E_{\text{measured}}}{E_{\text{reference}}} = \frac{(1 - \nu^2)}{(1 - \nu^2)} \frac{k_{\text{thermal tuned}} \cdot S \cdot V}{k_{\text{thermal tuned}} \cdot S \cdot V} \sqrt{\frac{R_{\text{nominal}}}{R_{\text{estimated}}}} \left(\frac{(Z - S \cdot V)}{(Z - S \cdot V)}\right)^{\frac{3}{2}} \quad 3.10$$

or

$$\frac{E_{\text{measured}}}{E_{\text{reference}}} = \sqrt{\frac{R_{\text{nominal}}}{R_{\text{estimated}}}} \quad 3.11$$

From Equation 3.11, one can estimate the tip radius for an applied indentation on a chosen reference sample (Equation 3.12). The same indentation should be applied to the unknown sample in order to have a good agreement with the modulus calibration. In practice, the system does not show the indentation depth (the real material's deformation under the tip) in real time, but a calculated deformation from the force-distance curves within a certain fitting region. The displayed deformation is slightly lower than the real deformation because the default Deformation Fit Region is 85% of the full deformation. Therefore, deformation shown by the software is different from sample indentation but has close correlation and it is the parameter used in real time to ensure the agreement with the calibration.

$$R_{\text{estimated}} = R_{\text{nominal}} \left(\frac{E_{\text{measured}}}{E_{\text{reference}}}\right)^2 \quad 3.12$$

The developed procedure is composed of different steps: Adjustment of laser alignment and feedback loop, determination of the Deflection Sensitivity, cantilever's Spring Constant and Tip Radius. The procedure is done as follows:

### Laser Alignment and Feedback Loop

After installation of the cantilever on the AFM head, the laser alignment was adjusted using the knobs and centered on the photodiode detector in order to have the maximum reflection signal. The first reference sample used for calibration of the system is the sapphire. After engagement on the sample's surface, one needs to adjust the feedback look using the Sync Distance parameter. The Sync Distance is the distance between the start point of an extend-retract cycle and the point of peak force, used by the system to control the feedback loop and the maximum applied force on the sample. Using a deflection-time representation, as illustrated on Figure 3.7 (a), the Sync Distance can also be understood as the time in which the minimum Z position of the cantilever is attained, which implies the maximum deflection of the cantilever (PeakForce). Figure 3.7 (b) show force-distance curves with three possible situations where the Sync Distance is too early (or too short) (b)-1, i.e., the feedback force will be read before the actual maximum applied force; the correct position (b)-2, in which the feedback measurement is done on the maximum applied load and thus both extend and retract curves are aligned; and finally when it is too late (or too long) (b)-3, in which the feedback is taken on the retract curve, thus after the actual maximum force was applied. The Sync Distance is adjusted by imaging the sapphire sample allowing the proper control of the feedback and calculation of the mechanical properties from the force-distance curves.

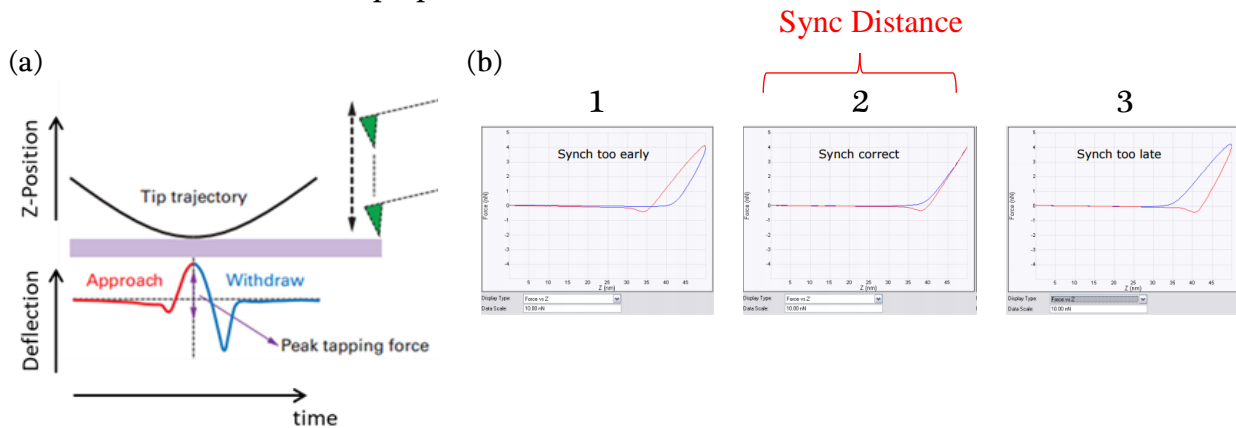


**Figure 3.7.** a) Schematic representation of the tip trajectory and deflection signal in function of time. In this representation, the Sync Distance parameter represents the time correspondent to the maximum deflection (Peak Force). (b) Images of the proper adjustment of the Sync Distance. 1) Sync too early; 2) Correct Sync Distance and 3) Sync too late.

### Determination of the Deflection Sensitivity

The nominal values of tip radius ( $R_{\text{nominal}}$ ) and spring constant ( $k_{\text{nominal}}$ ) provided by the manufacturer were entered in the system for the preliminary measurement and evaluation of the Deflection Sensitivity.

The Deflection Sensitivity was first measured doing a deflection-distance curve (Ramp Mode) on the standard sapphire sample. The sapphire is a rigid material, thus no deformation is induced by the tip on its hard surface. An example of the deflection-distance curve on the sapphire surface is given on Figure 3.8. The deflection sensitivity is then measured on the linear part of the curve, as illustrated on Figure 3.8. This parameter highly depends on the cantilever used and the laser reflectivity on the cantilever's surface which can be enhanced by reflective coatings on its back. Thus, the deflection sensitivity must be measured for each cantilever before analysis of a sample. Back to imaging mode, the Sync Distance is readjusted using the same force used for the deflection-

distance curve and the Deflection Sensitivity is updated in order to take into account the perturbations of the oscillatory and scanning movements of the tip.

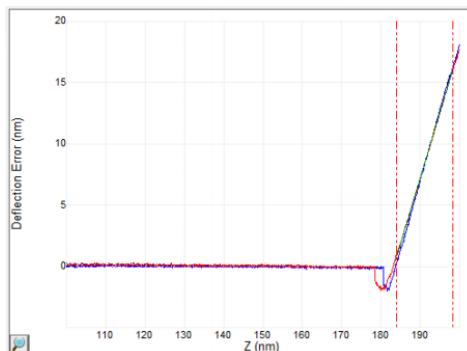


**Figure 3.8.** Deflection-distance curve on the sapphire sample showing the limits for deflection sensitivity determination.

Considering the sensibility range of the cantilevers used in this study, the deflection sensitivity was then validated using the standard Polystyrene-Low Density Polyethylene (PS-LDPE) sample provided by Bruker. The modulus of the Polystyrene is 2.7 GPa and the one of LDPE is 0.1 GPa, which gives a modulus ratio of 27, or equivalent to 1.431 in log scale. In this case, the deflection voltage ( $V$ ), the spring constant ( $k$ ) and the deflection sensitivity ( $S$ ) are equal for both phases, since they are probed at the same time. This means that if the  $\Delta\text{Log}E$  measured is equal to 1.431, then the deflection sensitivity is correct, in accordance with Equation 3.9 as illustrated on Figure 3.9. If not verified, the laser alignment was readjusted to optimize the signal and a new measurement of the deflection sensitivity on the sapphire sample was performed.

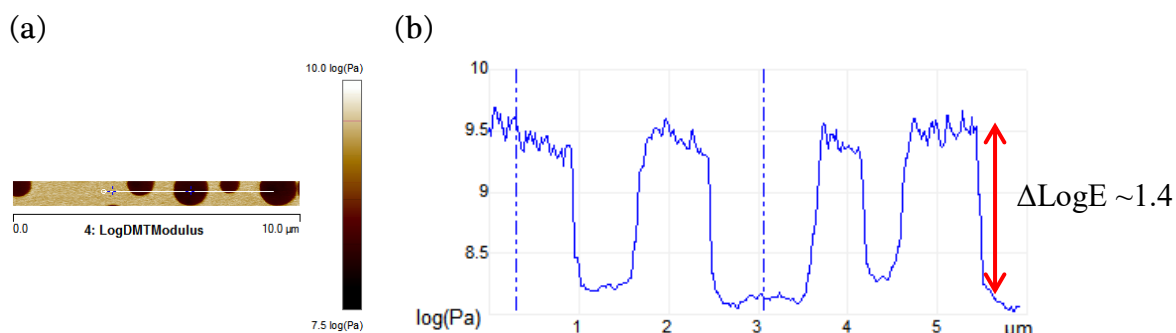


**Figure 3.9.** (a) AFM Log Modulus image of PS-LDPE standard sample. PS appearing in white yellow and LDPE in dark brown. (b) Log Modulus section corresponding to the line on the image showing a log difference of about 1.4 between both phases.

### Determination of Spring Constant and Tip Radius Estimation

The actual spring constant ( $k_{\text{thermal tune}}$ ) of the cantilever was then determined using the Thermal Tune method. The advantage of using the standard PS-LDPE sample at the previous step of deflection sensitivity validation is that one can use the same sample for tip radius estimation, depending on the modulus range of the sample of interest to be measured further. The Young's modulus ( $E_{\text{measured}}$ ) of one of the reference sample phases (PS or LDPE) was measured using the nominal tip radius ( $R_{\text{nominal}}$ ), imposing deformation depths from 2 nm to 10 nm at the phase of interest, to operate within the limits of the DMT model (as presented on Chapter 2) used by Nanoscope Software to calculate the mechanical properties from the force-distance curves. With these measurements, one can now estimate the actual tip radius for an imposed deformation on the

chosen standard sample phase (PS or LDPE) using Equation 3.12, presented here once again for the sake of convenience:

$$R_{estimated} = R_{nominal} \left( \frac{E_{measured}}{E_{reference}} \right)^2 \tag{3.12}$$

The tip radius ( $R_{estimated}$ ) is then corrected in the software, which gives now the proper value (2.7 GPa for the PS or 0.1 GPa for the LDPE) for a certain imposed deformation on the chosen reference. Samples are then imaged with a peakforce setpoint inducing a similar deformation depth as the one used for calibration.

It is important to notice that while imaging the PS-LDPE sample, once the tip radius is estimated based on one of the standard sample phases (PS or LDPE) the modulus measured for the other phase on the image is either under or overestimated depending on the cantilever chosen, since the deformation imposed on both phases can be very different, hence, the tip-sample area of contact. This bias of the PFQNM cannot be avoided and should be taken into account when probing multiphase samples with great modulus difference.

Different cantilever types are used for different ranges of sample modulus, i.e., a single cantilever cannot have a good sensitivity for materials with a too big modulus difference. Nevertheless, according to the Young’s modulus range of the samples of interest, this procedure can be adapted for different cantilever types (higher or lower rigidity) by adapting different references samples (two materials with different known modulus to validate the cantilever’s deflection sensitivity).

A summary of the presented procedure is presented on Figure 3.10.

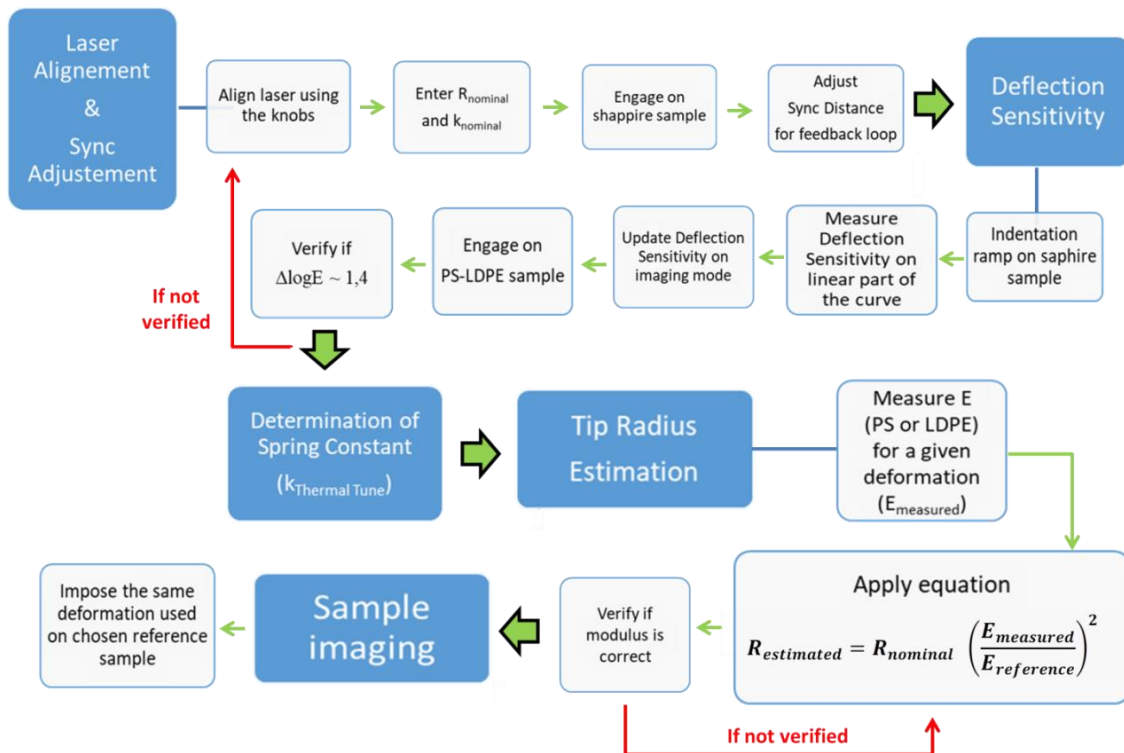


Figure 3.10. Algorithm of the calibration procedure

## 2.2. Raman Spectrometer

Confocal Raman spectroscopy was performed in backscattering mode using a LabRam HR (Laser He Ne-632,8nm-17mW), with a 100x long working distance objective and an X, Y micro-motorized stage. Data were treated using LabSpec Software version 6.3.40. The typical analyzed range was from 400 to 3400 $\text{cm}^{-1}$  with a grating of 600 gr/mm, a hole of 200  $\mu\text{m}$  and a slit of 100  $\mu\text{m}$ , to guarantee confocal configuration and spectral resolution. The typical acquisition time was 10 seconds per accumulation with 2 to 4 accumulations per spectrum. To avoid photothermal polymer degradation by the laser beam, a neutral density filter of 25 or 50% was used.

### 2.2.1. Raman Calibration Method

Raman calibration for chemical analysis was done following the procedure proposed by Horiba-Jobin Yvon. The spectrometer must be calibrated considering three parameters: Zero Order, Sinus Arm and Laser Confocality.

Zero order is the term used to define when the grating within the spectrometer behaves like a mirror, reflecting incoming light rather than refracting it into several wavelengths. It must be calibrated for each grating used (600 or 1800 gr/mm, in our case). After selecting a grating, the spectrograph is moved to the zero order position. Using the 100x objective, a real time display of 1 s and a ND Filter of 1% the acquisition is started. An intense peak near 0 nm is seen. The Offset Shift parameter was corrected to shift the peak back at 0 nm (from yellow to blue line), as illustrated on Figure 3.11.

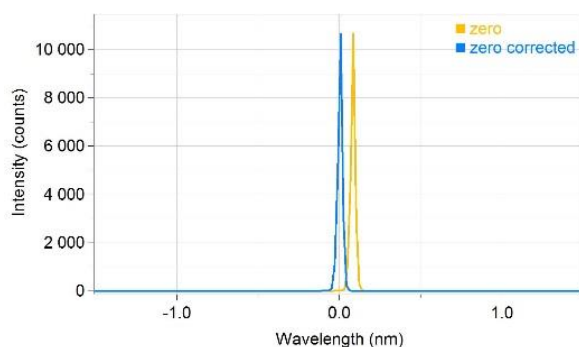


**Figure 3.11.** Offset shift correction of the Zero Order

After the start point for the grating has been set, the movement of the grating relative to the wavelength of the diffracted light must be calibrated. This movement is induced by a so called *sinus arm*, driven by stepping motor. Any deformation of the sinus arm during the movement of the grating will induce shifts in the wavelengths of Raman light on the CCD detector.

Focusing on a Silicon sample with the 100x objective, the acquisition window was centered to the position of the Si band (520  $\text{cm}^{-1}$ ). Using a real time display of 1 s, the Coeff parameter was adjusted in order to center the strong Si band to its reference position (520,7  $\text{cm}^{-1}$  from the red to the green line) as shown on Figure 3.12 (a). Changing the Coeff parameter will adjust the grating position taking into account the deformation of the sinus arm.

The Laser Confocality is then evaluated, i.e., the laser power provided in confocal configuration is compared to the total power emitted. The Silicon standard sample was focused with the 100x objective and a spectrum relative to the Si peak at 520  $\text{cm}^{-1}$  was acquired with an acquisition time of 1 second, ND filter of 100% and confocal configuration, i.e., with a slit of 100  $\mu\text{m}$  and a hole of 200  $\mu\text{m}$ . The hole was then changed to 1000  $\mu\text{m}$  and a new spectrum was acquired. The intensity

ratio between the confocal configuration (200  $\mu\text{m}$  hole) and the reference spectrum (1000  $\mu\text{m}$  hole) must be superior to 50% (meaning that still half of the light comes through the pinhole). An example is given on Figure 3.12 (b), where the intensity on confocal configuration (blue line) corresponds to 51.8% of the reference intensity (green line). If the ratio is lower than 50%, then the laser's confocality is not good and the internal confocal optical parts of the system must be realigned.

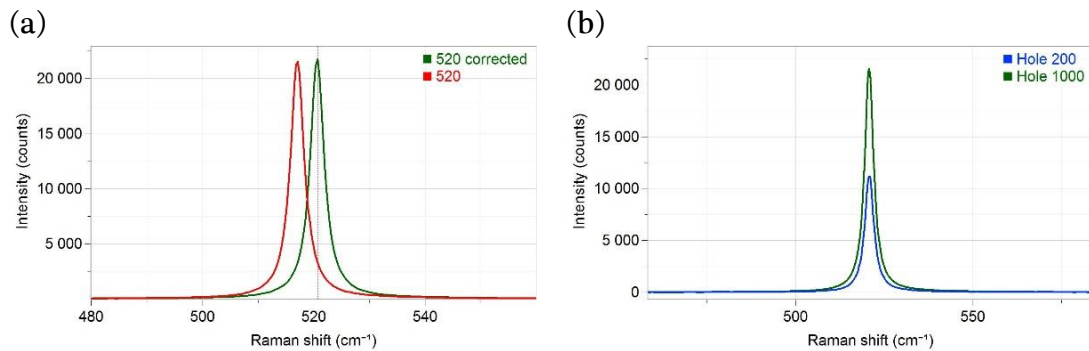


**Figure 3.12.** (a) Calibration of the sinus bar position by the correction of the Si peak at 520  $\text{cm}^{-1}$  (b) Evaluation of the confocality by the ratio of intensities measured with a hole of 200 and 1000  $\mu\text{m}$ , here a ratio of 51.8% was found.

### 3. Co-localization Methods

Two strategies have been developed in order to obtain good AFM/Raman co-localization data, depending on the intensity of the Raman response of the investigated material. The Raman spectrometer is equipped with two confocal microscopes. The one facing the AFM is dedicated to co-localized AFM-Raman experiments and will be called the co-localized Raman microscope. The second one, which is positioned with direct access in front of the user (standard position for LabRam HR), will be called the regular Raman microscope (Figure 3.13).



**Figure 3.13.** Co-localized AFM/Raman setup. The red arrows show the Co-localized Raman Microscope installed in front of the AFM and the Regular Raman Microscope positioned with direct access in front of the user

#### 3.1. Co-localization with the Co-localized Raman Microscope

For samples with intense Raman response, the co-localization is done using the co-localized Raman microscope. During the co-localization process, the AFM motorized stage is simply used to move the sample from the AFM to the co-localized Raman microscope, and reciprocally, as illustrated on Figure 3.14. First the sample is visualized optically with the co-localized Raman microscope, which has a much better resolution than the AFM optical microscope, to select the area of interest, then, the sample is moved with the motorized stage from the Raman objective to the



AFM tip for AFM imaging. Finally the sample is moved back to the co-localized Raman microscope for Raman mapping. The Raman analysis is done after the AFM analysis because the Raman laser heating is potentially destructive for the sample, in particular for organic materials.

This approach is suitable for fast mappings, with acquisition times below 30 minutes. Indeed, during this time scale, the thermal drift of the co-localized setup (sample on the AFM stage drifting below the co-localized Raman microscope) is negligible and does not affect the measurements. Long time scale thermal drift occurs mainly due to the dilatation/contraction of the table-top (lateral thermal drift) and of the Raman feet (vertical thermal drift), due to the day/night temperature variations of the room (despite air-conditioning), because the sample when observed by the Raman is on the AFM stage and not attached to the Raman. For short acquisition times, the co-localization error induced by the displacement from the AFM to Raman or Raman to AFM is only of about  $3\ \mu\text{m}$  and in most of the cases this error of registration can be corrected by scanning, on the AFM, a larger surface than the co-localized final area, and identifying registration points in both AFM and Raman images.

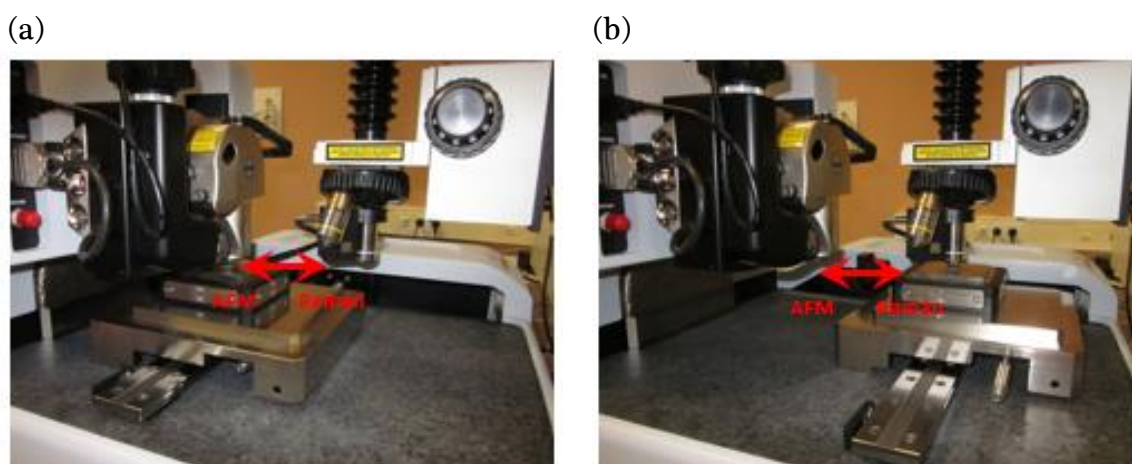


**Figure 3.14.** (a) Stage below AFM head for topographic/nanomechanical analysis and (b) below the co-localized Raman microscope for chemical analysis

### 3.2. Co-localization with the Regular Raman Microscope - Shuttle Stage

In general, polymers respond weakly to Raman and due to their thermal sensitivity, low laser power must be used, which increases the acquisition time substantially. For example, the acquisition time of a Raman mapping with dimensions of  $10 \times 10\ \mu\text{m}^2$  and a step of  $0.5\ \mu\text{m}$  between each point (20 lines of 20 points = 400 points) can be up to 10 hours. In this case, a lateral thermal drift as small as few  $\mu\text{m}$ 's during the analysis is already too large, causing mapping distortion. A vertical thermal drift even smaller can result in a complete loss of focus and therefore of the Raman signal. To address this problem, we have to use the Regular Raman Microscope, which is not affected by thermal drifts since in this case the sample is on the Raman's stage which cannot drift. To co-localize de AFM and Raman images in these conditions, a specific strategy has been developed using a shuttle stage between both instruments. This transfer shuttle allows transferring the sample from the AFM stage to the regular Raman microscope stage, and vice versa, without losing the area of interest. Two docks for the shuttle stage were fixed, one on the AFM stage, the other on the Regular Raman Microscope stage. These docks receive and magnetically maintain the shuttle stage in position. The shuttle stage itself has a magnet to maintain the sample during transfer and imaging but also two targets glued on its surface (Figure 3.15 (a)). These two targets are required for the

triangulation of the area of interest making possible a perfect repositioning (error of about  $3\ \mu\text{m}$  in both x and y directions). This method takes into account any angle shift existing when docking the shuttle stage for analysis, as illustrated on Figure 3.15 (b).

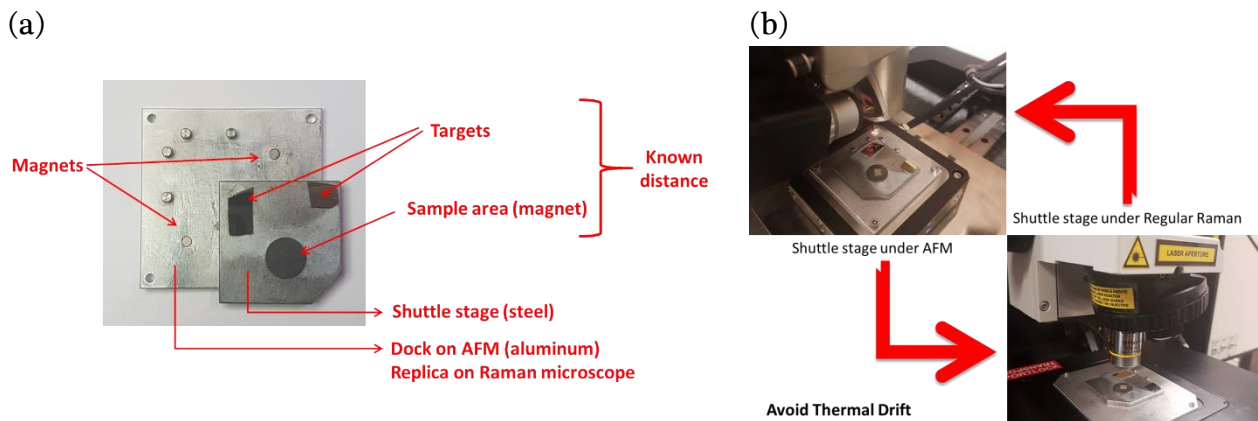


**Figure 3.15.** ((a) Shuttle stage design showing the dock to be installed on both AFM and Raman and the shuttle stage itself with both targets and the sample area. (b) Illustration of the shuttle stage strategy.

This shuttle stage strategy has the advantage that both instruments can be used simultaneously even when doing co-localized analyses, since the sample is not on the AFM stage during the Raman mapping (or the reverse). However it is naturally a time consuming process compared to the co-localization using the co-localized Raman microscope (targets localization, calculations using an excel spreadsheet to find the final x and y coordinates of the area of interest). In addition with the shuttle stage strategy, both the AFM and Raman motorized stages need to be calibrated exactly the same way. As it is impossible a correction factor needs to be applied to the x and y translations to obtain the same displacements for both stages from the targets to the sample. The precision of the correction factor is critical when the displacements are big. Finally, due to the height of the sample in the holder, about 10 mm higher than the level of the targets, there is a risk of collision of the AFM head with the holder during the process.

These issues can be addressed if the sample is installed in a vice holder which has targets printed on its surface. These targets should be near the sample and if possible at the same focal plane. We have therefore milled targets with micrometric dimensions on the surface of the holders with Focused Ion Beam (FIB), as shown on Figure 3.16. Since the distance to be travelled from the targets to the sample is way less important and the sample is practically at the same topographic level as the targets (50 to  $100\ \mu\text{m}$  above, instead of millimeters), the co-localization procedure becomes much faster, more accurate (the precision of the co-localization is improved to less than  $3\ \mu\text{m}$ ) and without any risk of collision between the AFM tip and the sample.

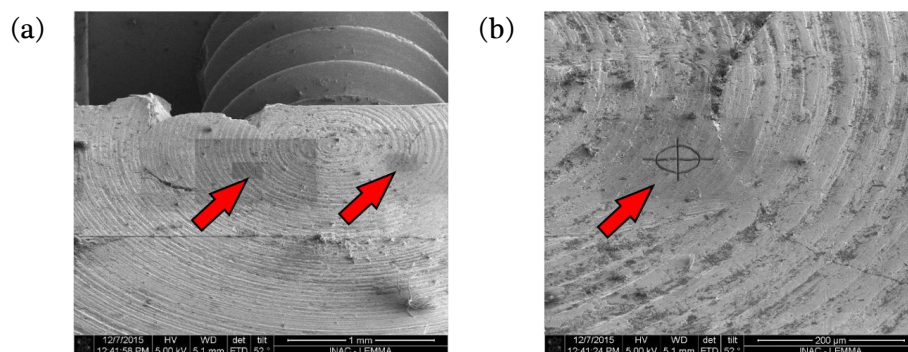


**Figure 3.16.** (a) SEM image of the Micro-Targets milled by FIB on the surface of the sample holder (b) Detail of one micro-target.

## 4. Complementary Analyses

### 4.1. Scanning Electron Microscopy (SEM)

Ultramicrotomed surfaces of hybrid membranes samples were analyzed with a scanning electron microscope Zeiss Ultra 55 (INAC, Grenoble, France) with a FEG source (Schottky type) operated at 0.8 keV (with a resolution of 1.7 nm) in Secondary Electron (SE) mode (with an In-Lens detector for the topographic images) and at 1.5 kV in Backscattered Electron (BSE) mode for complementary chemical contrast images. In the case of the hybrid membranes, it was possible to avoid the use of gold or carbon coating in order to preserve the original topography of the samples using low voltage to prevent charge build-up at the sample's surface.

### 4.2. Transmission and Scanning Transmission Electron Microscopy (TEM/STEM)

Morphologies of the Polyamide 6/Acrylonitrile-butadiene-styrene (PA6/ABS) blends were analyzed by TEM using a Magellan 400L scanning transmission electron microscope (LCE, São Carlos, Brazil) operating in transmission mode. A two-step selective staining technique was used to generate the phase contrast. The sections were first exposed to osmium tetroxide vapor ( $\text{OsO}_4$ ) for 15h and then to ruthenium tetroxide vapor ( $\text{RuO}_4$ ) for 2h to respectively stain the PB and SAN phases.

For the hybrid membranes, the thin sections were analyzed with a scanning transmission electron microscope HITACHI S-5500 (INAC, Grenoble, France) with a cold-FEG source operated at 15 keV in Bright Field mode to provide complementary high-resolution ( $< 1\text{nm}$ ) morphological information. No staining step was necessary due to the strong natural contrast between the sPEEK and the sol-gel phase.

### 4.3. $\mu$ -ATR-FTIR imaging

ATR-FTIR imaging measurements were carried out on a Thermo Scientific Nicolet iN 10MX equipped with a liquid nitrogen cooled focal plane array detector (FPA) and a removable Germanium micro-ATR crystal (Refractive index,  $n=4$ ). The Germanium conical tip and the linear array detector allow mapping over an area of  $100 \times 25 \mu\text{m}^2$ , with the effective pixel size of  $6.25 \times 6.25 \mu\text{m}^2$ . Each measurement consists of at least 240 spectra co-added at  $8 \text{cm}^{-1}$  spectral resolution and has been rationed against a background spectrum which was measured prior to each new sample measurement.

Imaging with the Ge crystal for  $\mu$ -ATR-FTIR implies that the micro crystal must be brought into intimate contact with the surface, applying a sufficient contact force. The Ge crystal has a diameter of  $350 \mu\text{m}$  which is about 10 times larger than the thickness of our polymer membranes ( $\sim 30 \mu\text{m}$  thick). This means that for a membrane cross-section analysis, a membrane standing out of the vice holder is exposed to a high stress during analysis which generally results into membrane's bending or breaking making cross-section analysis impossible. Therefore, the membrane needs a mechanical reinforcement to withstand the pressure of the ATR crystal. Rather than using epoxy embedding (to avoid chemical contamination and/or diffusion of the embedding resin into the polymer), we have used a polymeric backing made of an inert polymer (PP). The membrane was sandwiched between two reinforcement sheets and aluminum foil (for handling), as shown on Figure 3.17, then installed on the vice holders for cryo-ultramicrotomy. The schematic representation of the  $\mu$ -ATR-FTIR imaging is presented on Figure 3.18.

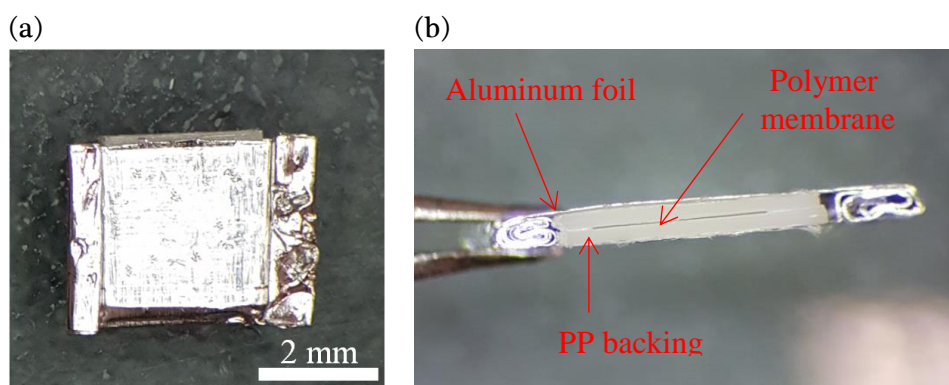


**Figure 3.17.** (a) Polymeric membrane sample sandwiched between aluminum foil and PP sheets on side view  
(b) Top view of the sandwiched sample

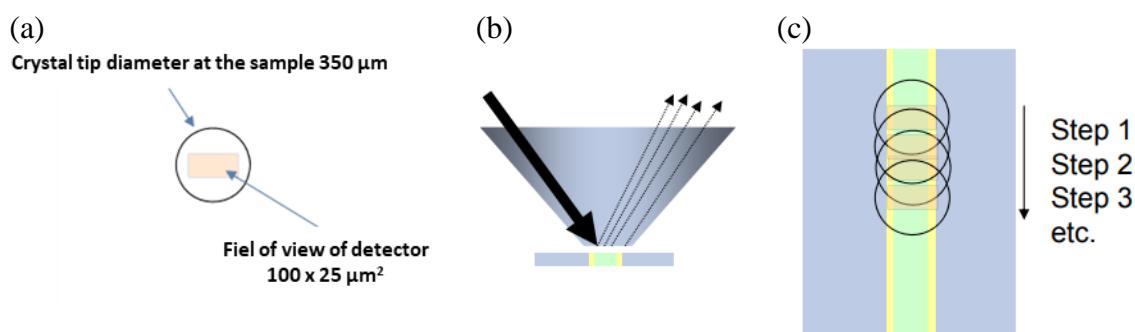


**Figure 3.18.** Schematic representation of  $\mu$ -ATR-FTIR imaging. (a) Field of view of the detector and contact area of the crystal. (b) Germanium conical tip on sample. (c) Mapping of a large area of the sample with multiple steps

## 5. Conclusions of Chapter 3

We have developed different characterization strategies making possible the co-localization of information from AFM and Raman microscopes. For that, Cryo-Ultramicrotomy was adapted to give access to the cross-section (surface + bulk) of the material without the use of embedding, avoiding chemical contamination. A strategy using dry nitrogen was also developed to avoid frost deposition after cryo-ultramicrotomy, to protect water sensitive samples. The cryo-ultramicrotomed samples have a perfectly flat surface suitable for co-localized AFM/Raman analysis, SEM and  $\mu$ -ATR-FTIR, and the cutting also provides ultrathin sections for complementary Transmission Electron Microscopy analyses.

Different co-localization strategies were developed depending on the Raman intensity response of the samples. For samples that respond intensely to Raman, the AFM motorized stage is simply used to move the sample from the AFM to the co-localized Raman microscope, and reciprocally. This approach is suitable for fast mappings, with acquisition times below 30 minutes. For polymer samples that respond weakly to Raman, a strategy using a shuttle stage between both instruments was developed, allowing transferring the sample from the AFM stage to the regular Raman microscope stage, and vice versa, without losing the area of interest and allowing long time acquisition mappings, up to more than 10 hours. Furthermore, it has the advantage that both instruments can be used simultaneously even when doing co-localized analyses. The co-localization precision was improved to less than 3  $\mu\text{m}$  thanks to the association of the shuttle stage strategy with milled targets on the surface of the vice holders, limiting the repositioning displacement (in X, Y and also Z direction).

The calibration methodology for AFM nanomechanical analysis was developed based on the mathematical deduction of the main parameters controlling the measurement of the Young's modulus of the material, using a theoretical nanomechanical model (Hertzian). The presented procedure can be adapted for different cantilever types and using different reference samples, considering the Young's modulus range of the samples of interest.

The developed methodologies for AFM/Raman co-localized analyses were published in the International Journal of Polymer Analysis and Characterization. The paper entitled "AFM-Raman Co-localization Setup: Advanced Characterization Technique for Polymers" exemplifies the co-localization strategy by the study of hybrid membranes for fuel cell application.<sup>159</sup>

## 6. Conclusions du Chapitre 3 en Français

Nous avons développé différentes stratégies de caractérisation permettant la co-localisation de l'information des microscopes AFM et Raman. Pour cela, la Cryo-Ultramicrotomie a été adaptée pour donner accès à la section transversale (surface + intérieur) du matériau sans enrobage (pas de contamination chimique, impact thermique ou mécanique). Une stratégie utilisant de l'azote sec a également été développée pour éviter l'effet de dépôt de givre sur des échantillons sensibles à l'eau. Les échantillons cryo-ultramicrotomés ont une surface parfaitement plane adaptée à l'analyse AFM/Raman co-localisée, SEM et  $\mu$ -ATR-FTIR, et la procédure de coupe fournit également des sections ultra-fines pour des analyses complémentaires de microscopie électronique de transmission. La précision de co-localisation a été améliorée grâce à la stratégie de la plate-forme navette à l'aide de cibles à la surface des porteurs, ce qui limite le déplacement pour le repositionnement (en X, Y et Z).

Différentes stratégies de co-localisation ont été développées en fonction de l'intensité de la réponse Raman des échantillons. Pour les échantillons qui répondent intensément au Raman, la platine motorisée de l'AFM est simplement utilisée pour déplacer l'échantillon de l'AFM vers le microscope Raman co-localisé et réciproquement. Cette approche convient aux mappings rapides, avec des temps d'acquisition inférieurs à 30 minutes. Pour les échantillons de polymères qui répondent faiblement à Raman, une stratégie utilisant une navette entre les deux instruments a été développée, permettant de transférer l'échantillon de la platine AFM à celle du microscope Raman régulier, et vice versa, sans perdre la zone d'intérêt et permettant l'acquisition des mappings de longue durée, jusqu'à plus de 10 heures. En outre, il est avantageux que les deux instruments puissent être utilisés simultanément même lorsqu'ils effectuent des analyses co-localisées. La précision de la co-localisation a été améliorée à moins de 3  $\mu\text{m}$  grâce à l'association de la stratégie de la navette avec des cibles gravées à la surface des portes-échantillons, limitant le déplacement de repositionnement (en X, Y et Z également).

Les méthodologies développées pour les analyses co-localisées AFM/Raman ont été publiées au journal *International Journal of Polymer Analysis and Characterization*. L'article intitulé «AFM-Raman Co-localization Setup: Advanced Characterization Technique for Polymers», illustre la stratégie de co-localisation par l'étude des membranes hybrides pour piles à combustible.<sup>159</sup>



# **CHAPTER 4**

---

## **Compatibilization of Polymer Blends based on PA6/ABS**



## PROLOGUE

In this chapter, we will present the morphological and chemical analysis of polymer blends based on Polyamide 6 (PA6) and Acrylonitrile-Butadiene-Styrene (ABS) copolymer, compatibilized with a Styrene-Acrylonitrile grafted with Maleic Anhydride (SAN-MA). The blends were prepared on the Department of Materials Engineer at the Federal University of São Carlos (DEMa-UFSCar/São Carlos, Brazil).

We will present here a brief introduction to the materials used (PA6 and ABS) and the fundamentals of blend compatibilization. Then, we will present the study of the blends using the co-localized AFM/Raman setup, first applied on a non compatibilized PA6/ABS blend and second on compatibilized systems with SAN-MA copolymer. The study of the non-compatibilized blend allowed for the optimization of the co-localization procedure and for the proper assignment of the phases using both AFM and Raman techniques. The study of the compatibilized blends was first interested on the effect of the blending protocol on the development of the morphology of the blends. We were able to show by complementary AFM and STEM analyses that the addition of the SAN-MA copolymer in different steps of the blending can develop different final morphologies, which have an impact on their rheological properties. Finally, we were interested on the fundamental aspects of the PA6 polymorphs ( $\alpha$  and  $\gamma$ ) distribution in the materials. Using co-localized AFM/Raman analyses, we have shown that the presence of the compatibilizer favors the formation of the  $\gamma$  polymorphs and its amount and distribution depends on the blending protocols.

### French Prologue

Dans ce chapitre, nous présenterons l'analyse morphologique et chimique des mélanges de polymères à base de Polyamide 6 (PA6) et de copolymère Acrylonitrile-Butadiène-Styrène (ABS), compatibilisé avec un Styrene-Acrylonitrile greffé avec de l'Anhydride Maléique (SAN-MA). Les mélanges ont été préparés au Département d'Ingénierie des Matériaux à l'Université Fédérale de São Carlos (DEMa-UFSCar / São Carlos, Brésil).

Nous présenterons ici une brève introduction aux matériaux utilisés (PA6 et ABS) et les fondements de la compatibilization des mélanges polymères. Ensuite, nous allons présenter l'étude des mélanges à l'aide du système de co-localisation AFM/Raman, d'abord appliquée sur un mélange PA6/ABS non compatibilisé et deuxièmement sur des systèmes compatibilisés avec un copolymère SAN-MA. L'étude du mélange non compatibilisé a permis d'optimiser la procédure de co-localisation et d'affecter correctement les phases en utilisant les techniques AFM et Raman. L'étude des mélanges compatibilisés s'intéresse d'abord à l'effet du protocole de mélange sur le développement de la morphologie des mélanges. Nous avons pu montrer par des analyses complémentaires AFM et STEM que l'addition du copolymère SAN-MA à différentes étapes du mélange peut développer différentes morphologies finales, qui ont un impact sur leurs propriétés rhéologiques. Enfin, nous nous intéressons aux aspects fondamentaux de la distribution des polymorphes PA6 ( $\alpha$  et  $\gamma$ ) dans ces matériaux. À l'aide d'analyses AFM/Raman co-localisées, nous avons montré que la présence du compatibilisant favorise la formation des polymorphes  $\gamma$  et que sa quantité et sa distribution dépendent des protocoles de mélange.

## 1. Theoretical Background and Motivation

### 1.1. Polyamide 6 (PA6)

Polyamides (or Nylons) are characterized by the presence of an amide (-COONH-) in the backbone chain.<sup>160</sup> The polyamide produced from  $\epsilon$ -caprolactam is called Polyamide 6, once it has six carbon atoms derived from the lactam, as shown on Figure 4.1.

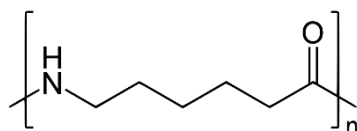


Figure 4.1. Polyamide 6 structure

The olefin sequences on the PA6 structure are non-polar and flexible at room temperature. The amide groups, however, are very polar, being capable of attracting the neighboring chains to form hydrogen bonds between them.<sup>161</sup> The symmetry and regularity of the backbone chain allied to the hydrogen bonds make the PA6 a semi-crystalline thermoplastic with high crystallinity, which control its physical and mechanical properties.

In general, the polyamides were considered as the first engineering polymers, since they have very attractive features for engineering applications.<sup>161</sup> Indeed, polyamide 6 has high toughness above its glass transition temperature ( $T_g \sim 50^\circ\text{C}$ ), high rigidity, good chemical resistance to hydrocarbons and good resistance to abrasion due to inherent low-friction properties. Its crystalline melting temperature is  $\sim 220^\circ\text{C}$ , beyond which it presents a very low melt viscosity, which allows the injection molding of parts with complex forms such as micro-gears. Its high rigidity, chemical and heat resistance make the PA6 a good substitute for low strength metals like for example in components in the engine compartment of vehicles. Additionally its high polarity favors the interaction of the polymer chains with the polar surface of organophilic clays, making possible the production of nanocomposites based on polymer/clay systems.<sup>38,51,162</sup>

Due to their polar nature, polyamides tend to absorb moisture from their surroundings, until certain equilibrium is reached, which can have a negative effect on dimensional stability. The increasing moisture content can impact the materials properties, increasing the impact resistance and flexibility, however, it decreases the polyamide strength and stiffness below the glass transition temperature ( $< 50\text{--}80^\circ\text{C}$ ). The extent of moisture content is dependent on temperature, crystallinity and thickness of the product, being critical when it occurs on the pellets before processing. To prevent negative effects of moisture absorption during service a preconditioning drying step is often adopted before extrusion/injection of the molded part. But the most important downside of the material is related to its notch-sensitive behavior below its glass transition temperature compared to other polymers. Figure 4.2 shows the impact strength of notched samples of commonly used plastics such as Acrylonitrile-Butadiene-Styrene (ABS), Polystyrene (PS) and Polycarbonate (PC). The Polyamide 6 (Nylon 6 in the figure) appears with an impact strength 8 times lower than Polycarbonate (PC).<sup>163</sup>

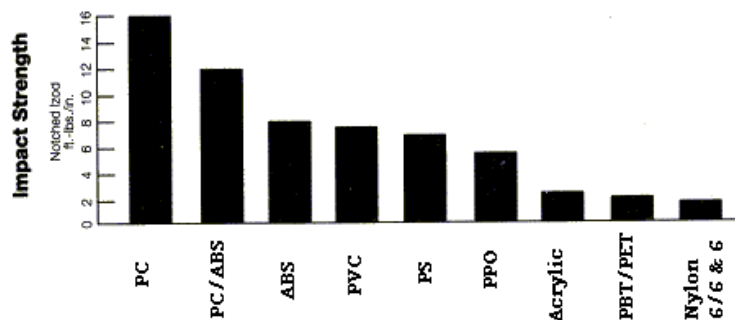


Figure 4.2. Impact strength (notched izod) of different polymeric materials<sup>163</sup>

This brittle behavior shows that the material is very sensitive to crack propagation. Therefore its impact resistance is poor and it tends to fail in a brittle manner at low temperatures.<sup>164</sup> One strategy to mitigate this mechanical behavior is to introduce rubber particles to improve the mechanism of energy absorption and crack propagation. The addition of low modulus materials decreases notch-sensitivity, increasing toughness at low temperatures. Examples from the literature used a series of different polymers, such as natural rubber, ethylene propylene diene rubber (EPDM), polybutadiene (PB) and copolymers, like Styrene–Ethylene/Butylene–Styrene block copolymer (SEBS) and Acrylonitrile–Butadiene–Styrene (ABS).<sup>165–167</sup> In this work, we will focus on the blending of PA6 with ABS.

## 1.2. Acrylonitrile-Butadiene-Styrene (ABS)

ABS were originally made by blending a lightly crosslinked natural rubber (NBR) into a Styrene-Acrylonitrile (SAN) copolymer. Nowadays such materials are commonly made by polymerizing styrene and acrylonitrile around polybutadiene in a polybutadiene latex, forming polybutadiene molecules grafted with SAN (PB-g-SAN). The resultant material is then blended with styrene-acrylonitrile (SAN). The chemical structures of the components and an example of the microstructure are presented on Figure 4.3. As illustrated on the TEM image of Figure 4.3 (b), the morphology is complex. The PB rubber particles (dark on the image) appear uniformly dispersed in the fragile matrix of SAN (white), which is also present in sub-inclusions inside the PB particles. PB-g-SAN lies on the interphase between the SAN matrix and the dispersed PB, being responsible for anchoring both phases and thus allowing PB to increase the final tenacity of the material.<sup>168</sup>

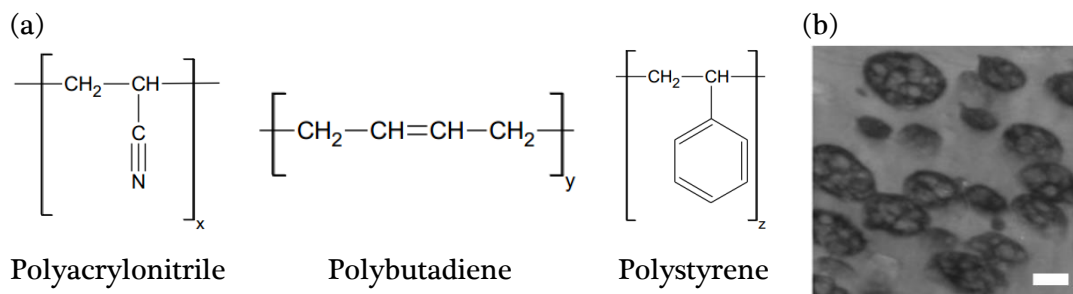


Figure 4.3. (a) Structures of the ABS components: Polyacrylonitrile, polybutadiene and polystyrene. (b) TEM image showing the morphology of a ABS (SAN65.9/PB-g-SAN34.1 w/w with 44%wt PB content in PB-g-SAN). The rubber particles (PB) appear in dark and the SAN matrix in white, which is also present in sub-inclusions inside the rubber particles. The scale bar represents 200 nm. Adapted from<sup>169</sup>

The SAN phase usually comprises more than 70% of the ABS total composition. On the one hand, the amount and molecular weight of the SAN are the principle variables controlling the properties of the matrix. If increased, the strength and rigidity of the ABS increases. On the other hand, the increasing amount of rubber controls the impact resistance of the material. However, as the rubber content increases, the strength, hardness, heat resistance and rigidity of the ABS decrease. Finally, the properties of the material are highly affected by the size and distribution of the dispersed phase, the cross-linking density of PB, copolymer composition and amount of PB-g-SAN. In general, ABS is a hard tough material with good resistance to impact even at low temperatures.

By blending ABS with other polymers it is possible to extend the range of use and a variety of properties, such as heat distortion temperature, impact strength, flame retardancy, processing conditions and weatherability.<sup>168</sup>

### 1.3. Mixing and compatibilization of polymer blends

Blends can be obtained by mechanical mixing in the molten state. In this technique, two or more resins are blended in mixing equipment, typically double screw extruders or internal mixers. Additionally it is possible to incorporate fillers, reinforcements and additives. The blending process involves high temperatures (above the softening/melting temperature of the components) and high shear, promoting the homogenization and dispersion of the constituents of the polymer blend. Under the action of the shearing force, the dispersed elements are elongated and broken down, as illustrated on Figure 4.4. Size reduction of the dispersed domains continues till the total force of the particle equals the surface tension which is responsible for particle coalescence. The competitive process between breaking down (size reduction) and particle coalescence (surface tension minimization) is always present in unstable polymeric heterophase systems. For low content of dispersed phase, the equilibrium radius of the particles depends on its surface tension, the shearing forces applied and the viscosity difference between the continuous and the dispersed phases. When the viscosities of the two components are similar, the mechanical shear can be effectively transferred to the mixture to enforce a good dispersion of the phases. Blends with a greater disparity in the components melt viscosity show larger domains, but it decreases with the increasing shearing forces and low surface tensions.<sup>170,171</sup> In conclusion, the lower the melt viscosity difference between the two constituents of the mixture, the better the dispersion.

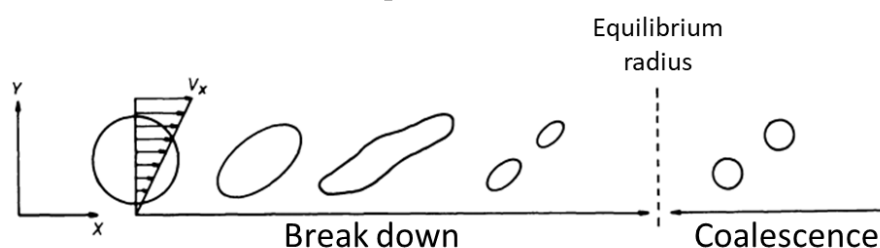


**Figure 4.4.** Schematic representations of particle break down under a shearing stress field and coalescence.

Adapted from <sup>170</sup>

In order to reduce the competitive process of particle coalescence in unstable heterophase systems, proper formulations can be developed to control the morphology and characteristics of polymer blend. To reduce the surface tension and improve miscibility, compatibilization can be achieved by chemical or physical means. Physical compatibilization lies on the use of copolymers bearing different blocks, each one compatible with one of the components of the blend. The physical entanglements of the chains of each polymer with the correspondent block of the compatibilizer engender a reduction of the interfacial tension between the phases and inhibit the coalescence

process during mixing (Figure 4.5).<sup>4</sup> The second approach of chemical compatibilization takes advantage of specific chemical functions presented on the structure of polymers to create a covalent bond between them (cross-linking).

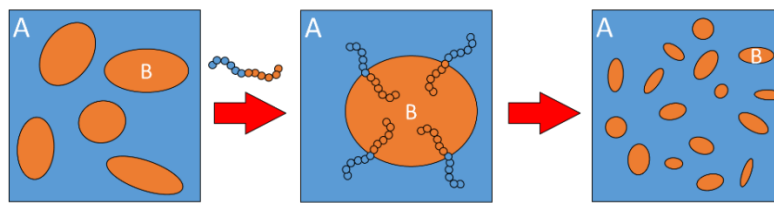


**Figure 4.5.** Scheme of the effect of physical compatibilizers on the morphology of initially immiscible blends showing fine and smaller particles dispersed in the matrix

In the case of the PA6/ABS blend, the compatibilizer is generally a polymer and/or a block copolymer capable of reacting with the amine end group of PA6 and simultaneously miscible with the SAN blocks of the ABS. According to several studies<sup>172-176</sup> copolymers containing maleic anhydride (MA) groups can be used in the compatibilization of PA6/ABS blend due to the reactivity of MA with the polyamide matrix. In these studies, Styrene-Acrylonitrile functionalized with Maleic Anhydride (SAN-MA) and Methyl Methacrylate-Maleic Anhydride (MMA-MA) appear as strong candidates for the compatibilization of the blend, since both SAN and MMA blocks are miscible in ABS. In the present study, we will be interested on the compatibilization of PA6/ABS blends with SAN-MA.

Examples from the literature on this blend suggest a chemical reaction between the amine end groups of the polyamide and the anhydride end group of the compatibilizer during processing, forming SAN-MA-g-PA6 copolymer which acts itself as a compatibilizer (Figure 4.6). To be efficient, this SAN-MA-g-PA6 copolymer must be located at the interface of the ABS and PA domains.<sup>177-180</sup> This creates a better dispersion of the ABS phase into the PA matrix (smooth interphase), improving the stability of the morphology and blend's mechanical properties.<sup>3,177,178,181,182</sup>

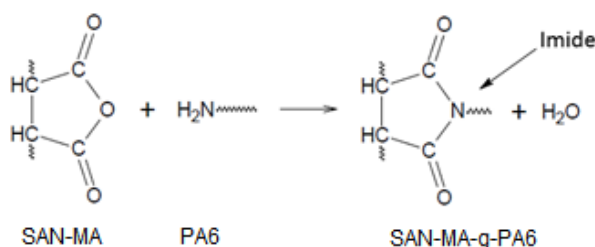


**Figure 4.6.** Scheme of the imidization reaction between Maleic Anhydride and PA6.

#### 1.4. Objectives of work

The improvements in toughness of rigid polymers by melt blending and compatibilization have already been extensively studied. However, the complexity of the variables influencing the mechanisms of toughening is still of commercial and academic interest, since the many variables influencing the toughening lead to a diversity of involved mechanisms at micro and nanoscale.<sup>183-185</sup> Complementary local characterization techniques like AFM/TEM and Raman can give additional information about the process-structure-properties interplays at multiple scales.

This chapter will address the morphological and chemical study of PA6/ABS blends compatibilized with SAN-MA with the co-localized AFM/Raman setup, in order to give new fundamental insights of the effect of the blending protocol on the morphology of the blends, as well as the distribution of the compatibilizer and its impact on the PA6 crystalline structure.

## 2. Study of compatibilization of PA6/ABS blends with SAN-MA

The study of the compatibilization of PA6/ABS blends is an ongoing publication entitled “New insights on the compatibilization of PA6/ABS blends: A co-localized AFM-Raman study” submitted to the journal “Polymer” on November 2017 and will be presented in an adapted format.

In this work, we will first be interested on using the co-localized AFM-Raman analyses to characterize a reference PA6/ABS blend, in order to properly assign the chemical and nanomechanical signatures of each component of the blend. The study of the compatibilized blends will focus in two aspects. First, the effect of the blending protocols on the morphology of the compatibilized blends will be studied by complementary AFM and TEM analyses, to be correlated with their rheological properties. Finally, we will be interested on the fundamental aspects of the effects of the compatibilizer and the blending protocol on the amount and distribution of the PA6 polymorphic phases, as revealed by co-localized AFM-Raman analysis.

### 2.1. Materials used

PA6 commercially known as B300 and supplied by Polyform (density 1.13 g/cm<sup>3</sup>, MFI 2.9 g.10 min<sup>-1</sup> at 230°C and 2.16 kg) was used as the matrix phase. ABS commercialized as Cyclocac Resin EX58 (52.8 wt % butadiene, 12.4 wt % acrylonitrile, and 34.6 wt % styrene) was kindly provided by SABIC and used as the dispersed phase. The SAN-MA with a composition of 65.7 wt% styrene 33 wt% acrylonitrile and 1.3 wt% maleic anhydride was provided by D.R. Paul from the University of Texas at Austin. The repeat unit of each polymer is reported on Figure 4.7.

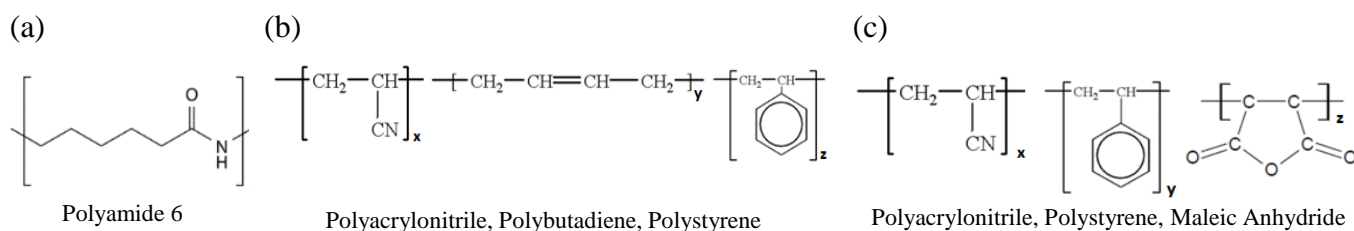


**Figure 4.7.** Chemical structures of (a) PA6 and (b) components of ABS copolymer and (c) components of SAN-MA copolymer

### 2.2. Blending protocols

The polymeric blends were prepared at the Federal University of São Carlos (UFSCar, Brazil). Details of the blending procedure are presented on Annex 1.1. Four blends were prepared:

1. PA6+ABS (reference material): the two polymers were blended in a single extrusion step.
2. (PA6/ABS/SAN-MA): the three polymers were blended in a single extrusion step.
3. (ABS/SAN-MA)+PA6: ABS and SAN-MA were preblended in a first extrusion step. Subsequently the obtained product was blended with PA6 in a second extrusion step.
4. (PA6/SAN-MA)+ABS: PA6 and SAN-MA were preblended in a first extrusion step. Subsequently the obtained product was blended with ABS in a second extrusion step.

The composition of the binary reference blend and the compatibilized blends were fixed respectively at 60/40 wt % (PA6/ABS) and 57.5/37.5/5 wt % (PA6/ABS/SAN-MA). The materials obtained by extrusion were quenched in water, granulated, dried and injection molded at 245 °C, into standard specimens for mechanical and thermomechanical analysis. For each formulation,

sections about 1 mm thick were cut (scroll-saw) from the center part of standard injection molded specimens then cryo-ultramicrotomed as described on Chapter 3.

### 2.3. Phase identification of the reference sample by Raman and AFM analyses

A co-localized AFM-Raman spectroscopy analysis of the reference PA6+ABS sample was done in order to correlate the topography of the phases to their assigned chemical signature and then to their mechanical properties. First, a rapid AFM image of the sample was acquired to identify interesting zones for further co-localization with Raman, since the polymer phases could not be seen by optical microscopy. Figure 4.8 (a) shows the AFM topographic image of a  $20 \times 20 \mu\text{m}^2$  area. Despite the low roughness of the image due to the sample preparation (cryo-ultramicrotomy), two different phases can be seen. One phase appears as large domains (more than  $10 \mu\text{m}$  in length) with high roughness ( $R_a=27.5 \text{ nm}$ ) inside the other phase which shows a lower roughness ( $R_a = 11 \text{ nm}$ ). It is important to outline that the analyzed surface issued from cryo-ultramicrotomy is flat. Therefore any topographical contrast results from the differences of penetration depth of the AFM tip in the sample, thus from the modulus contrast between each component, i.e., the component with lower modulus appears lower on topography due to the deeper tip indentation depth.

The colocalized Raman mapping corresponding to the sample area highlighted by a red square on Figure 4.8 (a) is composed of 441 Raman spectra (area of  $10 \times 10 \mu\text{m}^2$  with  $0.5 \mu\text{m}$  steps). From this mapping file we produced four analysis mappings, Figure 4.8 (b) to (e), based on the integration of the vibration bands of respectively the PA6 matrix (NH vibration band at  $3300 \text{ cm}^{-1}$  (area between  $3250$  and  $3350 \text{ cm}^{-1}$  relative to the baseline)), the Polybutadiene (PB) (integration of the C=C vibration of PB at  $\sim 1660 \text{ cm}^{-1}$  ( $1657\text{-}1680 \text{ cm}^{-1}$ )), the Polyacrylonitrile (PAN) (integration of the CN vibration of PAN at  $\sim 2240 \text{ cm}^{-1}$  ( $2200\text{-}2280 \text{ cm}^{-1}$ )) and the Polystyrene (PS) (integration of the aromatic CH vibration of PS at  $\sim 3055 \text{ cm}^{-1}$  ( $3020\text{-}3120 \text{ cm}^{-1}$ )) of the ABS phase. The complete assignment of the Raman bands of each component is presented in Annex 1.2. On Figure 4.8(b), the bright area on the Raman map (area rich in PA6) corresponds to the AFM image low topography and low roughness matrix. Consequently, the mappings related to the ABS phase observation (Figure 4.8 (c), (d) and (e)) have inverted contrasts (high intensity where Figure 3(b) shows a low one, and a low intensity where Figure 4.8 (b) shows a high one), highlighting the PA6/ABS phase separation. One can see that the PA6 Raman signal never decreases to zero on Figure 4.8(b), even inside the ABS domains. It is important to notice that the AFM analysis is based on a surface analysis (depth of penetration of the AFM tip of few nm to tens of nm as function of the material rigidity), while the Raman spectra has a deeper spatial response (depth probed of about  $1 \mu\text{m}$  due to confocal configuration used) which explains why the PA6 signal is never zero, indicating that the PA6 matrix can be detected below an ABS domain observed at the sample surface by AFM. Furthermore, the limited lateral resolution of the confocal Raman micro spectroscopy of about  $1 \mu\text{m}$  in every direction, explains the much better image resolution obtained by AFM (lateral resolution of few nm).

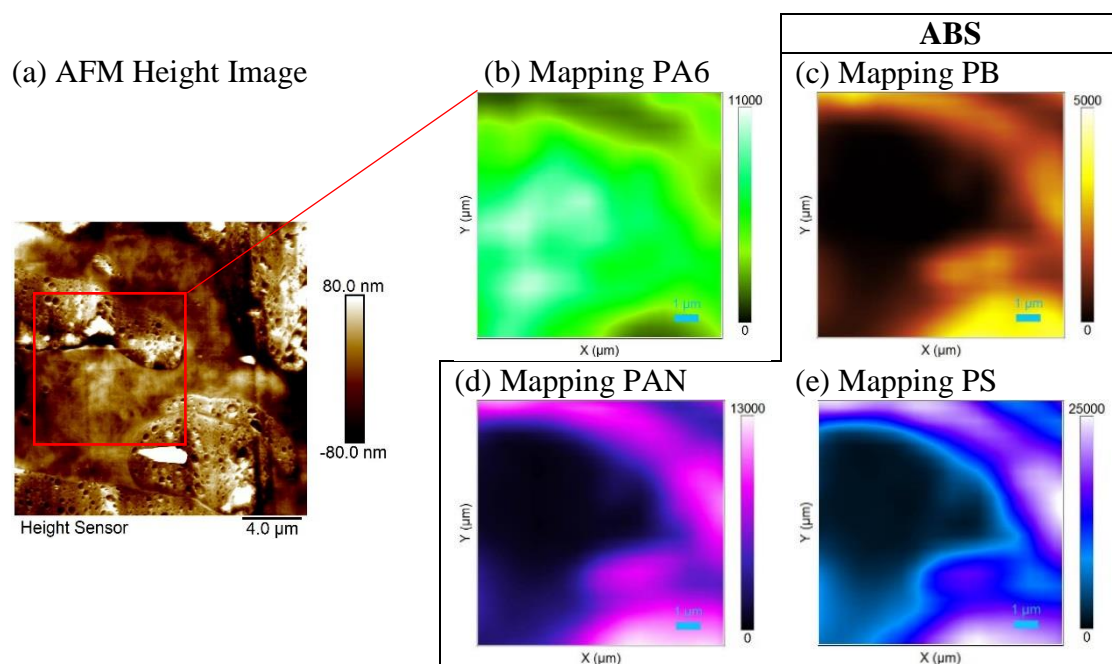


**Figure 4.8.** AFM-Raman co-localized analysis of sample PA6+ABS (a) AFM Image; Colocalized Raman mapping relative to: (b) Polyamide 6 ( $3230\text{-}3350\text{cm}^{-1}$ ) (c) Polybutadiene ( $1657\text{-}1680\text{cm}^{-1}$ ) (d) Acrylonitrile ( $2200\text{-}2280\text{cm}^{-1}$ ) and (e) Polystyrene ( $3020\text{-}3120\text{cm}^{-1}$ )

AFM images of the reference sample PA6+ABS with dimensions of  $5 \times 5 \mu\text{m}^2$  were acquired with PeakForce QNM mode on a reduced surface to look in detail at the morphology of the ABS/PA interface (Figure 4.9). Both topography and modulus images (Figure 4.9 (a) and (b)) show 3 phases: The first one in depression on the topographic image (black domains) due to its low modulus (the tip goes deeper in the material), a second one, stiffer with a high modulus which appears as a dominant phase on the topographic image due to the limited penetration of the tip in the material and a third one with an intermediate modulus/height. Once again, after cryo-ultramicrotomy the surface is flat, therefore any topographical contrast results from the modulus contrast between each component. Correlating the previous Raman chemical maps and the physical properties of each phase one can postulate that the stiffer phase corresponds to the PS and PAN blocks of the ABS domains (in agreement with the calibration performed on the PS standard, and expected due to the low amount of acrylonitrile: 12% of this phase) and the soft domains correspond to the PB of ABS, which are surrounded by a continuous PA6 phase. As expected, deformation and adhesion images (Figure 4.9 (c) and (d)) clearly highlight the high deformation and adhesion observed for the small spherical domains detected inside the stiffer phase.

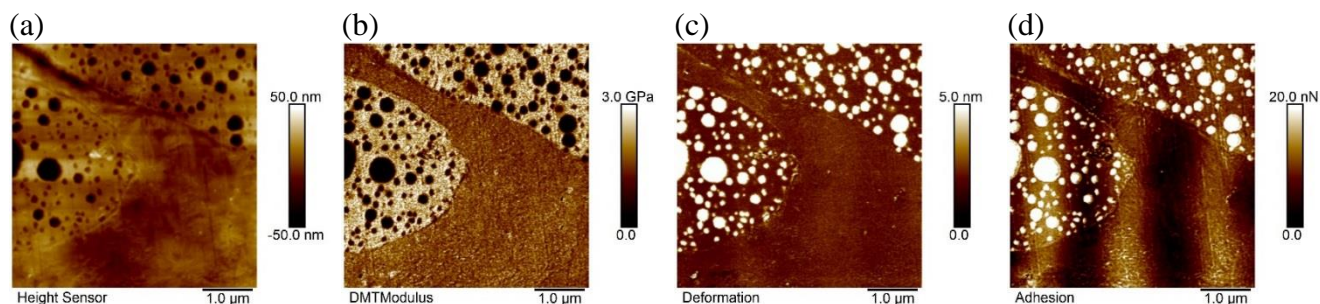


**Figure 4.9.** Complementary AFM  $5 \times 5 \mu\text{m}^2$  images of a PA6+ABS blend: (a) Topography (b) Modulus (c) Deformation (d) Adhesion



The calibration of the AFM tip allows for measuring the Young's Modulus of each phase, which gives about 1.68 GPa for the PA6 matrix, and about 2.60 GPa for the stiffer PS-PAN phase which include soft PB domains with a Young's modulus of 0.45 GPa. The thermal properties of each component, their modulus measurements and values from the literature are reported on Table 4.1. We remark that the measurements done with the PeakForce QNM mode are coherent with the general trend of the typical bulk modulus of the polymers for the PA6 and PS-PAN domains. However, one can observe that the PB phase with a measured Young's modulus of 0.45GPa is somewhat stiffer than what expected from the literature (0.01 GPa). This discrepancy can originate from the contribution of the stiffer PS-PAN, since the PB phase is confined into a PS-PAN phase. In addition, the relative calibration takes into account an estimation of the tip radius used to probe the PS in the standard PS/LDPE sample. Since the deformation applied to the PB domains is higher than the one used for calibration (>10 nm rather than 2 nm), the effective tip radius in contact with this phase is underestimated and therefore the measured modulus is overestimated. Nevertheless, the complementary and co-localized AFM-Raman analyses allowed for the complete assignment of the phases by their chemical signatures and nano-mechanical properties.

**Table 4.1.** Mechanical and thermal properties of each component of the blend<sup>186,187</sup>

Sample	$E_{\text{measured}}$ (GPa)	$E_{\text{literature}}$ (GPa)	Tg (°C)	Tm (°C)
Polybutadiene	0.45	0.002 – 0.01	-28	126-156
Polyamide 6	1.68	1.1 – 3.2	70	215-225
Polystyrene	-	2.7 – 3.4	100	-
Polyacrylonitrile	-	3.1 – 3.8	97	320
Poly(Styrene-Acrylonitrile)	2,60	2.8 – 4.0	100	-

## 2.4. Effect of blending protocol on morphology

We will now be interested on the effect of the compatibilizer on the general morphology of the blend and further on the effect of the blending protocol on the final morphology.

As previously observed, a PA6+ABS blend appears very heterogeneous with a well defined interface between each phase due to the low compatibility of ABS with PA6. Figure 4.10 shows 15x15  $\mu\text{m}^2$  AFM modulus images of the reference sample PA6+ABS (Figure 4.10 (a)) and a compatibilized blend (PA6/ABS/SAN-MA) (Figure 4.10(b)).

The non-compatibilized blend PA6+ABS (Figure 4.10(a)) presents ABS domains (high modulus-yellow) with more than 10  $\mu\text{m}$  in length surrounding PB spheres with an average diameter of  $265 \pm 148$  nm. The compatibilized blend presented in Figure 4.10(b), however, appears with dispersed ABS domains with average lateral dimensions of  $1.1 \pm 0.4$   $\mu\text{m}$  surrounding PB spheres with a slightly lower average diameter of  $233 \pm 130$  nm. Furthermore, the number of PB spheres per ABS domain decreases significantly with the addition of a compatibilizer in the blend. These reductions are attributed to the ability of SAN-MA to promote steric stabilization of ABS, suppressing the coalescence phenomena.<sup>188,189</sup>

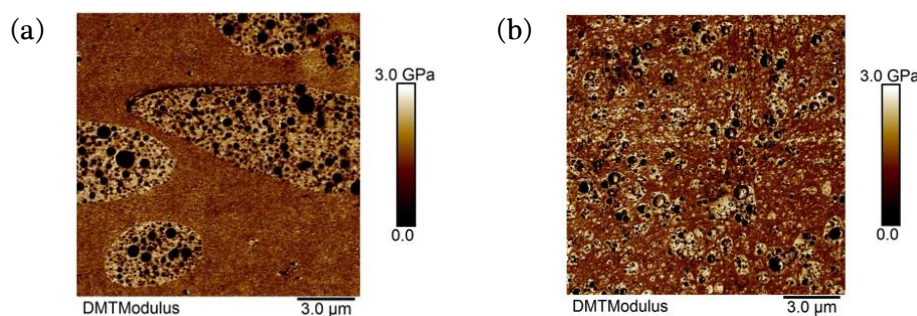


**Figure 4.10.** AFM  $15 \times 15 \mu\text{m}^2$  Modulus images of (a) reference sample PA6+ABS and (b) compatibilized sample (PA6/ABS/SAN-MA)

One can now look at the impact of the processing conditions on the final morphology of the blends. The effect of the different blending protocols is shown in details on AFM and TEM images of Figure 4.11. Figure 4.11(a) and (b) show, respectively,  $10 \times 10 \mu\text{m}^2$  AFM modulus images and TEM images of samples 1-(PA6/ABS/SAN-MA), 2-(ABS/SAN-MA)+PA6 and 3-(PA6/SAN-MA)+ABS.

Regardless the blending protocol employed it is easily observed that, compared to PA6+ABS, the simple incorporation of SAN-MA leads to a significant reduction in the ABS domain size for all the ternary blends. Notwithstanding, the impact of the blending protocol should be studied in detail, since different morphology and very slight changes in the average size and distribution of the domains can result in different mechanical properties or in the brittle-tough transition of the blend.<sup>190</sup> One can see on Figure 4.11 (a) that the stiffer phase of the ABS, brighter on the image, related to PS-PAN blocks, is always present surrounding the PB phase (dark), as indicated by the red arrows. It should be noticed that some of the PB spheres appear brighter than expected on the images. Indeed, the high indentation depth imposed on the PB phase can be sufficient to probe the stiffer phase under it, especially if the PB phase is thin. Sample (PA6/ABS/SAN-MA) on Figure 4.11(a)-1 shows well-distributed and dispersed domains of ABS phase with a mean size of  $1.1 \pm 0.4 \mu\text{m}$  in length and PB particles with average diameter of  $230 \pm 130 \text{ nm}$ . The respective TEM image on Figure 4.11 (b)-1 makes clear that the sample exhibits a particle-in-matrix morphology, i.e., spherical domains of ABS dispersed in PA6. Sample (ABS/SAN-MA)+PA6 (Figure 4.11(a)-2 and (b)-2) presents ABS clusters that can have more than  $2 \mu\text{m}$  in length (mean diameter of  $1.5 \pm 0.8 \mu\text{m}$ ), with more PB spheres per ABS cluster when compared to the other samples, although the average PB spheres diameter was the same of the previous sample:  $230 \pm 130 \text{ nm}$ . The different chemical contrast obtained on the TEM image of a larger area (Figure 4.11 (b)-2) reveals interconnected ABS domains, resulting in an almost co-continuous structure. Finally, sample (PA6/SAN-MA)+ABS on Figure 4.11(a)-3 and (b)-3 also exhibit particle-in-matrix morphology, with dispersed ABS domains with an average diameter of  $1.2 \pm 0.5 \mu\text{m}$  and PB spheres with  $230 \pm 130 \text{ nm}$ . However, one can see heterogeneous areas of low modulus on (PA6/SAN-MA)+ABS, where the distribution was not effective (surrounded by a red dashed line on Figure 4.11 (a)-3), probably PA6 with less SAN-MA. The lack of compatibilizer can affect the dispersion of the ABS domains neighboring this area. Indeed, ABS domains appear larger than far from the low modulus area, the red arrow indicating an ABS domain with more than  $3 \mu\text{m}$  in length in comparison to domains with about  $1 \mu\text{m}$  at the surrounding areas. The blending protocol has a clear effect on the morphology of the blends, inducing the formation of particle-in-matrix morphologies (samples (PA6/ABS/SAN-MA) and (PA6/SAN-MA)+ABS) or almost co-continuous morphologies (sample (ABS/SAN-MA)+PA6). Furthermore, the size of the ABS domains depends on the morphology, i.e., smaller ABS domains ( $\sim 1.1 \mu\text{m}$ ) being formed in the particle-in-matrix rather than aggregates reaching more than  $2 \mu\text{m}$  when the almost co-continuous morphology is obtained.

One can observe that the combination of AFM and TEM allows a fine identification of the morphology and phases distribution, using mechanical and chemical contrasts. On the one hand, TEM is very effective to reveal the general morphology of the samples and, on the other hand, AFM allows a more precise investigation of the phase surrounding the PB spheres, which is possible by TEM only for specific system and with time-taking and careful staining procedure. The use of AFM gives additional nanomechanical information to clarify the distribution of the SAN blocks at the nanoscale, providing a very effective method to reveal subtle changes in the PA6/ABS interface.

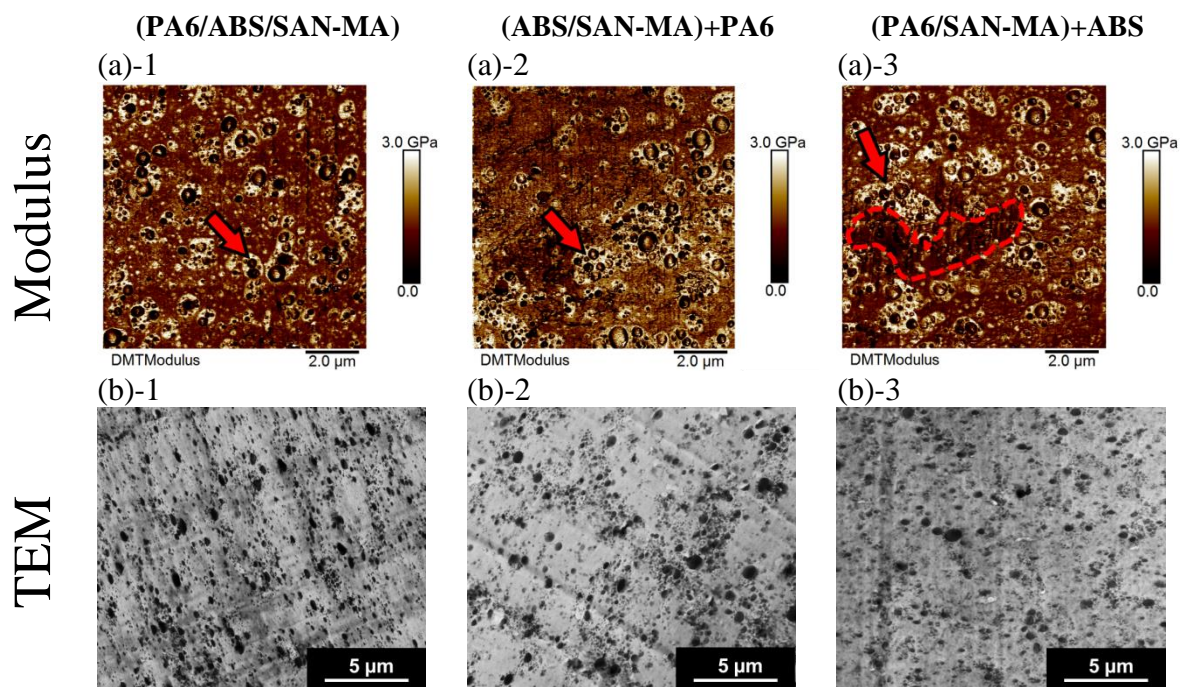


**Figure 4.11.** (a) AFM  $10 \times 10 \mu\text{m}^2$  Modulus images, (b) TEM images. Samples: 1-(PA6/ABS/SAN-MA); 2-(ABS/SAN-MA)+PA6 and 3-(PA6/SAN-MA)+ABS;

## 2.5. Effect of the morphology on the rheological behavior

In general, the rheological behavior of multiphase systems can be closely related to the resulting morphologies and structural properties. The influence of SAN-MA compatibilizer and the different blending protocols on the rheological properties are shown on Figure 4.12 (details on the rheological measurements are shown in Annex 1.3). One can observe on Figure 4.12(a) that the simple addition of SAN-MA does not have a significant effect on the complex viscosity ( $\eta^*$ ) of PA6+ABS system since sample (PA6/ABS/SAN-MA) exhibit a very similar response compared to the binary blend. In contrast, a significant impact on the rheological properties can be observed if SAN-MA is first added to the ABS phase prior to the blending with PA6, however no effect is observed if SAN-MA is first added to the PA6 phase prior to the blending with ABS. Indeed, especially at low frequencies, (ABS/SAN-MA)+PA6 exhibited a significant increase in melt viscosity compared to the other samples. According to *Jafari et al.*<sup>191</sup> this effect can be attributed to the increase of the flow resistance due to the extra tensions resulted from the higher anchoring effect of the almost co-continuous morphology of the (ABS/SAN-MA)+PA6, as already observed in Figure 4.11. A similar behavior can be observed for the storage modulus ( $G'$  on Figure 4.12 (b)) and loss modulus ( $G''$  on Figure 4.12 (c)) which are slightly higher for (ABS/SAN-MA)+PA6 than what was observed for the other compatibilized blends, and can also be related to its almost co-continuous morphology.<sup>191,192</sup> Both samples (PA6/ABS/SAN-MA) and (PA6/SAN-MA)+ABS presented similar rheological behaviors

due to their particle-in-matrix morphology. In Figure 4.12(b), one can notice the modest beginning of a plateau on PA6+ABS curve at low frequencies. According to *Solomon et al.*<sup>193</sup>, the apparent plateau is accordant to the response of a viscoelastic solid or a viscoelastic fluid with high relaxation time. In the case of sample PA6+ABS, the presence of large and heterogeneous ABS domains might be hampering morphological rearrangements, thus, increasing its relaxation time at lower frequencies. Nonetheless, since the incorporation of SAN-MA is the responsible for the better phase dispersion, such plateau is not observed in the ternary blends.

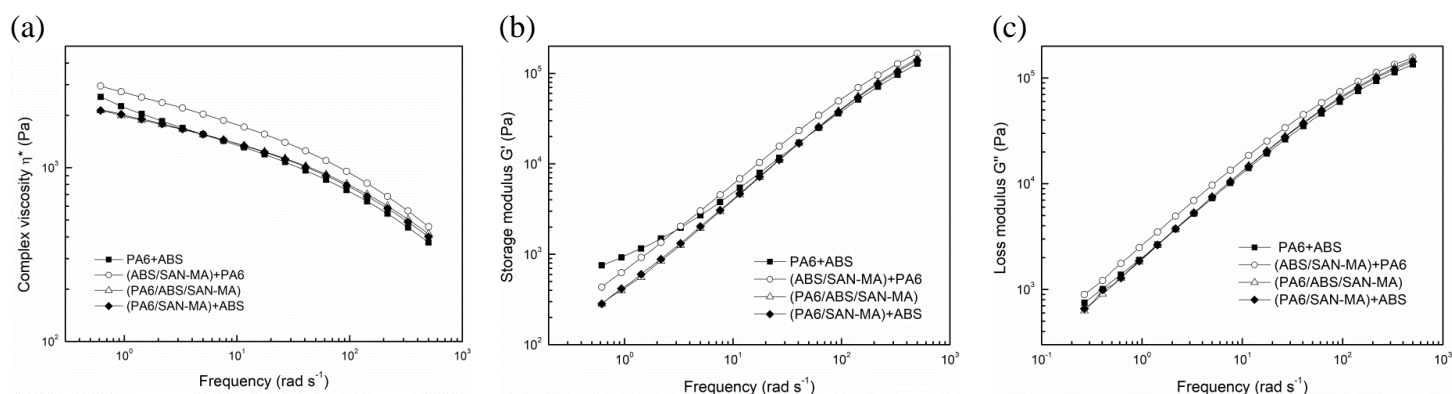


**Figure 4.12.** Rheological behavior of (PA6/ABS) and ternary blends. (a) Complex viscosity; (b) Storage modulus ( $G'$ ) and (c) Loss modulus ( $G''$ ).

### 2.5.1. Discussions of the effect of blending protocol on morphology and rheological properties

One can now analyze the impact of the blending protocol on the morphology and phase distribution of the compatibilized polymer blends. The different blending protocols aim at the optimization of the interactions between the compatibilizers and the components of the blends, the compatibilizer being effective if located at the PA6/ABS interface. Blending SAN-MA with PA6 in a first step should favor the chemical interaction between the anhydride groups of SAN-MA with the amine end groups of the polyamide, then, the physical interaction with the ABS would be achieved in a second step of extrusion. On the other hand, blending the SAN-MA with ABS should favor the physical entanglement of the compatibilizer with the PS-PAN blocks of the ABS prior to the chemical reaction with PA6. Morphological differences due to blending protocol effect were previously reported by *Castro et al.*<sup>194</sup> for a very similar system and explored by the *viscosity ratio* approach. It is well-established that maleic anhydride-based copolymers can chemically react with amine groups of PA6, increasing its viscosity. Analogously to *Castro et al.*<sup>194</sup>, when (PA6/SAN-MA)+ABS protocol is used, the formation of PA6-g-SAN-MA is favored during the first extrusion step and the grafted-copolymer shows higher viscosity values compared to neat polyamide. Once the viscosity of ABS is also higher than PA6, it is expected that the viscosity ratio of PA6-g-SAN-MA/ABS is closer to unity compared to the respective PA6/ABS pair. With the viscosity ratio of the components at least closer to unity, a finer break-up of dispersed phase would be expected.<sup>195</sup> Indeed, AFM and TEM analyses (Figure 4.11), confirmed the particle-in-matrix morphology. However, AFM analysis for the (PA6/SAN-MA)+ABS showed areas of lower modulus, probably PA6 without compatibilizer, surrounded by larger ABS domains (Figure 4.11 (a)-3) which are characteristic of a local lack of compatibilizer and were not seen for the 2 other blending protocols. We hypothesize that, considering that the SAN-MA reacted with the amine end groups and was diluted on the majority phase of the blend (PA6=57.5 wt%) prior to the blending with the minority phase

(ABS=37.5/5 wt%), the local amount and mobility of the compatibilizer available for interaction during the second extrusion may be limited by dilution, which can locally hamper the effectiveness of the compatibilization creating heterogeneous areas where the compatibilization of the ABS phase was less effective. When (ABS/SAN-MA)+PA6 protocol is employed, the compatibilizer is expected to be preferentially located in the ABS phase. In this case, the dilution of the compatibilizer in the ABS is done in a more selective way, once the compatibilizer SAN-MA doesn't interact with the PB, which corresponds to about 50% of the ABS phase. The physical entanglement between SAN-MA and the S-AN moieties of the ABS phase is favored. During the second extrusion with the majority phase PA6, one should expect that the availability of the compatibilizer at the interface for chemical reaction of the Maleic Anhydride with PA6 is better and not affected by a deleterious dilution effect. For this blend, however, the formation of an almost co-continuous morphology was evidenced by AFM, TEM and rheological analyses. One can suppose that the viscosity ratio of PA6 to ABS might be close to the volumetric ratio, which according to Paul & Barlow model<sup>196</sup> is the main criterion to obtain a co-continuous morphology. Since there are "in-situ" graft reactions occurring during the blending steps, the viscosity ratio quantification is not trivial. Nevertheless, the co-continuous morphology can also be related to the presence of compatibilizer preferentially at the interface, which lowers the interfacial tension and, according to Pötschke<sup>197</sup>, leads to broader composition ranges of co-continuous morphologies. Finally, in (PA6/ABS/SAN-MA) an intermediate situation was observed, favoring at the same time the interactions between the SAN-MA with both S-AN moieties (physical entanglement) and PA6 (chemical reaction), consequently improving miscibility. TEM and AFM confirmed the particle-in-matrix structure, with finely distributed ABS domains presenting a diameter of about 1  $\mu\text{m}$  and no heterogeneous areas of PA6 without compatibilizer.

A schematic representation of the developed morphologies from the different blending protocols is presented on Figure 4.13.

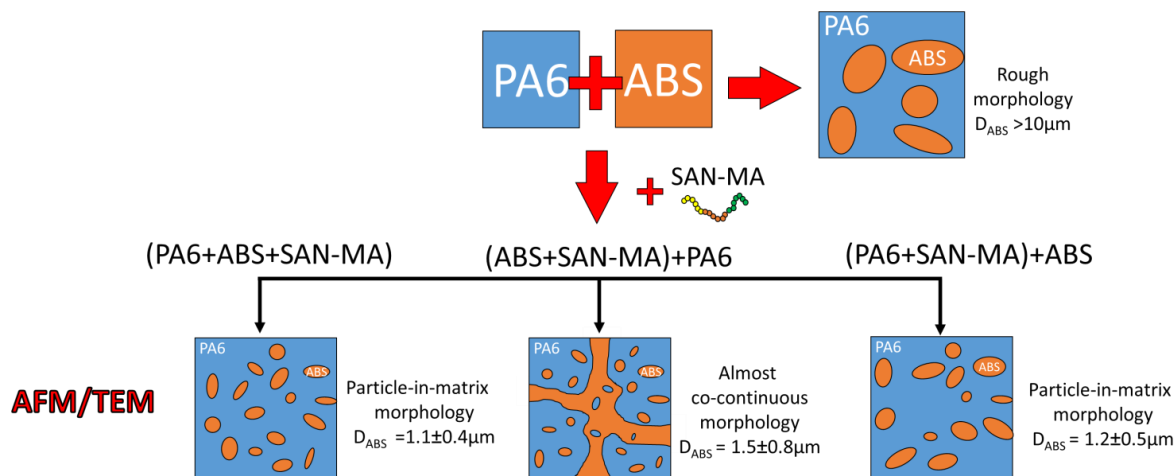


Figure 4.13. Schematic representation of the AFM/TEM analyses and results.

## 2.6. Effect of SAN-MA compatibilizer on PA6 structure

Raman spectroscopy can be useful for identification and evaluation of phase distribution in blends by probing their intrinsic chemical signature. In addition, this technique makes possible the acquisition of complementary and valuable structural information.<sup>198</sup> In this part of the study, the effect of the compatibilizer and of the blending protocol on the amount PA6 polymorphic crystalline phases will be first quantified by DSC and then its distribution will be characterized by co-localized AFM-Raman analysis. This advanced characterization will bring new insights on the impact of the compatibilizer and of the blending protocol onto the blend's morphology and properties.

### 2.6.1. PA6 polymorphs quantification by Differential Scanning Calorimetry (DSC )

The thermal behaviors of the blends were analyzed by DSC in order to quantify the amount of the PA6 polymorphic crystalline phases in each sample. The thermograms of the first heating of the samples are shown on Figure 4.14. The first heating cycle can be correlated to the further Raman analysis of the cryo-ultramicrotomed samples and the second heating cycle allows erasing their thermal history in order to evidence the physical-chemical interactions between the components. One can observe that there are two melting peaks for each sample, which evidences the coexistence of two crystalline forms, called gamma ( $\gamma$ ) and alpha ( $\alpha$ ), with melting temperatures of about 211 ( $T_{m1}$ ) and 221°C ( $T_{m2}$ ), respectively. Although no significant change was seen on the melting temperature ( $211 \pm 2^\circ\text{C}$  and  $221 \pm 1^\circ\text{C}$ ) one can observe that the enthalpy of fusion of the PA6  $\gamma$ -phase increases when the PA6 is blended corresponding to an increasing ratio of  $\gamma$  over  $\alpha$ -phase. The compatibilized blends exhibit a less intense but larger peak at 211°C than the PA6+ABS blend, characteristic of a larger distribution of the crystallites' dimensions.

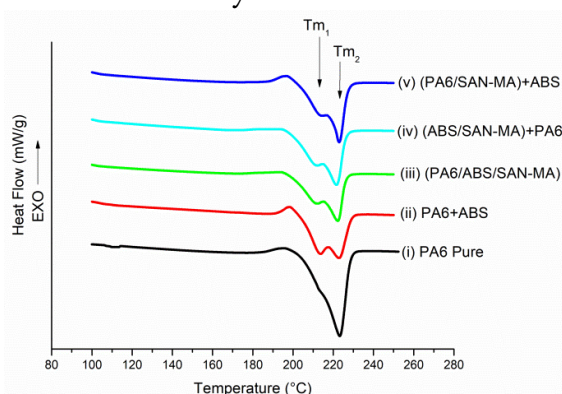


**Figure 4.14.** DSC thermograms obtained during the first heating cycle of samples (i) PA6; (ii) PA6+ABS; (iii) (PA6/ABS/SAN-MA); (iv) (ABS/SAN-MA)+PA6 and (v) (PA6/SAN-MA)+ABS

The characteristic data of the first heating cycle of the samples are summarized on Table 4.2. Pure PA6 sample presented 28% of crystallinity, which decreased to 25% in the presence of ABS and increased again to about 28% with the addition of ABS+SAN-MA, which may indicate, within analysis uncertainty, that ABS and SAN-MA have opposite effects on PA6's crystallization. The deconvolution of the melting peaks of the thermograms was done to quantify the amount of  $\alpha$  and  $\gamma$  phases in each sample (details in Annex 1.4). The reference sample of pure PA6 presents 64% of  $\alpha$  and 36% of  $\gamma$  crystals. However, all the blends present more than 44% of  $\gamma$ -phase, with 51% for the sample (PA6/SAN-MA)+ABS making it the only one for which the  $\gamma$ -phase is the majority phase, indicating that the direct addition of SAN-MA in the PA6 may favor the formation of  $\gamma$ -phase.

**Table 4.2.** Effect of SAN-MA Incorporation and Blending Sequence on the Melting and Crystallization Parameters of PA6, PA6+ABS and Ternary Blends on the first heating cycle

Sample	First heating cycle					
	$T_{m1}$ (°C)	$T_{m2}$ (°C)	$\Delta H_m$ (Jg <sup>-1</sup> )	$X_c$ (%)	$X^\alpha$ (%)	$X^\gamma$ (%)
<b>PA6</b>	213	222	67	28	64	36
<b>PA6+ABS</b>	212	222	36	25	55	45
<b>(PA6/ABS/SAN-MA)</b>	209	220	40	29	54	46
<b>(ABS/SAN-MA)+PA6</b>	209	220	39	28	56	44
<b>(PA6/SAN-MA)+ABS</b>	212	221	37	27	49	51

$T_{m1}$  = Melting temperature of  $\gamma$ -phase  
 $T_{m2}$  = Melting temperature of  $\alpha$ -phase

The second heating cycle (Figure 4.15/Table 4.3) allowed comparing the thermal properties of the samples after erasing their thermal history (identical and controlled cooling conditions after the melting step). First one can observe that the crystallization that took place in the DSC (during the cooling step) reached higher crystallization ratio for all the samples but lower  $\gamma$  over  $\alpha$ -phase ratios, which certainly comes from a difference of crystallization temperature. This question will not be studied extensively here. Like for the first heating cycle, the addition of ABS decreased the PA6 crystallinity (from 41% for pure PA6 down to 36% for PA6+ABS, and increased the amount of  $\gamma$ -phase of 20% (from 15 to 18%), almost similar to the 25% increase observed during the first heating cycle (from 36 to 45%). If the addition of SAN-MA compatibilizer had no significant impact on the material crystallinity index ( $\pm 2\%$ ), its impact on the polymorphic phases amount is confirmed, all the compatibilized blends presenting higher content of  $\gamma$ -phase than the non-compatibilized one. One can observe that the ratio of  $\gamma$ -phase increases significantly from 18% for the binary blend to 32% for the (PA6/SAN-MA)+ABS formulation. These results indicate that the  $\gamma$ -phase is favored when SAN-MA is added to the blend, especially when it is done directly to the PA6 phase, confirming what was observed during the first heating cycle.

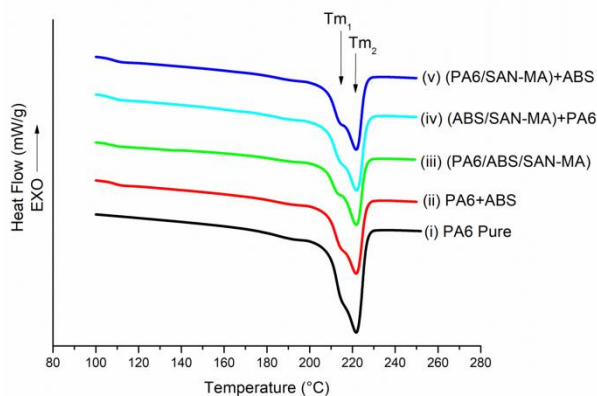


**Figure 4.15.** DSC thermograms obtained during the second heating cycle of samples (i) PA6; (ii) PA6+ABS; (iii) (PA6/ABS/SAN-MA); (iv) (ABS/SAN-MA)+PA6 and (v) (PA6/SAN-MA)+ABS

**Table 4.3.** Effect of SAN-MA Incorporation and Blending Sequence on the Melting and Crystallization Parameters of PA6, PA6+ABS and Ternary Blends on the cooling and second heating cycle.

Sample	Cooling		Second heating cycle					
	$T_c$ (°C)	$\Delta H_c$ (Jg <sup>-1</sup> )	$T_{m1}$ (°C)	$T_{m2}$ (°C)	$\Delta H_m$ (Jg <sup>-1</sup> )	$X_c$ (%)	$X^\alpha$ (%)	$X^\gamma$ (%)
<b>PA6</b>	190	90	212	220	99	41	85	15
<b>PA6+ABS</b>	189	48	212	219	52	36	82	18
<b>(PA6/ABS/SAN-MA)</b>	188	45	212	220	47	34	77	23
<b>(ABS/SAN-MA)+PA6</b>	188	49	213	220	49	36	77	23
<b>(PA6/SAN-MA)+ABS</b>	188	48	213	220	53	38	68	32

$T_c$  = Crystallization temperature  
 $\Delta H_c$  = Crystallization enthalpy

$T_{m1}$  = Melting temperature of  $\gamma$ -phase  
 $T_{m2}$  = Melting temperature of  $\alpha$ -phase

## 2.6.2. Distribution of PA6 polymorphs studied by co-localized AFM-Raman analyses

We will now be interested on the distribution of the PA6 polymorphic phases in the blends by co-localized AFM-Raman analysis. First, one must properly assign the Raman response of the  $\alpha$  and  $\gamma$  phases. In order to do so PA6 samples in different crystallographic forms were prepared: one amorphous and two crystalline samples. Sample Alpha presented only  $\alpha$  crystals and sample

Gamma only  $\gamma$  crystals. DSC and X-Ray diffraction (DRX) were performed to characterize their structure and crystallinity index. Details are given in Annex 1.5.

Figure 4.16 presents the characteristic Raman spectra of the  $\alpha$ ,  $\gamma$  and amorphous phases. The peak at  $1125\text{ cm}^{-1}$  corresponds to the C-C symmetric vibrations for trans conformation of the backbone, the signature of the monoclinic  $\alpha$ -phase of PA6, while the  $1080\text{ cm}^{-1}$  peak is attributed to the C-C vibration of gauche conformation, signature of the hexagonal  $\gamma$ -phase.<sup>198-200</sup> One can see that the  $\gamma$ -phase has also a characteristic peak at  $960\text{ cm}^{-1}$  (CO-NH) but due to its low intensity, it was not used for phase identification. The amorphous phase presents both  $1080$  and  $1125\text{ cm}^{-1}$ , characteristic of gauche and trans conformations, globally with low intensity and no preferable conformation. The increase of crystallinity in each of the crystalline forms engenders the prevalence of one band relative to the other. Thus, it is possible to quantify the presence of each phase by the characteristic intensity ratio of the bands at  $1080$  and  $1125\text{ cm}^{-1}$  ( $I_{1080}/I_{1125}$ ).

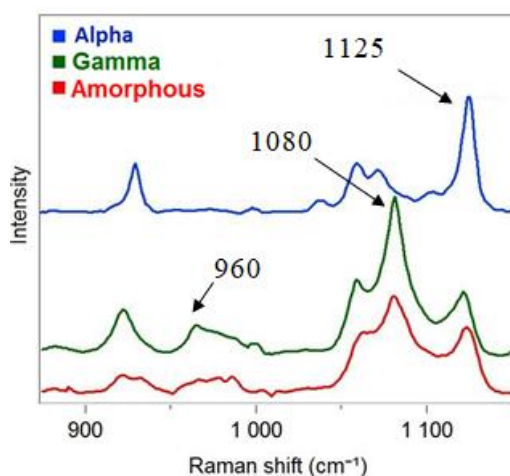


**Figure 4.16.** Typical Raman spectra of Polyamide alpha, gamma and amorphous phases.

Table 4.4 reports the  $I_{1080}/I_{1125}$  Raman ratio calculated from the literature<sup>201</sup> and experimentally from at least 10 different spectra. The amorphous samples presented an  $I_{1080}/I_{1125}$  ratio of about 1.40. Increasing the overall amount of  $\alpha$ -phase naturally decreased the  $I_{1080}/I_{1125}$  ratio down to about 0.33 for sample Alpha. Contrarily, the  $I_{1080}/I_{1125}$  ratio increased to about 2.0 with the increase of  $\gamma$ -phase for sample Gamma. Since the Raman intensity characteristic of one phase is proportional to its content in the material<sup>102,202</sup>, the differences between the experimentally calculated values and the literature are related to different samples' crystallinities. It is expected that areas of the compatibilized blends with high crystallinity of  $\gamma$ -phase would have  $I_{1080}/I_{1125}$  ratio of about 2.5 or above if locally the material crystallinity is higher than the crystallinity of the polyamides used as references. Conversely, a locally higher content of  $\alpha$ , amorphous or a mixture of phases should decrease this ratio.<sup>102,202</sup> Details are presented in Annex 1.5.

**Table 4.4.** Characteristic band intensity ratios from literature and calculated experimentally.

	$I_{1080}/I_{1125}$		
	Amorphous	Alpha ( $\alpha$ )	Gamma ( $\gamma$ )
Literature <sup>201</sup>	-	0.42	2.5
Experimental	1.40	0.33	2.0



Figure 4.17 (a)-1 3 are Raman mappings relative to the PB phase (integration between 1657-1680  $\text{cm}^{-1}$ ) overlapped on binary AFM modulus images (PB spheres shown in black) of the compatibilized samples: 1-(PA6/ABS/SAN-MA), 2-(ABS/SAN-MA)+PA6 and 3-(PA6/SAN-MA)+ABS. Individual Raman mappings and corresponding AFM images were shown in Annex 1.6. Due to the micrometric resolution of the Raman, the PB spheres included in the ABS phase cannot be individually distinguished, but zones with higher concentration of PB spheres are visible on the Raman mappings. The AFM/Raman co-localization is confirmed by the good correlation between the PB Raman mappings and the PB clusters seen by AFM. It is worth reminding that the AFM is based on a surface analysis, while the Raman probes a depth of about 1  $\mu\text{m}$ , being able to detect ABS domains below the sample surface probed by AFM. These Raman mappings were analyzed to display the  $I_{1080}/I_{1125}$  ratio for each sample (Figure 4.17 (b) 1 to 3).

Sample (PA6/ABS/SAN-MA) presents areas with  $I_{1080}/I_{1125}$  ratio values around 2.5 (green areas on Figure 4.17(b)-1) which characterize a high amount of PA6 in  $\gamma$  form ( $I_{1080}/I_{1125} > 2$  VS  $I_{1080}/I_{1125} \sim 1.4$  for the amorphous phase), homogeneously distributed in the sample. Sample (ABS/SAN-MA)+PA6 on Figure 4.17(b)-2 presents equivalent ratio values ( $\sim 2.5$ /green) but a different distribution. Areas with a higher  $\gamma$  concentration appear in green, especially over the richer PB areas (corresponding to the ABS domains), and lower  $I_{1080}/I_{1125}$  ratio appear in orange/red, which can be related to a mixture of  $\alpha$ , amorphous and  $\gamma$  phase. The differentiation between  $\alpha$  and the amorphous phase contribution was attempted using the  $\gamma$ -phase characteristic peak at 960  $\text{cm}^{-1}$  however, a clear conclusion could not be obtained (details in Annex 1.6). Notwithstanding, the subtraction of a spectrum with low  $I_{1080}/I_{1125}$  ratio from one with a high ratio revealed only peaks relative to the PA6 in  $\gamma$ -phase (shown in Annex 1.6), which confirms that the areas with high  $I_{1080}/I_{1125}$  ratio present more  $\gamma$ -phase than the low ratio zones, but it is not possible to affirm if these low ratio zones are composed of mixtures of phases or amorphous zones. Finally, sample (PA6/SAN-MA)+ABS presents  $I_{1080}/I_{1125}$  ratio values around 2.5 and higher (blue areas on Figure 4.17(b)-3), which is an indication of a high content of  $\gamma$ -phase in the PA6, not only over the ABS domains. This result is in accordance with the previous DSC analysis of this sample, i.e., when SAN-MA is added directly to the PA6 the  $\gamma$ -phase is favored.

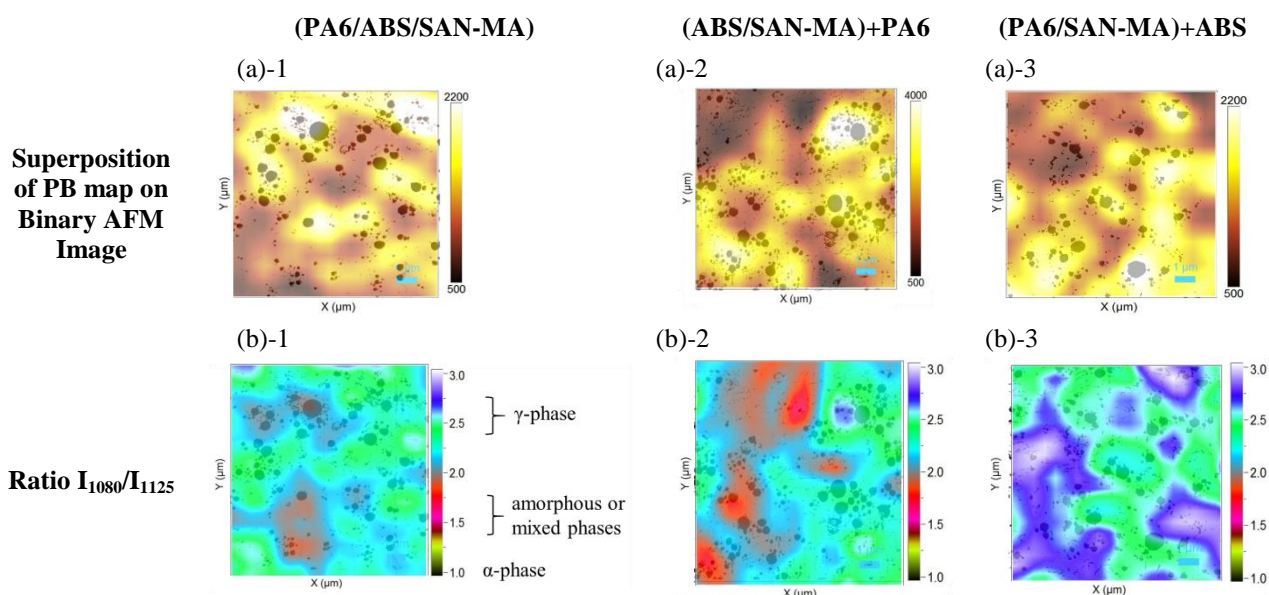


**Figure 4.17.** (a) Superposition of PB Raman mapping (band integration between 1657-1680  $\text{cm}^{-1}$ ) on the binary AFM Modulus image, showing the PB phase in black. The higher the amount of PB, the brighter is the pixel. (b) Ratio of the peak intensities  $I_{1080}/I_{1125}$  for : 1-(PA6/ABS/SAN-MA); 2- (ABS/SAN-MA)+PA6 and 3-(PA6/SAN-MA)+ABS.

The  $I_{1080}/I_{1125}$  Raman ratio can also give an insight on the local crystallinity of the probed areas. The mean values of the  $I_{1080}/I_{1125}$  ratio for samples (PA6/ABS/SAN-MA), (ABS/SAN-MA)+PA6 and (PA6/SAN-MA)+ABS were  $2.2\pm 0.2$ ,  $2.2\pm 0.3$  and  $2.6\pm 0.3$ , respectively. This shows that the first two samples, despite a different phase distribution, have a similar crystallinity index for the mapped areas, while the mapped area of the last sample (PA6/SAN-MA)+ABS has a higher crystallinity index. Previous DSC analysis also showed samples (PA6/ABS/SAN-MA) and (ABS/SAN-MA)+PA6 with similar crystallinities and about 45% of  $\gamma$ -phase, while sample (PA6/SAN-MA)+ABS presented 51% of  $\gamma$ -phase. These results indicate that the blending protocols have an effect on the distribution of the PA6 polymorphic phases in the blend, i.e., when the blending protocol leads to the concentration of the compatibilizer near the ABS domains, a higher content of  $\gamma$ -phase at the interface of these domains is seen. Similarly, when the compatibilizer is added in the PA6, higher content of  $\gamma$ -phase can be found in PA6 zones, not necessarily near the ABS domains.

### 2.6.3. Discussions of the effect of SAN-MA compatibilizer on PA6 structure

The DSC and co-localized AFM-Raman analyses presented on Figure 4.14 and 4.17, respectively, illustrates the impact of the compatibilizer and the blending protocols on the PA6 polymorphic phases' amount and distribution. DSC analyses have shown that the addition of SAN-MA directly in the PA6 favors the  $\gamma$ -phase. Raman mappings are in accordance with the previous DSC analyses, which showed samples (ABS/SAN-MA)+PA6 and (PA6/SAN-MA)+ABS with similar amount of  $\gamma$ -phase (~45%) and sample (PA6/SAN-MA)+ABS with more  $\gamma$ -phase than the others (51%). One can consider the mapped areas as representative of the materials and deduce that the distribution of the PA6's polymorphic phases is directly related to the compatibilizer preferred location induced by the blending protocol.

Sample (PA6/ABS/SAN-MA), presented a homogeneous distribution of PA6  $\gamma$ -phase with no preferred locations (Figure 4.17 (b)-1). Sample (ABS/SAN-MA)+PA6, with a similar amount of  $\gamma$ -phase, showed a heterogeneous distribution of  $\gamma$ -phase (Figure 4.17 (b)-2), presenting high content of  $\gamma$ -phase over the ABS domains, where the compatibilizer is preferentially located due to the blending protocol. Finally, sample (PA6/SAN-MA)+ABS (Figure 4.17 (b)-3) presented a higher mean value of the  $I_{1080}/I_{1125}$  ratio, related to the higher crystallinity of the probed area, and an heterogeneous distribution, with high  $I_{1080}/I_{1125}$  ratio observed at areas even far from the ABS domains. In this case, the mixing protocol suggests that the compatibilizer is concentrated in the PA6, which leads to the formation of a higher content of  $\gamma$ -phase. This behavior can be attributed to disturbances in the homogeneous nucleation process of PA6 due to the compatibilizer presence, which limits the polymer chain mobility, favoring the crystallization of the less stable  $\gamma$ -phase.<sup>198,203</sup> Disturbances on the crystallization of PA6 have already been reported for composites and compatibilized blends<sup>194,199,204</sup>, but this work is the first to report the influence of the blending protocol on the distribution of the PA6's polymorphic phases in the blend.

A schematic representation of the different PA6 polymorphic phases' amount and distribution developed from the different blending protocols is presented on Figure 4.18.

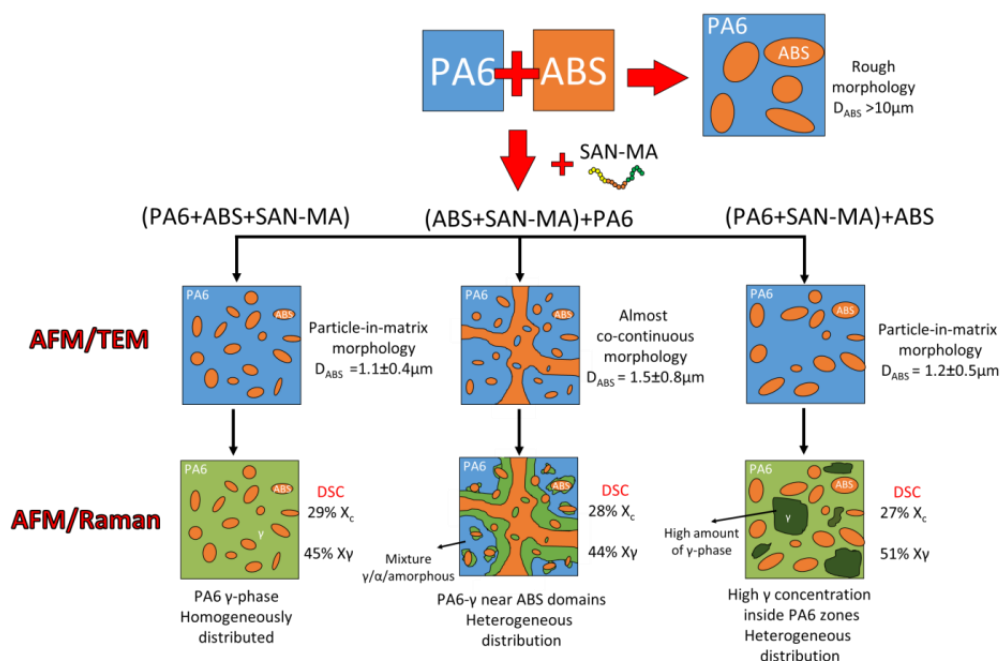


Figure 4.18. Schematic representation of the analyses and results.

### 3. Conclusions of Chapter 4

The co-localized AFM/Raman analyses done on the binary and compatibilized PA6/ABS blend exemplify the power of this technique for morphological, nanomechanical and chemical characterization of polymer blends. Based on the chemical information collected by Raman and the nanomechanical information issued from AFM a clear phase attribution was performed. Atomic Force Microscopy allied to Transmission Electron Microscopy allowed the characterization of the effect of different blending protocols on the morphology of the blends, as well as the dispersion and distribution of the sub-phases of the ABS at nanometric scale. It has been shown that the addition of the compatibilizer on the ABS phase prior to the PA6 phase induces the formation of an almost co-continuous morphology, rather than a particle-in-matrix morphology when the compatibilizer is added prior in the PA6 or in a single extrusion step. The morphological analysis helped the interpretation of the rheological measurements. The almost co-continuous morphology exhibited a significant increase in melt viscosity, especially at low frequencies, and its rheological properties ( $G'$  and  $G''$ ) were higher than what was observed for the samples with particle-in-matrix morphology, attributed to the increase of the flow resistance due to the extra tensions resulted from the higher anchoring effect of the almost co-continuous morphology.

The coupling of AFM with Raman spectroscopy provided new fundamental insights on the effect of the compatibilizer on the Polyamide crystalline structure. Raman analyses of the distribution of the different polyamide polymorphs ( $\alpha$ ,  $\gamma$  and amorphous) showed good correlation with DSC analyses, allowing the interpretation of the effects of the compatibilizer on the structure of the Polyamide matrix. It was shown that the compatibilizer influences the crystallization of the Polyamide, favoring the formation of the less stable  $\gamma$  polymorphic phase. Furthermore, the distribution of the  $\gamma$ -phase in the blend depends on the blending protocol due to the different preferred locations of the compatibilizer induced by the process. High amount of  $\gamma$ -phase is present near the ABS domains when the compatibilizer is blended with ABS prior to PA6. Contrarily, high amounts of  $\gamma$ -phase are seen inside the PA6 phase when the compatibilizer is blended with PA6 prior

to ABS. Finally, a homogeneous distribution of  $\gamma$ -phase is acquired when the components are blended in a single step.

We verify that for all the different blending protocol used, the general morphology of the compatibilized blends, i.e., the distribution and sizes of ABS domains, was improved when compared to the reference PA6+ABS sample. However, we have shown that the presence of the compatibilizer and the blending protocol can have an impact on the amount and distribution of the different polymorphic phases of the polyamide. Further research must be performed to correlate this fundamental knowledge to the functional properties of the material, for example mechanical strength, impact resistance and heat distortion temperature.

In addition to the fundamental knowledge of the morphology of these specific polymer blends, the developed strategy allying morphological and chemical characterization by AFM, SEM and Raman spectroscopy on cryo-ultramicrotomed samples opens new possibilities for a better understanding of the micro and nanoscale behavior of the compatibilization interplays in polymer blends and composites, i.e., to design and tailor their functional properties from the nanoscale.

### 3.1. Summary of conclusions of Chapter 4

The complete assignment of the components of the blends was achieved using their chemical signatures and nano-mechanical properties

The morphology of the blends, as revealed by AFM and TEM, depend on the blending protocol:

- (PA6+ABS+SAN-MA): particle-in-matrix morphology
- (ABS+SAN-MA)+PA6: almost co-continuous morphology
- (PA6+SAN-MA)+ABS: particle-in-matrix morphology

The developed morphologies have different rheological properties.

The almost co-continuous morphology presented higher storage modulus ( $G'$ ) and loss modulus ( $G''$ ) than the particle-in-matrix one, due to the higher anchoring effect

DSC and Raman analysis show that SAN-MA compatibilizer favors the formation of the  $\gamma$  polymorph, especially when the SAN-MA is added directly in contact with PA6

Co-localized AFM/Raman analyses show that the distribution of the  $\gamma$  polymorph depends on the blending protocol:

- SAN-MA prior on ABS phase:  $\gamma$  polymorph near the ABS domains – heterogeneous distribution
- SAN-MA directly on PA6: high content of  $\gamma$  far from ABS domains – heterogeneous distribution
- SAN-MA blended simultaneously with PA6/ABS:  $\gamma$  polymorph homogeneously distributed

#### 4. Conclusions du Chapitre 4 en Français

Les analyses co-localisées AFM/Raman effectuées sur les mélanges PA6/ABS binaire et compatibilisés illustrent la puissance de cette technique pour la caractérisation morphologique, nanomécanique et chimique des mélanges polymères. Sur la base des informations chimiques recueillies par Raman et des informations nanomécaniques issues de l'AFM, une attribution de phase claire a été effectuée. La microscopie de force atomique alliée à la microscopie électronique de transmission a permis de caractériser l'effet de différents protocoles de mélange sur la morphologie des mélanges, ainsi que la dispersion et la distribution des sous-phases de l'ABS à l'échelle nanométrique. Il a été démontré que l'addition du compatibilisant sur la phase ABS avant la phase PA6 induit la formation d'une morphologie presque co-continue, plutôt qu'une morphologie des particules dans matrice lorsque le compatibilisant est ajouté avant la PA6 ou dans une seule étape d'extrusion. L'analyse morphologique a contribué à l'interprétation des mesures rhéologiques. La morphologie presque co-continue a présenté une augmentation significative de la viscosité à l'état fondu, en particulier à basse fréquence. Ses propriétés rhéologiques ( $G'$  et  $G''$ ) étaient supérieures à celles observées pour les échantillons à morphologie particule dans matrice, attribuée à l'augmentation de la résistance à l'écoulement due aux tensions supplémentaires issues de l'effet d'ancrage plus élevé de la morphologie presque co-continue.

Le couplage AFM-Raman a fourni de nouvelles connaissances fondamentales sur l'effet du compatibilisant sur la structure cristalline de la polyamide. Les analyses Raman de la distribution des différents polymorphes de la PA6 ( $\alpha$ ,  $\gamma$  et amorphe) ont montré une bonne corrélation avec les analyses DSC, ce qui permet d'interpréter les effets de l'agent compatibilisant sur la structure de la matrice de polyamide. Il a été démontré que le compatibilisant influence la cristallisation de la polyamide, favorisant la formation de la phase polymorphe  $\gamma$  moins stable. En plus, la distribution de la phase  $\gamma$  dans le mélange dépend du protocole de mélange en raison des différentes distributions du compatibilisant induit par le processus. Une quantité élevée de phase  $\gamma$  est présente près des domaines ABS lorsque le compatibilisant est mélangé avec de l'ABS avant la PA6. Au contraire, des quantités élevées de phase  $\gamma$  sont observées à l'intérieur de la phase PA6 lorsque le compatibilisant est mélangé avec la PA6 avant l'ABS. Finalement, une distribution homogène de la phase  $\gamma$  est acquise lorsque les composants sont mélangés en une seule étape.

Nous vérifions que, malgré le protocole de mélange utilisé, la morphologie générale des mélanges, c'est-à-dire la distribution et la taille des domaines ABS, a été améliorée par rapport à l'échantillon PA6+ABS de référence. Cependant, nous avons montré que la présence du compatibilisant et du protocole de mélange peut avoir un impact sur la quantité et la répartition des différentes phases polymorphes de la polyamide. D'autres recherches doivent être effectuées pour corrélérer ces connaissances fondamentales aux propriétés fonctionnelles du matériau (par exemple résistance mécanique, résistance aux chocs et température de distorsion thermique).

En plus des connaissances fondamentales de la morphologie de ces mélanges de polymères, la stratégie développée alliant la caractérisation morphologique et chimique par spectroscopie AFM, SEM et Raman sur des échantillons cryo-ultramicrotomés ouvre de nouvelles possibilités pour une meilleure compréhension du comportement micro et nanométrique de la compatibilisation dans les mélanges de polymères et composites, c'est-à-dire pour concevoir et adapter leurs propriétés fonctionnelles à partir de la l'échelle nanométrique.

#### 4.1. Résumé des conclusions du Chapitre 4 en Français

L'analyse co-localisée AFM/Raman a permis l'affectation complète des composants des mélanges en utilisant leurs signatures chimiques et leurs propriétés nano-mécaniques

La morphologie des mélanges, telle que révélée par AFM et TEM, dépend du protocole de mélange:

- (PA6+ABS+SAN-MA): morphologie des particules dans matrice
- (ABS+SAN-MA)+PA6: morphologie presque co-continue
- (PA6+SAN-MA)+ABS: morphologie des particules dans matrice

Les morphologies développées ont des propriétés rhéologiques différentes. La morphologie presque co-continue a présenté un module de stockage ( $G'$ ) et un module de perte ( $G''$ ) plus élevés que le type de particules dans la matrice, en raison de l'effet d'ancrage plus élevé

Les analyses DSC et Raman montrent que le compatibilisant SAN-MA favorise la formation du polymorphe  $\gamma$ , surtout lorsque le SAN-MA est ajouté directement en contact avec la PA6

Les analyses co-localisées AFM/Raman montrent que la distribution du polymorphe  $\gamma$  dépend du protocole de mélange:

- SAN-MA avant la phase ABS: polymorphe  $\gamma$  près des domaines ABS - distribution hétérogène
- SAN-MA ajouté sur PA6: contenu élevé de  $\gamma$  loin des domaines ABS - distribution hétérogène
- SAN-MA mélangé simultanément avec PA6 / ABS: polymorphe  $\gamma$  réparti de manière homogène



# CHAPTER 5

---

## Hybrid Membranes for Fuel Cell



## PROLOGUE

In this chapter, we will present the study of alternative membranes for Fuel Cell operation, based on the hybridization of a sulfonated polyether-etherketone (sPEEK) membrane with an active network by sol-gel chemistry. The membranes were prepared at the laboratory SyMMES (Grenoble, France) as part of the thesis works of Isabel Zamanillo López and Natacha Huynh.

We will present here a brief introduction to the Fuel Cell technology and the fundamentals of solid polymer electrolytes and sol-gel reactions. Then, we will present the fabrication of hybrid membranes based on two different sol-gel precursors. The study of hybrid membranes based on (3-mercaptopropyl)-methyldimethoxysilane (SHDi) precursors allowed for the understanding of the effect of each step of fabrication on the membrane's morphology, nanomechanical properties and stability over time. The second study, hybrid membranes based on (3-mercaptopropyl)-trimethoxysilane (SHTriM) focused on the effect of the varying amount of sol-gel phase on the morphology of the hybrid membranes. Furthermore, direct observation of the morphology by AFM allowed to orient the selection of an appropriate fitting model for SANS interpretation, giving complementary structural information about the SG phase and the sPEEK matrix. Finally, we stress out that the complete morphological and chemical characterization of the membranes was only possible thanks to the use of cryo-ultramicrotomy allied to co-localized AFM/Raman setup and complementary characterization techniques, which contributions will be outlined.

### French Prologue

Dans ce chapitre, nous présenterons l'étude de membranes alternatives pour pile à combustible, basée sur l'hybridation d'une membrane de polyéther-éthercétone sulfonée (sPEEK) avec un réseau actif par chimie sol-gel. Les membranes ont été préparées au laboratoire SyMMES (Grenoble, France) dans le cadre des travaux de thèse d'Isabel Zamanillo López et Natacha Huynh.

Nous allons vous présenter ici une brève introduction à la technologie des piles à combustible et les fondamentaux des électrolytes polymères solides et des réactions sol-gel. Ensuite, nous présenterons la fabrication de membranes hybrides à base de deux précurseurs sol-gel différents. L'étude de membranes hybrides à base du précurseur (3-mercaptopropyl)-méthyldiméthoxysilane (SHDi) a permis de comprendre l'effet de chaque étape de fabrication sur la morphologie de la membrane, ses propriétés nanomécaniques et sa stabilité au cours du temps. La seconde étude portant sur des membranes hybrides à base de (3-mercaptopropyl)-triméthoxysilane (SHTriM) a montré l'effet de la quantité croissante de phase sol-gel sur la morphologie des membranes hybrides. Par ailleurs, l'observation directe de la morphologie par AFM a permis d'orienter la sélection d'un modèle d'ajustement (fit) approprié pour l'interprétation des analyses SANS, en fournissant des informations structurelles complémentaires sur la phase SG et la matrice sPEEK. Finalement, nous soulignons que la caractérisation fine de la morphologie et de la chimie des membranes n'a été possible qu'avec l'utilisation de la cryo-ultramicrotomie alliée à la co-localisation AFM/Raman et à des techniques de caractérisation complémentaires, dont les contributions seront soulignées.

## 1. Theoretical Background and Motivation

### 1.1. Hydrogen Fuel Cells Fundamentals

Renewable energy sources as solar and wind, which are weather dependent, are intermittent by nature. Thanks to the Proton Exchange Membrane Water Electrolyzer (PEMWE) hydrogen technologies offer a chemical storage solution to smooth intermittent electricity production. This chemical energy remains available to be later restored in the form of electricity by proton Exchange Membrane Fuel Cells (PEMFC). The PEMWE/PEMFC couple is therefore a solution for sustainable development if renewable hydrogen is used. In general, PEMFC can also be used as a power source in a variety of applications, such as transport, portable, stationary and emergency backup power applications. In this study, we will be particularly interested in PEMFCs that use hydrogen fuel, a promising system for zero CO<sub>2</sub> and pollutant emission.

PEMFC is composed of a Membrane Electrode Assembly (MEA) which includes gas diffusion layers, the catalyst layers (electrodes) and the proton exchange membrane used as electrolyte, as illustrated on Figure 5.1. During operation, hydrogen molecules adsorb on the anode catalysts (left), and protons and electrons are formed by the resulting electrochemical reaction (oxidation). The electrons flow through the external circuit, delivering electrical energy (lighting lamp) and finally reduce oxygen into oxygen ions at the cathode (right). Protons meanwhile migrate through the electrolyte membrane and react with these oxygen ions, forming water as a byproduct.<sup>205</sup>

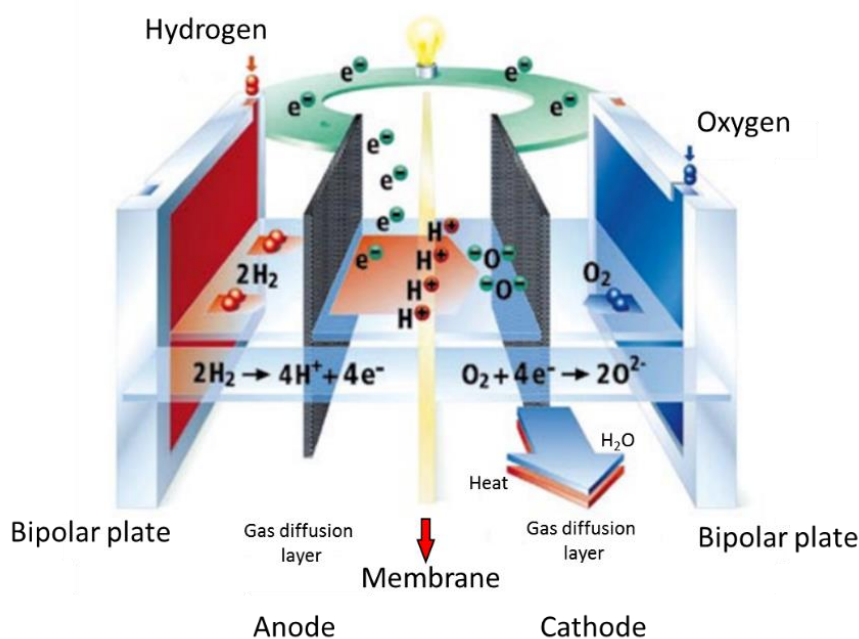


Figure 5.1. Operating principle of a fuel cell. Adapted from <sup>205</sup>

The electrochemical reactions are: oxidation of hydrogen at the anode (Equation 5.1) and reduction of oxygen at the cathode (Equation 5.2).



The role of the polymer membrane electrolyte is to transport the protons generated at the anode to the cathode to allow the oxygen reduction's reaction to take place. For effective Fuel Cell operation, the membrane must be highly proton conducting, but should not conduct electrons, avoiding short circuit, and sufficiently gas-tight to avoid gas crossover (resulting in hot-spots and destruction).<sup>206</sup>

To ensure the perennial emergence of this technology, the membrane must allow the PEMFC operation at high temperature (100-150°C) and therefore low relative humidity (10-50%). Researchers have focused on the development of PEMFCs operating at high temperatures (> 100 °C) because it has been proved that operating above 100°C increases the speed of electrochemical reactions, decreases the sensitivity of the catalyst to carbon monoxide (responsible for "poisoning" of the MEA) and simplifies the cooling system and water management.<sup>207,208</sup>

In Fuel Cell devices, certain stresses or constraints lead to accelerated materials ageing. For example, membrane mechanical failure is accelerated by the swelling (due to hydration) and shrinkage (dehydration) that occurs at each start/stop operation. Membranes showing little or no change in dimension at different water contents will extend MEA lifetime.<sup>209</sup> The membrane also has to withstand chemical degradation due to attack by radicals and other reactive species. MEA degradation often manifests itself as a gradual decay in fuel cell performance followed by a sudden catastrophic failure of the cell due to gas crossover through tears in the membrane. The ability of the membrane to resist to the mechanical stresses and chemical attack is the limiting factor in the lifetime of PEMFC.<sup>210</sup> For practical applications, the membrane's lifetime must exceed 8000h and 50000h respectively for PEMFC transport and stationary applications.<sup>206,211,212</sup> The role of proton conducting membrane is therefore central in the operation of the cell.

## 1.2. Polymer Membrane Electrolytes

The chemical functions conferring the proton conductivity to the solid polymer electrolyte (also called ionomer) are acid functions, most often of the sulfonic type  $-\text{SO}_3\text{H}$ . The ion exchange capacity of the polymer corresponds to the amount of ionic sites relative to the polymer mass, which is directly related to the proton conductivity of the membrane and consequently to the performance of the Fuel Cell. Notwithstanding, as already state above, due to the complexity of the factors contributing to membrane degradation, other properties are important to assure the long term reliability and performance of the device, such as low gas permeation ( $\text{H}_2$  and  $\text{O}_2$ ), good mechanical strength, no electronic conductivity, electrochemical resistance and chemical stability. According to Jones *et al.*<sup>210</sup>, no single property can be used as a stand-alone metric for membrane durability.

There are basically two families of polymers used in PEMFC: fluorinated and non-fluorinated polymers. Perfluorinated membranes are the ones that currently offer the most satisfaction both in terms of performance and durability. To date, Nafion® is the most widely accepted as a reference membrane due to its excellent functional and electrochemical properties up to 80°C. Its structure consists of a perfluorinated hydrophobic skeleton with pendant chains terminated by sulfonic acid groups  $-\text{SO}_3\text{H}$  (Figure 5.2). The perfluorinated polymer has been chosen for its excellent proton conductivity, arising from a very good hydrophilic/hydrophobic nanophase separation, as well as for its electronic insulating properties and very good chemical stability. In the presence of water, there is a differential swelling of the hydrophobic and hydrophilic phases and the appearance of channels (hydrophilic zones) allowing the transport of the protons. However, the thermomechanical relaxation of Nafion® occurs around 100 °C, which imposes a maximum operating temperature of the order of 80° C, representing a direct limit to the application of Nafion® to high temperature PEMFCs.<sup>213</sup> In addition, the decrease of Nafion's proton conductivity above 80°C, associated with low relative humidity, along with high membrane's cost (>500 €/m<sup>2</sup>), which represents more than 80% of

the cost of the MEA stack, make difficult its use in a PEMFC for a low cost passenger electric car.<sup>206</sup> A competitive cost can only be reached with improved performance or with the development of alternative membranes.<sup>214,215</sup>

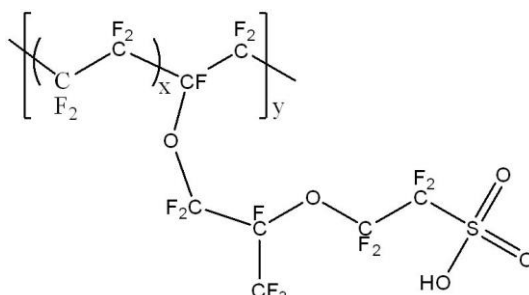


Figure 5.2. Nafion® structure

Non-fluorinated membranes, mainly polyaromatic polymers, represent an alternative to Nafion®, being less expensive and with suitable thermomechanical properties for higher operating temperatures ( $>100\text{ }^\circ\text{C}$ ).<sup>207</sup> However, they are more sensitive to the chemical degradation and therefore their lifetime is generally lower than that of perfluorinated membranes, e.g., from hundreds up to few thousands hours of operation against more than 20000 h for Nafion at  $80^\circ\text{C}$ .<sup>216</sup> One of the solutions to overcome these problems is to develop alternative non-fluorinated aromatic composite membranes with improved chemical stability.

### 1.2.1. Sulfonated Polyether-etherketone (sPEEK)

In this work, we have used sPEEK membranes as an alternative to Nafion®. Its structure is presented on Figure 5.3. sPEEK has better mechanical strength, better thermal stability and is less expensive than Nafion®. However, it is less chemically stable in operating conditions under the attack of  $\text{H}_2\text{O}_2$  (a byproduct resulting from incomplete electrochemical reactions and gas crossover).<sup>217</sup>

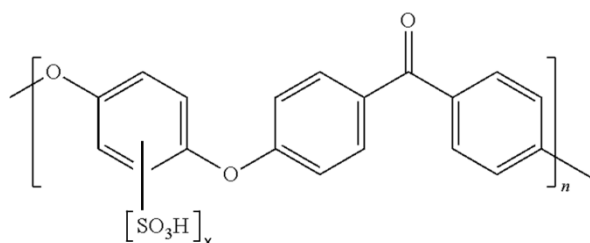


Figure 5.3. (a) sPEEK structure (X=0.4)

The hydrophobic/hydrophilic phase separation, essential to the good conductivity of the membranes, is much more pronounced in Nafion® than in sPEEK. In the polyaromatic membrane, the polymer backbone is less hydrophobic and less flexible, due to the presence of aromatic groups, than for a perfluorinated one. Thus, the ionic channels are narrower and branched with many "dead ends" (unconnected channels). In addition, the  $-\text{SO}_3\text{H}$  functions are less acidic than in Nafion® which results in a less labile proton.<sup>218</sup> All these factors reduce the ionic conductivity.<sup>211</sup>

New solutions for these problems are based on the synthesis of new polymer architectures (new polymers, interpenetrating polymer networks, 3D structures by reticulation, etc.) or modification of the existing membranes. Mendil-Jakani *et al.*<sup>219</sup> have shown that hydrothermal treatments above  $60^\circ\text{C}$  had strong impact on quality of the hydrophilic/hydrophobic interfaces, water uptake, and conductivity. Thermally treated membranes presented a nano-phase separation in

liquid water even at room temperature, which is not observed for pristine sPEEK membrane. Portale *et al.*<sup>220</sup> have shown that high proton conductivities of about 100 mS/cm, which is equivalent to the conductivity of a native Nafion® membrane in liquid water at room temperature, can be reached on swelled sPEEK membranes in temperatures of about 70°C. However, for temperatures above 87 °C, irreversible swelling occurs and the membrane mechanical properties degrade rapidly, resulting in a rapid drop of the proton conductivity. Influences of membrane fabrication steps have also been shown by Fichet *et al.*<sup>221,222</sup> on Semi-Interpenetrating Polymer Networks (semi-IPNs) combining a fluorinated network with sPEEK, showing that the drying time can induce a decrease of the water uptake and conductivity due to its effect on the hydrophilic/hydrophobic nano-separation.

Another way is the addition of an inorganic phase to promote better mechanical properties, to enhance the proton conductivity (addition of a mineral acid) or to improve water retention at high temperatures. If the use of inert reinforcements generally reduces the proton conductivity, it results in greater mechanical properties, limiting dimensional changes. The introduction of inorganic oxide and solid acid components (metal oxides, zeolites, metal hydrogen phosphates and heteropolyacids) can lead to an improvement in the proton conductivity under low RH.<sup>209</sup> The preparation methods for inorganic–organic membranes include on the one hand the *in situ* precipitation of inorganic particles in functionalized polymer solutions or in pre-cast ionomer membranes, and on the other hand the formation of interpenetrating inorganic and organic networks.<sup>218</sup> Other strategies reported by extensive reviews by Jones and Rozière<sup>223,224</sup>, Alberti and Casciola<sup>225</sup> and Savadogo<sup>226</sup> include polymer blending, partial cross-linking and organic–organic composite membranes, but up to now, these modifications did not lead to expected improvements and often generated a critical loss of proton conduction.<sup>221</sup> However, mechanical reinforcement to prevent mechanical failure from wet/dry humidity cycling may be insufficient<sup>210,211</sup>, and these strategies do not systematically take into account the required enhancement of the chemical resistance of the membrane. The introduction of stabilizing units to increase the membrane's chemical stability at high temperature can be achieved with the fabrication of hybrid membranes with tailored sol-gel precursors. This strategy simultaneously provides mechanical reinforcement and chemical stabilization, which is a powerful approach to overcome the aforementioned limitations.<sup>227–231</sup>

### 1.3. Sol-Gel method

To create a hybrid material, the *in-situ* formation of an inorganic network can be achieved by soft chemistry-based processes, from molecular, colloidal or polymeric precursors that are formed at low temperatures and pressures. The sol-gel method is one of the most used for the preparation of hybrid materials for its versatility and low processing temperature. It involves the preparation of a stable suspension of colloidal (nanometric) solid particles (*sol*) from metal alkoxides or inorganic salts, which is converted by the hydrolysis and polycondensation of the precursors into a three-dimensionally continuous solid network supporting a continuous liquid phase (*gel*). The gelation of the sol-gel system can be engendered by covalent links, entanglement of chains, van der Waals forces or hydrogen bonds, depending on the precursor's chemistry.<sup>232,233</sup> The precursors are well tailored molecules able to condensate into a multidimensional structure with completely different properties.<sup>234</sup> An example of well-known sol-gel process is based on silane precursors. Silane precursors have a generic structure of  $R_{4-n}Si-OX_n$ , with  $n$  ranging from 1 to 4 and where  $R$  is an organic group, and the  $Si-OX$  bond is able to hydrolyze into silanol groups ( $Si-OH$ ) which will then condensate into  $Si-O-Si$  bonds. The condensation degree reached by the molecules will depend on the amount of hydrolysable bonds, forming dimers, linear chains or three-dimensional networks. Figure 5.4 below shows a schematic example of the hydrolysis and condensation of a siloxane precursor bearing two hydrolysable groups ( $-OX$ ) on its structure. Since

the hydrolysis and condensation reactions occur simultaneously, competing with each other, the control of the condensation degree will depend on the careful control of different process parameters, such as temperature, pH, concentration of precursors and agitation.

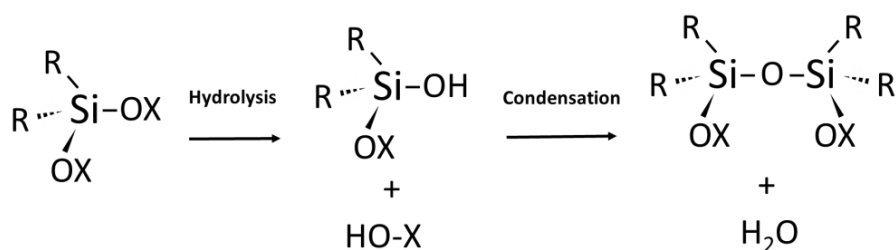


**Figure 5.4.** Representation of hydrolysis and condensation of a generic precursor molecule

In addition to the combination of the different properties of inorganic (hardness, chemical, thermal stability) and organic materials (toughness, elasticity, low density), specially tailored functional molecules (-R) can be introduced into the inorganic phase, allowing new possibilities to create multifunctional materials.

#### 1.4. Objectives of work

Fuel Cells still require significant lifetime enhancement and cost reductions if they are to compete with established technologies. The challenge in developing high performance membranes is achieving the required mechanical strength and durability especially at elevated temperatures.<sup>210</sup> The sol-gel method appears as a powerful approach to simultaneously improve the mechanical strength and chemical resistance of the polymer electrolyte. The process parameters are critical to define the properties and morphology of the final membrane, as are thermal post-treatments used for conditioning and optimizing the functional properties of the membranes (proton conductivity, membrane swelling and thermomechanical strength).<sup>211,218,221,235</sup> Therefore, it is of prime importance to qualify the impact of each step of fabrication on the physical and chemical properties of the hybrid membrane. However, this imposes difficulties on the access to the bulk of the polymer membrane for direct observation of the morphology and probing its chemical properties.

This chapter will be focused on the morphological and chemical characterization of alternative membranes based on sPEEK with two different SG precursors bearing active groups for chemical stabilization. Cryo-ultramicrotomed samples were prepared for co-localized AFM/Raman analyses, as well as complementary Electron Microscopy (STEM) and  $\mu$ -ATR-FTIR to study the process-structure-properties interplays of membranes fabrication.

## 2. Study of hybrid membranes based on dimethoxysilane (SHDi) precursors

We will first be interested on the study of a class of hybrid membranes based on (3-mercaptopropyl)-methyldimethoxysilane precursors, produced during the thesis of Isabel Zamanillo López. This work entitled “Co-localized AFM-Raman: A powerful tool to optimize the Sol-Gel chemistry of Hybrid Polymer Membranes for Fuel Cell” was submitted to the journal *Polymer* on September 2017 and will be presented here in an adapted format.

### 2.1. Materials used

Sulfonated poly(ether ether ketone) (sPEEK) commercial membranes purchased from Fumatech® (E-750) with an ionic exchange capacity (IEC) of 1.33 meq.g<sup>-1</sup>(milli molar SO<sub>3</sub>H per gram of polymer) were used as host membranes for the preparation of hybrid membranes by Sol-Gel (SG) chemistry.

SG precursor: (3-mercaptopropyl)-methyldimethoxysilane (SHDi) (Figure 5.5), was purchased from Sigma Aldrich. This precursor satisfies the requirements to obtain a reactive hybrid membrane, i.e., the hydrolysis of the alkoxy groups leads to the formation of alkoxy groups and their condensation to the formation of an inorganic SG phase (Figure 5.5) with a linear chemical structure bearing mercaptopropyl organofunctional groups. Therefore, the SG phase allows introducing into the host sPEEK membrane the antioxidant thiol group to improve the lifetime of the sPEEK phase.

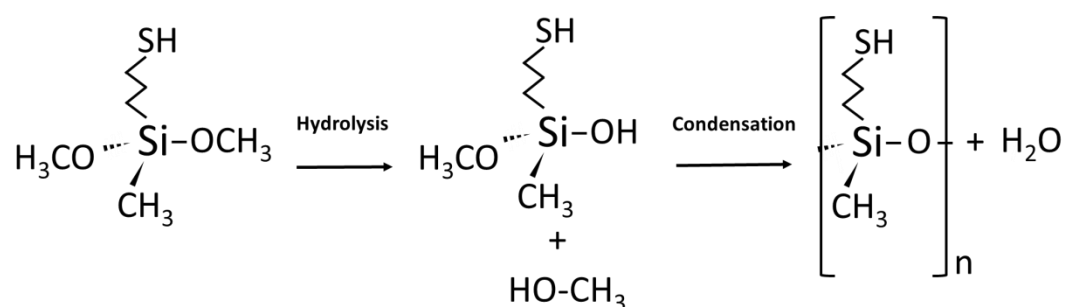


**Figure 5.5.** Sol-Gel phase formation by hydrolysis and condensation of SG precursor

The hybrid membranes collected and characterized after the different stages of fabrication are illustrated on Figure 5.6 and summarized in Table 5.1. The commercial sPEEK membrane is first nanostructured to be transformed in a host membrane (Step 1), then the SG precursors are impregnated inside the membrane (Step 2), the linear SG structure forming a 3D network phase into the host sPEEK membrane and finally two thermal treatments are done: one to improve the extent of condensation (Step 3 - Post-condensation/PC) and the other to improve the proton conductivity of the hybrid membrane (Step 4 – HydroThermal/HT). The details of the membranes fabrication process are presented in Annex 2.1. The SG phase uptake was determined by Thermogravimetric Analysis (TGA) according to Equation 5.3 taking into account the SiO<sub>2</sub> weight residue at 700°C and the weight of dry hybrid membrane at 200°C (a temperature corresponding to the complete water desorption). Details of the procedure are described in Annex 2.2. To characterize the inner morphology of the hybrid membranes, they were properly opened by cry-ultramicrotomy as described in Chapter 3.

$$\%SG = \frac{\frac{m \text{ SiO}_2 \text{ residue at } 700 \text{ }^\circ\text{C}}{M\text{SiO}_2} \times MSG}{m \text{ hybrid membrane at } 200 \text{ }^\circ\text{C} - \left( \frac{m \text{ SiO}_2 \text{ residue at } 700 \text{ }^\circ\text{C}}{M\text{SiO}_2} \times MSG \right)} \times 100\% \quad 5.3$$

Where  $M \text{ SiO}_2 = 60.08 \text{ g/mol}$  and  $MSG = \text{Molar Mass of the SG repeat unit of the condensed SG phase from SHDi precursor} = 134.32 \text{ g/mol}$ .

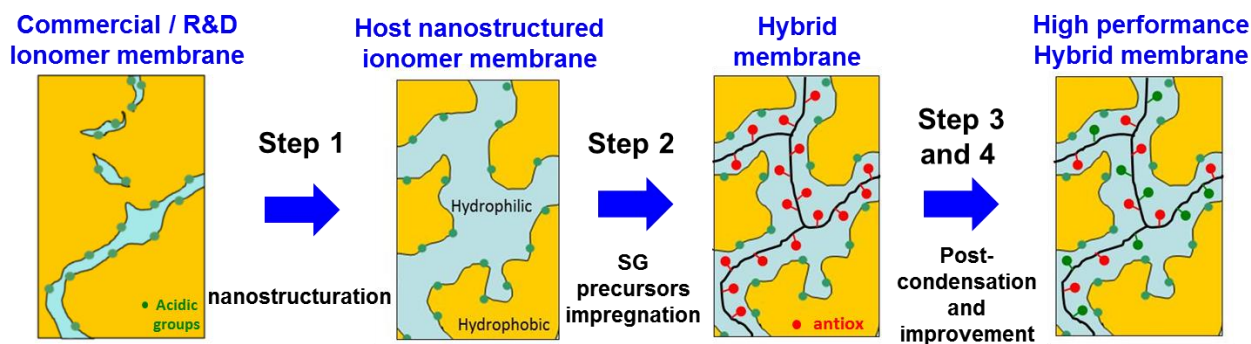


Figure 5.6. Schema of the different steps of fabrication of the hybrid membranes

Table 5.1 Sample and fabrication step

Sample	Step of fabrication
Hyb-I	Hybrid Membrane after impregnation/condensation
Hyb-PC	Post-Condensed Hybrid Membrane in 6.3 %RH at 74°C for 72 hours
Hyb-PC-HT	Post-Condensed and Hydrothermally Treated (80°C/72h) Hybrid Membrane

## 2.2. Micro-scale distribution of the SG along the membrane's cross-section

The micro-scale morphology of the final hybrid membrane (post-condensed and hydrothermally treated) Hyb-PC-HT was studied in order to get a first idea of the SG/sPEEK phases distribution. Figure 5.7 (a) shows an optical photography of the cryo-ultramicrotomed cross-section of the membrane taken with the optical microscope of the AFM. The cryo-ultramicrotomy procedure provided samples with very low roughness, and with minimum topography artifacts, despite some vertical lines caused by small scratches on the diamond knife.

The Young's modulus AFM image presented on Figure 5.7(b) corresponds to the first 10  $\mu\text{m}$  of the left side of the membrane's cross-section (illustrated by a red square on the optical image). First, one can see that at this scale the membrane's morphology is almost homogeneous (brown and yellow colors mixed) except for the first micrometers (between one and two micrometers) near the outer surface where the presence of a skin with a higher modulus is detected (yellow color).

The modulus of the host sPEEK and the SG phases taken separately were measured by AFM at 1.85 and 0.3 GPa respectively, which gives yellow (higher modulus) and brown (lower modulus) colors with the chosen color scale. Therefore, the presence of the higher modulus skin could be attributed either to a partial crosslinking of the SG phase (oxidation of the SH groups leading to SS covalent bonds due to their high  $\text{O}_2$  sensitivity) and therefore an increase of the Young modulus, or a depletion of the low modulus SG phase at the surface, potentially due to the washing step required after impregnation/condensation of the SG precursors to avoid the formation of a pure SG layer at the membrane's surfaces, or maybe due to the sPEEK host membrane morphology giving less space for the SG phase at the membrane's surface.



Colocalized Raman analysis was performed both on the membrane's bulk and skin to give additional information to interpret the AFM image. The complete Raman assignment of the bands relative to the sPEEK and the SG phase is shown in Annex 2.3. Figure 5.7(c) shows 2 spectra, one acquired on the membrane's skin (blue colors associated to the blue cross on the AFM image) and one acquired on the bulk (green color/green cross). Both spectra show 2 distinct peaks between 2700 and 3200 $\text{cm}^{-1}$ . The peak centered at  $\sim 3080\text{ cm}^{-1}$  is assigned to the contribution of the CH groups of the aromatic ring of the sPEEK. The peak centered at  $\sim 2900\text{ cm}^{-1}$  refers to the aliphatic  $-\text{CH}$  vibrations of the SG phase. From this assignment, we clearly observe that the SG uptake is not homogeneous inside the membrane. The spectra collected on the skin (blue) shows a much lower ratio of SG vs. sPEEK than the spectra of the bulk (green). The co-localized Raman information give us the proof that the higher modulus skin of the hybrid membrane observed by AFM corresponds to a depleted layer where the SG concentration is lower, either because the sPEEK host membrane accepts a lower SG uptake on its skin (due to higher crystallization ratio for example), or due to SG partial removal from the sPEEK host during the washing step.

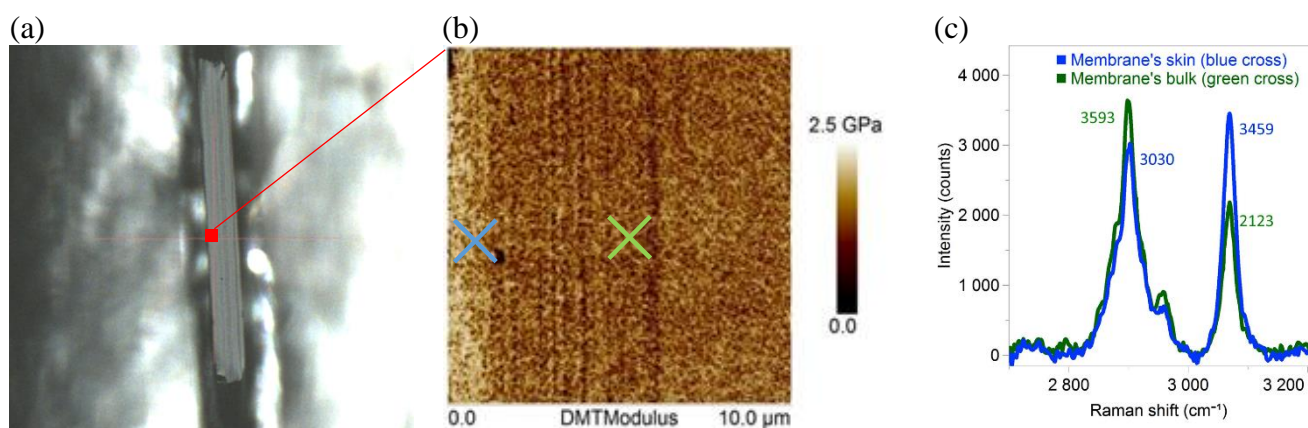


**Figure 5.7.** (a) Optical Image of the cryo-ultramicrotomed surface of sample Hyb-PC-HT; (b) AFM modulus image of the first 10 $\mu\text{m}$  of the cross-section from the left of the outer surface (corresponding to the red square drawn over (a)); (c) Co-localized Raman analysis of the membrane's skin (blue cross) and bulk (green cross).

The distribution of the SG phase inside the membrane was determined by the ratio between the area of the peak assigned to the SG (between 2785 and 3015 $\text{cm}^{-1}$ ) and the area of the peak assigned to the sPEEK contribution (between 3020 and 3120 $\text{cm}^{-1}$ ) after normalizing the Raman spectra relative to the sPEEK, as shown on Figure 5.8 (a). The SG phase distribution across the membrane is presented on Figure 5.8 (b). One can observe that the SG uptake at the outer surfaces of the membrane is lower than in the bulk (roughly divided by two) and that the depletion is limited to the first micrometers on both sides, confirming the AFM observation. The SG depleted skin's thickness was measured by AFM to be between 1 and 2 $\mu\text{m}$  and about 3 $\mu\text{m}$  by Raman analysis. This discrepancy arises from the lower lateral resolution of the Raman vs. AFM. As observed on Figure 5.8 (b), the SG content of the membrane's skins is equivalent on both sides, however the cross-section analysis revealed a slow decrease of the SG uptake when going from the left to the right of the cross-section. One can suspect a difference of accessibility of the SG precursors' for each side of the membrane, with for example temporary contact between one side of the membrane and the surface of the reactor during the impregnation step. A stronger agitation of the reactive medium should therefore be applied to improve that point.

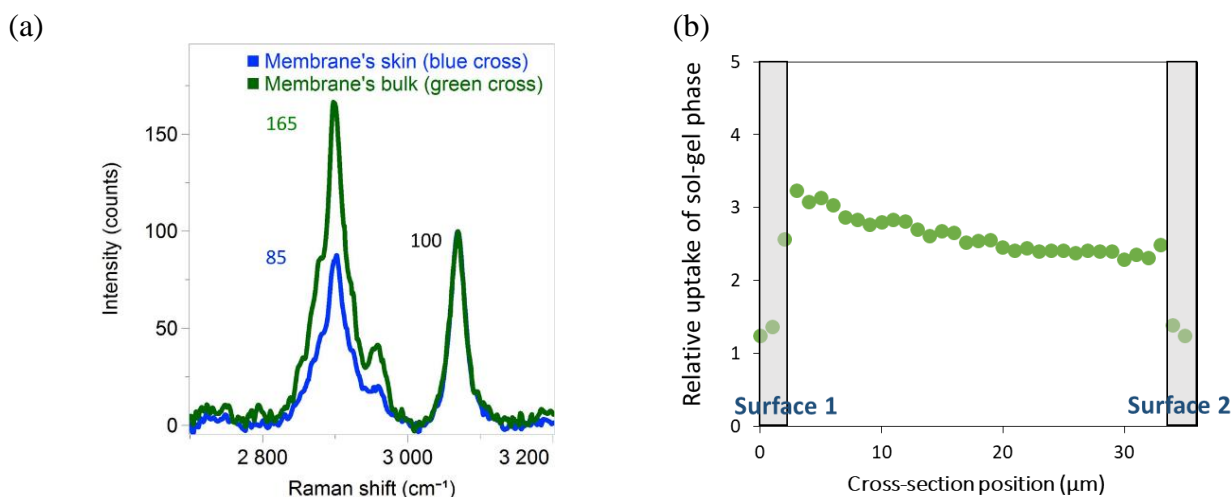


**Figure 5.8.** (a) Membrane's skin and bulk normalized spectra (normalization relative to the CH-band intensity of sPEEK at 3080 cm<sup>-1</sup>) (b) Relative SG phase uptake inside the Hyb-PC-HT membrane's cross-section (area ratio between the band between 2785 and 3015cm<sup>-1</sup> and the band between 3020 and 3120cm<sup>-1</sup>; membrane thickness: 35 μm)

### 2.3. Impact of the processing steps on the hybrid membrane's morphology

The nanoscale morphology of the hybrid membranes after each step of the fabrication process (Hyb-I, Hyb-PC and Hyb-PC-HT) was imaged by AFM and STEM, in order to study the impact of the different treatments (PC and HT) on the distribution of phases and their mechanical properties. The AFM height images of the 3 membranes presented on Figure 5.9 (a), (d) and (g) do not allow distinguishing clearly the phase's morphologies. The microstructure of the hybrid membranes is much better revealed by the different Young's modulus of each phase, with the modulus images shown on Figure 5.9 (b), (e) and (h). The calibration of the AFM tip allows the determination of the Young's Modulus of each phase, which gives 1.85 GPa for the sPEEK and a range from 0.5 to 1.0 GPa for the Sol-Gel depending on the membrane history (to be discussed further), which appears as brown dark domains of about 40-100 nm dispersed on the membrane structure. Complementary STEM images shown on Figure 5.9 (c), (f) and (i) were taken in Bright Field mode on the thin sections collected during the cryo-ultramicrotomy preparation of each sample (details given in Chapter 3). One can observe very contrasted images. Indeed, the sPEEK and the SG interact differently with the electron beam due to the presence of silicon atoms (higher atomic number) in the SG structure, thus a chemical contrast is observed without the need for sample staining. The SG phase appears darker in the image, since it scatters more electrons than the sPEEK phase. The STEM images confirm the distribution of the SG phase inside the membranes and shows that even inside the sPEEK phase there are nanometric domains of SG (dark spots) which are difficult to visualize on the AFM modulus image.

It should be noticed that the AFM Modulus image of Figure 5.9 (b) relative to the membrane analyzed after the impregnation/condensation step (Hyb-I), shows larger domains of SG phase when compared to the complementary STEM image on Figure 5.9 (c). This can be explained by the fact that the STEM analysis is done in transmission and the volume of the section is analyzed (about 100 nm thick). Therefore one can visualize the sPEEK phase inside the SG domains, which is not the case when probing the mechanical properties of the cross-section surface by AFM (only the first nm are analyzed). Bright round shapes can be seen on the STEM image of Figure 5.9 (c), which are related to damages on the section due to a long exposure of the sample to the electron beam (small holes through the section). Comparing the sample Hyb-I (before thermal PC treatment) with the post-

condensed sample Hyb-PC, both modulus (Figure 5.9 (b) and (e)) and STEM (Figure 5.9 (c) and (f)) images show an improvement of the phase separation, the size of the SG domains decreases with the smallest ones disappearing. This results evidence the impact of the condensation and densification of the SG phase after the post-condensation treatment at 74°C for 24h (condensation of residual Si-OH groups into Si-O-Si bonds). On the other hand, comparing Figure 5.9 (f) and (i) one can see that the hydrothermal treatment (HT) applied on sample Hyb-PC did not have a strong impact on the morphology (distribution of each phase remaining unaffected).

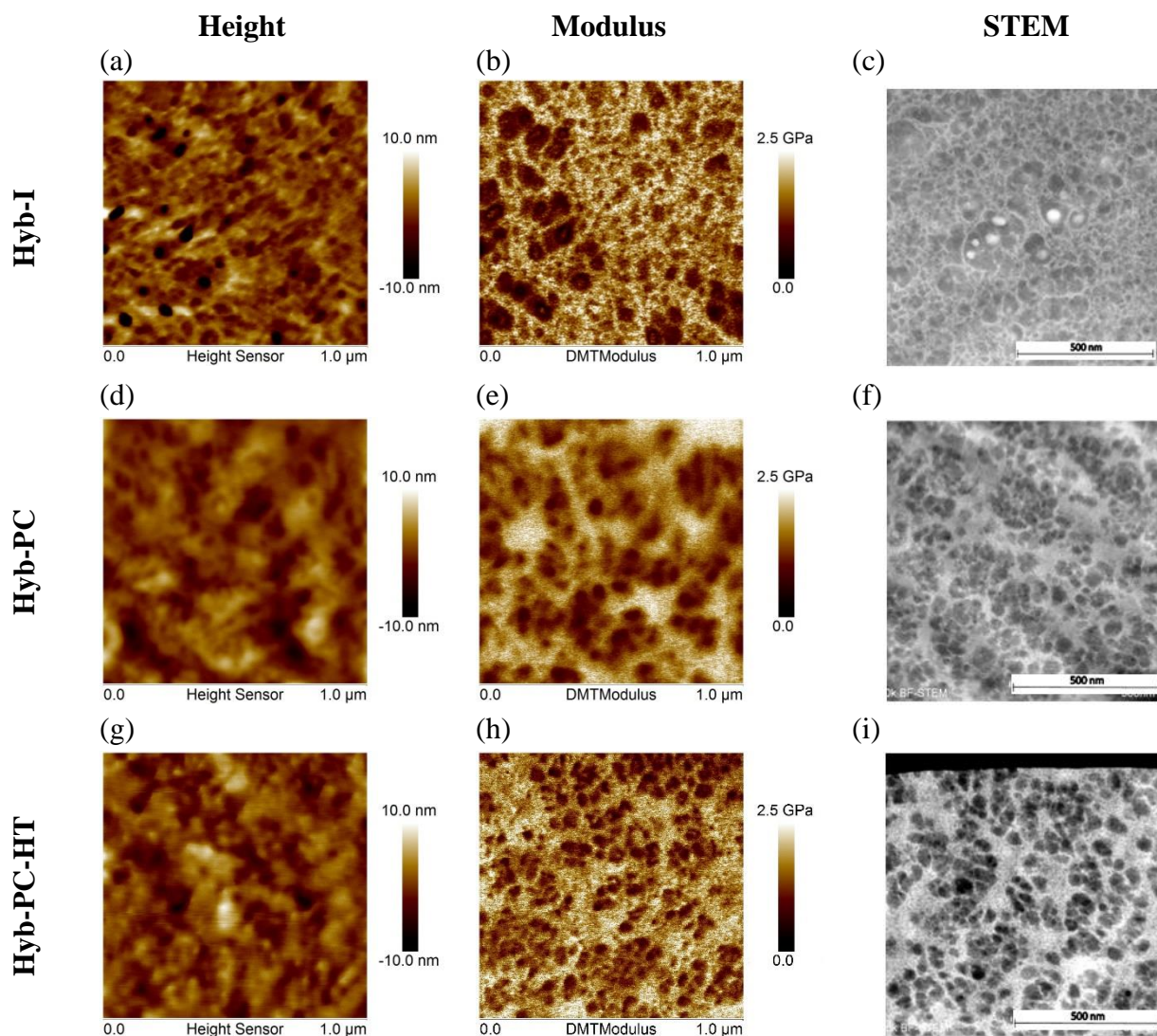


**Figure 5.9.** Hybrid membranes' structure at different stages of the fabrication process revealed by AFM and STEM. Sample Hyb-I: (a - AFM Height; b - AFM Modulus and c- STEM); Sample Hyb-PC: (d - AFM Height; e - AFM Modulus and f - STEM); and sample Hyb-PC-HT: (g - AFM Height; h - AFM Modulus and i - STEM).

#### 2.4. Impact of the processing steps on the hybrid membrane's nanomechanical properties and SG uptake

The evolution of the modulus of the Sol-Gel phase was recorded after each fabrication step (Table 5.2). Sample Hyb-I presented a SG phase with a modulus of about 0.5 GPa. However, we found a modulus of 0.3 GPa for a pure SG phase (analyzed alone and free of mechanical stresses). This discrepancy can originate from the contribution of the stiffer sPEEK phase, since the SG phase is surrounded by the sPEEK phase in hybrid membranes. After the post-condensation treatment, the SG phase in sample Hyb-PC presented a modulus of 0.7 GPa. Finally the hydrothermally treated sample Hyb-PC-HT had a SG phase with a modulus of 1.0 GPa. The clear increase of the Young modulus of the SG phase along with the successive treatments confirms the effects of these post treatments on improving the SG phase condensation and densification.

Thermogravimetric Analysis (TGA) was done in order to follow the hybrid membrane composition after each step, giving additional information. Details of the procedure used are shown in Annex 2.2. Results are shown on Table 5.2. Sample Hyb-I presents 240% of SG phase uptake after impregnation. One can observe that the SG phase uptake of the hybrid membrane is unchanged after the post condensation treatment (240% Hyb-PC) whereas it drops to 115% after the hydrothermal treatment (Hyb-PC-HT). Therefore we understand that the increase on the Young modulus of the SG phase from sample Hyb-I to Hyb-PC is related to the improvement of the SG condensation (no significant change of the SG uptake in the hybrid membrane), whereas the observed increase of modulus after the hydrothermal treatment (from 0.7 for Hyb-PC to 1.0 GPa for Hyb-PC-HT) could be related to the elution of oligomers (SG phase uptake drops from 240 to 115%) that were acting as plasticizers of the SG phase.

**Table 5.2** Modulus of each phase of the hybrid membranes (AFM measurement) and SG phase uptake (TGA)

Sample	sPEEK Modulus (GPa)	SG Modulus (GPa)	%SG
Hyb-I	1.85	0.5	240
Hyb-PC	1.85	0.7	240
Hyb-PC-HT	1.85	1.0	115

#### 2.5. Insights on the SG condensation process thanks to the water trapped at the ultramicrotomed surfaces

Images of freshly cryo-cut samples (cut at -120°C, imaged at RT) of hybrid membranes at different stages of the fabrication process were obtained by Optical Microscopy (OM), using the 100x long objective of the Raman Microscope, and are presented on Figure 5.10. These optical images can give the first insights on the mechanical stability behavior of the membranes during the cryo-ultramicrotomy process. The three samples endured the process with no cracks or tearing. However, despite the good quality of the cryo-cuts, dark stains were observed on the cross-section of Hyb-I (Figure 5.10 (a)) and Hyb-PC (Figure 5.10 (b)), but not on the cross-section of Hyb-PC-HT (Figure 5.10 (c)). We found that these stains were, caused by the presence of liquid water issued from the melting of ice crystals (deposited on the sample's surface during the cutting process) when the sample warms back to room temperature. To be noticed: the same samples ultramicrotomed at room temperature (RT) did not present such dark stains (confirming that it was due to the water condensation after the cryo process and not from the sample itself). However, due to the low glass transition temperature of the SG phase the quality of the RT-ultramicrotomed surface was very poor (surface deformation due to shearing forces).

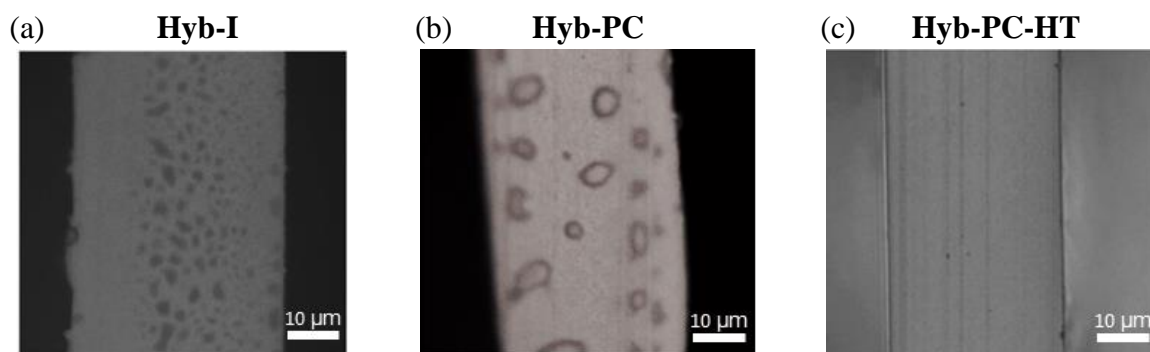


**Figure 5.10.** Optical microphotographs evidencing both the quality of the cryo-ultramicrotomed membranes cross-sections of hybrid membrane at each step of the fabrication process: (a) after impregnation/condensation (Hyb-I membrane); (b) after post-condensation step (Hyb-PC membrane) and (c) after hydrothermal treatment (Hyb-PC-HT membrane), and the presence of water droplets for (a) and (b).

At the time we cryo-ultramicrotomed these samples, it was not possible to avoid the formation of water droplets on the cutted surfaces. However this originally unwanted phenomenon turned out to reveal very important information about the condensation extent of the SG phase. AFM images (Figure 5.11) acquired with PeakForce QNM confirm the presence of liquid on the cryo-ultramicrotomed surface of the membrane Hyb-I and Hyb-PC. Figure 5.11 (a) to (d) relative to the Hyb-I membrane confirm the presence of droplets on the cross-section. Indeed, the droplets appear on the images as areas with lower Young's Modulus (dark brown) and higher Adhesion and Deformation (yellow/white) than the polymer matrix (yellow on the Modulus image and brown on Adhesion/Deformation). The post-condensed sample Hyb-PC opened surface on the other hand seems to have been locally swollen by water, with the affected zones having a less defined contour with, however, like for the droplets observed for Hyb-I membrane, a higher topography, lower modulus and higher adhesion than the matrix, as shown on Figure 5.11 (e) to (h). Finally, as already observed by optical microscopy (AFM results not shown), no water or surface modification induced by water diffusion was detected by AFM on the cryo-ultramicrotomed surface of the post condensed and hydrothermally treated membrane (Hyb-PC-HT).

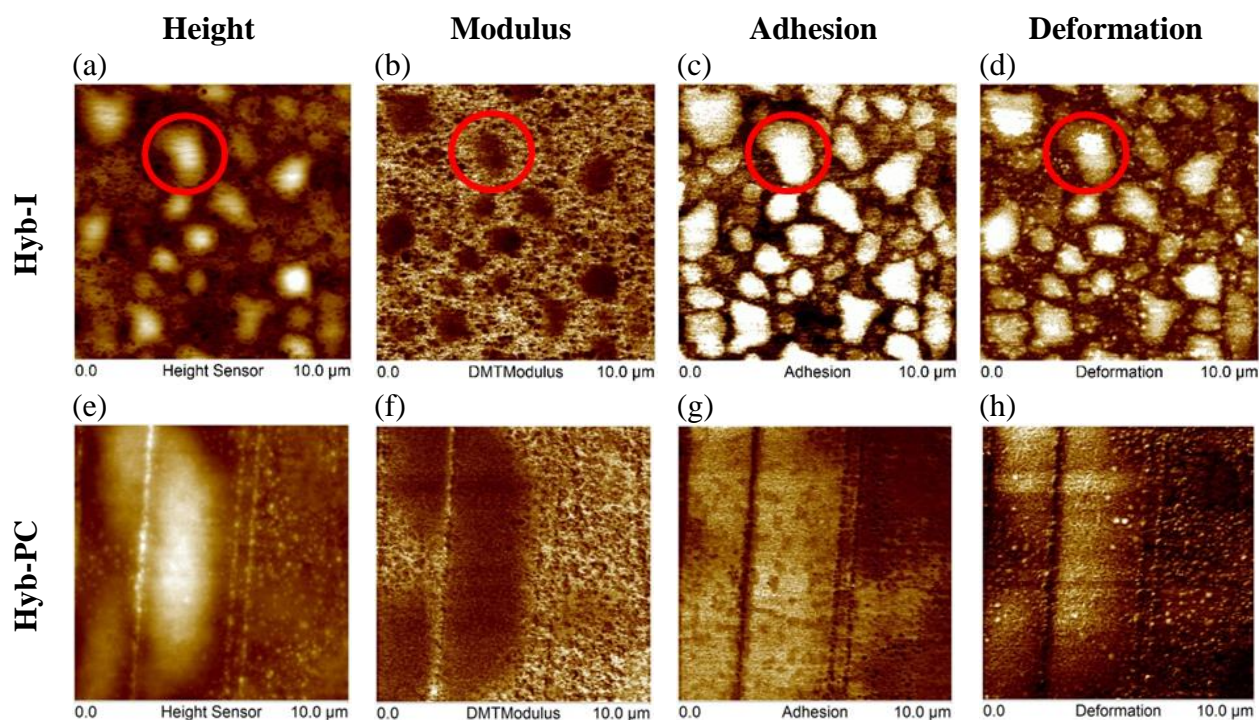


**Figure 5.11.** AFM images confirm the presence of water droplets on the cross-section of sample Hyb-I from (a) to (d); and a zone swollen by water on sample Hyb-PC from (e) to (h)

## 2.6. Morphological evolution over time

We have followed the evolution of the water droplets areas of Hyb-I membranes over time, expecting a fast drying of the absorbed water. Figure 5.12 presents the Height and Adhesion AFM images of sample Hyb-I chronologically taken up to 90 days after sample preparation. Instead of the expected drying of the water droplets, we observed the appearance of small objects inside the water droplets about 15 days after cryo-ultramicrotomy, which can be seen on the adhesion image of Figure 5.12(b) as small dark dots of low adhesion (red arrow) inside the water droplets (high adhesion areas). Figure 5.12 (c) presents the same area (red circle) analyzed 15 days later (30 days after cutting). The growth of the objects over time is evidenced by the increasing size of the dark dots inside the liquid zones, from 100 nm to 250 nm for the object followed here by the red arrow. Three months after cutting, it was noticed that the undefined objects observed on the cross-section of the Hyb-I membrane had evolved into well-defined crystals, always located inside the water droplets, as shown on Figure 5.12(d) (zoomed inset). It should be noticed that over the same length of time (after cutting) the post-condensed sample Hyb-PC presented no sign of any crystal growth inside the water swollen areas presented on Figure 5.11. In addition, pure sPEEK membrane did not show neither water droplets remaining at the surface of the cryo-ultramicrotomed membrane nor any objects growing subsequently at its surface.

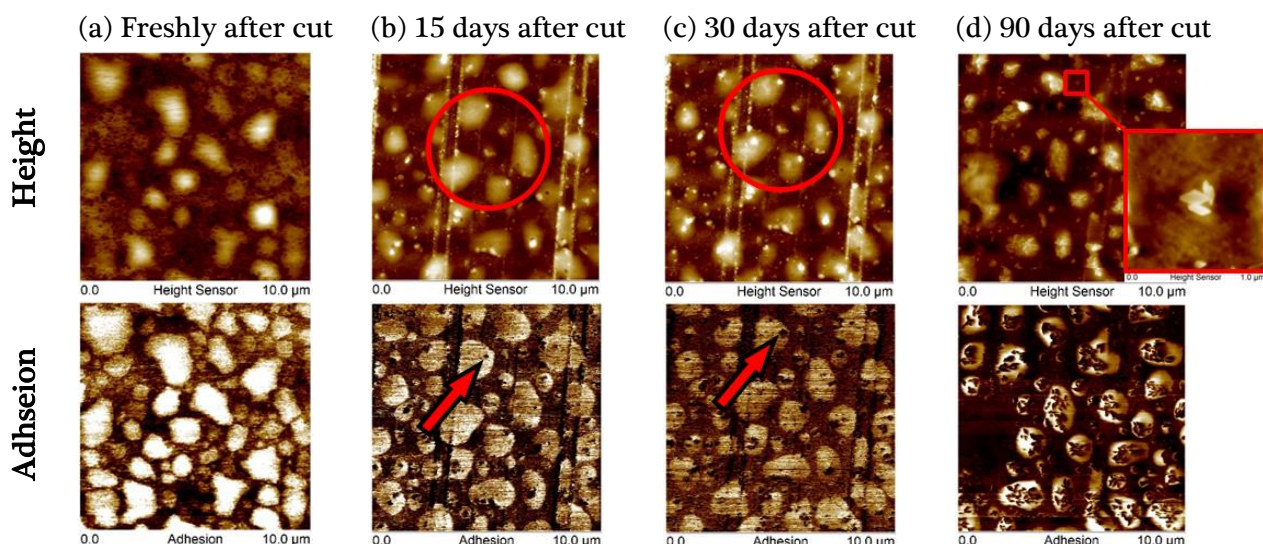


**Figure 5.12.** AFM Height and Adhesion images of the cryo-ultramicrotomed surface of Hyb-I membrane taken just after cutting (a), 15 days after cutting (b), 30 days after cutting (c) and 90 days after cutting (d). The red arrows highlight the growth of non-adhesive objects inside de water droplets. The zoomed inset on image (d) evidences the regular shape of the growing objects.

As the host sPEEK membrane does not contain any water soluble species (at room temperature) one can suspect that these crystallites originate from species migrating from the SG phase (before the post-condensation treatment). In order to confirm this hypothesis a chemical analysis of the observed growing objects was necessary.

## 2.7. Nano-manipulation and nanomechanical characterization of growing crystals

The nanodimensions of the growing objects made it impossible to do direct Raman analysis, since the confocal Raman with a volume resolution of about  $1\mu\text{m}^3$  could not discriminate the signal of nano-objects only present at the very surface of the sample. We had to pile them up in order to analyze their chemistry and to do so we used the AFM tip as a nano-broom to gather the particles from a large area of  $20\times 20\mu\text{m}^2$  (Figure 5.13(a)) to achieve a concentration compatible with the Raman analysis. This nano-manipulation successfully produced a pack of particles of about  $5\mu\text{m}$  in the x and y directions and more than 200 nm in the z direction, as shown by AFM on Figure 5.13 (b).

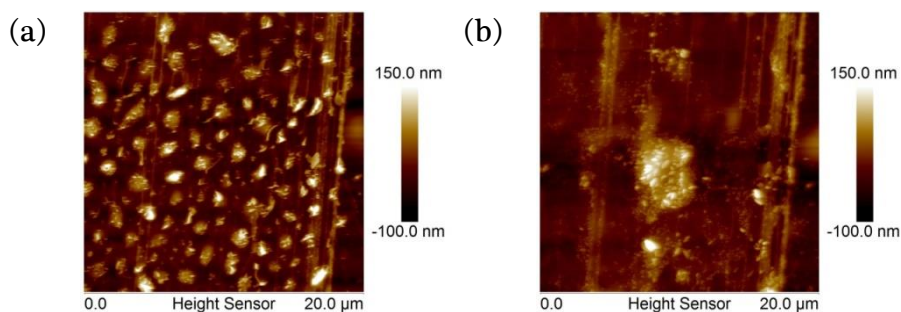


**Figure 5.13.** AFM Height images of the cryo-ultramicrotomed Hyb-I membrane before (a) and after nano-sweeping the growing objects (b).

The topography image presented on Figure 5.14(a) evidences the very regular rhombus shape of the particles inside the pack (red arrow), characteristic of crystalline materials. As a confirmation, the crystals were observed to have higher modulus (about 4.8 GPa) than the polymer matrix (1.85 GPa) as illustrated by the modulus image of Figure 5.14 (b). The crystals also present a lower adhesion (about 5nN) than the surrounding liquid (about 100 nN) and the polymer matrix (about 40 nN), and a lower deformation (about 3 nm) than the surrounding liquid (about 30 nm) and the polymer matrix (about 8 nm), as observed respectively on the adhesion and deformation images of Figure 5.14(c) and (d).

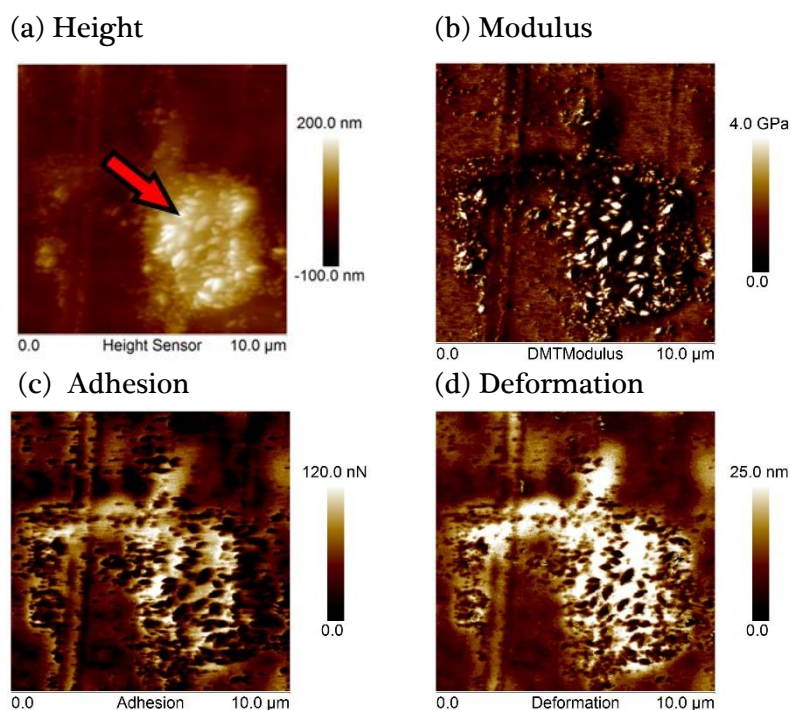


**Figure 5.14.** AFM images of the pack of particles (a) Topography, (b) Modulus, (c) Deformation and (d) Adhesion

### 2.7.1. Co-localized AFM/Raman analysis on the crystals

A 10x10  $\mu\text{m}$  Raman mapping (400 to 3250  $\text{cm}^{-1}$  range) co-localized with the AFM-scanned area of Figure 5.14 was recorded in order to do a chemical analysis of the crystals. The same Raman bands were observed everywhere on the mapping, however, the pack of particles showed a much stronger SG/sPEEK ratio (area of the peaks between 2785 and 3015  $\text{cm}^{-1}$  - assigned to the SG structure - divided by the area of the peak found between 3020 and 3120  $\text{cm}^{-1}$  - assigned to the sPEEK structure) than the surrounding membrane's cross-section surface. The co-localized Raman mapping of this ratio is shown on Figure 5.15(b). We therefore found that the crystals have the same chemical signature as the SG phase, and this result confirms the hypothesis that these crystals originate from the migration and crystallization of species chemically similar to the SG precursors.



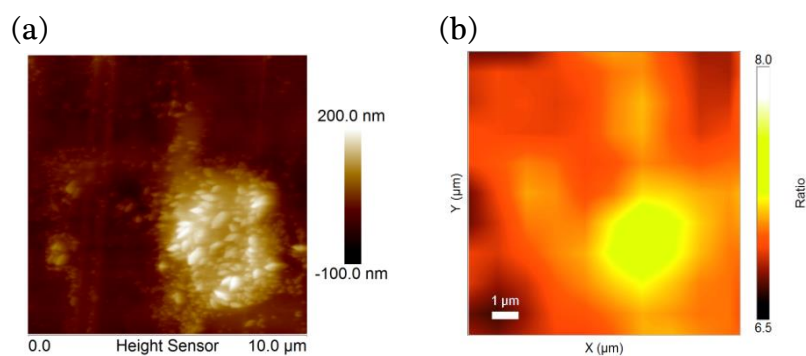


**Figure 5.15.** (a) Pack of growing objects piled-up by the AFM tip on sample Hyb-I (b) Raman mapping of the ratio SG/sPEEK

## 2.8. Morphological Analysis by Scanning Electron Microscopy (SEM)

SEM imaging is potentially more destructive for the samples, since the electron beam and the high vacuum can cause irreversible changes on the sample's surface. Therefore, it has been performed as the final step of characterization to provide additional morphological analysis with chemical contrast.

SEM images of samples Hyb-I and Hyb-PC were acquired in two different modes of operation collecting respectively the “Secondary Electrons” (SE) and the “Back-Scattered Electrons” (BSE). Details of each mode were given in Chapter 2, section 5.2.1. Figure 5.16 (a) shows the topography (SE image) of a pack of particles evidencing the regular rhombus shape of the crystals (red arrow). It has been observed that the liquid phase (already observed by optical and atomic force microscopies) evaporates under the heat of the electron beam, leaving empty spaces between crystals, as can be seen on the red-circled zone of Figure 5.16 (a). Heat buildup of the sample under the electron beam, generally considered as a drawback of the technique, finds here its usefulness. On the BSE image shown on Figure 5.16 (b) for the same sample area as Figure 5.16 (a), three different contrasts were observed, the membrane's surface (darker areas), the crystals (brighter areas) and an intermediate brightness area surrounding (not systematically) the crystals. This intermediate phase not always observed surrounding the crystals is attributed to the remaining liquid or to the surface where the liquid was before its evaporation under electron beam. As the SG precursor contains silicon atoms (higher atomic number: 14 for silicon versus 8 for oxygen and 6 for carbon) the brighter the area on the BSE image the more it contains silicon and therefore SG or SG precursors. This observation corroborates the Raman observation: the crystals originate from the migration and crystallization of species chemically similar to the SG precursors. It also evidences that the liquids zones are rich on non-condensed SG precursors/oligomers that reduce its evaporation rate.

The swollen zones (already observed by optical and atomic force microscopies) of sample Hyb-PC were also imaged by SEM and are shown on Figure 5.16 (c) SE mode and (d) BSE mode. Only a slight topographic contrast is observed on Figure 5.16 (c) with the swollen zones being smoother than the rest of the cross-section, however a higher contrast is evidenced by the BSE mode on Figure 5.16 (d). This contrast highlights the higher concentration of non-condensed SG precursors/oligomers inside the swollen zone. One can also see that the image's brightness is slightly higher at the center of the swollen zone than on its periphery, probably because of the progressive evaporation of the liquid droplet during the 90 days preceding the SEM observation.

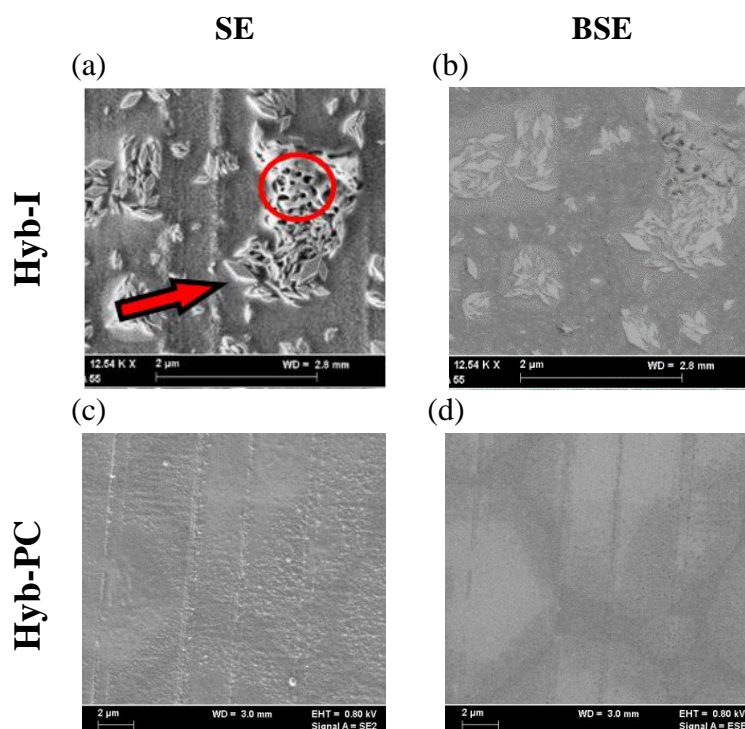


**Figure 5.16.** SEM images taken 90 days after cryo-ultramicrotomy of the cross-section of sample Hyb-I (a – SE mode; b – BSE mode) and of sample Hyb-PC (c – SE mode; d – BSE mode).

## 2.9. Discussion of the characterization of hybrid membranes based on SHDi precursor

The results presented above have demonstrated that by impregnating a SG precursor's solution into a commercial sPEEK membrane we obtained, after a multi-step process, hybrid membranes. We were also able to follow the evolution of the morphology, chemical composition and physical properties of the membranes after each of these steps by co-localized AFM-Raman and complementary SEM analysis as discussed below.

After the **impregnation/condensation step** (sample Hyb-I) the membrane presented a high SG phase uptake of 240% determined by TGA (Table 5.4), which evidences the effectiveness of the impregnation process. The phase distribution (between the SG and sPEEK phases) was analyzed by AFM and STEM (Figure 5.9(b) and (c)), making possible the measurement of the young modulus of each phase: 1.85 GPa for the sPEEK matrix and 0.5 GPa for the SG phase. The SG phase found in the hybrid membrane appears stiffer than the corresponding free (condensed out of the membrane) SG phase (0.5 versus 0.3 GPa). This observation can be explained by three factors: 1) a different condensation degree of the SG prepared outside and inside the membrane, 2) the confinement, as the SG is surrounded by the sPEEK matrix, and 3) the presence of nanodomains of sPEEK inside the SG phase, making this later stiffer. Indeed the high-resolution STEM images have shown that SG and sPEEK phases are not pure and contain nanodomains of the other phase.

The cross sections of Hyb-I and Hyb-PC membranes were found to have drops of liquid at their surface after cryo-ultramicrotomy, which were not the case for Hyb-PC-HT cross-sections, as illustrated by Figure 5.21. Understanding the origin of this observation gave us valuable additional information. We found that in a general manner it was the ice deposition on the cold freshly opened cross-section issued from cryo-ultramicrotomy, and its melting when warming up from cryo to ambient temperature, that was at the origin of the liquid found at the surface of the cross-sections (no such liquid was observed after Ultramicrotomy performed at room temperature). However, if

for the Hyb-PC-HT cross-sections this water evaporates fast from the cross-section, it was not the case for the Hyb-I and Hyb-PC cross-sections. The ulterior crystallization phenomenon observed in the liquid found at the surface of Hyb-I cross-sections (Figure 5.12) and the understanding that the observed crystals had a chemical composition similar to the SG phase thanks to a co-localized AFM-Raman analysis (Figure 5.15), led us to the diagnosis presented now. When the cryo-ultramicrotomed surfaced cross-section is taken out of the cryo-environment, the air humidity forms ice crystal on the opened surface, and as the temperature rises, ice melts. If no soluble species are present in the membrane, then the water evaporates leaving no traces. However if soluble species can diffuse to the water, the water is then trapped at the cross-section surface for a much longer time. Then, the trapped water allows for the swelling of the sPEEK phase, and the dissolution and migration of additional hydrophilic chemical species to the membrane surface. As sPEEK was re-acidified and rinsed before impregnation, we observed no trapped water for pure sPEEK membranes. The hydrophilic chemical species were then understood to come from the SG phase and to be uncondensed or partially-condensed SG precursors, as confirmed by the co-localized AFM-Raman analysis (Figure 5.15). After a certain time the concentration of these water-soluble species in the liquid phase reaches a critical point and we observed the nucleation of crystals in the liquid. The crystallization process lowers the concentration of the water species in the liquid, and after a certain time length the hybrid membrane stops releasing soluble species, i.e., diffusion takes place only in a limited swollen volume of the membrane below each water droplets, this limited volume not being an infinite reservoir. Then the evaporation of the water becomes possible. From these observations we understand that even though the hybrid membrane contains a high amount of SG, the condensation process was not yet completed after the impregnation step, making a post-condensation step mandatory.

As expected, the thermal treatment of **post-condensation** had no impact on the weight ratio of SG in the membrane (240% by TGA for Hyb-PC, identical to the one found for Hyb-I). However one can observe on the AFM and STEM images of Figure 5.9(c) and (f) a densification of the SG domains. The Young modulus of the SG phase increases from 0.5 to 0.7 GPa and the size of the SG domains decreases, with the smallest ones disappearing, as a consequence of the PC step. In addition, the effect of the water condensed at the membrane's surface after cryo-ultramicrotomy provides here again useful information. If the Hyb-PC membrane shows traces of droplets of condensed water on its cross-section (optical contrast observed on Figure 5.21, higher topography and adhesion observed on Figure 5.11), this sample shows no trace of crystal nucleation, contrarily to the non-treated Hyb-I membrane. We can therefore understand that water soluble species are still released from the SG phase (which explains the trapped water droplets at the surface of the membrane cross-section) but these species either reach a lower concentration on the water, or are not able to crystallize due to a higher molecular weight for example). Figure 5.16 (d) confirms the presence of non-condensed SG precursors/oligomers in the water-swollen areas of the membrane, which appear brighter in BSE mode (higher concentration of silicon containing species).

Finally after the last step (HT) which consists on a 72h **hydrothermal treatment** at 80°C, we observed no trace of condensed water at the membrane's surface after cryo-ultramicrotomy, which imply the absence of water soluble species in the hybrid membrane, which are essential to reduce the rate of evaporation of water). This demonstrates that these species still observed after the PC step were washed away during the HT step. This elution should be, at least in part, responsible for the SG uptake decreasing from 240% to 115% (TGA results Table 2). If the morphology of the SG phase distribution seems unmodified by the HT step (when comparing Hyb-PC and Hyb-PC-HT on Figure 5.9), an increase of the SG modulus was observed from 0.7 to 1.0 GPa (Table 2). This modulus increase can be related to the elution of species that previously acted as plasticizers of the SG phase. It should be noted that the elution of the water-soluble species from the SG phase is critical in order

to avoid their elution during the Fuel Cell operation, which could affect the device's efficiency. Further research must be performed to evaluate the performance of the membrane during FC operation.

## 2.10. Complementary $\mu$ -ATR-FTIR analysis – Feasibility and preliminary results

$\mu$ -ATR-FTIR is a complementary technique which allows following the evolution of the SG phase condensation or effects of oxidative degradation, by the identification of chemical signatures that are undetectable or have low intensity by Raman, such as the Si-O-Si bonds presented in the SG structure and carboxylic groups.

Figure 5.17 (a) shows an example of  $\mu$ -ATR-FTIR imaging of the intensity of the Si-O-Si band on the cross-section of membrane Hyb-I, superposed to the optical image. It is worth reminding that the  $\mu$ -ATR-FTIR analysis uses a germanium (Ge) crystal with a tip diameter of 350  $\mu\text{m}$ , which is about 10 times larger than our polymer membranes ( $\sim 30$   $\mu\text{m}$  thick). Therefore, to be cut using the cryo-ultramicrotome, the membranes were sandwiched between PP sheets (200  $\mu\text{m}$  each) for mechanical reinforcement as described on Chapter 3. The image shows basically three different zones: the PP backing appearing in dark blue, due to the absence of Si-O-Si bands on its structure, the edges of the membrane appearing in light blue and the bulk of the membrane with an essentially green color. Figure 5.17(b) shows the FTIR spectrum of sample Hyb-I (after impregnation/condensation) in the middle of membrane's cross-section. Among the bands of interest, the bands of Si-O-Si network ( $1080\text{ cm}^{-1}$ ) and the SG precursors ( $\text{CH}_2$ ,  $\text{CH}_3$  and  $\text{O-CH}_3$  near  $2900\text{ cm}^{-1}$ ) can give insights on the degree of condensation of the SG phase through the cross-section and after the post-condensation step, i.e., the decrease of  $-\text{CH}_3$  and  $-\text{O-CH}_3$  bands (the  $\text{CH}_2$  groups not participating on the hydrolysis/condensation) with the increase of the Si-O-Si band. In addition, this technique allows to detect any trace of material oxidation due to the strong absorption of the  $\text{C=O}$  ( $\sim 1700\text{ cm}^{-1}$ ) of the species formed.

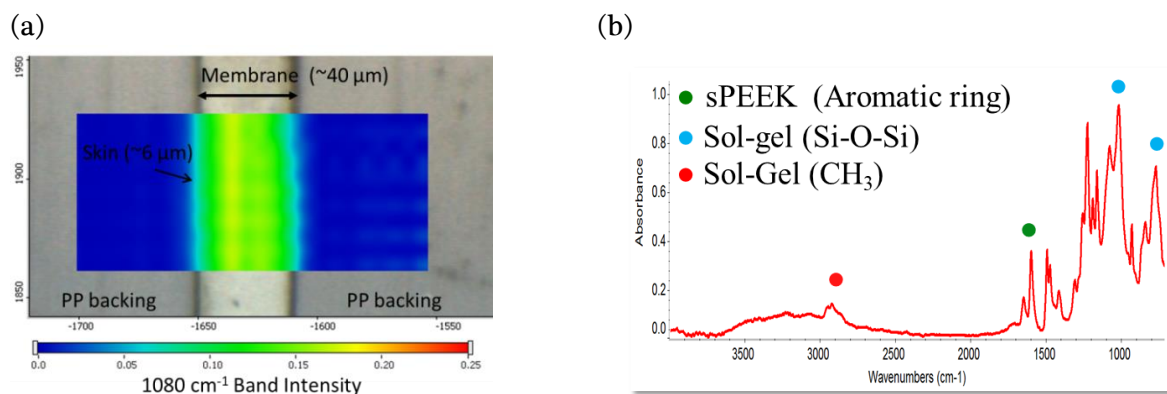


**Figure 5.17.** (a) Example of  $\mu$ -ATR-FTIR imaging of sample Hyb-I (30  $\mu\text{m}$ ) sandwiched between two PP sheets ( $\sim 200$   $\mu\text{m}$  each). The mapping is relative to the peak at  $1080\text{ cm}^{-1}$  (Si-O-Si), red meaning high intensity of the band and blue zero intensity. (b) FTIR spectrum of sample Hyb-I (after impregnation/condensation) in the middle of membrane's cross-section.

The lower intensity of the Si-O-Si bands at the edges (thickness of  $\sim 6$   $\mu\text{m}$ ) might be related to the depleted SG skin revealed by co-localized AFM/Raman analysis, or to a lower degree of condensation at the outer surface compared to the bulk. The former hypothesis was refuted by the analysis of the ratio between the area of the Si-O-Si band ( $1080\text{ cm}^{-1}$ ) relative to the area of the aliphatic CH groups ( $\sim 2900\text{ cm}^{-1}$ ), which presented a constant ratio ( $I_{1080}/I_{2900} \sim 2$ ) throughout the thickness of the membrane (not shown). Therefore, the low intensity of the Si-O-Si band seen at the

outer surface is related to the depleted SG skin. We remark that this zone appears much larger than in AFM/Raman analyses due to the lower resolution of the  $\mu$ -ATR-FTIR.

In order to evaluate the effectiveness of the post-condensation treatment on the hybrid membranes, sample Hyb-I and Hyb-PC were analyzed. To outline the chemical modification induced by this thermal treatment, spectra from the center of each membrane were acquired for comparison. Figure 5.18 show the subtraction of Hyb-I from Hyb-PC spectra. The spectral difference shows a decrease of the bands at 2900, 1460 and 1025  $\text{cm}^{-1}$ . These bands can be related to methanol ( $\text{CH}_3\text{-OH}$  – from OMNIC Nicolet Sampler Library), as shown on Figure 5.18 for comparison. Methanol elimination (by vaporization due to the thermal treatment applied) is a signature of an additional hydrolysis and condensation processes occurring during the post-condensation thermal treatment. One should expect an increase of the of Si-O-Si bonds ( $\sim 1080\text{cm}^{-1}$ ), but the methanol elimination masks the increase of Si-O-Si IR band. Nevertheless, we can conclude that the post-condensation treatment increases the SG condensation degree. Furthermore, no bands relative to the C=O groups ( $\sim 1700\text{ cm}^{-1}$ ) were identified in both samples, which is a sign that no oxidation of the material occurred during the fabrication process.

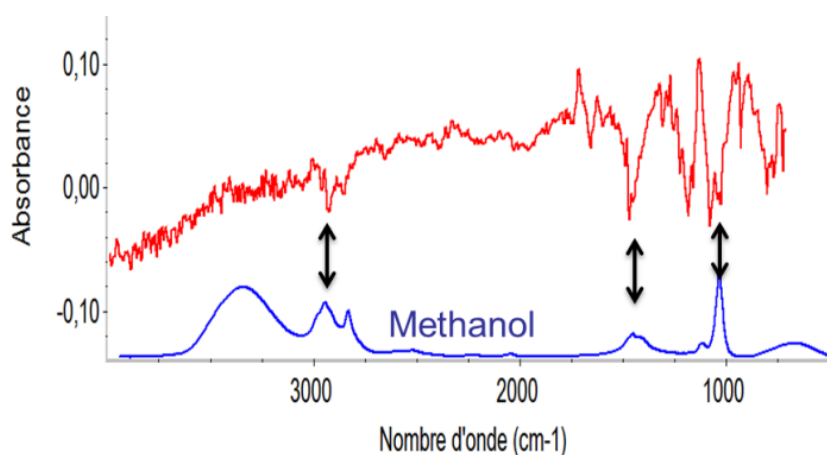


**Figure 5.18.** Subtraction of Hyb-I from Hyb-PC spectra (red line) showing the decrease of the bands at 2900, 1460 and 1025  $\text{cm}^{-1}$  and reference methanol spectrum (blue).

### 2.11. Conclusions of the Study of Hybrid membranes based on SHDi precursor

In this study, we were interested on the morphological evolution of the hybrid membranes with the different fabrication steps. We revealed the formation of a depleted skin layer (lower SG concentration) about one micrometer thick on both sides of the membrane whereas the SG phase concentration is almost constant through the rest of the membrane thickness. A stronger agitation of the reactive medium is proposed to obtain a constant SG concentration inside the membrane, however the origin of the depleted skins has still to be understood (heterogeneous SPEEK host membrane morphology, or impact of the washing step). Complementary optical microscopy, AFM, and SEM of the hybrid membranes cross-sections after cryo-ultramicrotomy have shown the diffusion of water-soluble species from the SG phase of Hyb-I and Hyb-PC membranes into the atmospheric water condensed at the cross-section surface. The crystallization of these species only observed for Hyb-I membrane, gave us an insight on their higher concentration and/or lower molecular weight before the PC step. We used the AFM tip to nano-manipulate the crystals to obtain a pile making possible a co-localized AFM-Raman analysis to find that the crystals were chemically similar to the SG precursors.

The quantitative nano-mechanical data collected by AFM revealed a densification of the SG phase through the fabrication process (with a Young modulus increasing from 0.5 to 0.7 from Hyb-I to Hyb-PC and then 1.0 GPa from Hyb-PC to Hyb-PC-HT). The first increase was attributed to an improved condensation of the SG phase and the second modulus increase to the elution of the water-soluble species (not fully condensed species originally acting as plasticizers) during the final hydrothermal treatment.

Finally,  $\mu$ -ATR-FTIR imaging on the cross-section of hybrid membranes was achieved, revealing methanol elimination during the post-condensation thermal treatment, which is a signature of the hydrolysis and condensation processes. Therefore, the post-condensation treatment increases the SG condensation degree.

### 3. Study of hybrid membranes based on trimethoxysilane (SHTriM) precursors

We will now present the study of another class of hybrid membranes based on a different kind of precursor issued from the Ph.D. thesis of Natacha Huynh in the laboratory SyMMES (Grenoble, France). In this part of the study, we will focus on the effect of the different chemistry and amount of the precursor on the membranes' morphologies. Furthermore, the complementarity between the morphological AFM analyses and Small Angle Neutron Scattering (SANS) data from N. Huynh's work will be presented.

#### 3.1. Materials used

The Sol-Gel (SG) precursor used in this part of the study was a (3-mercaptopropyl)-trimethoxysilane (SHTriM), purchased from Sigma Aldrich. Its chemical structure and the first step of hydrolysis and condensation are shown in Figure 5.19. Rather than linear chains, this precursor should allow the formation of tridimensional chemical structures within the sPEEK host membrane.

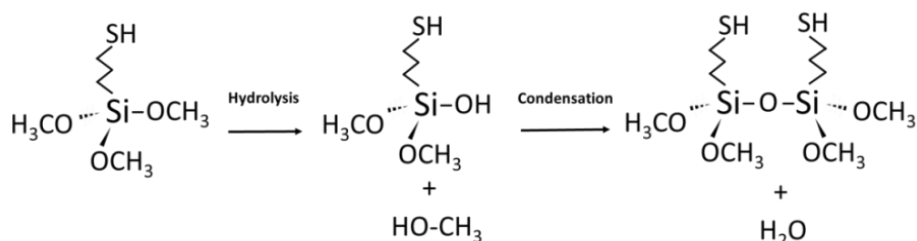


**Figure 5.19.** SHTriM sol-gel precursor structure before and after a first step of hydrolysis and condensation

The different hybrid membranes collected and characterized after the each stage of fabrication are summarized in Table 5.3. The details about the membranes fabrication process are presented in Annex 2.4. Membranes are denoted Hybrid\_X, with X being the theoretical targeted SG uptake after impregnation. Rather than using TGA like for the SHDi membranes, the actual SG uptake after impregnation (%SG<sub>w</sub>) was determined by weighting the membranes before and after hybridization, then using Equation 5.4, where  $m_{\text{sPEEK}}$  is the mass of the nanostructured host membrane and  $m_{\text{hyb}}$  is the mass of the hybrid membrane after impregnation. The different membranes were cut in cryo-ultramicrotomy as described on Chapter 3.

$$\%SG_w = \frac{m_{\text{hyb}} - m_{\text{sPEEK}}}{m_{\text{sPEEK}}} \quad 5.4$$

**Table 5.3** Samples, step of fabrication and SG content determined by weighting

Sample	Step of Fabrication	%SG <sub>w</sub>
Hybrid_10	Hybrid Membrane after impregnation/condensation	10.3
Hybrid_10_PC	Post-Condensed in 10 %RH at 80°C for 24 hours	10.5
Hybrid_10_PC_HT	Post-Condensed and Hydrothermally Treated (80°C/72h)	5.1
Hybrid_20_PC_HT		19.3
Hybrid_30_PC_HT		29.5

### 3.2. Effect of the thermal treatments on the membrane's morphology

The morphology of samples Hybrid\_10, Hybrid\_10\_PC and Hybrid\_10\_PC\_HT are shown on Figure 5.20, which is a “composition” of the three AFM modulus images, corresponding to the first 10  $\mu\text{m}$  of the left side of the membranes' cross-sections. The SHTriM based membranes' morphologies are almost homogeneous through their thicknesses, with the SG phase appearing as round shape domains of low modulus (brown color) distributed into the sPEEK matrix (yellow color), except for the first 500 nm near the outer surface, where the skin with less SG phase (fewer darker spots) is observed once again (surrounded by the red dashed lines). These SHTriM membranes seem to present non connected domains of SG, distributed in the sPEEK matrix. This comes from the fact that these membranes have a much lower SG uptake than the SHDi membranes presented before in this chapter (10 vs 240%SG).

Sample Hybrid\_10 and Hybrid\_10\_PC have the same SG uptake after impregnation (10.3 and 10.5% respectively) but sample Hybrid\_10\_PC\_HT presented only 5.1%. One could think that this loss of 50% of SG phase is an effect of the thermal treatment, however, the three samples are issued from three different batches and sample Hyb\_10\_PC\_HT already presented less SG from the first step of impregnation ( $\sim 7\%$ ), due to issues during impregnation (non-homogeneous distribution of the precursors in the impregnation bath). Thus, we can consider that there is a small elution effect (within the measurement incertitude) due to the hydrothermal treatment (HT), but not 50%. Visually, the morphology of sample Hybrid\_10\_PC\_HT seems to present smaller SG domains than Hybrid\_10 and Hybrid\_10\_PC. Indeed, the size of the SG domains was found to be  $85\pm 24$  nm,  $87\pm 27$  nm and  $78\pm 18$  nm respectively for Hybrid\_10, Hybrid\_10\_PC and Hybrid\_10\_PC\_HT. The difference in the size of the SG domains of sample Hybrid\_10\_PC\_HT seems to be mainly related to its smaller SG uptake, rather than an effect of the thermal treatments, which should be confirmed with the further studies of membranes with different SG uptakes.

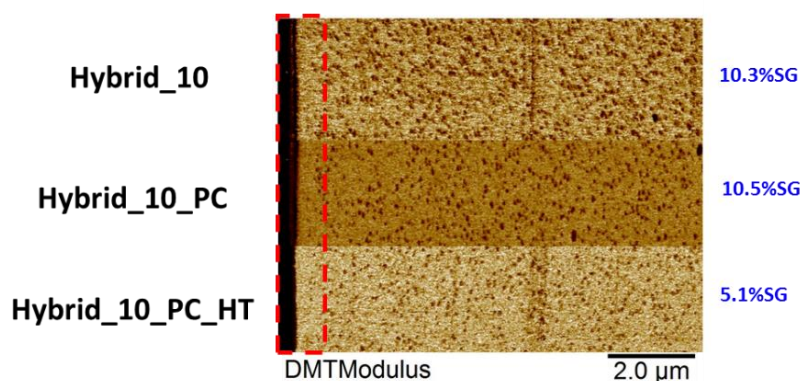


**Figure 5.20.** Composition of three AFM modulus images of the first 10  $\mu\text{m}$  of the left side of the membranes' cross-sections.

Differently from the SHDi hybrid membranes, no trapped water or elution of the water-soluble species from uncondensed or partially-condensed SG precursors was seen on the cryo-ultramicrotomed membranes' surfaces over time. Indeed, the developments on the fabrication based on the work with the SHDi hybrid membranes (optimization of treatment temperatures and times) guaranteed a better condensation of the SG phase, which decreases its hydrophilicity. Furthermore, the different chemistry of the precursors allows for the formation of three dimensional structures rather than linear chains, which hampers the mobility of low molecular weight oligomers or partially condensed precursors.



### 3.2.1. Effect of the SG uptake on the morphology

Figure 5.21 shows AFM modulus images ( $5 \times 5$  and  $1 \times 1 \mu\text{m}^2$ ) of samples Hybrid\_10\_PC\_HT, Hybrid\_20\_PC\_HT and Hybrid\_30\_PC\_HT, which present 5.1, 19.3 and 29.5% of SG uptake respectively. From the  $5 \times 5 \mu\text{m}^2$  images (Figure 5.21 (a) to (c)) the mean diameter of SG domains was measured:  $78 \pm 18$  nm,  $110 \pm 48$  nm and  $135 \pm 63$  nm, respectively for samples Hybrid\_10\_PC\_HT, Hybrid\_20\_PC\_HT and Hybrid\_30\_PC\_HT. As expected, the mean diameter of the SG phase increased with its increasing uptake. The mean SG phase diameter ( $D_{\text{AFM}}$ ), the sPEEK and SG modulus measured on the  $1 \times 1 \mu\text{m}^2$  images (Figure 5.21 (d) to (f)) are presented on Table 5.4. The SG phase appeared with about 0.89 GPa and the sPEEK phase with about 1.85 GPa. The lower difference between the SG phase modulus and the sPEEK modulus presented on sample Hybrid\_10\_PC\_HT (1 GPa and 1.85 GPa) can originate from the contribution of the stiffer sPEEK phase confining the smaller SG domains.

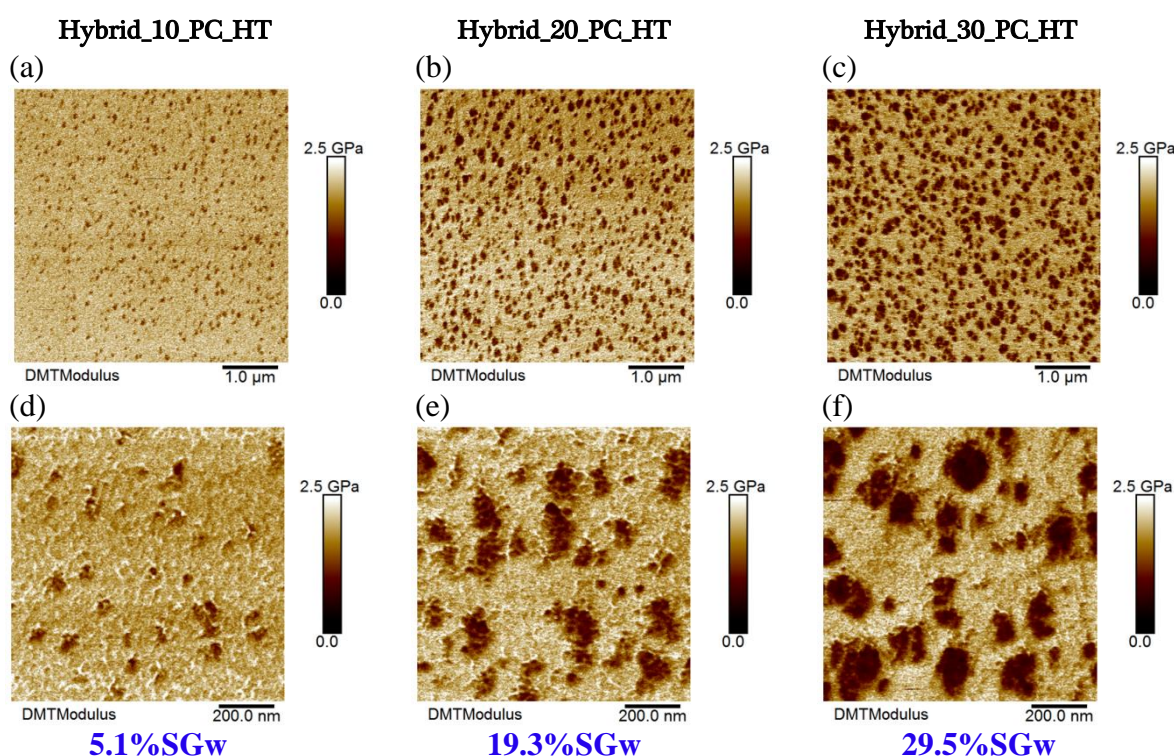


Figure 5.21. AFM modulus images of samples (a) Hybrid\_10\_PC\_HT (b) Hybrid\_20\_PC\_HT and (c) Hybrid\_30\_PC\_HT

Table 5.4 Modulus of each phase of the hybrid membranes (AFM) and percentage of SG phase (TGA)

Sample	%SGw	$D_{\text{AFM}}$ (nm)	sPEEK Modulus (GPa)	SG Modulus (GPa)
Hybrid_10_PC_HT	5.1	$78 \pm 18$	1.85	1.00
Hybrid_20_PC_HT	19.3	$110 \pm 48$	1.89	0.88
Hybrid_30_PC_HT	29.5	$135 \pm 63$	1.85	0.85

### 3.3. Complementarity between AFM and SANS

SANS experiments were done as part of the thesis of Natacha Huynh (SyMMES, Grenoble, France). AFM analyses of the membranes' morphology were of prime importance for the interpretation of the SANS data. To illustrate this, we will first present a brief introduction to the fundamentals of SANS and then the SANS results will be presented with a focus on the complementarity with AFM analysis.

#### 3.3.1. Fundamentals of Small Angle Neutron Scattering

A SANS experiment consists in irradiating a sample with a monochromatic neutron beam and measuring the scattered intensity as a function of the scattering vector  $q$  defined as  $\vec{q} = \vec{k}_f - \vec{k}_i$  where  $k_i = 2\pi/\lambda$  and  $q = \frac{4\pi}{\lambda} \sin\theta$  are the norm of the wave vector and the norm of the scattering vector respectively with  $2\theta$  the scattering angle (Figure 5.22).

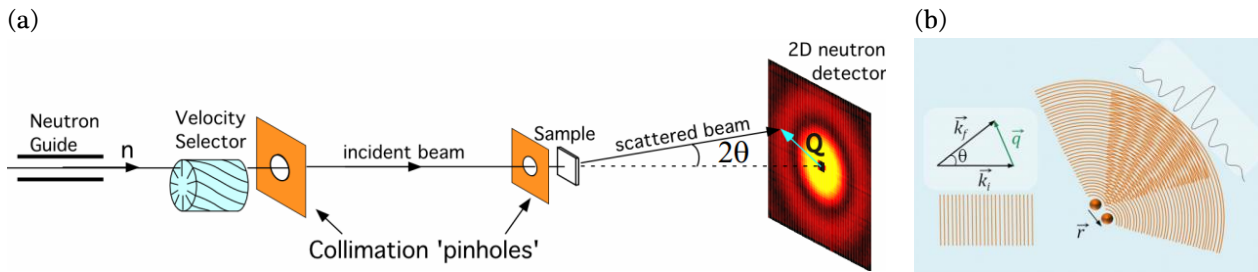


**Figure 5.22.** (a) Schematic setup of SANS experiments. (b) Principle of scattering and definition of scattering vector  $q$ . Interferences between two spherical waves scattered by two atoms separated by  $r$  in real space.<sup>236</sup>

SANS is a technique that enables to probe the 3-D structure of materials in the range of 1 to 300 nm and provides statistically averaged information on a sample volume of about  $1 \text{ mm}^3$ . For condensed and dispersed particles consisting of homogeneous isotropic scattering centers, this scattered intensity contains quantitative information on their size, volume, shape (form factor  $P(q)$ ), interaction (structure factor  $S(q)$ ). For  $n$  centrosymmetric particles of volume ( $V$ ), the intensity is given by Equation 5.5<sup>237</sup> :

$$I(Q) = \frac{n}{V} v^2 \Delta\rho^2 \cdot P(Q) \cdot S(Q) \quad 5.5$$

where  $\Delta\rho^2$  is the contrast factor ( $\Delta\rho$  is the difference of scattering length density between two phases).

The specific properties of neutrons (possibility of tuning the scattering intensity by using the isotopic substitution, e.g. contrast variation method) allow extracting selectively the structural information of one phase from a multiphase system that cannot be obtained by other experimental techniques (contrast matching principle). The principle of the contrast matching is shown on Figure 5.23. In a pure two phases system, when the scattering length density ( $\rho$ ) of one of the phase corresponds to the scattering length density value of the solvent ( $\rho_{\text{solvent}}$ ) then the scattering signal vanishes. As a consequence, the scattering signal of the other phase can be extracted. For more details, the interested reader can refer to the literature.<sup>237</sup>

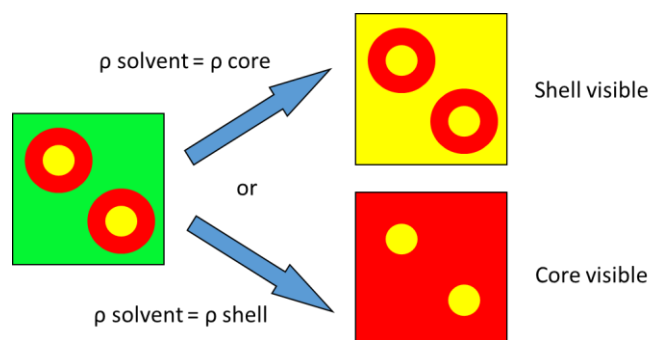


**Figure 5.23.** Contrast matching principle

### 3.3.2. SANS experiments

SANS measurements were carried out on the D22 spectrometer at the high flux reactor Institut Laue Langevin (ILL – Grenoble, France) on samples Hybrid\_20\_PC\_HT and Hybrid\_30\_PC\_HT. Figure 5.24 shows the SANS spectra of sample Hybrid\_20\_PC\_HT, equilibrated in two different ratio of the H<sub>2</sub>O-D<sub>2</sub>O mixture, allowing to match either the sPEEK phase signal or the sol-gel phase signal, *i.e.*, in a 50%-50% and 83.5%-16.5% H<sub>2</sub>O-D<sub>2</sub>O mixture respectively.

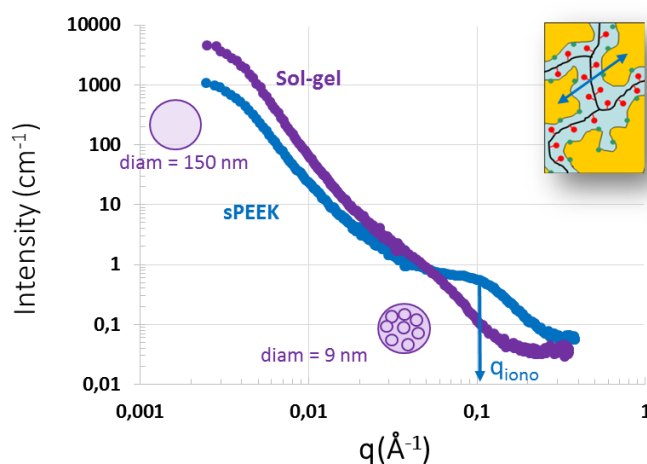


**Figure 5.24.** SANS spectra of the sPEEK (blue, obtained for 83.5%-16.5% H<sub>2</sub>O-D<sub>2</sub>O) and Sol-Gel (purple, obtained for 50%-50% H<sub>2</sub>O-D<sub>2</sub>O) phases obtained by selective phase matching with contrast variation method. The incoming wavelength was  $\lambda=6$  Å. Sample-detector distances of 2.8 m and 17.6 m were used to cover the extended range of momentum transfer  $0.003 < Q < 0.4$  Å<sup>-1</sup>, allowing to probe sizes and correlations in the range of 2-300 nm.

The SANS profile of the sPEEK phase (blue) displays a well-defined peak located at  $q \sim 0.1$  Å<sup>-1</sup>. This peak is called the ionomer peak, which is the fingerprint of a well-defined nano-segregated morphology, *i.e.*, the hydrophilic/hydrophobic nanophase separation of sPEEK, as described in the literature.<sup>219,238,239</sup> It can therefore be concluded that the sol-gel process has allowed preserving the nano-segregated morphology of the host sPEEK membrane. A similar result have was obtained on SAXS analyses of Nafion®/silicate hybrids by Wilkes *et al*<sup>240</sup>, which have shown that the original phase separated morphology of unfilled Nafion® persists despite the insertion of the sol-gel- derived silicon oxide phase.

The SANS profile of the sol-gel phase displays two main structural features (low- $q$  signal which seems to follow sphere scattering, *i.e.*, constant intensity scaling as  $q^0$ , followed by a Porod's

behavior (intensity decays as  $q^{-4}$ ), and a bump at intermediate scattering range) at two different length scales which indicates that the sol-gel phase is a hierarchically organized system.

At this stage, it is worth reminding that the structural information that can be obtained from SANS profiles analysis are model-dependent and that a scattering profile (Fourier space) can correspond to several structural organization in the real space. In order to select the appropriate fitting model, it is therefore of prime importance to cross-correlate, on the one hand, structural information to chemical information of the material and, on the other hand, to other morphological information extracted from direct observation with techniques such as AFM and SEM. The organization of the sol-gel phase into spherical-shaped domains of diameter ( $D_{SG-AFM}$ ) in the range of 80-150 nm has been evidenced by the direct AFM observations (Figure 5.21). These findings have allowed to orient the selection of an appropriate fitting model for SANS, the so-called Beaucage model.<sup>241</sup> It models hierarchically organized structures, in the present case, elementary spherical aggregates organized into larger spheres (see the sketches in Figure 5.24).

The characteristic dimensions measured from AFM and SANS analyses are presented on Table 5.5 for comparison. The mean diameter of the SG aggregates measured by SANS ( $D_{SG-SANS}$ ) for sample Hybrid\_20\_PC\_PT was 154 nm, in reasonable accordance with the average diameter measured with AFM ( $D_{SG-AFM} = 110 \pm 48$  nm). Sample Hybrid\_30\_PC\_PT presented  $D_{SG-SANS}$  of 173 nm and  $D_{SG-AFM}$  of  $135 \pm 63$  nm. It is important to notice that while the AFM analysis was done in the dry state, the SANS experiments were carried out in hydrated membranes. Although the SG phase is able to slightly swell in the presence of water, the differences observed between AFM and SANS results cannot be explained by the different swelling state. Indeed, SANS measurements done with dry membranes showed similar results (data not shown) as compared to the hydrated one. Therefore, the differences in large sphere diameter observed between the AFM and SANS measurements result mainly from the different averaging procedures of each analysis. The AFM probes a very local area of the sample, while SANS provides statistically averaged information on a sample volume of about  $1 \text{ mm}^3$ . Nevertheless, the measurements can be considered as in very good agreement, given the standard deviations of the AFM analyses and the fitting procedure used in SANS. Furthermore, both techniques evidence that the diameter of the SG aggregates increase with the increasing SG content, from a mean of 110 to 135 nm by AFM and from 154 to 173 nm by SANS, when going from 20 to 30% of SG.

Besides the diameter of the SG aggregates ( $D_{SG-SANS}$ ), SANS can also give two complementary information not probed by AFM. The first one is the size of the elementary SG particles ( $d_{SG-SANS}$ ). Both samples presented  $d_{SG-SANS}$  of  $\sim 9$  nm besides the increase on the aggregate diameter  $D_{SG-SANS}$  with the increasing SG uptake, which is an expected result. The second complementary information is the inter-domain distance between the hydrophobic and hydrophilic phases of the sPEEK ( $d_{iono}$ ). As the SANS experiments were carried out in hydrated membranes, the typical hydrophilic/hydrophobic nanophase separation can be revealed only by SANS. The inter-domain distances  $d_{iono}$  measured from the ionomer peaks  $q_{iono}$  (corresponding Bragg spacing  $d_{iono} = 2\pi/q_{iono}$ ) were 6.3 nm for sample Hybrid\_20\_PC\_HT and 4.8 nm for sample Hybrid\_30\_PC\_HT. This can be an indication that the presence of the SG phase limits the swelling of the host sPEEK membrane, probably because of the tridimensional SG's chemical structure.

**Table 5.5** AFM and SANS measurements of the hybrid membranes

Sample	%SG <sub>w</sub>	AFM	SANS		
		$D_{SG-AFM}$ (nm)	$D_{SG-SANS}$ (nm)	$d_{SG-SANS}$ (nm)	$d_{iono}$ (nm)
Hybrid_20_PC_HT	19.3	$110 \pm 48$	154	8.8	6.3
Hybrid_30_PC_HT	29.5	$135 \pm 63$	173	9.0	4.8

### 3.4. Co-localized AFM/Raman cross-section analysis

The distribution of the SG phase inside the membrane was determined with Raman by the ratio between the area of the peak assigned to the SG (between 2800 and 3015 $\text{cm}^{-1}$ ) and sPEEK contributions (between 3020 and 3130 $\text{cm}^{-1}$ ), hereby called  $R_{\text{SG/sPEEK}}$ . The SG phase distributions across the membranes are presented on Figure 5.25, with the respective AFM modulus images of the first 10  $\mu\text{m}$  of the left side of the cross-section of the samples Hybrid\_10\_PC\_HT, Hybrid\_20\_PC\_HT and Hybrid\_30\_PC\_HT. As expected, the amount of SG at the outer surfaces on both sides of the membranes is lower than in the bulk (depleted SG skin visualized by AFM). The SG depleted skin's thickness was measured by AFM to be of about 500 nm and about 1  $\mu\text{m}$  by Raman analysis, due to the lower lateral resolution of the Raman vs. AFM. The Raman ratio  $R_{\text{SG/sPEEK}}$  is rather constant in the bulk of the membranes, an improvement when compared to the cross-section analysis of the SHDi based membrane (Figure 5.8), maybe due to the use of a stronger agitation of the reactive medium. One can see that the average ratio value inside the membrane depends on the SG uptake, which is expected.

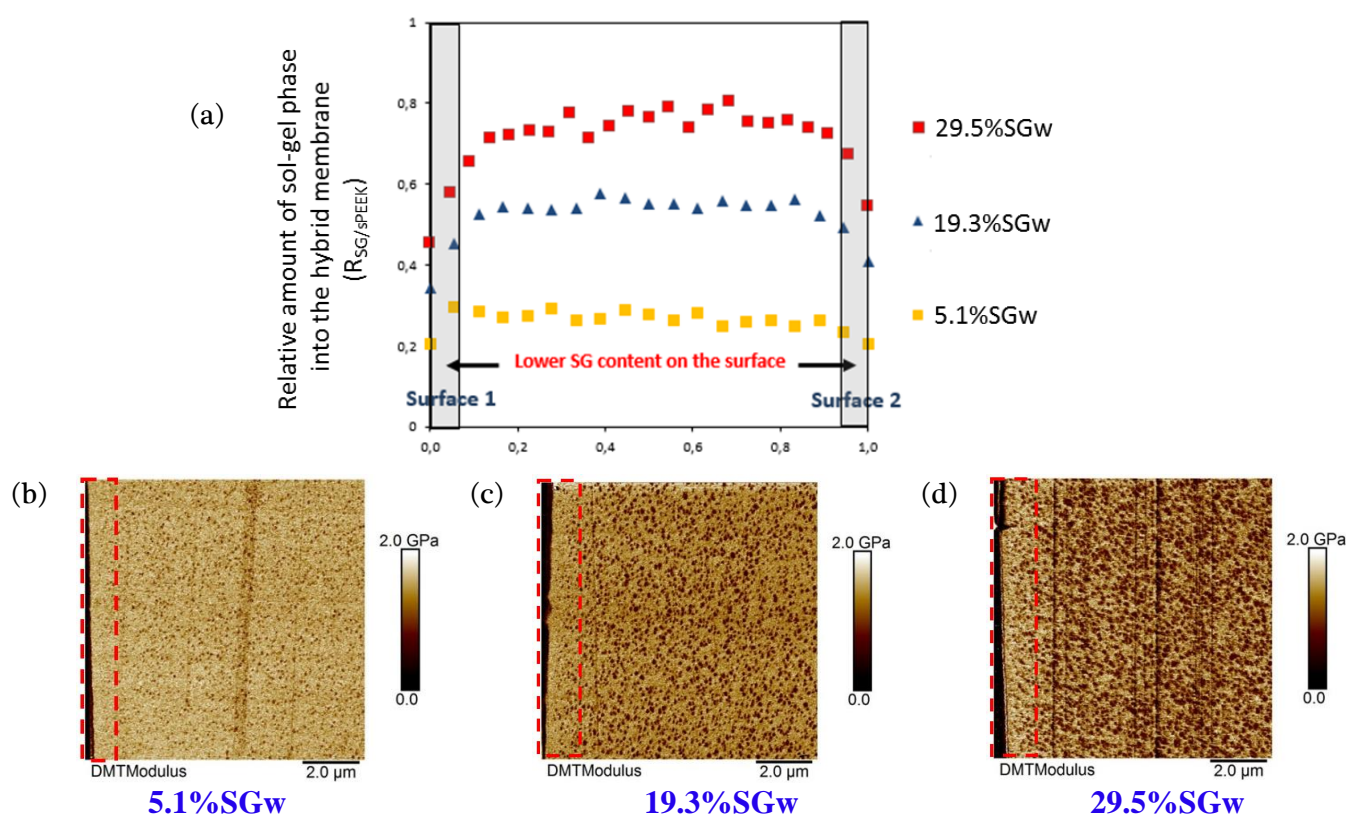


**Figure 5.25.** (a) Relative amount of SG phase through the membranes' cross-sections (area ratio between the bands between 2800 and 3020  $\text{cm}^{-1}$  and the band between 3020 and 3130 $\text{cm}^{-1}$ ) for samples presenting different SG uptakes. Membranes' thicknesses were normalized. (b) to (d) present AFM modulus images of the first 10  $\mu\text{m}$  of the left side of the membranes' cross-sections (a) Hybrid\_10\_PC\_HT (b) Hybrid\_20\_PC\_HT and (c) Hybrid\_30\_PC\_HT. Red dashed lines surround the SG depleted zone at the outer surface.

The average relative SG uptake measured by Raman ( $\bar{R}_{\text{SG/sPEEK}}$ ) taken from the mean values through the cross section of the membranes (not considering the edges) was traced following the SG uptake determined by weighting (%SGw) for membranes varying from 5 to 30%SGw (Figure 5.26). This data treatment is possible thanks to the homogeneous distribution of the SG phase inside the membrane, except for the edges, which was not the case for the SHDi membranes. The analysis of a

pure sPEEK membrane was also done to take into consideration any contribution from its structure on the CH range (2800 to 3015 $\text{cm}^{-1}$ ) and from the background noise, as illustrated on Figure 5.26 (a). As can be seen on the experimental data (green points) on Figure 5.26 (b),  $\bar{R}_{SG/sPEEK}$  increases linearly with the increasing %SGw. The corrected data by subtraction of the sPEEK mean value from the hybrid membranes ones give a linear correlation (red points) departing from zero, as expected for a membrane presenting no SG phase. Thus, it is possible to determine an equation to correlate  $\bar{R}_{SG/sPEEK}$  and %SGw (Equation 5.6) from experimental data.

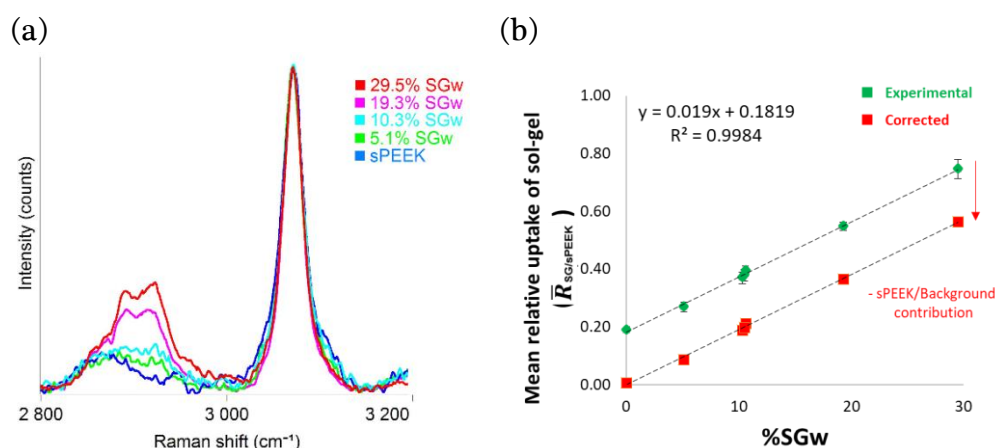


**Figure 5.26.** (a) Example of spectra on the cross-section of sPEEK and hybrid membranes with %SGw varying from 5 to 30% (b) Mean relative uptake of SG phase ( $\bar{R}_{SG/sPEEK}$ ) as a function of the SG uptake measured by weighting (%SGw). Experimental points are shown in green and the corrected points from the subtraction of the sPEEK spectra are shown in red.

$$\bar{R}_{SG/sPEEK} = 0.019 \times \%SG + 0.1819 \quad 5.6$$

Using Equation 5.6 we are able to calculate the SG uptake of membranes based on the SHTriM precursor using their Raman signature. Therefore, confocal Raman analysis by depth profiling of fresh made membranes can provide non-destructive rapid confirmation if the targeted SG uptake was attained, requiring no sample preparation. Furthermore, this Raman quantitative analysis will be of interest on further studies of ageing and degradation of the membranes after Fuel Cell operation allowing the quantification of any oxidation or loss of SG phase.

### 3.5. Conclusions of the Study of Hybrid Membranes based on SHTriM precursors

The hybrid membranes based on SHTriM precursors were studied by following the morphological evolution with the different elaboration steps and with the increasing SG phase uptake. Differently from the SHDi hybrid membranes, no trapped water or elution of the water-soluble species from uncondensed or partially-condensed SG precursors was seen on the cryo-ultramicrotomed membranes' surfaces over time, mostly due to the different chemistry of the precursors that allow the formation of tridimensional structures instead of linear chains and the optimization of the membrane fabrication procedure after the study of the SHDi membranes.

AFM analysis of the cryo-ultramicrotomed membranes revealed the morphology of the membranes on their cross-sections, with the presence of the depleted SG skin at the outer surface and a good distribution of the SG in the bulk. It is important to notice that these membranes were not rinsed after the impregnation procedure, and nevertheless, the depleted SG skin is present. Apparently, simply taking off the membrane from the precursors/water/ethanol mixture solution is already sufficient to prevent the formation of a SG coat at the outer surface of the membrane making not necessary the rinsing step. One can see that the size of the depleted zones of the samples at each step of fabrication is mainly constant, which could be an indication that this skin is not produced by the process, but is rather related to the sPEEK morphology. The depletion of SG at the outer surfaces therefore should come from the host sPEEK membranes' morphology, which accommodates less SG phase at the membrane's outer surface. A higher crystallinity index of the sPEEK near the outer surface could explain the lack of free volume for the SG phase. Therefore, we propose as future work the evaluation of the local crystallinity of the sPEEK phase by Raman on these SG depleted zones and in the bulk. It has been shown in literature that Raman carbonyl band (C=O) of PEEK depends on crystallinity, the C=O stretching mode observed at  $1651\text{ cm}^{-1}$  in amorphous PEEK and at  $1644\text{ cm}^{-1}$  in crystalline PEEK.<sup>242,243</sup> Ellis *et al*<sup>244</sup> have also shown that the band at  $1596\text{ cm}^{-1}$  increases relative to that at  $1607\text{ cm}^{-1}$  (both related to C=C stretch) with increasing crystallinity. Other Raman spectroscopy studies and reviews available can help answering this question.<sup>102,245</sup>

AFM analysis also revealed the growth of the SG domains diameter with the increasing SG uptake, from  $78\pm 48\text{ nm}$  for a membrane with 5.1% of SG uptake up to  $135\pm 63\text{ nm}$  for 29.5% SG uptake. The sizes of the SG domains were mainly related the SG uptake and not affected by the thermal treatments. AFM also allowed for the quantitative nano-mechanical analysis of the components: the sPEEK phase appearing with a modulus of about 1.8 GPa and the SHTriM based SG phase with a modulus of about 0.9 GPa. The SG domains appear as isolated clusters and do not seem to have a link between them at the studied scale. However, it is possible that there are silicon oxide bridges between them. It is worth remembering that the SG precursors impregnate into a network of channels in the membrane before hydrolysis and condensation. Mauritz *et al*<sup>229,231,240</sup> have studied hybrid membranes based on Nafion<sup>®</sup> and the sol-gel process, in which they concluded that although the inorganic phase was to be found predominantly as isolated clusters, some of these were linked by silicon oxide bridges, presumed to be formed in the later stages of reaction. In order to address this hypothesis, we have prepared samples for 3D reconstruction by FIB/SEM serial sections. The experiments are currently under work in collaboration with the laboratory LEMMA (Grenoble, France).

The round shape of the SG domains observed by AFM directed the choice of the fitting model used for the SANS analysis. SANS data showed that the SG phase presents a hierarchically organized system, composed of elementary particles ( $d_{\text{SG-SANS}} \sim 9\text{ nm}$ ) which aggregate into the round shape domains seen by AFM. SANS could give more complementary information: the inter-domain distance between the hydrophobic and hydrophilic phases of sPEEK ( $d_{\text{iono}}$ ). It has been shown that

despite the presence of SG phase, the hybrid membrane conserves the hydrophobic/hydrophilic nanophase separation of the host sPEEK. However, the increasing SG uptake limits the swelling of the host sPEEK membrane ( $d_{\text{ino}}$  decreasing from 6.3 to 4.8 nm when going from 19.3 to 29.5%SGw), which can be related to the possible links between the clusters, forming a 3D network SG phase. The combination of AFM and SANS techniques was shown to give valuable information for the comprehension of the hybrid membranes' structures.

The chemical homogeneity of the membranes on their cross-section was evaluated by co-localized AFM/Raman analysis, and it was found to be improved when compared to the previously studied SHDi based membrane, due to an optimization of the impregnation conditions. A linear correlation between the Raman signal and the SG uptake was observed, allowing the determination of an equation to quantify the SG uptake directly from Raman data. These experiments confirm that a quantitative Raman analysis of the SG content of the membranes can be done, even for very low SG uptakes down to <5%. Finally, it provides a new tool for quantitative analysis of SG uptake for further studies of ageing and degradation of the membranes after Fuel Cell operation.

#### 4. Summary of Conclusions of Chapter 5

In this chapter we presented the study of the bulk morphology of alternative hybrid membranes for Fuel Cell based on a sPEEK host membrane and two different Sol-Gel precursors. We need to stress that the fine characterization of the membranes was only possible thanks to the association of cryo-ultramicrotomy (providing very flat cross-sections without topographic artifact, parallel to the Raman objective, and also ultrathin sections for STEM) with co-localized AFM-Raman and complementary STEM, SEM, SANS and  $\mu$ -ATR-FTIR analyses. Each of the complementary techniques provided important information for the comprehension of the hybrid membranes' characteristics and optimization of their fabrication process. Below are presented a summary of the conclusions of this chapter sorted out for each technique:

<b>AFM:</b>	<ul style="list-style-type: none"> <li>• Direct observation of the bulk hybrid membranes morphologies was achieved thanks to the mechanical contrast of the phases (Modulus, Adhesion, Deformation)</li> <li>• Modulus images revealed a high modulus skin at the outer surface</li> <li>• Nanomechanical analysis revealed the evolution of the SG phase (SHDi) with the fabrication steps and the adhesion images revealed the elution and crystallization of water-soluble species from membranes at the early stages of fabrication</li> <li>• Nano-manipulation of crystals allowed for co-localized AFM/Raman analysis</li> <li>• Direct observation of the shape of the SG domains (SHTriM) guided the choice of the fitting model for SANS</li> </ul>
-------------	---



<b>Raman:</b>	<ul style="list-style-type: none"> <li>• Punctual chemical analysis on skin and bulk allowed the conclusion that the high modulus skin observed by AFM is a depleted SG zone</li> <li>• The SG distribution was evaluated at the cross-section, revealing a slow decrease of SG content from one side to the other for SHDi, which was improved for SHTriM</li> <li>• Co-localized chemical information with AFM revealed the nature of the eluted species and crystals, i.e., partially condensed molecules of the precursor</li> <li>• Quantitative chemical analysis was done to correlate Raman response to %SG uptake, which will allow the evaluation of SG uptake changes in aged hybrids</li> </ul>
<b>STEM:</b>	<ul style="list-style-type: none"> <li>• Direct observation of the bulk morphology with high resolution (&lt;1 nm) by the chemical contrast revealed sPEEK phase even inside the SG domains</li> <li>• The technique opens the possibility of doing high resolution elemental analysis by EDS/EELS</li> </ul>
<b>SEM:</b>	<ul style="list-style-type: none"> <li>• Direct observation of the bulk hybrid membranes morphologies using topography and chemical contrast (SE/BSE) confirmed the presence of non-condensed SG precursors/oligomers in the water-swollen areas of the membranes in the early stages of fabrication</li> </ul>
<b><math>\mu</math>-ATR-FTIR:</b>	<ul style="list-style-type: none"> <li>• Chemical analysis at the bulk of the membranes allowed revealing methanol elimination as a signature of an additional hydrolysis and condensation processes occurring during the post-condensation thermal treatment</li> </ul>
<b>SANS:</b>	<ul style="list-style-type: none"> <li>• Contrast matching allowed extracting structural information selectively of each phase, which cannot be obtained by other experimental techniques</li> <li>• Spectra indicated that the SHTriM SG phase is hierarchically organized, i.e., elementary particles forming the round shape aggregates seen by AFM</li> <li>• The hydrophobic/hydrophilic nanophase separation of sPEEK was revealed even at the presence of SG by the presence of the ionomer peak</li> <li>• The inter-domain distance <math>d_{\text{iono}}</math> decreases with the increasing SG uptake due to the SG 3D structure that limits the sPEEK swelling</li> </ul>

We would like to stress out that the diffusion of water-soluble species into atmospheric water condensed at the cross-section surface of membranes have also been seen in a different system based on Polyethylene Terephthalate (PET) membranes (presented in Annex 2.5). However, due to the highly porous nature of the PET membranes, we were not capable of performing the nano-manipulation of the observed crystals for proper chemical assignment and identification. Nevertheless, the phenomenon is another evidence that hydrophilic species can migrate from the bulk of polymer materials to the water trapped at the cryo-ultramicrotomed surface.

Our next objective it to use the same characterization strategy to quantify the physical and chemical modifications induced into SG/sPEEK hybrid membranes during fuel cell operation in order to understand the structure/functional properties/durability relationship of these hybrid

systems. Indeed, in a general manner, in-depth studies of ageing under realistic operation conditions are still needed to enable further materials improvements toward the targeted performances.

## 5. Résumé des Conclusions du Chapitre 5 en Français

Dans ce chapitre, nous avons présenté l'étude de la morphologie de membranes hybrides alternatives pour pile à combustible à base d'une membrane hôte sPEEK et de deux précurseurs Sol-Gel différents. Nous devons souligner que l'inspection fine des membranes n'a été possible que grâce à l'association de la cryo-ultramicrotomie (fournissant des sections transversales très plates sans artifact topographique, parallèlement à l'objectif Raman, et des sections ultra-fines pour STEM) avec une co-localisation AFM-Raman et analyses complémentaires comme STEM, SEM, SANS et  $\mu$ -ATR-FTIR. Chacune des techniques complémentaires a fourni des informations importantes pour la compréhension des caractéristiques des membranes hybrides et l'optimisation de leur processus de fabrication. Ci-dessous nous présentons un résumé des conclusions de ce chapitre pour chaque technique:

<b>AFM:</b>	<ul style="list-style-type: none"> <li>• L'observation directe des morphologies de l'intérieur des membranes hybrides a été réalisée par le comportement mécanique des phases (module, adhésion, déformation)</li> <li>• Les images de module ont révélé une morphologie avec un module élevé à la surface extérieure</li> <li>• L'analyse nanomécanique a permis de suivre l'évolution de la phase SG des membranes hybrides SHDi avec les étapes de fabrication et les images d'adhésion ont révélé l'éluion et la cristallisation des espèces hydrosolubles à partir des membranes aux premières étapes de fabrication</li> <li>• La nano-manipulation des cristaux a permis l'analyse co-localisée AFM/Raman</li> <li>• L'observation directe de la forme des domaines SG des membranes hybrides SHTriM a guidé le choix du modèle de montage pour SANS</li> </ul>
<b>Raman:</b>	<ul style="list-style-type: none"> <li>• L'analyse chimique ponctuelle de la surface extérieur et dans le volume a permis de conclure que la peau de module élevé observée par l'AFM est une zone appauvrit en SG</li> <li>• La distribution SG a été évaluée à travers la coupe transversale, révélant une diminution lente de la teneur en SG d'un côté à l'autre pour les membranes SHDi, ce qui a été amélioré pour les membranes SHTriM</li> <li>• Les informations chimiques co-localisées avec AFM ont révélé la nature des espèces élués et des cristaux, c'est-à-dire des molécules partiellement condensées du précurseur</li> <li>• Une analyse chimique quantitative a été effectuée pour corrélérer la réponse Raman vs %SGw, ce qui va permettre une évaluation des changements de la prise en SG dans les hybrides après vieillissement</li> </ul>

<b>STEM:</b>	<ul style="list-style-type: none"> <li>• L'observation directe de la morphologie en haute résolution (&lt;1 nm) par le contraste chimique a révélé la phase sPEEK même à l'intérieur des domaines SG (SHDi)</li> <li>• La technique ouvre la possibilité d'effectuer une analyse élémentaire haute résolution par EDS/EELS</li> </ul>
<b>SEM:</b>	<ul style="list-style-type: none"> <li>• L'observation directe des morphologies de l'intérieure des membranes hybrides utilisant la topographie et le contraste chimique (SE/BSE) a confirmé la présence de précurseurs/oligomères SG non condensés dans les zones gonflées par l'eau des membranes dans les premières étapes de fabrication</li> </ul>
<b><math>\mu</math>-ATR-FTIR:</b>	<ul style="list-style-type: none"> <li>• L'analyse chimique de l'intérieur des membranes a permis de révéler l'élimination du méthanol en tant que signature d'un processus d'hydrolyse et condensation supplémentaire intervenant lors du traitement thermique de post-condensation</li> </ul>
<b>SANS:</b>	<ul style="list-style-type: none"> <li>• La variation de contraste permet d'extraire sélectivement les informations structurales de chaque phase, qui ne peut pas être obtenue par d'autres techniques expérimentales</li> <li>• Les spectres ont indiqué que la phase SG (SHTriM) est hiérarchiquement organisée, c'est-à-dire des particules élémentaires formant les agrégats de forme ronde vus par AFM</li> <li>• La séparation des nano-phases hydrophobe/hydrophile du sPEEK a été révélée même en présence de SG par la présence d'un pic d'ionomère</li> <li>• La distance inter-domaine (<math>d_{\text{iono}}</math>) diminue avec l'augmentation de la prise en SG grâce à la structure SG 3D qui limite le gonflement du sPEEK</li> </ul>

Nous souhaitons souligner que la diffusion d'espèces hydrosolubles dans l'eau atmosphérique condensée à la surface des membranes coupée par cryo-ultramicrotomie a également été observée dans un système différent basé sur les membranes de polyéthylène téréphtalate (PET) (présenté à l'Annexe 2.5). Cependant, en raison de la nature hautement poreuse des membranes PET, nous n'étions pas en mesure d'effectuer la nano-manipulation des cristaux pour une identification chimique appropriées. Néanmoins, le phénomène est une autre preuve que les espèces hydrophiles peuvent migrer de la masse de matériaux polymères vers l'eau piégée sur la surface cryo-ultramicrotomée.

Notre prochain objectif est d'utiliser la même stratégie de caractérisation pour quantifier les modifications physiques et chimiques induites dans les membranes hybrides SG/sPEEK pendant l'opération de la pile à combustible afin de comprendre la relation structure-propriétés-durabilité de ces systèmes hybrides. En effet, d'une manière générale, des études approfondies du vieillissement dans des conditions de fonctionnement réalistes sont encore nécessaires pour permettre d'améliorer les matériaux vers les performances ciblées.

# CHAPTER 6

---

## Copolymer Electrolytes for Lithium Batteries

## PROLOGUE

In this chapter, we will present the morphological analysis of polymer electrolyte membranes for Lithium Batteries (LB). Samples were prepared in the laboratory “Laboratoire d’Electrochimie et de Physico-chimie des Matériaux et des Interfaces” (LEPMI/Grenoble, France), as part of the thesis work of Adrien Lassagne, and also the thesis work of Bérengère Pelletier at the Institut de Chimie Radicalaire (UMR 7273/ Marseille, France). We will present here a brief introduction to LB technology fundamentals and the use of polymer electrolytes, especially block copolymers based on Polyethylene Oxide (PEO), as solid electrolytes. Then, we will discuss the technological developments that had to be done for sample preparation, due to the high sensitivity of the samples to water. Finally, we will show the results of the study of three different kinds of electrolyte copolymers based on PEO. The first systems are based on PS-PEO-PS copolymers with the addition of lithium salt. The effect of the salt on the morphology of the copolymers will be evaluated by Atomic Force Microscopy and the revealed morphology compared to previously done by Small Angle X-Ray Diffraction (SAXS) analyses. The second study will be interested on the morphological changes induced by the modification of the PEO block by cross-linking and the increasing amount of PS block. Finally, the morphological analysis of a “single-ion” copolymer (PSTFSILi-PEO-PSTFSILi) will be presented.

### French Prologue

Dans ce chapitre, nous présenterons l'analyse morphologique de membranes d'électrolyte polymère pour les batteries au lithium (LB). Ces membranes ont été préparées au Laboratoire d'Electrochimie et de Physico-chimie des Matériaux et des Interfaces” (LEPMI/Grenoble, France), dans le cadre du travail de thèse d'Adrien LASSAGNE, ainsi celui de Bérengère PELLETIER à l'Institut de Chimie Radicalaire (UMR 7273 / Marseille, France). Dans une première partie, nous rappellerons le principe de la technologie LB, le rôle de l'électrolyte polymère situé au cœur du dispositif et pourquoi les copolymères à blocs à base d'oxyde de polyéthylène (PEO), peuvent être utilisés comme électrolytes solides. Ensuite, nous discuterons des développements technologiques qui doivent être faits pour la préparation des échantillons, en raison de la grande sensibilité des échantillons à l'eau. Enfin, nous montrerons les résultats de l'étude des trois types différents de copolymères d'électrolyte à base de PEO. Les premiers systèmes sont basés sur des copolymères PS-PEO-PS avec addition de sel de lithium. L'effet du sel sur la morphologie des copolymères sera évalué par la Microscopie de Force Atomique et la morphologie révélée sera comparé aux analyses de Diffraction de Rayons-X à Petit Angle (SAXS) précédemment réalisées. La deuxième étude sera intéressé par les changements morphologiques induits par la modification du bloc PEO par réticulation et la quantité croissante de bloc PS. Finalement, l'analyse morphologique d'un copolymère "mono-ion" (PSTFSILi-PEO-PSTFSILi) sera présentée.

## 1. Theoretical Background and Motivation

### 1.1. Lithium Batteries Fundamentals

Electrochemical generators are systems consisting of two electrodes (positive and negative) separated by an electrolyte, for converting chemical energy into electrical energy. The positive and negative electrodes are often referred as cathode (where the reduction takes place) and anode (oxidation), respectively. The electrolyte is a substance that produces an ionic conducting solution when dissolved in a polar solvent. Electrochemical reactions are carried out at the electrode/electrolyte interfaces allowing the direct conversion of chemical energy into electrical energy. If these reactions are reversible, then this is referred to as a secondary electrochemical generator or as an electrical accumulator. They induce an electron circulation in an external circuit, which generates electrical work. The electrolyte must be an electronic insulator and stable over a wide electrochemical window. Lithium metal was chosen as a negative electrode material because of its light weight and its high reducing power among all the alkali metals, with a theoretical mass capacity of  $3860 \text{ Ah.kg}^{-1}$ . Furthermore, lithium is a good electronic conductor, which allows it to be directly used as a current collector, representing a significant weight gain. The principle of operation of a lithium metal battery is shown on Figure 6.1.

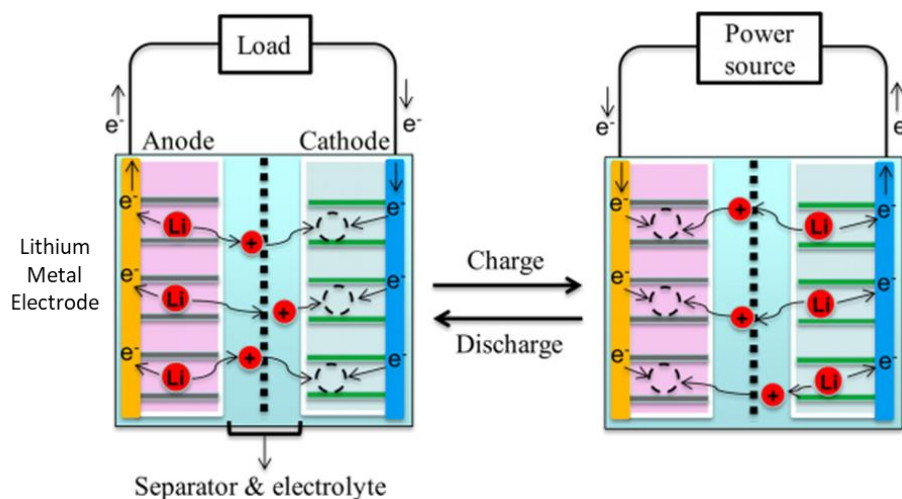


**Figure 6.1.** Principle of operation of a lithium metal battery. During the discharging process, lithium ions migrate through the electrolyte system, ion-conducting medium, and separator membrane, from anode to cathode (left image), while the transport direction is reversed during the charging process (right image).<sup>246</sup>

The main problem with rechargeable lithium metal technologies working with liquid electrolytes occurs during charging. During this step, lithium in  $\text{Li}^+$  form is reduced to lithium metal on the lithium electrode, forming a concentration gradient at high current density. This deposition does not occur homogeneously<sup>247,248</sup> thus forming dendrites (Figure 6.2). These dendrites can grow until reach the other electrode, creating a short-circuit that can cause the dendrite to melt by overheating and can ignite the electrolyte.<sup>249</sup> Because of these safety problems, the commercialization of the first lithium metal batteries was stopped in 1989. Since safety is a major issue, an increasing number of researchers are focusing on solid electrolytes, in particular trying to increase the conductivities at low temperature in order to reduce the operating temperatures.

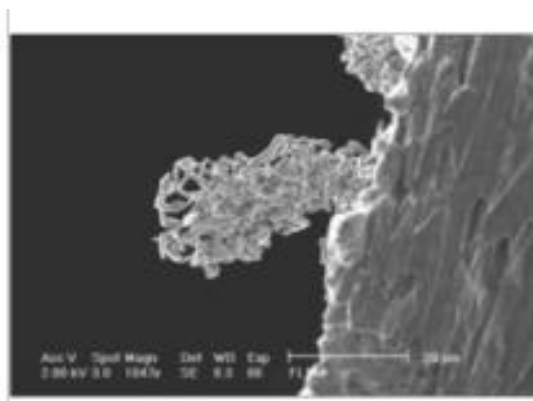


**Figure 6.2.** SEM image of Lithium dendrites at the Lithium Metal Electrode's surface.<sup>250</sup>

To address the growth of the dendrites, the replacement of the liquid electrolyte with a solid polymer electrolyte has been proposed because the dendritic lithium growth is mechanically limited by the solid medium.<sup>251,252</sup> This technology is called Lithium Metal Polymer (LMP). In an LMP system, a lithium salt is dissolved in a polymer matrix without the presence of a liquid solvent.

In order to meet the specifications of the LMP technology, the polymer electrolyte must have a sufficient ionic conductivity and mechanical strength. If the ionic conductivity is not sufficient, the resistance between the electrodes will be too great and it will be impossible to charge or discharge the battery. The mechanical strength is important to mechanically block the growth of the dendrites. Newman *et al.*<sup>252</sup> suggest the use of electrolytes with a shear modulus greater than 1 GPa. Both ionic conductivity and mechanical strength can be controlled by the nature of the polymers, their composition and developed morphology.

## 1.2. Polymer Electrolytes based on PEO

Polyethylene Oxide (PEO) is a semi-crystalline polymer with a melting temperature ( $T_m$ ) around 60 °C. It is able to solvate  $\text{Li}^+$  ions by means of the ether function of its repeating unit (Figure 6.3), which interact with the  $\text{Li}^+$  cations to form a sphere of solvation, responsible for the good dissociation of the salts.<sup>253</sup> They are then transmitted from one chain to another. This mechanism occurs only in the amorphous zones of the polymer. However, because of its high crystallinity, the ionic conductivity of PEO based electrolytes below their  $T_m$  is insufficient, thus the material must be used above its melting temperature. PEO low glass transition temperature ( $T_g = -60^\circ\text{C}$ ) ensures a high mobility of the chains when PEO is amorphous, which facilitates ion transport.<sup>254</sup>

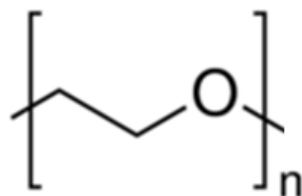


**Figure 6.3.** Polyethylene oxide (PEO) structure

LMP systems therefore use some of the stored energy to keep the PEO melted (usually between 80 °C and 90°C), which is why it is oriented towards applications with a large amount of energy such as electric vehicles or stationary storage. To lower the operating temperature, the melting temperature of the PEO must be lowered. This can be achieved by the introduction of defects within the molecular chain, breaking the regularity of the PEO and hindering its crystallization. However, PEO completely loses its mechanical strength at its amorphous state.

Therefore, copolymerization of PEO with rigid polymers, such as Polystyrene (PS), has been a strategy to ally the advantages of PEO (high conductivity) to new properties (PS higher mechanical strength) by controlling the copolymer composition.

### 1.3. Copolymers as Electrolytes

Block copolymers have many advantages because their properties are adjustable, depending on the chemical nature of the blocks, their size, the resulting morphology, etc. As it is well established, the phase nanoseparation is driven by the affinity of the different blocks, which is characteristic of the Flory-Huggins parameter ( $\chi$ ), depending on the nature of the polymers, the temperature and the number of units ( $N$ ). The resulting micro-phase separation of the blocks is generated by the minimization of the interfacial energy which depends on the surface to volume ratio. A schematic phase diagram is presented on Figure 6.4. Starting from 100% vol of polymer A up to 50% vol of polymer B, firstly, spheres of polymer B are obtained in a matrix of polymer A, then cylinders organized in hexagons, then gyroids and finally a lamellar structure. Knowing the phase diagram, it is theoretically possible to choose the volume fractions in order to achieve the desired morphologies.

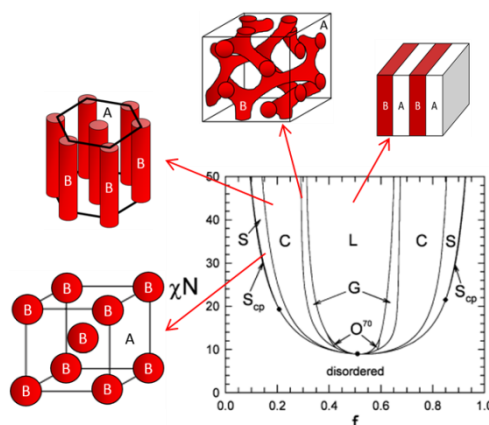


**Figure 6.4.** Theoretical phase diagram of a triblock copolymer. Schematic examples of morphologies are given. L: lamellar, C: cylindrical, S: spheres and G: gyroids.  $N$  is the degree of polymerization of the diblocks formed by snipping the triblocks in half. Adapted from <sup>255</sup>

Typically, co-continuous morphologies, developed from lamellar and gyroid structures, should guarantee the best compromise between conductivity and mechanical strength, thanks to better percolation of the phases.<sup>256</sup> The simplest method for achieving controlled structures is solvent evaporation. In the case of a preparation of the electrolyte by solvent-casting, the rate of evaporation of the solvent affects the structure and orientation of the morphology. Nevertheless, this only works properly for very thin films (<10  $\mu\text{m}$ ). The thickness of the solid electrolyte for Li Batteries varies from 10 to more than 100  $\mu\text{m}$ , which can induce the formation of morphological heterogeneities throughout its thickness.

The conductivity is also affected by the morphology of the ionic conducting phase, which should be continuous through the thickness of the electrolyte and provide the shortest possible travel distance (tortuosity  $\tau$ ) for the ions. The tortuosity depends directly on the volume fractions of each phase and on the morphology of the copolymer. The conductivities, as a function of the inverse of the tortuosity ( $1/\tau$ ) are presented on Figure 6.5 for three copolymers (PEO-PS) with different morphologies and along two perpendicular axes. The gyroids geometries should induce a good conductivity whatever the alignment of the phases while the conductivity of lamellar and cylindrical geometries are extremely dependent on the orientation of the domains.



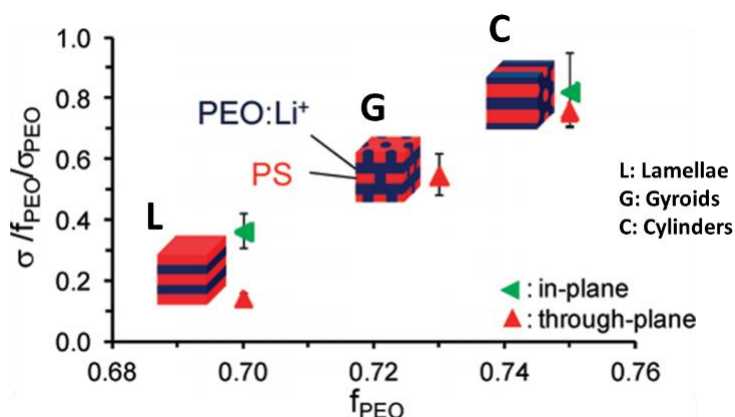


**Figure 6.5.** Conductivity of different morphologies and measurement directions. Adapted from <sup>257</sup>

In order to reduce the operating temperature of LMP-type batteries, researchers investigate a wide variety of solid copolymer electrolytes and lithium salts. Figure 6.6 shows the most frequently used lithium salts in polymer based electrolytes.<sup>258,259</sup> The PEO is the block which in the presence of a lithium salt ensures the conductivity of the electrolyte. PMMA and PS can be used as a second block of the copolymer, breaking the regularity of the PEO chain and hampering its general crystallization. They also act as mechanical reinforcement blocks, making the electrolyte harder than lithium dendrites and thus preventing dendrites from reaching the positive electrode to short-circuit the battery. It has been shown that PS-PEO-PS triblock copolymers with a PEO central block of  $35000 \text{ g}\cdot\text{mol}^{-1}$  were very good candidates for the lithium metal battery's industrial scale-up.<sup>260</sup>

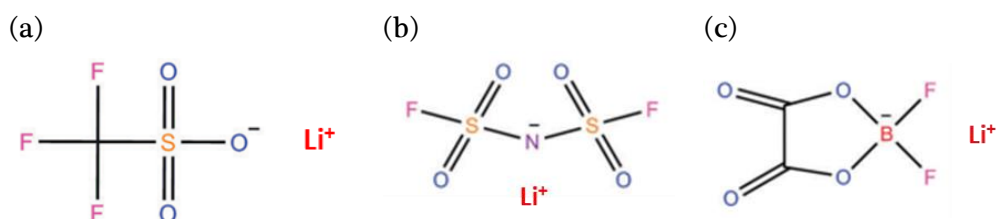


**Figure 6.6.** Examples of Lithium salts for lithium batteries: (a) lithium trifluoromethanesulfonate (LiTf "Triflate") (b) lithium bis(fluorosulfonyl)imide (LiFSI) (c) lithium bis(fluoromalonato)borate (LiDFOB). Adapted from<sup>258,259</sup>

Another approach is the use of the "single-ion" copolymers, which satisfies different expectations from traditional electrolytes. In these materials, the lithium salt is directly grafted onto the polymer chain, as illustrated on Figure 6.7 for different single-ion copolymers from the literature.<sup>261–263</sup> The direct consequence is the absence of concentration gradient of Lithium in the thickness of the electrolyte. As already mentioned, this concentration gradient at high current density is responsible for the nucleation of dendrites of lithium. This strategy would therefore make it possible to develop new solid electrolytes that could annihilate the nucleation of the dendrites. In PEO-Polyanion block copolymers, the Polyanion block acts as mechanical reinforcement, but also as an ion reservoir, without risk of salt precipitation.

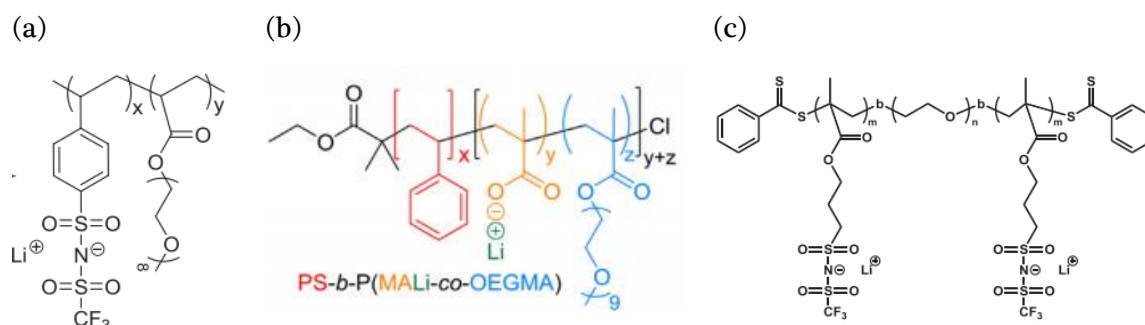


**Figure 6.7.** Examples of single-ion copolymers. (a) Li [PSTFSILi-g-MPEGA] (b) PS-b-P(MALi-co-OEGMA) and (c) poly(LiMTFSI)-b-PEO-b-poly(LiMTFSI). More details in <sup>261-263</sup>

#### 1.4. Morphological Analysis of Polymer Electrolytes

The morphological analyses of these copolymers reported in the literature are usually performed using Small Angle X-Ray Scattering (SAXS), Electron Microscopies (TEM/STEM) and AFM.

SAXS is a non-destructive technique particularly well suited for the determination of the nano-structure of block copolymers. In a SAXS instrument a monochromatic beam of X-rays is brought to a sample from which some of the X-rays (wavelength 0.1 to 0.2 nm) scatter and are recorded at very low angles (typically  $0.1-10^\circ$ ). This angular range contains information about the shape and size of macromolecular domains, characteristic distances of partially ordered materials. SAXS is capable of giving structural information of domains between 5 and 25 nm, and the repeat distances in partially ordered systems of up to 150 nm.<sup>264</sup> An example of a spectrum obtained in SAXS for a PEO-PS diblock copolymer synthesized by anionic polymerization is given in Figure 6.8.

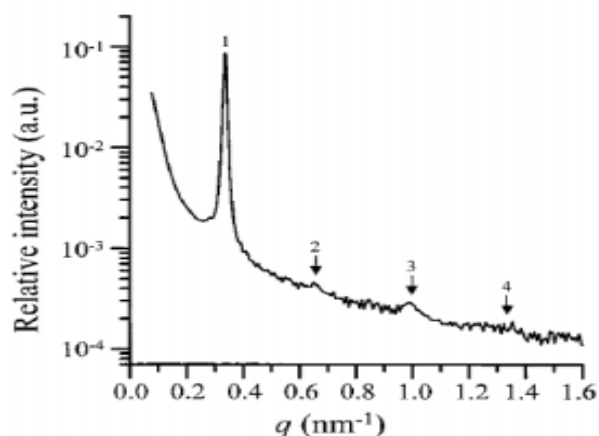


**Figure 6.8.** Example of SAXS spectrum of a PS-PEO diblock copolymer.  $M_n$  PS= 9200 g.mol<sup>-1</sup> and  $M_n$  PEO= 8700g.mol<sup>-1</sup>.<sup>265</sup>

The relative position of the correlation peaks corresponds to the reflections on the planes of the different structures, which allows the identification of the block copolymer's morphology. The periodicity of the domain ( $d_0$ ) can also be calculated from the value of the diffusion vector of the first-order peak ( $q^*$ ) by the equation:  $d_0 = 2\pi/q^*$ . From Figure 6.8, L. Zhu *et al*<sup>265</sup> determined that the relative position of the peaks indicate a lamellar morphology and the first-order scattering peak corresponds to a  $d_0$  of 18.7 nm.

Pelletier *et al.*<sup>266</sup> have used TEM analyses on ultramicrotomed sections from thin films obtained by solvent casting to study the morphology of PS-PEO-PS copolymers by direct observation. An example is given on Figure 6.9 (a) for a copolymer with a volumetric fraction of PEO ( $f_{\text{PEO}}$ ) of 0.27. The sample was stained with ruthenium (PEO phase) to enhance the contrast between PS and PEO phases. Since the sample was composed mostly of PS, the PEO phase appears narrow, and the inter-domain distance measured was about 41 nm.

They have also done AFM analysis on the surface of thin films prepared by spin coating from the same copolymer. AFM phase image on Figure 6.9 (b) shows the presence of the two domains due to the viscoelasticity difference between PS and PEO phases. A "labyrinthic" surface organization was observed. Given the composition of sample ( $f_{\text{PEO}} = 0.27$ ), the bright color domains correspond to the PS and the darkest to the PEO, the inter-domain distance being 45 nm.

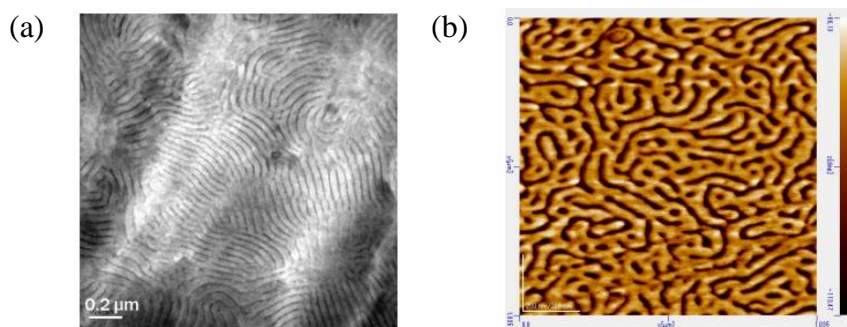


**Figure 6.9.** (a) TEM image ( $2 \times 2 \mu\text{m}^2$ ) and (b) AFM phase image ( $1 \times 1 \mu\text{m}^2$ ) of a PS-PEO-PS copolymer with composition  $f_{\text{PEO}} = 0.27$ .<sup>266</sup>

The block copolymers morphology is impacted by the substrate but also by the rate of solvent evaporation (impact on the kinetics of the microphases-separation). Therefore, the orientation of the phase separated structure with respect to the surface can change by varying the thickness of the sample during annealing, the nature and roughness of the substrate or the rate of solvent evaporation.<sup>267</sup> Therefore data obtained by SAXS or TEM from solvent casted membranes (after cryo-ultramicrotomy sectioning for TEM) can be different from data obtained by AFM on spin-coated samples.

### 1.5. Objectives of work

Despite the advances in the use of block copolymers, research still needs to be made to improve the performance of LMP batteries in terms of safety, autonomy and performance. In order to achieve this objective, it is essential to understand the functioning of Solid Polymer Electrolytes (SPEs) based on triblock copolymers and to establish correlations between the composition, the nanostructure, the mechanical properties and the ionic conductivity. The direct morphological characterization of thick films of these copolymers is still a challenge to be addressed. Furthermore, the addition of salt to the copolymer substantially increases its hydrophilicity, which makes difficult the sample preparation for direct observation.

In this context, this chapter will address the morphological study of a series of triblock PS-PEO-PS doped with a lithium salt and PSTFSiLi-PEO-PSTFSiLi copolymers, using cryo-ultramicrotomy to open the material for direct observation of the bulk membrane morphology using Atomic Force Microscopy.

## 2. Study PS-PEO-PS copolymers doped with lithium salt

### 2.1. Materials used

The copolymers used in this study were provided by the laboratory LEPMI. The structure of each copolymer system is presented on Figure 6.10. Figure 6.10(a) shows the structure of the PS-PEO-PS copolymer. PEO based copolymers with a modified block (Figure 6.10(b)) are denoted PCi. These synthesis were carried out with different PEOs, denoted PC<sub>18</sub> ( $M_{n_{PEO}}=18000\text{g}\cdot\text{mol}^{-1}$ ) and PC<sub>22</sub> ( $M_{n_{PEO}}=22000\text{g}\cdot\text{mol}^{-1}$ ) resulting in polymers having a special unit X distributed in a controlled manner throughout the chain. To enhance the conductivity of the polymer systems, lithium salt bis(trifluorosulfone)imide (LiTFSI) was mixed to the copolymers (Figure 6.10(c)).

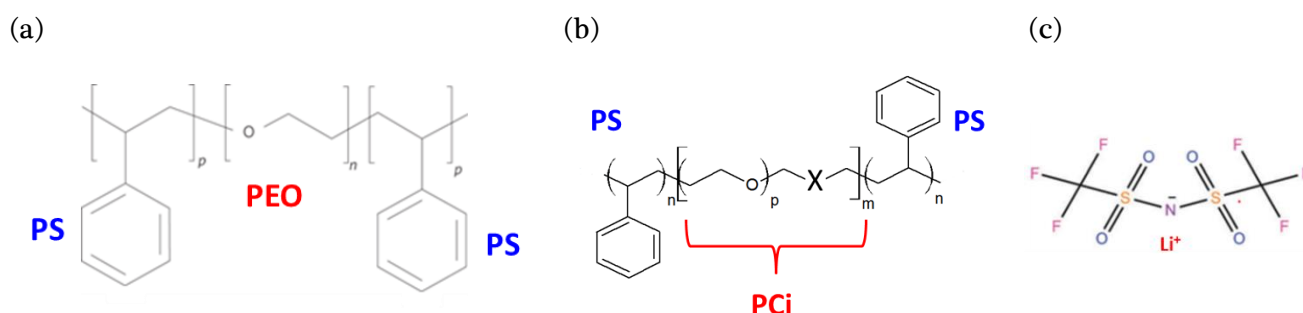


**Figure 6.10.** Structures of (a) PS-PEO-PS, (b) PS-PCi-PS ( $i=18$  or  $22$ ) and (c) lithium bis(trifluorosulfone)imide (LiTFSI)

The main objective of modifying the PEO is to reduce both its crystallinity and its melting temperature, and thus to form polymer electrolytes with a good conductivity at low temperature. In addition the X unit in the structure of the copolymer allows the cross-linking of the PEO domains. The X unit therefore impacts the morphology, mechanical properties and conductivity of the copolymer. The cross-linking reaction is schematically presented on Figure 6.11.

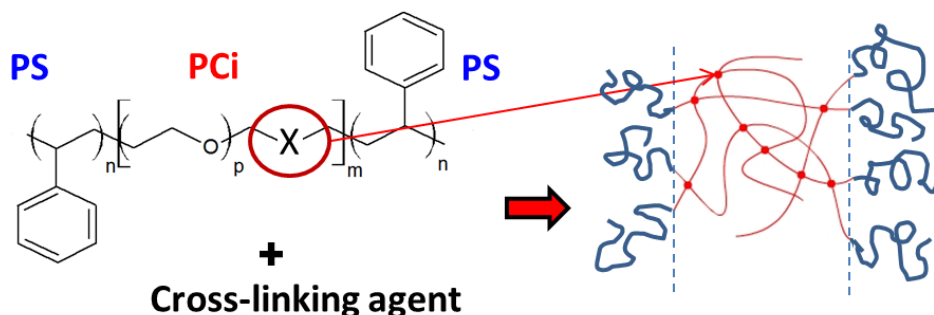


**Figure 6.11.** Schematic cross-linking reaction of PS-PCi-PS ( $i=18$  or  $22$ )

The compositions of the PS-PEO-PS or PS-PC<sub>i</sub>-PS copolymers and their calorimetric properties are summarized on Table 6.1. The calorimetric properties of the copolymers were determined by DSC by Lassagne and Pelletier.<sup>266,268</sup> For the calculation of the crystallinity index ( $X_c$ ) of the samples, the melting enthalpy  $\Delta H_m$  was weighted by the amount of sample and its composition. Thus,  $X_c$  corresponds only to the crystallinity of the PEO block, since the PS blocks are not able to crystallize.

**Table 6.1.** Composition and thermal properties of the copolymers studied.<sup>266,268</sup>

Ref.Sample	Copolymer	Cross-linked	LiTFSI	%wt Bloc PS	$f_{PEO}$ (vol)	$M_n$ (block PEO) g.mol <sup>-1</sup>	$M_n$ (blocks PS) g.mol <sup>-1</sup>	$M_n$ Copolymer g.mol <sup>-1</sup>	Tm °C	$X_c$ %
SPEOS	PS-PEO-PS	No	No	32.6	0.65	35000	16900	51900	50	36
SPEOS+LiTFSI	PS-PEO-PS	No	Yes	32.6	0.65	35000	16900	51900	38	22
SPC <sub>18</sub> S	PS-PC <sub>18</sub> -PS	No	Yes	23	0.78	18000	5346	23346	25	20
SPC <sub>18</sub> S_X	PS-PC <sub>18</sub> -PS	Yes	Yes	30	0.72	18000	7714	25714	18	20
SPC <sub>22</sub> S_X	PS-PC <sub>22</sub> -PS	Yes	Yes	22	0.79	22000	6241	28241	25	30

X = Cross-linked

## 2.2. Sample preparation for cross-section analysis

Samples of copolymer membranes were cryo-ultramicrotomed secured in a vice as shown in Chapter 3, without the need of epoxy embedding.

These membranes are highly sensitive to water due to the presence of LiTFSI salt. Even a low content of water (relative humidity) can modify the surface morphology. In order to address this problem, a specially designed device was developed in our laboratory to avoid frost deposition/melting on the cryo-ultramicrotomed surface and on the ultrathin sections collected when warming back to room temperature. Figure 6.12 (a) shows optical microscopy images of the cryo-ultramicrotomed surface obtained after no specific water control out of the cryo-ultramicrotome: the membrane's surface appears very rough and deformed. This is an indication that morphological modifications occurred after cutting. Indeed, big spherulites can be observed at the surface of the membrane due to the plasticization effect of the water. Figure 6.12 (a) also shows a thin section collected on a copper grid, completely solubilized by the condensed water. Figure 6.12 (b), on the other hand, shows both the intact membrane's surface and the intact thin section collected on a copper grid. We succeeded protecting the membrane's morphology from atmospheric water, avoiding any morphological changes.

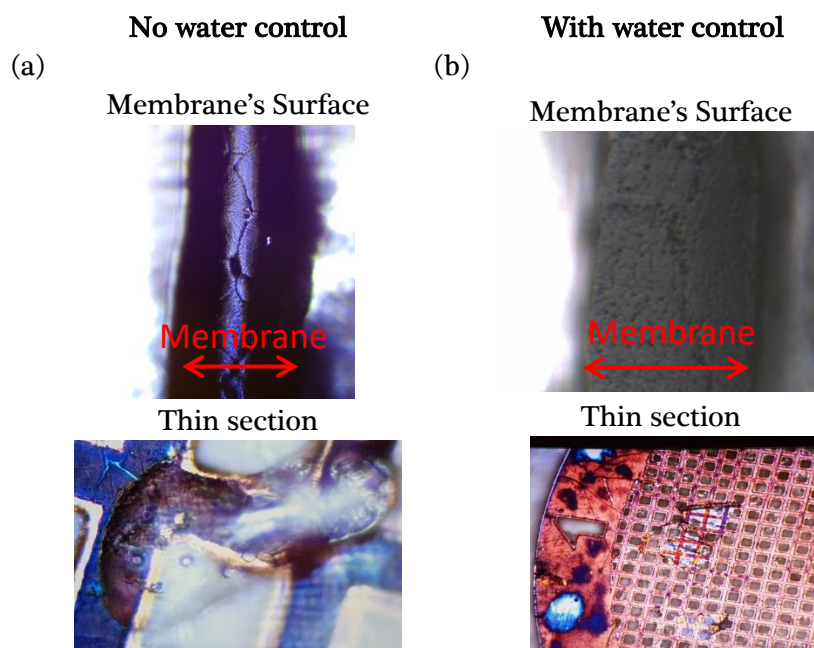


**Figure 6.12.** Optical photographs of the membrane's surface and thin sections on copper grid in different conditions: (a) affected surface and solubilized thin section after cryo-ultramicrotomy without control of frost deposition and (b) intact surface and thin section collected after optimized cryo-ultramicrotomy with water-control.

The cryo-ultramicrotomed membrane's surface was used from AFM analysis of the bulk morphology and correlated with SAXS experiments previously done by the laboratory LEPMI. To be noticed, we had not enough time to do TEM/STEM characterization of the collected thin sections. These complementary characterizations are proposed as future work.

## 2.3. Morphological study of PS-PEO-PS copolymers

### 2.3.1. Effect of the Lithium salt on the morphology

We will be first characterizing the morphology of samples SPEOS and SPEOS+LiTFSI, which present high molecular weight ( $M_n^{\text{copolymer}} = 51900 \text{ gmol}^{-1}$ ) and the opportunity to understand the impact of the addition of lithium salt on the polymer morphology.

AFM images using the Peak Force QNM mode were acquired under ambient conditions at room temperature and a relative humidity of about 50%.  $10 \times 10 \mu\text{m}^2$  area AFM height and modulus images of the copolymer membrane SPEOS (no salt) are shown on Figure 6.13 (a) and (b) respectively. One can see that the topography presents a series of vertical lines (not an AFM or cutting artifact), parallel to each other and to the outer surface (left of the image), and small round features with a higher topography distributed on the surface. It is important to remember that after cryo-ultramicrotomy any topographical contrast results from the differences of penetration depth of the AFM tip into the sample (since the cryo-ultramicrotomed surface is flat by definition, except if the surface gets polluted or deformed after the procedure). Meaning that, here, the topography reveals a modulus contrast: the component with lower modulus appears lower on topography due to the deeper tip indentation depth. One can notice that despite the higher topography of the small round features distributed on the surface, they appear with low modulus (black dots on the modulus image), meaning that their topography was developed after the cryo-ultramicrotomy procedure (otherwise low modulus areas are naturally depressed by the tip and not protruding from the

surface). Besides these features, the Modulus image presented on Figure 6.13 (b) also presents vertical lines with contrasted mechanical properties. One can conclude that the topographic and modulus images are representative of the lamellar morphology of the copolymer.

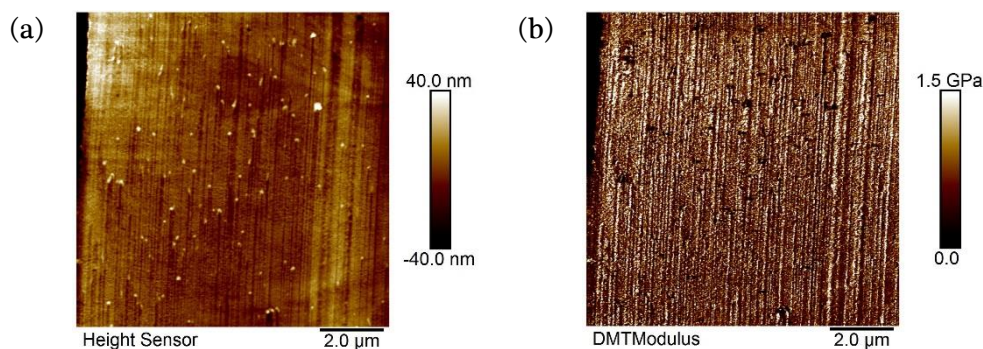


**Figure 6.13.** AFM images relative to sample SPEOS (a) Height and (b) Modulus images of a  $10 \times 10 \mu\text{m}^2$  area.

Figure 6.14 (a) and (b) are Height and Modulus images of a  $3 \times 3 \mu\text{m}^2$  area of the same sample. The small round features distributed on the surface appear with low modulus ( $< 200 \text{MPa}$ ), systematically at places where the lamellae seem to diverge from their regular pattern. These features can be related to impurities or remnant products from the copolymer synthesis, which can block the propagation of the lamellae growth, introducing these heterogeneities in the morphology. After the cryo-ultramicrotomy procedure, these products may be able to swell with the room relative humidity, which can explain their higher topography and low modulus.

The high modulus phase (white), logically associated to the PS phase ( $T_g \sim 90^\circ\text{C}$ ), appears with a mean modulus of about 2.3 GPa. The low modulus phase (dark brown), corresponding to the PEO blocks, appears with a mean modulus of 420 MPa. From the Modulus images, one can measure the thickness of the PS domains and their inter-distance. It is important to notice that the measurement of the thickness of the PS domains can be affected by the tip curvature radius (the larger the tip radius the larger will appear the PS domains), however, the inter-distance between domains is not affected by this artifact. The average thickness of the PS domains measured at the mid height of the modulus peaks was  $25 \pm 6 \text{ nm}$  and the average distance between them, from peak to peak, was  $63 \pm 18 \text{ nm}$ . On the topography section (Figure 6.14 (c)) done to measure the thickness of the PS, one can see that the PS blocks appear as high modulus peaks up to 3 GPa, which is in agreement with the system calibration.

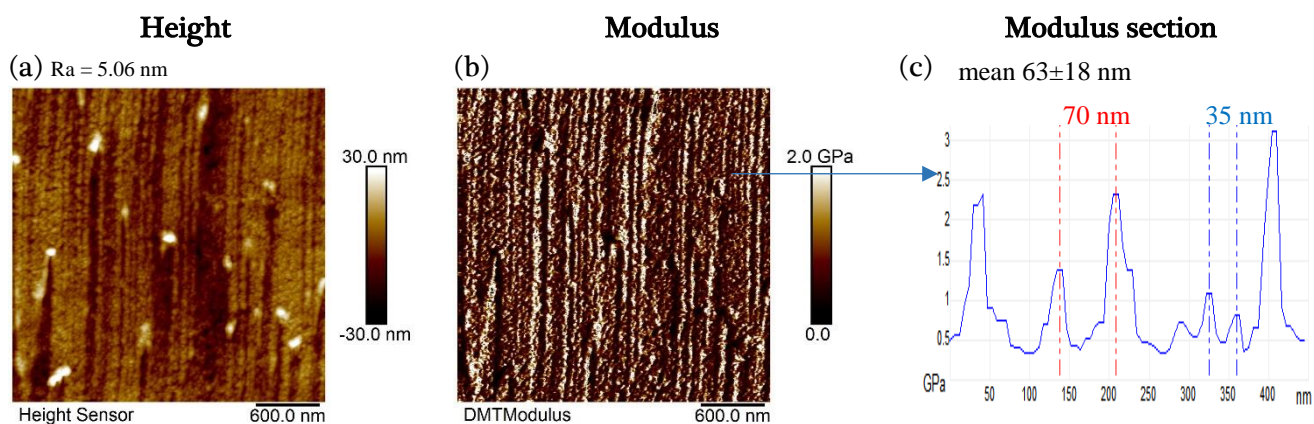


**Figure 6.14.** AFM images of a  $3 \times 3 \mu\text{m}^2$  area of sample SPEOS. (a) Height, (b) Modulus and (c) Topography section of the blue line on figure (b).

Topography images of the copolymer membrane with lithium salt SPEOS+LiTFSI are presented on Figure 6.15 (a) and (d) (dimension of  $3 \times 3 \mu\text{m}^2$  and  $1 \times 1 \mu\text{m}^2$ , respectively). On the modulus images shown on Figure 6.15 (b) and (e), the microstructure of the copolymer is revealed by the different Young's modulus of each phase. The low modulus phase (dark brown) with a mean modulus of 200 MPa is related to the low crystallinity PEO phase containing LiTFSI salt, which is lower than the PEO phase without salt (mean modulus of 420 MPa). The high modulus phase (white), related to the PS ( $T_g \sim 90^\circ\text{C}$ ), appears with a modulus up to 2.1 GPa (mean value of 1.28 GPa). The microstructure revealed on Figure 6.15 (b) is essentially lamellar, but the presence of the salt in the structure clearly affects the long range order of the self-assembly. The lamellae appear with shorter length and more spaced along the membrane. The thickness of the PS domains was measured at the mid height of the modulus peaks and a mean value of  $35 \pm 7 \text{ nm}$  was obtained. The average distance from peak to peak ( $d_{\text{PS}}$ ) was  $88 \pm 56 \text{ nm}$  (as shown on the modulus section analysis of Figure 6.15 (c)). It is important to take into account that lamellae with different angular orientations can show (as an artifact) larger inter-domain distances, which explains the high standard deviation of these measurements. Modulus section analyses inside the dark brown phase (example given on Figure 6.15 (f)) also revealed some regular features with modulus up to 370 MPa and spaced of  $31 \pm 4 \text{ nm}$  from each other ( $d_{\text{PEO}}$ ), probably related to the presence of 22.6% of crystalline PEO. The characteristic distances measured are schematically represented on Figure 6.16.

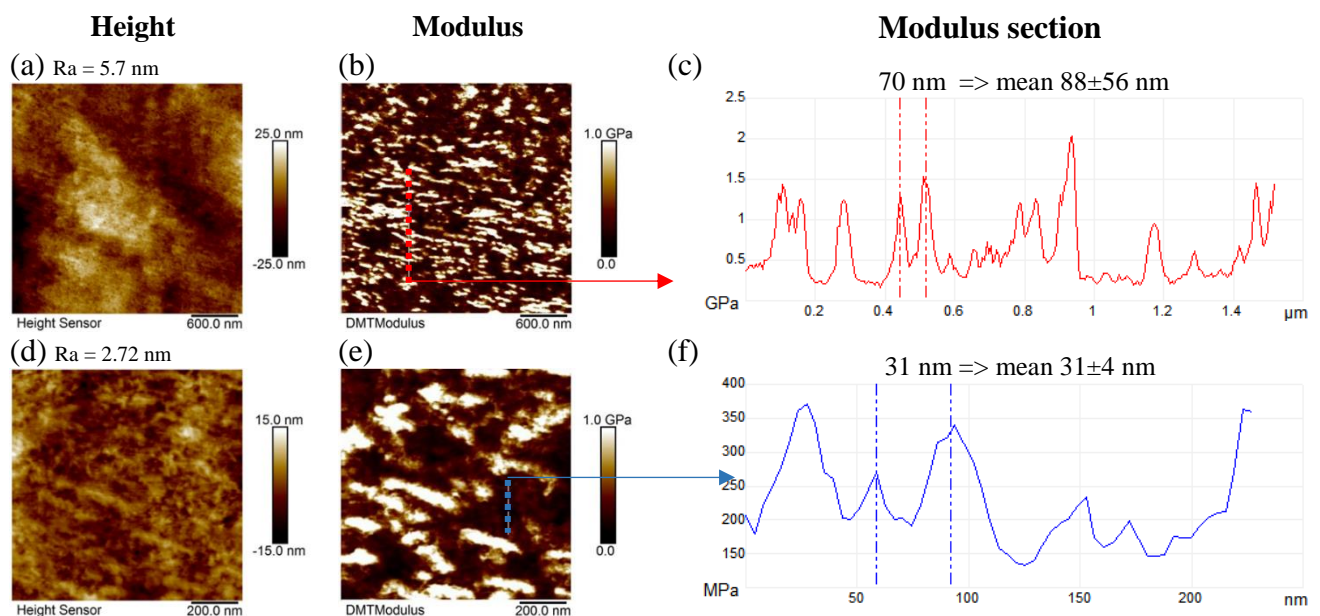


**Figure 6.15.** Copolymer SPEOS+LiTFSI morphology revealed by Height and Modulus AFM images. (a) Height and (b) Modulus of a  $3 \times 3 \mu\text{m}^2$  area; (c) represents the section of the red line on figure (b). (d) Height and (e) Modulus of a  $1 \times 1 \mu\text{m}^2$  area; (f) represents the section of the blue line on figure (e).



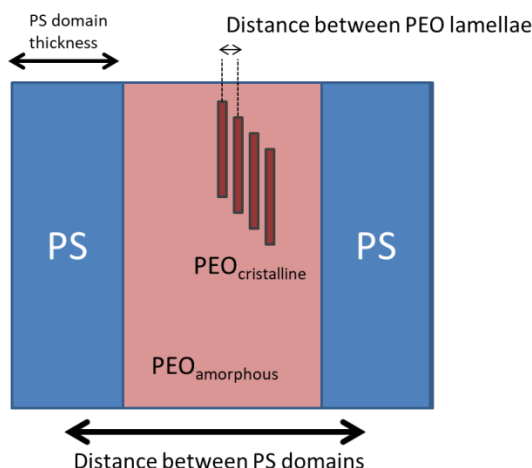


**Figure 6.16.** Schematic representation of the measured distances: the PS domain thickness, the distance between PS domains ( $d_{PS}$ ) and the distance between PEO lamellae ( $d_{PEO}$ ).

Using SAXS experiments, Pelletier<sup>266</sup> was able to determine the morphology of PS-PEO-PS copolymers with a PEO volume fraction ( $f_{PEO}$ ) of at the range of 0.38 to 0.48, appearing with lamellar morphology. However, Pelletier claims that it was impossible to determine the global morphology for sample SPEOS and SPEOS+LiTFSI ( $f_{PEO}=0.65$ ). Samples with high PEO content do not show well-defined structures by SAXS appearing typically with a very broad peak of low intensity.<sup>269</sup> Due to the absence of higher order scattering peaks, on the basis of SAXS patterns alone, the morphology cannot be clearly defined. Apparently the electronic contrast between the PEO and the PS blocks is not enough to allow the long range morphological analysis by SAXS. Nevertheless, an estimation of the characteristic inter domain distance ( $d_0$ ) of 31.5 nm was done by SAXS. Since this measurement was issued from a low intensity and broad peak, it should be considered with caution. The SAXS and AFM results are summarized on Table 6.2. Although SAXS could not provide the global morphology of the sample, the observation of a lamellar morphology by AFM is in agreement with the theoretical morphology determined for a copolymer with  $f_{PEO}=0.65$ .

**Table 6.2.** Theoretical morphology, SAXS and AFM results for sample SPEOS and SPEOS+LiTFSI<sup>266</sup>

Sample	Copolymer	$f_{PEO}$ (vol)	Theoretical Morphology	SAXS Morphology	$d_0^{SAXS}$ nm	AFM Morphology	$d_{PEO}^{AFM}$ nm	$d_{PS}^{AFM}$ nm
SPEOS	PS-PEO-PS	0.65	lamellar	-	33	lamellar	-	63±18
SPEOS+LiTFSI	PS-PEO-PS	0.65	lamellar	-	31.5	lamellar	31±4	88±56

Height and Modulus images corresponding to the first 10  $\mu\text{m}$  of the left side of the SPEOS+LiTFSI membrane's cross-section are shown on Figure 6.17 (a) and (b). Figure 6.17 (b) reveals highly oriented lamellae perpendicular to the membrane's surface, probably induced during the membrane's manufacturing.<sup>267</sup> The same trend was seen on the other side of the membrane's cross-section (not shown). The average thickness of the PS domains was  $28\pm 5$  nm, which is lower than at the bulk ( $35\pm 7$  nm) but the mean length of  $413\pm 132$  nm is almost the double than what measured in the bulk of the membrane ( $223\pm 76$  nm), as highlighted by the inset image on Figure 6.17 (b). However, the average distance between the PS domains was  $95\pm 53$  nm, similar to the previous  $88\pm 56$  nm measured in the bulk.

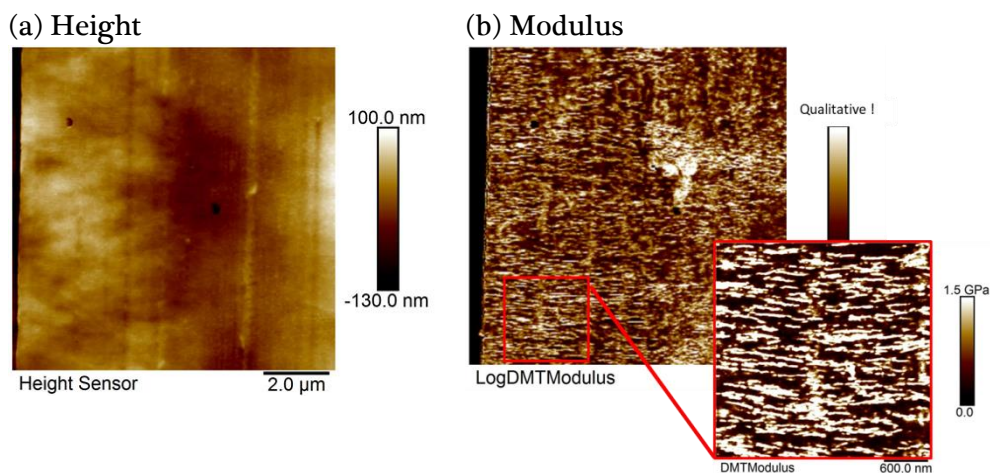


**Figure 6.17.** AFM Height (a) and Modulus (b) images of a  $10 \times 10 \mu\text{m}^2$  area of the sample SPEOS+LiTFSI from the surface to the bulk showing highly oriented lamellae perpendicular to the membrane's surface (left). The zoomed inset on (b) shows the lamellae on an area of  $3 \times 3 \mu\text{m}^2$ .

#### 2.4. Effect of reticulation on PS-PCi-PS copolymers morphologies

The next analyses are relative to samples  $\text{SPC}_{18}\text{S}$ ,  $\text{SPC}_{18}\text{S}_X$  and  $\text{SPC}_{22}\text{S}_X$  in order to evaluate the effect of cross-linking on mechanical properties and nanophase separation. Figure 6.18 shows the topographic and modulus AFM images of samples  $\text{SPC}_{18}\text{S}$ ,  $\text{SPC}_{18}\text{S}_X$  and  $\text{SPC}_{22}\text{S}_X$ . No regular structure was seen for the analyzed samples. Indeed, the measurements have been done at room temperature ( $T \sim 23^\circ\text{C}$ ), which is very close to the determined  $T_m$  of the samples: 25, 18.4 and  $25.2^\circ\text{C}$ , respectively for  $\text{SPC}_{18}\text{S}$ ,  $\text{SPC}_{18}\text{S}_X$  and  $\text{SPC}_{22}\text{S}_X$ . Thus, samples are essentially in an amorphous state. The mechanical strength of the sample is basically assured by the rigid PS blocks at room temperature.

Sample  $\text{SPC}_{18}\text{S}$  (22%PS) appears with low roughness and a homogeneous modulus distribution (mean modulus of 158 MPa), with no clear phase separation. Comparing sample  $\text{SPC}_{18}\text{S}$  with sample  $\text{SPC}_{18}\text{S}_X$  (Figure 6.18 (b)) which has a higher fraction of PS (30%) the effect of a higher content of PS and the cross-linking can be evidenced. In Sample  $\text{SPC}_{18}\text{S}_X$  (Figure 6.18 (b)) a better phase separation is seen, with elongated nodules seen on topography appearing with high modulus (up to 1.2 GPa) on the modulus image (Figure 6.18 (e)). The presence of round or elongated features is in accordance with the theoretical morphology for a copolymer with an  $f_{\text{PEO}} \sim 0.75$ , which can present spheres or cylinders. These features are probably related to the PS blocks of the copolymers, since the higher  $T_g$  of the PS blocks (about  $70^\circ\text{C}$  for a block with  $2850 \text{ g}\cdot\text{mol}^{-1}$ )<sup>270</sup> make them appear at the glassy state. An average distance between the PS domains ( $d_{\text{PS}}$ ) was measured, giving  $78 \pm 38$  nm from peak to peak on the modulus image. The cross-linking has also an effect on the mean modulus of the probed area, increasing from 158 MPa to 379 MPa. The mean value of the dark brown phase (amorphous cross-linked PEO with salt) was about 220 MPa, higher than the mean value of 158 MPa measured for sample  $\text{SPC}_{18}\text{S}$ .

Sample  $\text{SPC}_{22}\text{S}_X$  (Figure 6.18 (c)) is also cross-linked but has longer blocks of PEO ( $M_{\text{PEO}} = 22000 \text{ g}\cdot\text{mol}^{-1}$ ), i.e., the molar weight between each cross-links ( $M_c$ ) is bigger. One can see by the topographic and modulus images (Figure 6.18 (c) and (f)) that the elongated high modulus nodules are more distant from each other (average distance of  $96 \pm 38$  nm). The mean modulus dropped to about 164 MPa, the PEO (dark brown) appearing with a mean modulus of 110 MPa and the PS phase (bright) with 360 MPa (up to 500 MPa). This drop is probably related to the presence of longer chains of PEO between the cross-linkers. A summary of the above measurements are presented on Table 6.3.

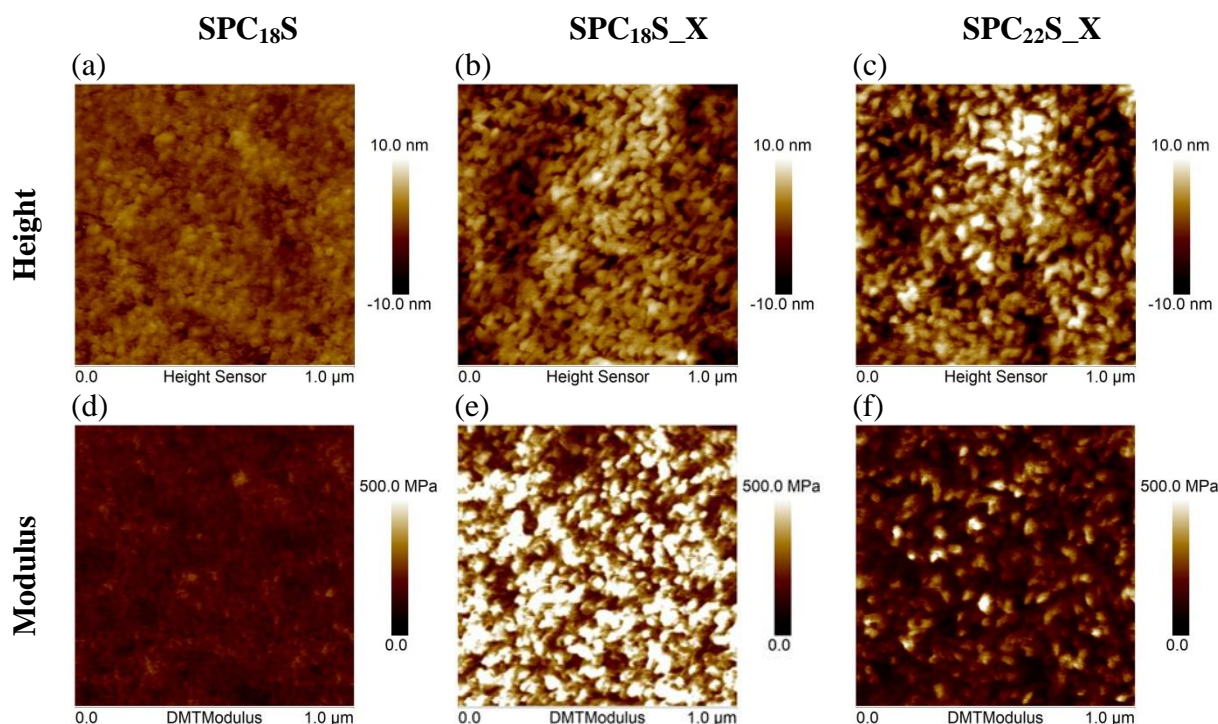


**Figure 6.18.** AFM Height of the copolymer systems: (a) SPC<sub>18</sub>S, (b) SPC<sub>18</sub>S\_X and (c) SPC<sub>22</sub>S\_X and the corresponding Modulus images (d) (e) and (f). Images are 1x1μm<sup>2</sup>.

It is important to consider the lengths of the polymer chains when analyzing the measured distances. The maximum physically possible length of the polymer, called contour length ( $L$ ), corresponds to the fully extended polymer chain. This defines the maximum distance between the different blocks. In order to minimize its free energy, the polymer chain reduces the distance between its two free ends, maximizing its entropy. Consequently, the effective distance between the two ends is way less than the contour length when free of mechanical stresses. Considering the shortest PEO blocks of the analyzed copolymers with  $M_n=18000 \text{ g mol}^{-1}$ , the contour length is estimated to be of the order of 200 nm. The contour length for a PS block with  $M_n=3500 \text{ g mol}^{-1}$  is of the order of 14 nm. The inter-domains distance from the center of a PS domain to another PS domain would be given by half the length of a PS block plus the PEO length plus half the other PS block length ( $1/2\text{PS} + \text{PEO} + 1/2\text{PS} \approx 214 \text{ nm}$ ). The maximum distances measured ( $\sim 134 \text{ nm}$ ) are still under this value. Even if we consider that the glassy PS blocks could stretch the flexible amorphous PEO blocks to their maximum extension, the measured distances are still realistic, since they are always inferior to the sum of the contour lengths of the blocks.

**Table 6.3.** AFM PeakForce QNM analysis of samples SPC<sub>18</sub>S, SPC<sub>18</sub>S\_X and SPC<sub>22</sub>S\_X

Sample	Copolymer	%wt Bloc PS	$f_{\text{PEO}}$ (vol)	$M_n$ (Block PEO) g.mol <sup>-1</sup>	$M_n$ (Blocks PS) g.mol <sup>-1</sup>	$E_{\text{PEO}}$ MPa	$E_{\text{PS}}$ MPa	$E_{\text{mean}}$ MPa	$d_{\text{PS}}^{\text{AFM}}$ nm
SPC <sub>18</sub> S	PS-PC <sub>18</sub> -PS	23	0.78	18000	5346	-	-	158	-
SPC <sub>18</sub> S_X	PS-PC <sub>18</sub> -PS	30	0.72	18000	7714	220	800	379	76±38
SPC <sub>22</sub> S_X	PS-PC <sub>22</sub> -PS	22	0.79	22000	6241	110	360	164	96±38

Lassagne<sup>268</sup> tested the effect of cross-linking on the Young modulus at 40°C for samples with composition of  $f_{\text{PEO}}=0.79$  ( $M_{\text{nPEO}} = 23000 \text{ g mol}^{-1}$ ,  $M_{\text{nPS}} = 6250 \text{ g mol}^{-1}$ ). For these samples with 21%vol PS he could see an increase of modulus from 0.15 MPa to 3.3 MPa at 40°C. As expected, the cross-linking of the central block of a structured material had a significant impact on its mechanical behavior.

Moreover, SAXS analysis of these materials (Table 6.4) showed that they exhibited a certain phase separation, but the morphology could not be determined. The second order peak was broad and had low intensity, meaning a large dispersion. From the first order peak, Lassagne estimated inter-domain distances of the samples. The distance was slightly enlarged for sample SPC<sub>22</sub>S\_X due to the higher molecular weight of the PEO block, the characteristic distance ( $d_0$ ) increasing from 20 for sample SPC<sub>18</sub>S to 32 nm. Differences between AFM and SAXS measurements can originate from the local measurements obtained by AFM versus the statistical measurements obtained from SAXS (here from low intensity and broad peaks). Nevertheless, the inter-distances measured by both techniques have the same order of magnitude.

**Table 6.4.** SAXS results for samples SPC<sub>18</sub>S, SPC<sub>18</sub>S\_X and SPC<sub>22</sub>S\_X<sup>268</sup>

Sample	Copolymer	%wt PS	$f_{\text{PEO}}$ (vol)	Morphology	$d_0$ nm
SPC <sub>18</sub> S	PS-PC <sub>18</sub> -PS	23	0.78	not determined	20
SPC <sub>18</sub> S_X	PS-PC <sub>18</sub> -PS	30	0.72	--	--
SPC <sub>22</sub> S_X	PS-PC <sub>22</sub> -PS	22	0.79	not determined	32

### 3. Study of “single ion” copolymer electrolyte

#### 3.1. Material used

The structure of the “single-ion” copolymers studied is presented on Figure 6.19. The composition of the copolymer and its thermal properties determined by DSC by Lassagne are presented on Table 6.5.

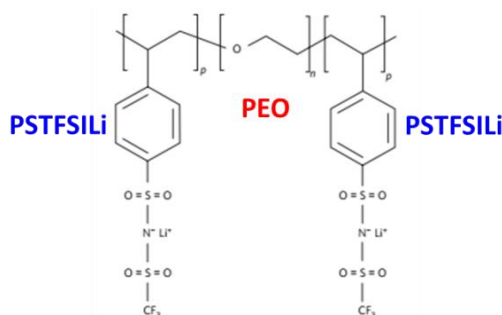


**Figure 6.19.** Structure of the PSTFSILi-PEO-PSTFSILi copolymer

**Table 6.5.** Composition of the PSTFSILi-PEO-PSTFSILi copolymer

Copolymer	%wt Bloc PSTFSILi	$f_{\text{PEO}}$ (vol)	%vol PSTFSILi OE/Li 25	$M_n$ (PEO) $\text{g}\cdot\text{mol}^{-1}$	$M_n$ (PS) $\text{g}\cdot\text{mol}^{-1}$	$M_n$ Copolymer $\text{g}\cdot\text{mol}^{-1}$	Tg °C	Tm °C	Xc %
PSTFSILi-PEO- PSTFSILi	23.5	0.81	23.75	35000	10752	45752	1.7	62.4	42.9

Samples were prepared for AFM analysis of the cross-section by cryo-ultramicrotomy with the same methodology described for the PS-PEO-PS copolymers at Section 2.2.

### 3.2. Morphology of PSTFSILi-PEO-PSTFSILi copolymer

The PeakForce QNM analysis of a  $3 \times 3 \mu\text{m}^2$  area of the sample is shown on Figure 6.20. One can see by the topography and modulus images (Figure 6.20 (a) and (b)) a lamellar morphology. The mean thickness of the lamellae was  $22 \pm 9 \text{ nm}$  and the average distance measured between them was  $27 \pm 10 \text{ nm}$ . The proper assignment of the phases can be done based on the work of Lassagne.

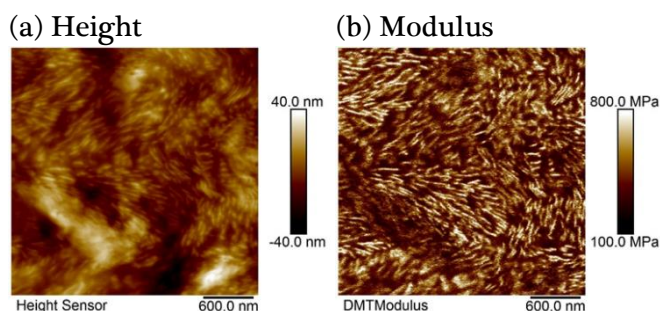


**Figure 6.20.** AFM (a) Height and (b) Modulus images of a  $1 \times 1 \mu\text{m}^2$  area of sample PSTFSILi-PEO-PSTFSILi.

Lassagne has shown that the miscibility of this system is improved by the presence of the salt grafted on the structure. Indeed, he could show that certain compositions of the copolymer ( $< 20\% \text{ wt}$  of PS) presented one single glass transition temperature ( $T_g$ ), characteristic of miscible systems. For low concentration of PSTFSILi, the PSTFSILi blocks are completely miscible inside the amorphous PEO phase. Increasing the content of PSTFSILi will promote a certain phase separation, but with an interphase with a constant composition near 50/50w (determined by the evolution of the  $T_g$  with  $f_{\text{PEO}}$ ). The schematic representation is shown on Figure 6.21. SAXS experiments showed that the nano-phase separation was only present below the melting temperature of the PEO phase. Thus, the clear phase separation present at room temperature is engendered by the crystallization of PEO (PEO rejecting PSTFSILi out of crystalline lamellae). Indeed, this sample presented 42.9% of crystallinity and a melting temperature of  $62.4^\circ\text{C}$ . From these results, we can conclude the proper assignment of the phases seen by AFM: High modulus phase is the crystalline PEO and the low modulus phase is the amorphous PEO mixed with PSTFSILi.

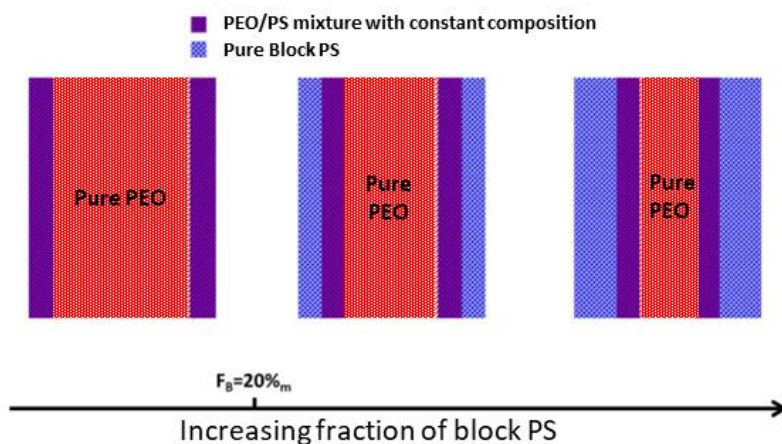


**Figure 6.21.** Schematic representation of the evolution of the morphology with the composition of single-ion copolymers at room temperature. Adapted from <sup>268</sup>

Figure 6.22 (a) to (d) are relative to the PeakForce QNM analysis of a  $1 \times 1 \mu\text{m}^2$  area. As indicated by the red arrows, the lamellae, relative to the crystalline PEO, appear with high modulus (bright yellow), with a mean value of 800 MPa, low adhesion (dark brown/ 7 nN) and low deformation (dark brown/ 3 nm). The blue arrows indicate the mixture of amorphous PEO and PSTFSiLi phases, appearing with a lower modulus (brown/  $\sim 380$  MPa), high adhesion (bright yellow/ 12 nN) and high deformation (yellow/ 6 nm).

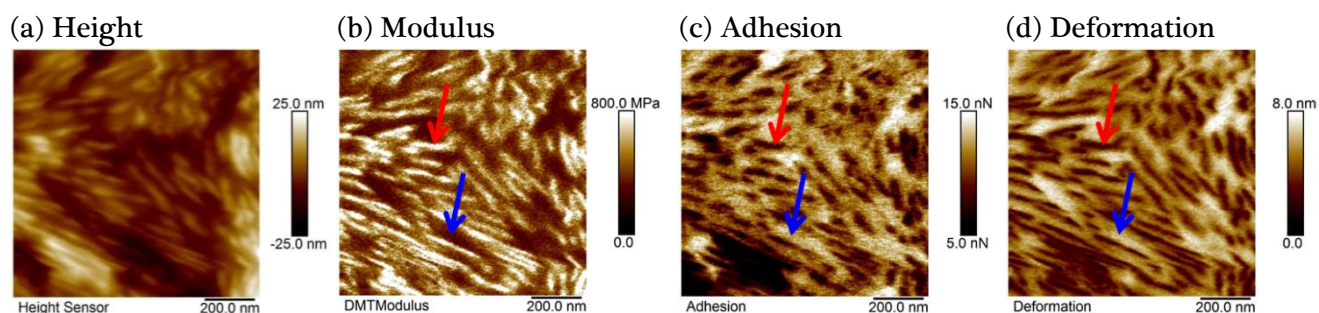


**Figure 6.22.** AFM images of a  $1 \times 1 \mu\text{m}^2$  area of sample PSTFSiLi-PEO-PSTFSiLi. (a) Height, (b) Modulus, (c) Adhesion and (d) Deformation. Red arrow points on a crystalline PEO lamella and blue arrow on the amorphous phase composed of amorphous PEO blended with PSTFSiLi.

The lamellar morphology observed at room temperature by AFM is in total agreement with the morphology determined by SAXS (Table 6.6) for a copolymer with the same composition by Lassagne and Louise Frenck.<sup>268,271</sup> The inter-domain distance measured by SAXS was 25 nm, which is in very good agreement with the  $27 \pm 10$  nm measured by AFM.

**Table 6.6.** SAXS results for the “single-ion” sample and inter-lamellar distance measured by AFM

Copolymer	%wt Block PS	$f_{\text{PEO}}$ (vol)	Morphology	$d_0^{\text{SAXS}}$ nm	$d^{\text{AFM}}$ nm
PSTFSiLi-PEO- PSTFSiLi	23.50	0.81	lamellar	25	$27 \pm 10$

Tensile tests at  $40^\circ\text{C}$  of both systems are shown on Figure 6.23 (a). The higher crystallinity, with the PEO lamellar morphology can explain the higher mechanical properties observed for the PSTFSiLi-PEO-PSTFSiLi systems in comparison to the doped PS-PEO-PS ones. However, the presence of crystalline PEO limits the conductivity of the sample below the PEO melting temperature. Figure 6.23 (b) shows the evolution of the conductivity with temperature. One can see that for sample PSTFSiLi\_81 ( $f_{\text{PEO}}=0.81$ /blue line) the conductivity is very low at temperatures near  $40^\circ\text{C}$ , but increases considerably above  $55^\circ\text{C}$ . Indeed, the ionic conductivity only increases when the melting of the PEO crystalline domains gives sufficient mobility to the PEO chains.

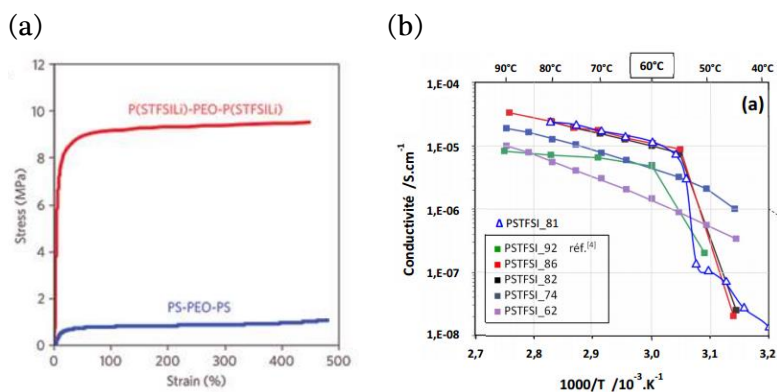


**Figure 6.23.** (a) Tensile test at 40°C of a PSTFSILi-PEO-PSTFSILi and a PS-PEO-PS copolymer. (b) Evolution of conductivity of PSTFSILi-PEO-PSTFSILi copolymer as a function of temperature.<sup>260</sup>

Probing the surface of a larger area, it was possible to reveal the presence of grains of self-assembled domains. Figure 6.24 (a) shows the topography of a  $3 \times 3 \mu\text{m}^2$  area, in which is possible to perceive slightly depressed topography boundaries in between adjacent zones. These boundaries appear clearer on the corresponding Error Channel image (Figure 6.24 (b)). Figure 6.24 (c) highlights the grain boundaries with dashed red lines as guides to the eyes.

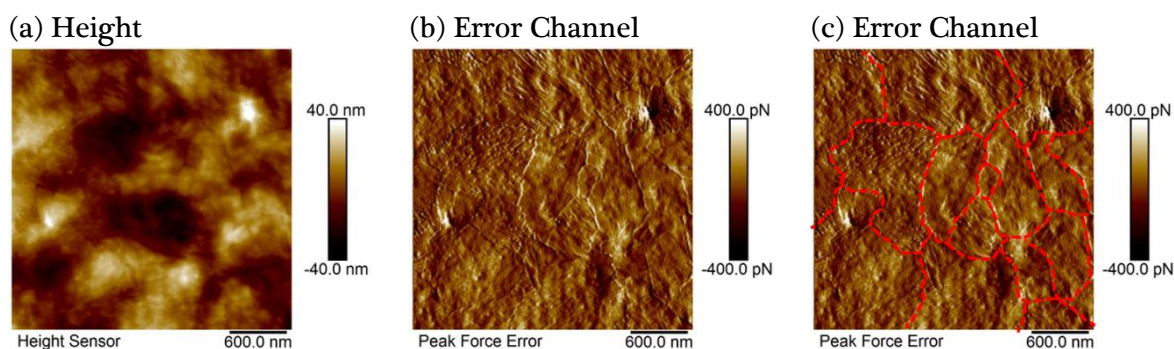


**Figure 6.24.** AFM images of a  $3 \times 3 \mu\text{m}^2$  area of the sample TF1514. (a) Height, (b) and (c) Error Channel. The dashed red lines added on image (c) highlight the grain boundaries.

These grains affect the ionic conductivity of electrolytes based on block copolymers. When the lithium ions move between the electrodes, the ionic conductivity can take place in two ways: intra-grain and inter-grain transport. Considering the intra-grain transport the key factors are the number of dimensions of the conductive pathway (two dimensions for a lamellar structure or 3D for a cylindrical or gyroid structure) and the orientation of the domains. For example, in a 2D lamellar system (Figure 6.25), only a fraction of the domains contribute positively to the transport of ions, which also depends on the orientation of the lamellae.<sup>272,273</sup> If the non-conductive block (red) is perpendicular to the arrival of the lithium ions, the transport will be stopped and consequently the conductivity will be zero (Figure 6.25 (c)).

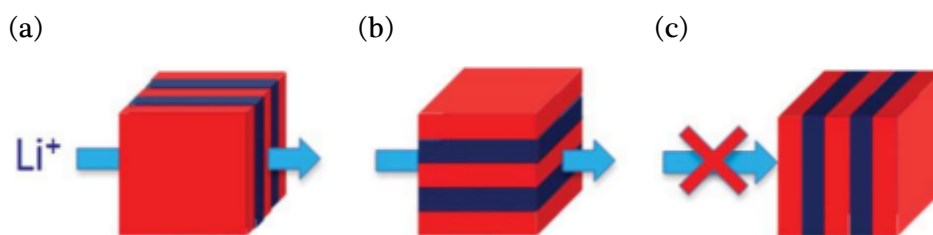


**Figure 6.25.** Schematic representation of the effect of domain orientation on the ionic transport for a lamellar morphology. The red domain representing the non-conductive phase and the blue domain the conductive phase.<sup>246</sup>

Considering the inter-grain transport, the overall ionic conductivity of the electrolytes will be lowered by the bending of the conductive channels (Figure 6.26 (b) ), by reducing their size between two grains or completely stopped if the orientation of the adjacent grain is in a perpendicular orientation (Figure 6.26 (c)).<sup>274</sup>

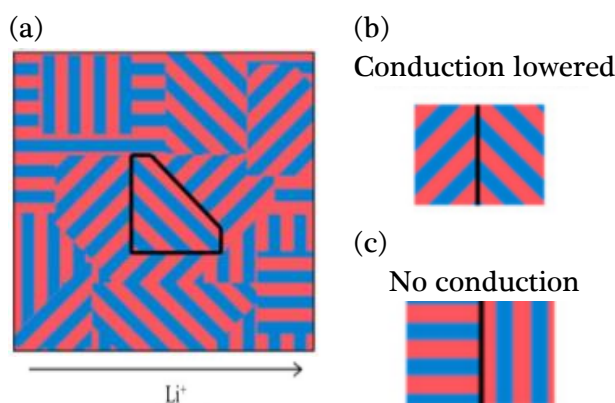


**Figure 6.26.** (a) Schematic representation of an electrolyte based on a block copolymer showing the discontinuity of the domains. Non-conductive domains are in red, the conductive domains in blue and grain boundaries in black. (b) Decrease in conductivity due to the presence of channel bending. (c) Absence of conduction due to the perpendicular orientation of two grains.<sup>275</sup>

Thus, the AFM images evidence that besides the presence of crystallinity, the presence of grain boundaries of self-assembled domains may limit the ionic conductivity.

### 3.3. Surface morphology and properties evolution with hydration degree

We have used a low spring constant AFM tip ( $k \sim 0.4 \text{ N/m}$ ) to probe the very top surface of the sample. In this case, only qualitative mechanical analysis is achieved. Figure 6.27 shows AFM complementary images of a  $3 \times 3 \mu\text{m}^2$  area of the “single-ion” sample. It is possible to notice four domains (the larger one being surrounded by a red dashed line) with different mechanical properties than the rest of the scanned area. These domains present high modulus (white on Figure 6.27 (b)) but at the same time high adhesion and high deformation (white on Figure 6.27 (c) and (d)). A lamellar structure can be observed on the deformation image. This is an unexpected and contradictory behavior, since a material with high modulus usually appears with low deformation. We assume that this contradiction may be caused by AFM measurement artifacts, since a strong adhesion can result in erroneous modulus and deformation calculation<sup>276–282</sup>. According to Ebenstein *et al.*<sup>282</sup> when the adhesion dominates the tip-sample interactions, nanomechanical models like Hertzian and DMT can underestimate the contact area and the effective load experienced by the sample, resulting in an overestimation of the sample modulus. This can explain why the modulus



measurement of is so high in the high adhesion domains. Still according to Ebenstein *et al.*<sup>282</sup> another possible source of uncertainty may lie in the assumption that the jump-to-contact point observed in the force-distance curves represents initial contact between the tip and the sample. Attractive surface forces can cause an early jump-to-contact, leading to overestimation of deformation from the force-distance curves.

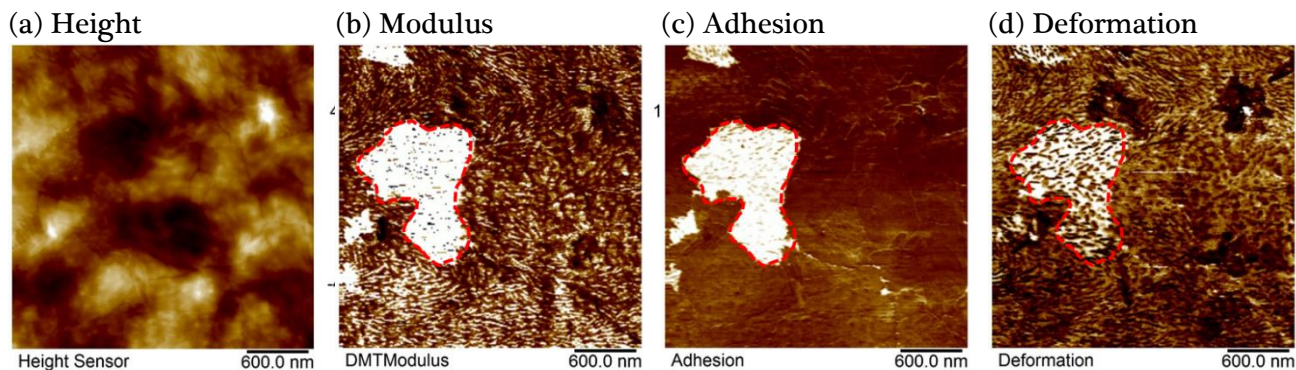


**Figure 6.27.** AFM images of a  $3 \times 3 \mu\text{m}^2$  area of the “single-ion” sample PSTFSILi-PEO-PSTFSILi. (a) Height, (b) Modulus, (c) Adhesion and (d) Deformation. The red dashed line delimits a grain with different behavior compared to the others.

Keeping in mind the possible artifact observed by AFM, we can analyze the AFM images obtained. Figure 6.28 shows the deformation image with a relative scale. The lamellae inside the domain appear with a lower relative deformation (about 0.2 nm/black on the image) than the lamellae out of the domain (about 0.68 nm/brown). However, the phase excluded from the PEO lamellae appears with higher deformation (about 1.54 nm/white) than for the equivalent phase on the adjacent grains (about 1.18 nm/yellow), but with higher modulus and adhesion, as shown previously on Figure 6.27. This can be the sign that the lamellae inside these particular domains are directly exposed to the air (and to the AFM tip) while the rest of the sample present a soft top layer giving a slightly higher deformation above the lamellae. We observed by AFM the progressive disappearance of the high modulus, high adhesion and high deformation domains, when the originally dry sample equilibrates with the relative humidity of the room. Figure 6.29 shows AFM Adhesion images of a  $10 \times 10 \mu\text{m}^2$  area of the “single-ion” sample with the evolution of two different domains. One can see that the high adhesion zones shrink over time until their complete disappearance after about 8 hours. The diameter of the high adhesion domain pointed by the red arrow decreased linearly over time at a rate of about 275 nm per hour. The sample was subsequently dried at room temperature under nitrogen flux for 2 days and the phenomenon could be observed again. We therefore assume that the soft top layer that grows at the surface of the sample is composed of adsorbed water and amorphous PEO mixed with PSTFSILi.

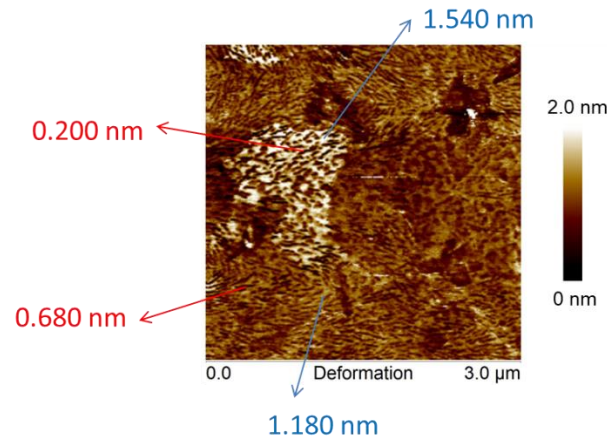


**Figure 6.28.** AFM deformation image of a  $3 \times 3 \mu\text{m}^2$  area of the “single-ion” sample PSTFSILi-PEO-PSTFSILi. Red arrows indicate the mean values of deformation of the lamellae inside the domain and on the adjacent grains. Blue arrows indicate the mean values of the mixture PEO+PSTFSILi inside the domain and on the adjacent grains.

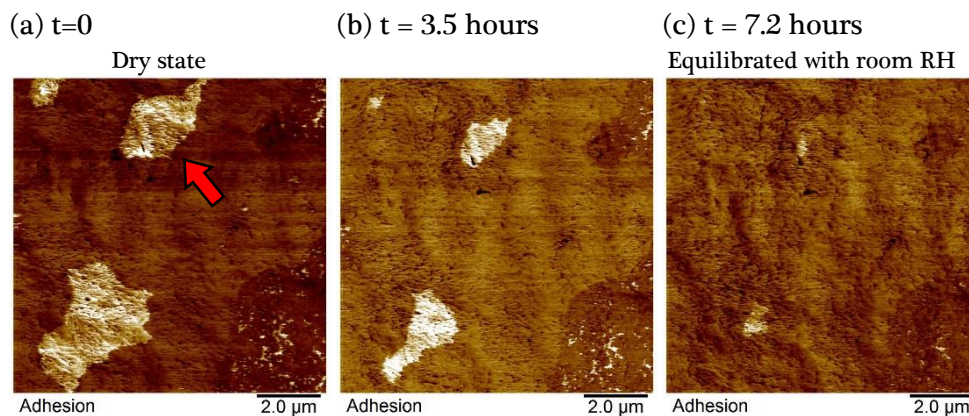


**Figure 6.29.** AFM adhesion images of a  $10 \times 10 \mu\text{m}$  area showing the evolution of the high adhesion grains with time. (a) Initial state,  $t=0$ ; (b) after 3.5 hours and (c) after 7.2 hours.

To explain the presence of a much stronger adhesion on the amorphous PEO mixed with PSTFSILi surrounding the crystalline PEO lamellae inside of the dry domains, we propose the following interpretation: in the dry state the  $\text{CF}_3$  groups of PSTFSILi block can strongly interact with the AFM tip, whereas this specific interaction is absent when the sample is hydrated through water adsorption from the air. Houston *et al.*<sup>283</sup> have shown that a self-assembled monolayer film terminated by  $\text{CF}_3$  end group presented an increase in adhesion by almost a factor of 4 compared to  $\text{CH}_3$  end groups, as measured by interfacial force microscope (IFM) for the interaction between the films and a tungsten tip. This interpretation of the AFM measurements can lead to a schematic representation of the sample’s surface, presented on Figure 6.30.

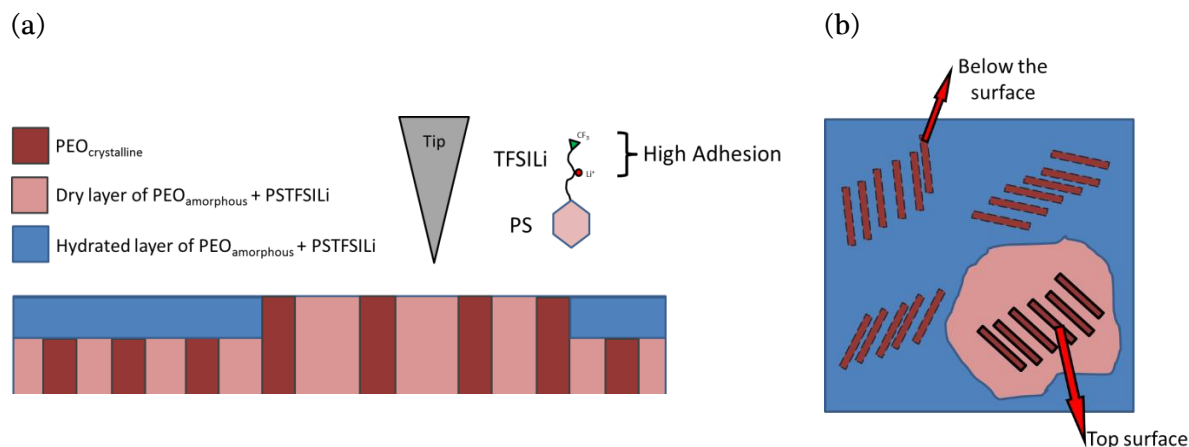


**Figure 6.30.** Schematic representation of the surface properties of the “single-ion” sample PSTFSILi-PEO-PSTFSILi. (a) Side view and (b) Top view

As evidenced by Figure 6.29, the hydration degree (equilibrium with room RH) of the sample can change the mechanical behavior of the surface of these domains. One hypothesis is that when the crystalline PEO at the surface equilibrates with the room relative humidity, part of its crystallinity is broken and the mixture of amorphous PEO and PSTFSILi blocks is hydrated. The hydrophobic  $\text{CF}_3$  groups turn away from the hydrated surface, decreasing adhesion. This change in crystalline order takes place from the edges to the interior of the domains because, in general, polymers at the edges of crystalline domains can relax more easily, once they have fewer neighbors and hence experience fewer constraints. Consequently, they can reduce their number of chain folds much faster than molecules inside the domains.<sup>267</sup> This causes the gradual increase of hydration of the amorphous PEO and PSTFSILi blocks mixture, decreasing the local adhesion (no more  $\text{CF}_3$  groups at the surface). This hypothesis is schematically presented on Figure 6.31.

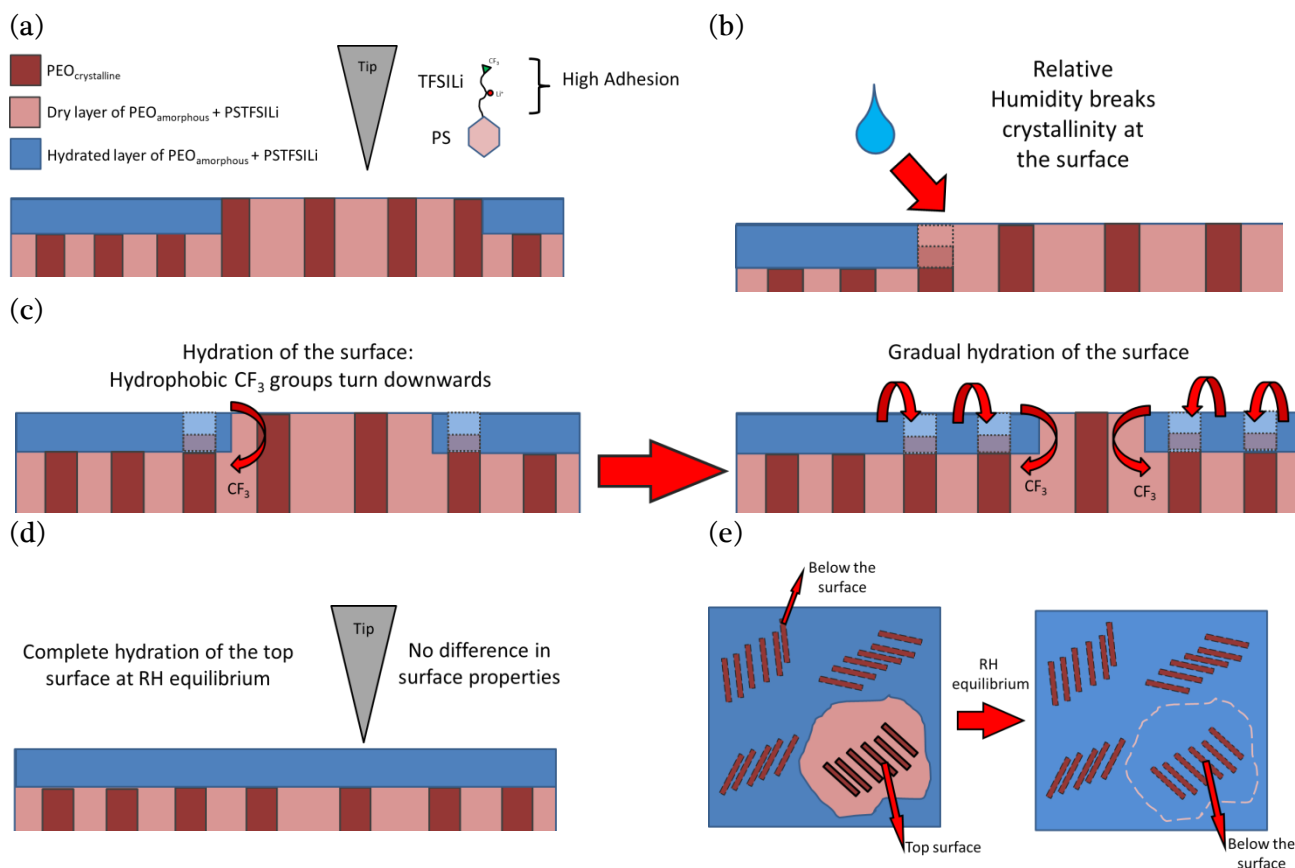


**Figure 6.31.** Schematic representation of the effect of hydration on the surface properties of the “single-ion” sample PSTFSiLi-PEO-PSTFSiLi. (a) Excluded PSTFSiLi blocks from the crystalline PEO at the surface. (b) Water from the relative humidity breaks the crystallinity of the PEO chains at the edge of the grain boundary. (c) The PSTFSiLi blocks solubilize in the amorphous PEO gradually from the edge to the interior. (d) Complete solubilization of the PSTFSiLi blocks in the amorphous PEO makes the modulus, adhesion and deformation signals drop. (e) Top view of the schematic representation showing the dry state and after RH equilibrium.

Raman spectroscopy could be able to provide valuable information to clarify if the local surface properties of these grains are in accordance with the hypothesis. However, due to the limited Confocal Raman resolution ( $1 \mu\text{m}^2$ ), it will not be possible to probe the chemical signature of the surface of these domains. To address this hypothesis, we propose as future work a co-localized AFM/Raman analysis using a TERS instruments, due to the high resolution and sensitivity of this technique. The experiments must be first done with the sample in a dry state and then in equilibrium with the room conditions (Relative Humidity of about 50%). After equilibration, we might be able to verify if the local chemistry of these grains change (presence of CF<sub>3</sub> groups or PEO crystallinity) have changed.

The co-localized AFM/Raman analyses using the Confocal Raman microscope can be used to probe heterogeneities in a bigger scale, such as possible changes on the membranes’ morphologies and chemistry after cycling in the batteries.

#### 4. Conclusions of Chapter 6

The objective of this study was to reveal the bulk morphology of new Lithium batteries electrolytes made of PEO based copolymers with different structures.

An innovative strategy had to be developed for sample preparation of these materials by cryo-ultramicrotomy due to the high sensibility of these copolymers to water. Thanks to the achieved developments we were able to obtain suitable samples for AFM analysis (cryo-ultramicrotomed surface of the membrane) and also ultra-thin sections for complementary Electron Microscopy analysis (TEM/STEM). This developed technique is robust and should be used for sample preparation for further studies on all kinds of samples, avoiding contact with water and any hydration effect.

Morphological analyses were done by AFM with the PeakForce QNM mode on PS-PEO-PS copolymers with different compositions and doped with lithium salt. Images of the non-doped copolymer showed a very regular lamellar structure, except for some localized heterogeneities where apparently remnant products of the synthesis could break the regularity of the morphology. The effect of the LiTFSI salt in the morphology of the electrolytes could be evidenced, with the partial breakdown of the lamellar morphology regularity. Furthermore, we observed an orientation of the lamellae perpendicular to the membrane's surface, probably related to the processing of the electrolyte, which can have an impact on the conductivity. The inter-domain distances could be measured directly from the modulus images, by the nanomechanical differences between the phases. The morphologies revealed by AFM could provide a clear morphological determination when the SAXS was not conclusive.

Samples with modified PEO blocks were analyzed. The impact of the PEO block cross-linking was evaluated by the nanomechanical properties of the different phases. We could verify the general trend of increasing modulus with the cross-linking degree and PS content of the samples, in accordance with macroscopic tensile tests previously done with similar samples. The increase on the spacing between the phases with the increasing length of the PEO block and the consequentially drop of modulus was also observed.

The study of a "single ion" copolymer revealed a different phase separation morphology, in which lamellar stacks of crystalline PEO are surrounded by a mixture of amorphous PEO mixed with the PSTFSILi block. The presence of grain boundaries of self-assembled domains was evidenced in the thickness of the material. Domains with contradictory surface nanomechanical properties (simultaneously high modulus, adhesion and deformation) were identified and the origins of this unexpected behavior were discussed. Nevertheless, the nanomechanical properties of these domains were followed over time and we could verify their evolution until the equilibrium with the room relative humidity. A hypothesis to explain this phenomenon is the presence of  $\text{CF}_3$  groups from the PSTFSILi blocks, in the dry state, that can strongly interact with the tip. These interactions gradually decrease with the hydration degree of the surface through water adsorption from the air. Complementary high resolution chemical analysis by TERS is proposed as future work in order to address this hypothesis.

#### 4.1. Summary of Conclusions of Chapter 6

Sample preparation by cryo-ultramicrotomy was achieved for highly water sensitive samples, avoiding any morphological/structural changes due to the melting of ice issued from frost deposition

The addition of salt in the morphology of PS-PEO-PS copolymers induces a partial breakdown of the lamellar regularity as evidenced by AFM modulus images of the bulk of the membranes

The lamellae near the outer surface of the PS-PEO-PS membranes are longer and perpendicular to the surface when compared to the lamellae in the bulk, probably related to the processing method of the electrode

The inter-domain distances could be measured directly from the AFM modulus images, by the nanomechanical differences between the phases, complementing SAXS analyses

The direct observation of the morphologies by AFM could provide a clear morphological determination when the SAXS was not conclusive.

Nanomechanical measurements of modified PS-PEO-PS was achieved, revealing an increasing modulus with the cross-linking degree and PS content of the samples

The morphology of the “single-ion” copolymer was revealed by AFM modulus images and its interpretation was possible thanks to complementary SAXS analyses

There are grain boundaries of self-assembled domains in the thickness of the “single-ion” copolymer

The surface nanomechanical properties of self-assembled domains change over time until equilibrium with the room relative humidity

Hypothesis: The strong interactions of  $\text{CF}_3$  groups from the PSTFSILi blocks with the AFM tip may decrease with the hydration degree, causing the modification of the nanomechanical properties. Analysis by TERS is proposed as future work in order to address this hypothesis

## 5. Conclusions du Chapitre 6 en Français

L'objectif de cette étude était de révéler la morphologie de nouvelles électrolytes à piles au lithium constituées de copolymères à base de PEO avec différentes structures.

Une stratégie innovante devait être développée pour la préparation des échantillons de ces matériaux par cryo-ultramicrotomie en raison de la grande sensibilité de ces copolymères à l'eau. Grâce aux développements réalisés, nous avons pu obtenir des échantillons appropriés pour l'analyse AFM (surface cryo-ultramicrotomée de la membrane) et aussi des sections minces pour une analyse complémentaire de microscopie électronique (TEM / STEM).

Des analyses morphologiques ont été effectuées par AFM avec le mode PeakForce QNM sur des copolymères PS-PEO-PS avec différentes compositions et dopés avec du sel de lithium. Les images du copolymère non dopé ont montré une structure lamellaire très régulière, à l'exception de certaines hétérogénéités localisées où les produits apparemment restants de la synthèse pourraient rompre la régularité de la morphologie. L'effet du sel LiTFSI dans la morphologie des électrolytes pourrait être mis en évidence, avec la rupture partielle de la régularité de la morphologie lamellaire. En outre, nous avons observé une orientation des lamelles perpendiculaires à la surface de la membrane, probablement liée au traitement de l'électrolyte, ce qui peut avoir une incidence sur la conductivité. Les distances inter-domaines peuvent être mesurées directement à partir des images de module, par les différences nanomécaniques entre les phases. Les morphologies révélées par l'AFM pourraient donner une détermination morphologique claire lorsque la SAXS n'était pas concluante.

Les échantillons avec blocs PEO modifiés ont également été analysés. L'impact de la réticulation du bloc PEO a été évalué par les propriétés nanomécaniques des différentes phases. Nous pourrions vérifier la tendance générale de l'augmentation du module avec le degré de réticulation et la teneur en PS des échantillons, conformément à des essais de traction macroscopiques précédemment réalisés avec des échantillons similaires. L'augmentation de l'espacement entre les phases avec la longueur croissante du bloc PEO et conséquemment une chute de module ont été également observés.

L'étude d'un copolymère "mono-ion" a révélé une morphologie de séparation de phase différente, dans laquelle des piles lamellaires de PEO cristallin sont entourées d'un mélange de PEO amorphe mélangé avec le bloc PSTFSILi. La présence de limites de grain des domaines auto-assemblés a été mise en évidence dans l'épaisseur du matériau. Des domaines ayant des propriétés nanomécaniques de surface contradictoires (simultanément, module élevé, adhérence et déformation) ont été identifiés et les origines de ces comportements inattendus ont été discutées. Néanmoins, les propriétés nanomécaniques de ces domaines ont été suivies au fil du temps et nous pourrions vérifier leur évolution jusqu'à l'équilibre avec l'humidité relative de la pièce. Une hypothèse pour expliquer ce phénomène est la présence de groupes  $CF_3$  sur les blocs PSTFSILi, qui peuvent fortement interagir avec la pointe, à l'état sec. Ces interactions diminuent progressivement avec le degré d'hydratation de la surface par adsorption d'eau de l'air. Une analyse chimique complémentaire de haute résolution par TERS est proposée comme un travail futur afin de répondre à cette hypothèse.

### 5.1. Résumé des Conclusions du Chapitre 6 en Français

La préparation d'échantillons par cryo-ultramicrotomie a été obtenue pour des échantillons fortement sensibles à l'eau, évitant tout changement morphologique/structurel dû à la fonte de la glace issue du dépôt de givre au cours de la préparation de l'échantillon

L'addition de sel de Lithium dans la morphologie des copolymères PS-PEO-PS induit une rupture partielle de la régularité lamellaire, comme en témoignent les images AFM de module

Les lamelles près de la surface extérieure des membranes PS-PEO-PS sont plus longues et perpendiculaires à la surface par rapport aux lamelles dans le volume de la membrane, probablement liées au procédé de mise en forme de l'électrode

Les distances inter-domaines peuvent être mesurées directement à partir des images AFM de module, par les différences nanomécaniques entre les phases, complétant les analyses SAXS

L'observation directe des morphologies par AFM a pu fournir une détermination morphologique claire lorsque le SAXS n'était pas concluant.

Les mesures nanomécaniques du PS-PEO-PS modifié ont été réalisées, révélant un module croissant avec le degré de réticulation et la teneur en PS des échantillons

La morphologie du copolymère "single-ion" a été révélée par des images AFM de module et son interprétation était possible grâce à des analyses SAXS complémentaires

Il existe des limites de grain des domaines auto-assemblés dans l'épaisseur du copolymère "single-ion"

Les propriétés nanomécaniques de surface des domaines auto-assemblés changent avec le temps jusqu'à l'équilibre avec l'humidité relative de la pièce

Les fortes interactions des groupes  $\text{CF}_3$  des blocs PSTFSILi avec la pointe AFM peuvent diminuer avec le degré d'hydratation, provoquant la modification des propriétés nanomécaniques de surface. L'analyse par TERS est proposée comme un travail futur afin de répondre à cette hypothèse






# CONCLUSIONS

---

## GENERAL CONCLUSIONS

The complex polymeric systems' deep understanding is important and challenging for the development of new engineering solutions. In order to elucidate the process-structure-properties-durability interplays, co-localization of chemical, physical and morphological information is essential. Although challenging, it should bring direct and uncontroversial answers. The surface of a material is not always representative of its bulk properties, for example when considering the distribution of charges, morphology profiles and effects of ageing. Therefore, the characterization of both the surface and the bulk is of prime importance to design more efficient materials, making possible the optimization of fabrication processes, the characterization of the achieved properties and the understanding of degradation/ageing. This dual characterization becomes even more critical for thin polymeric materials (<100  $\mu\text{m}$ ) such as films and membranes, which can present accentuated properties profiles throughout their thickness. The surface and bulk contributions on the final properties can therefore be very distinct and critical for the materials performances, but it implies technical challenges to access and distinguish surface and bulk contributions.

The main objective of this thesis was to develop an experimental methodology of characterization capable of providing quantitative structural/morphological analyses, such as spatial distribution of phases, concentration (or abundance) of chemical species, nanomechanical properties, identification of specimens and statistical analyses (average domains sizes and inter-domain distances), at scales from tens of nanometers to tens of microns. At the center of our characterization strategy, we aimed the co-localization of morphological, nanomechanical and chemical information using a special setup combining Atomic Force Microscopy and Confocal Raman spectroscopy. The challenge was to achieve a precise repositioning of the sample under each microscope. Indeed, we have chosen to combine two of the best commercially available instruments but not specifically designed for co-localized analysis.



**AFM** Resolution : nm

Surface Analysis :

Information {

- Topographic
- Mechanic (PFQNM)
- Thermo Mechanic

**Confocal Raman** Resolution :  $\mu\text{m}$

Confocal Analysis (Bulk and Surface) :

Information {

- Chemistry
- Structure
- (orientation, crystallinity..)

Co-localization's CHALLENGE !

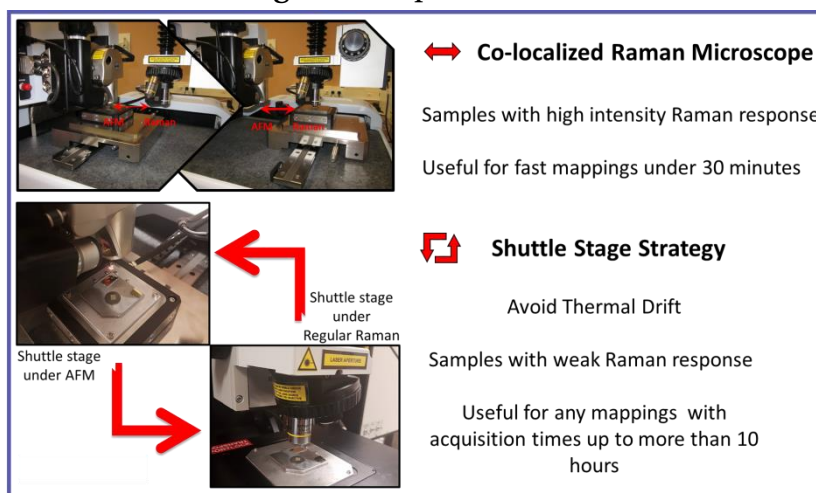
Control of:

- System stability
- Mechanical Vibrations
- Thermal Drift

Substantial improvements had to be performed to allow the co-localization of AFM/Raman information:

- A specially designed active piezoelectric table had to be installed under the AFM to suppress the noise from mechanical vibrations and operation of the Raman spectrometer;
- To limit the effects of thermal drift caused by temperature variations in the room, we replaced the feet of the Raman spectrometer to an alloy with low thermal expansion coefficient.

Finally, two different strategies were developed for co-localization (using the two Raman microscopes) depending on the sample's Raman response intensity. For samples that respond intensely to Raman, the AFM motorized stage is simply used to move the sample from the AFM to the Co-localized Raman microscope, and reciprocally. For polymers, which respond weakly to Raman, mapping acquisition time can be up to 10 hours (with dimensions of  $10 \times 10 \mu\text{m}^2$  corresponding to 441 points). In this case, a lateral thermal drift as small as few  $\mu\text{m}$ 's over several hours, makes mapping impossible due to distortions during the analysis. This is critical when using the Co-localized Raman Microscope, since the sample is placed on the AFM's stage and is thus subjected to the thermal drifts existing between both instruments. Therefore, a specific strategy was developed using a shuttle stage that allows transferring the sample between the AFM and the Regular Raman Microscope, allowing mappings with unlimited acquisition times. To limit the repositioning displacement (in X, Y and also Z direction), we have milled targets on the surface of the sample holders, which improved the co-localization precision (error of less than  $3 \mu\text{m}$  in both x and y directions). Such a small error can then usually be corrected when superposing AFM and Raman images.



The optimization of the system setup was essential, but not sufficient for proper co-localized characterization. A proper sample preparation was necessary in order to achieve the best performances with each instrument, i.e., sensitivity and spatial resolutions. At the same time, it must comply with sample quality requirements for characterization such as: access to the complete cross-section of the material (from the surface to the bulk) and no mechanical, thermal, chemical, structural or morphological modification during preparation. Cryo-ultramicrotomy was chosen as the best sample preparation method for our strategy, providing a suitable sample for both AFM and Raman analyses (low roughness, surface parallel to the sample holder) and preserving the intrinsic properties of the sample. Furthermore, the technique opens the possibility of multiple complementary analyses by Electron Microscopies (SEM, TEM and STEM) or  $\mu$ -ATR-FTIR for example.

Several technical limitations had to be addressed in order to make the sample preparation by Cryo-Ultramicrotomy possible. Among them, we highlight:

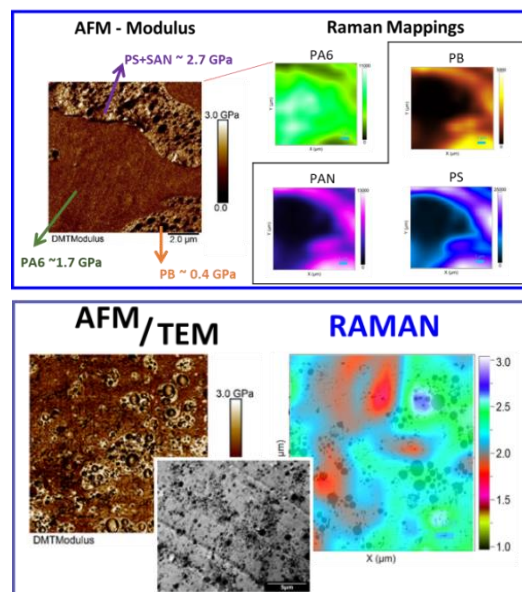
- The adaptation of a specific sample holder to allow for the preparation of thin membranes without embedding, suppressing any chemical modification (reaction/diffusion of the embedding medium);
- For water sensitive samples, a strategy was developed for suppression of frost deposition on the sample's surface when warming up to room temperature in order to avoid any morphological modification due to the sample swelling or solubilization;
- The use of inert polymer backings as mechanical reinforcements to achieve  $\mu$ -ATR-FTIR cross-section analysis of thin membranes.

During this Ph.D. work, three different polymer systems were studied: 1) blends based on Polyamide 6 (PA6) and Acrylonitrile-Butadiene-Styrene (ABS), compatibilized with a Styrene-Acrylonitrile grafted with Maleic Anhydride (SAN-MA) additive; 2) hybrid membranes for PEMFC application based on a sulfonated polyetheretherketone (sPEEK) and an active network prepared by sol-gel chemistry; and 3) block copolymers electrolyte based on PS-PEO-PS for lithium battery application.

### 1) Compatibilization of Polymer Blends based on PA6/ABS

The first study, presented in Chapter 4, was focused on the impact of the compatibilizer and the mixing protocols on the morphology of an immiscible PA6/ABS blend. The main results are:

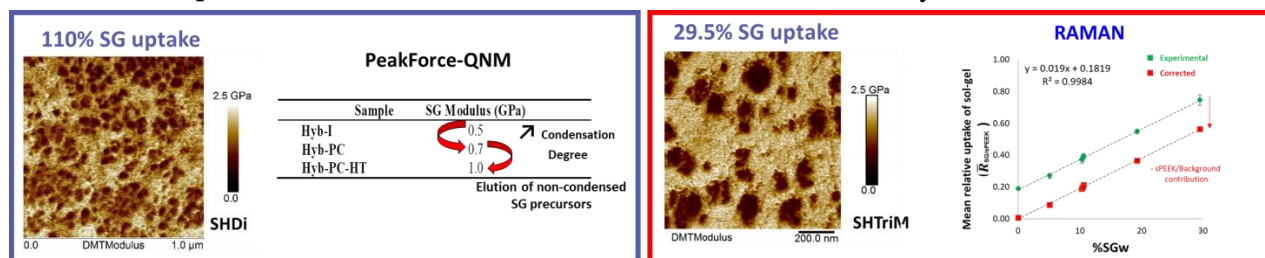
- The association of the AFM nanomechanical properties and the Raman chemical analysis can provide unambiguous identification of the components of the studied system. The nanomechanical analysis of the immiscible PA6/ABS blend was in agreement with the literature.
- The addition of the SAN-MA copolymer at different steps of the blending can develop different final morphologies (particle-in-matrix or almost co-continuous), impacting the rheology of the melted blends and therefore the dispersion and distribution of the sub-phases of the ABS at nanometric scale.
- The presence of the compatibilizer favors the formation of the  $\gamma$  crystalline phase, which amount and distribution depend on the blending protocols.



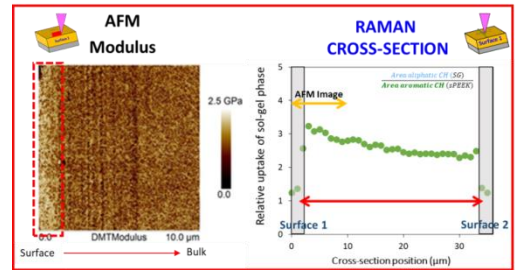
### 2) Hybrid Membranes for Fuel Cell

The second study, presented in Chapter 5, was focused on the fabrication of hybrid membranes for Fuel Cell based on two different sol-gel precursors. The main goal of this study was to qualify the impact of each step of the fabrication process (impregnation/condensation and thermal treatments) on the membranes' physical, nanomechanical and chemical properties, as well as their stability over time, using co-localized AFM/Raman and complementary analyses.

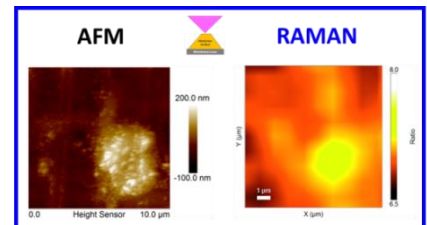
- The morphology of different membranes was revealed by the mechanical properties of the different phases. Quantitative nanomechanical and chemical analyses were achieved;



- The formation of a depleted skin layer (lower SG concentration) about one micrometer thick was observed on both sides of the membranes whereas the SG phase concentration was almost constant through the rest of the membrane thickness;

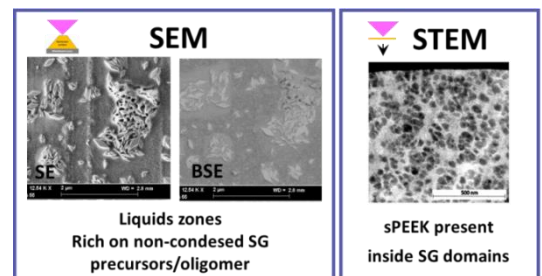


- Membranes on the early steps of fabrication exhibited on their cross-sectioned surface the diffusion and crystallization of water-soluble species from the SG phase into the atmospheric water condensed during the sample preparation.



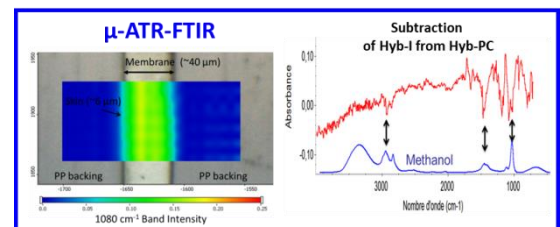
Crystals are chemically similar to the SG precursors:  
Non-condensed SG precursors/oligomers

Complementary Electron Microscopy analyses by SEM and STEM on the cryo-ultramicrotomed surfaces and the ultrathin sections collected also gave valuable information for the comprehension of the morphology and the process of diffusion and crystallization of the non-condensed SG precursors/oligomers.



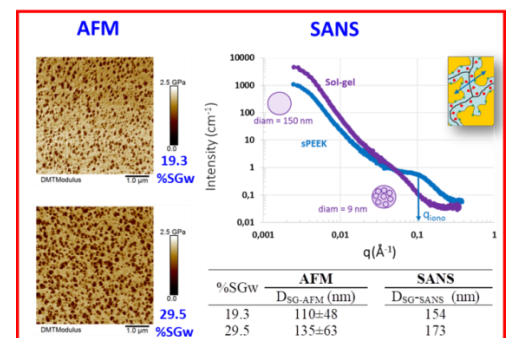
We have also adapted cryo-ultramicrotomy for complementary  $\mu$ -ATR-FTIR imaging of the cross-section of the hybrid membranes, which gave additional information about the membrane's processing:

- The post-condensation treatment increases the SG condensation degree evidenced by methanol elimination during this fabrication step.



Finally, we have allied morphological AFM analysis with another complementary technique, Small Angle Neutron Scattering (SANS), to go further into the comprehension of the material's structure. The morphology observed by AFM directed the choice of the fitting model used for the SANS analysis, which showed that:

- The SG phase presents a hierarchically organized system, composed of elementary particles which aggregate into round shape domains;
- The mean diameter of the SG aggregates measured by AFM ( $D_{SG-AFM}$ ) and by SANS ( $D_{SG-SANS}$ ) are in reasonable accordance considering the different averaging procedures. Both analyses confirm the increasing diameter of the SG domains with the SG uptake.



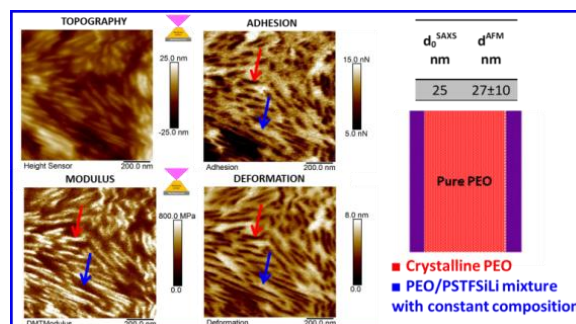
### 3) Copolymer Electrolytes for Lithium Batteries

The third study, presented in Chapter 6, focused on the morphological study of a series of triblock copolymers, used as polymer electrolytes in Lithium Metal Polymer (LMP) batteries. The addition of Lithium salt to the copolymer substantially increases its ionic conductivity but also its hydrophilicity, which makes difficult the sample preparation by cryo-ultramicrotomy for direct observation. The main developments were:

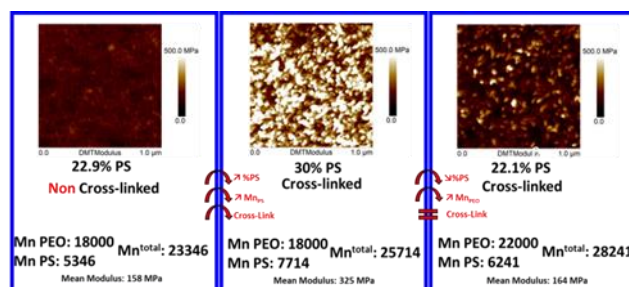
- An innovative strategy was developed for the cryo-ultramicrotomy procedure due to the material's high sensibility to water allowing obtaining suitable samples for AFM analysis (on the cryo-ultramicrotomed surface of the membrane) and also ultrathin sections for complementary Electron Microscopy analysis (TEM/STEM) avoiding their water-solubilization.

The three systems studied were based on PS-PEO-PS copolymers with Lithium salt or in "single-ion" form. The study focused on the nanomechanical and morphological analysis by AFM and its correlation with SAXS measurements. The main conclusions are the following:

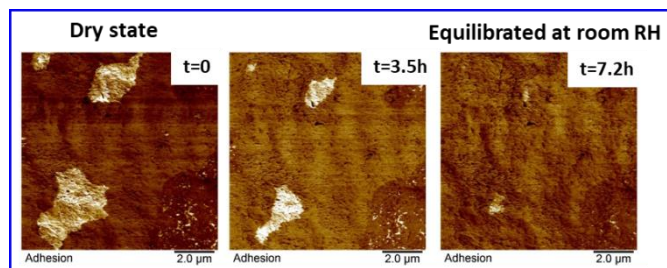
- The nanomechanical differences between the phases allowed morphological determination of the copolymers and measurement of the inter-domain distances. A good correlation with previously SAXS measurements was achieved;



- Quantitative nanomechanical measurements allowed following the evolution of the materials according to their chemical structure: effect of cross-linking and increasing length of PS and PEO blocks;



- The surface nanomechanical properties evolution from the dry state to the equilibrium with the room relative humidity was evidenced.



## Achievement of the Co-localization Strategy to study multiphase systems

For each of the three studies presented in this thesis, the AFM/Raman co-localization and the multi-technique strategy developed were useful for the acquisition of valuable information that could not be accessed by other means. This strategy can be applied to the study of a variety of different materials and can provide the following information:

### 1) Identification of phases

The association of the AFM nanomechanical properties and the Raman chemical analysis can provide unambiguous identification of the components of the studied system.

### 2) Distribution of phases (and additives)

The analysis of the phase's distribution on the material can be done by the direct association of AFM with Electron microscopies (SEM/STEM/TEM) data. This information can be correlated to fabrication processes, presence of additives and thermal treatments. Raman spectroscopy can provide additional information by probing the chemical signature of polymorphic phases or additives in the material, which cannot always be probed directly by nanomechanical properties.

### 3) From morphology to structural analysis

The nanomechanical differences between phases allow for direct observation of the nanostructure, measurement of inter-domain distances and correlation with analysis by complementary techniques such as SAXS and SANS, in order to go further into the comprehension of the material's structure. X-rays and Neutrons scattering techniques can provide additional information not probed by the nanomechanical differences evidenced by AFM. The association of these techniques allows for the complete morphological/structural comprehension of the material from nano to macroscopic scale, as exemplified by the characterization of the "single-ion" copolymers, for which the previous SAXS studies allowed the proper interpretation of the AFM images.

### 4) Co-localized quantitative nanomechanical and chemical analyses to follow the material

The developed strategy allows the chemical analysis of the cross-section of the material in order to qualify the impact of each step of fabrication on its physical, nanomechanical and chemical properties, as well as their stability over time. AFM nanomechanical measurements and Raman chemical analysis can be used qualitatively and quantitatively on the study of modifications in the chemical structure by cross-linking, additives, chemical treatments, annealing and ageing of polymeric materials. Complementary  $\mu$ -ATR-FTIR imaging on the cross-section of thin polymer membranes can also provide complementary information to Raman spectroscopy, revealing effects of undesired oxidation and chemical evolution after chemical/thermal treatments. The association of both techniques can be useful to optimize processes and identify degradation mechanisms to mitigate ageing effects.

### 5) Study of dynamic processes

Changes in morphology, nanomechanical and chemical properties of the samples can be followed in real time under different stimuli, such as humidity variations, addition of additives, temperature or processes such as crystallization. In this case, the kinetics of the phenomenon must be compatible with the frame-rate of the AFM images to be followed over time. The same kind of experiments can be performed under the Raman spectrometer by following specific bands related to functionalized groups, polymorphs or overall crystallinity under controlled conditions, for example, from zero humidity (under dry nitrogen flux) until 100% relative humidity. Raman spectroscopy is capable of acquiring spectra in less than a second in order to probe changes occurring in real time, being limited by the range of analysis and mainly by the intensity of the sample's Raman response.



## Perspectives

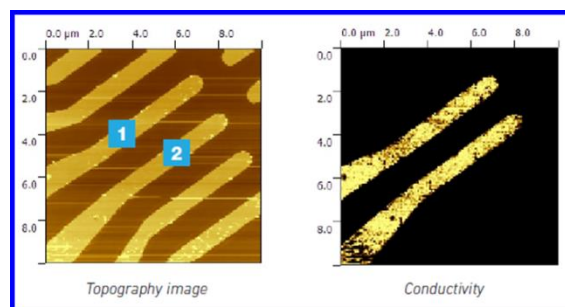
The potential for improving the amount of information that can be accessed using the AFM-Raman co-localized strategy lies on the capabilities of the different AFM modes of operation and complementary techniques. The main perspectives of work are listed as following:

### 1) Utilization of complementary AFM modes

Atomic Force Microscopy can probe a variety of properties of materials depending on the operation methods. Probing properties such as current, conductance, surface potential, and capacitance are increasingly important in a number of applications including research on semiconductors, solar cells and batteries, conductive polymers and nanoelectronics. Localized thermal analysis can also be of interest on the study of the effects of ageing in the material. Among the modes of operation we highlight three modes that can be used in addition to PeakForce QNM in order to help the comprehension of the process-structure-properties interplays and enlarge the range of studied materials:

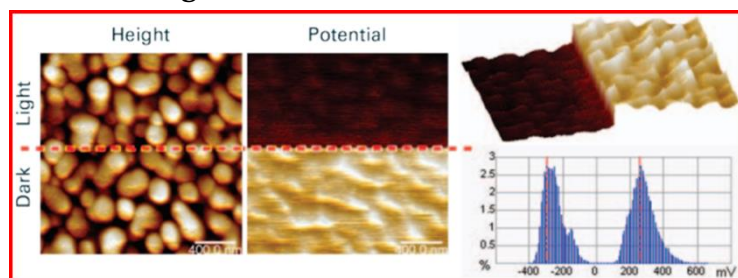
- **Conductive AFM (C-AFM):**

In this mode, a bias voltage is applied between tip and sample, allowing for simultaneously measurement of material's topography and the electric current flow at the contact point of the tip with the sample's surface. This technique can be useful for identifying and characterizing conductive pathways in polymer composites and electrolytes. These capabilities may be of interest on the imaging of ion conductivity of the hybrid membranes for Fuel Cell and copolymer electrolytes for lithium batteries in their cross-section rather than the surface, as well as nanocomposites containing carbon nanotubes and piezoelectric materials.<sup>284-288</sup>



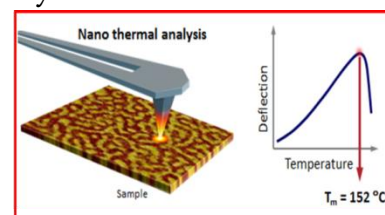
- **Kelvin probe force microscopy (KPFM):**

This mode images the surface potential distribution of a sample without direct electrical tip-sample contact. Applications include imaging the Kelvin potential or work function of a surface and measuring applied voltage differences between conductors. This mode can be associated with Peak Force (PeakForce KPFM™) in order to acquire simultaneously, highly correlated nanoscale topography, electrical and mechanical property mapping over a wide range of samples, such as organic (semi)conducting materials for thin film transistors, organic blends for photovoltaics and electrode materials, which can present surface potential variations under light/dark conditions attributed to changes in physical and chemical properties including particle size, phase of the surface layer and nanocrystalline deposits.<sup>289,290</sup>



- **Nano Thermal Analysis (Nano-TA):**

This mode enables high resolution thermal characterization with a spatial resolution of about 100 nm to correlate morphologic information to the local thermal properties of a material. Rather than a sample-averaged response as given by conventional thermal methods, such as differential scanning calorimetry (DSC), thermomechanical analysis (TMA), and dynamic mechanical analysis (DMA), Nano-TA can provide information on localized components/defects and profiles of thermal properties on the cross-section of coatings, films and membranes.<sup>291–295</sup>



The association of these different modes of operation with the nanomechanical properties given by the PeakForce QNM mode and chemical analysis by Raman can therefore be of interest to study a variety of polymeric materials.

## 2) Electron Microscopy modes and characterization of water-sensitive samples

Electron microscopy techniques such as SEM, TEM and STEM open a wide range of possibilities in terms of complementary characterization with the AFM-Raman co-localized strategy. Energy Dispersive X-ray Spectroscopy (EDS) and Electron Energy Loss Spectroscopy (EELS) are useful techniques for elemental analysis (atomic number  $Z > 10$ ) and can be of interest for the analysis of the interface of chemically modified nanofillers in nanocomposites and hybrid materials.

The developments achieved during the study of polymer electrolytes for Lithium batteries open new possibilities for the characterization of water-sensitive samples. The morphological studies by TEM/STEM on thin sections collected by cryo-ultramicrotomy are still to be done and will impose challenges on the control of the imaging parameters to avoid electron beam damage.

## 3) Studies of ageing

The developed strategy allying nanomechanical characterization by AFM with qualitative and quantitative chemical characterization by Raman spectroscopy and  $\mu$ -ATR-FTIR imaging is a powerful tool for the study of aged materials and degradation processes. Considering the hybrid membranes for Fuel Cell, our next objective is to use this analysis strategy to quantify the physical and chemical modifications induced into SG/sPEEK hybrid membranes after realistic Fuel Cell operation. The same strategy can be applied to the study of copolymers for Lithium batteries after cycling in order to first understand the chemical/structural changes induced by ageing and then to optimize the structure and design ageing mitigation strategies.

## 4) Correlation of microstructural analysis with final properties

Finally, further research must be performed to correlate the fundamental microstructural knowledge of the materials to their functional properties. In the case of the compatibilized PA6/ABS blends, for example, the effect of the different morphologies and distribution of phases should have an impact on the mechanical strength, impact resistance and heat distortion temperature of the blends, which is still to be studied. In the same context, the effects of different SG precursors, their amount and distribution in the hybrid membranes must be correlated to their proton conductivity, swelling behavior and mechanical properties in order to adjust the fabrication process to obtain membranes with optimum performances.


The work presented in this thesis has been valorized to the scientific community as follows:

- Publications**
- “AFM-Raman Co-localization Setup: Advanced Characterization Technique for Polymers” accepted for publication in the “International Journal of Polymer Analysis and Characterization” in September 2017
  - “Co-localized AFM-Raman: A powerful tool to optimize the Sol-Gel chemistry of Hybrid Polymer Membranes for Fuel Cell” accepted for publication in “Polymers” in January 2018
  - “New insights on the compatibilization of PA6/ABS blends: A co-localized AFM-Raman study” submitted to “Polymers” in November 2017
- Presentations**
- **Oral presentation** at the European Materials Research Society (E-MRS) 2017 Fall Meeting – Warsaw, Poland - 2017  
Title: Co-localized AFM-Raman on cryo-ultramicrotomed membrane cross-sections: A powerful tool to Optimize Hybrid PEM for Fuel Cell
  - **Poster presentation** at the International Conference on Advanced Energy Materials (AEM) – Guildford, England - 2017  
Title: Stabilized hybrid membranes for long-lived fuel cell. Presented by Natacha Huynh
  - **Oral presentation** at the 32<sup>nd</sup> International Conference of the Polymer Processing Society (PPS) – Lyon, France – 2016  
Title: A new process to convert proton exchange membranes into high performances and reliable hybrid membranes for fuel cell
  - **Poster presentation** at the 32<sup>nd</sup> International Conference of the Polymer Processing Society (PPS) – Lyon, France - 2016  
Title: AFM-Raman Co-localization setup: Advanced characterization technique for polymers
  - **Poster presentation** at the 4<sup>th</sup> International Soft Matter Conference (ISMC) – Grenoble, France - 2016  
Title: Advanced multitechnique characterization strategy: Cryo-ultramicrotomy allied with AFM-Raman and Electron Microscopy
  - **Oral presentation** at the 44<sup>th</sup> Colloque National du Groupe Français des Polymères (GFP) – Belvaux, Luxembourg - 2015  
Title: Co-localized AFM-Raman setup: a powerful tool to combine multi-technique and multiscale characterizations of polymer membranes
  - **Poster presentation** at the 44<sup>th</sup> Colloque National du Groupe Français des Polymères (GFP) – Belvaux, Luxembourg 2015  
Title: AFM-Raman and Electron Microscopies: Complementarities for polymer membrane characterization using cryo-ultramicrotomed cross-sections
  - **Poster presentation** at the European Polymer Conference (EUPOC) – Gargnano, Italy - 2015  
Title: Co-localized AFM-Raman setup: a powerful tool to study PEMFC membrane stabilization by active nano-networks
- Honours and awards**
- Award of **Best Poster Contribution** at the European Polymer Conference (EUPOC) - 2015

## CONCLUSIONS GENERALES EN FRANÇAIS

L'étude avancée de systèmes polymères complexes comme les mélanges compatibilisés, nanocomposites, copolymères à bloc, etc. est cruciale pour le développement de nouvelles solutions d'ingénierie. Afin d'élucider les relations « mise en œuvre-structure-propriétés-durabilité » de ces systèmes, la co-localisation d'informations chimique, physique et morphologique devient essentielle pour obtenir des réponses fiables. La surface d'un matériau n'est pas toujours représentative de ses propriétés globales, particulièrement en ce qui concerne la distribution des charges, les profils morphologiques et les effets de vieillissement. Par conséquent, la caractérisation de la surface et de l'intérieur des matériaux est également d'une importance primordiale pour concevoir des matériaux plus efficaces, permettant l'optimisation des processus de fabrication, la caractérisation des propriétés obtenues et la compréhension des processus de vieillissement. Cette double caractérisation devient encore plus critique pour les matériaux polymères minces (<100  $\mu\text{m}$ ) tels que les films et les membranes, qui peuvent présenter des variations de propriétés importantes dans leur épaisseur. Les contributions de la surface et du cœur sur les propriétés finales peuvent donc être très distinctes et critiques pour les performances des matériaux, mais leur caractérisation implique des difficultés techniques afin de distinguer les contributions de la surface et du cœur.

L'objectif principal de cette thèse était de développer une méthodologie expérimentale de caractérisation capable de fournir des analyses structurales/morphologiques quantitatives telles que la répartition spatiale des phases et leur analyse statistique (moyenne des tailles de domaines et des distances inter-domaine), l'identification et la mesure des concentrations des espèces chimiques, l'analyse des propriétés nanomécaniques, tout cela à des échelles de dizaines de nanomètres à des dizaines de microns. Au centre de notre stratégie de caractérisation, nous avons visé la co-localisation des informations morphologiques, nanomécaniques et chimiques par le couplage de la Microscopie de Force Atomique (AFM) et de la Microspectroscopie Confocale Raman. Le défi était de réaliser un repositionnement précis de l'échantillon sous chaque microscope. En effet, nous avons choisi de combiner deux des meilleurs instruments disponibles dans le marché mais pas spécifiquement conçus pour une analyse co-localisée.



**Co-localization's  
CHALLENGE !**

Control of:

- System stability
- Mechanical Vibrations
- Thermal Drift

**AFM** Resolution : nm

Surface Analysis :

Information — { Topographic  
Mechanic (PFQNM)  
Thermo Mechanic

**Confocal Raman** Resolution :  $\mu\text{m}$

Confocal Analysis (Bulk and Surface) :

Information — { Chemistry  
Structure  
(orientation, crystallinity..)

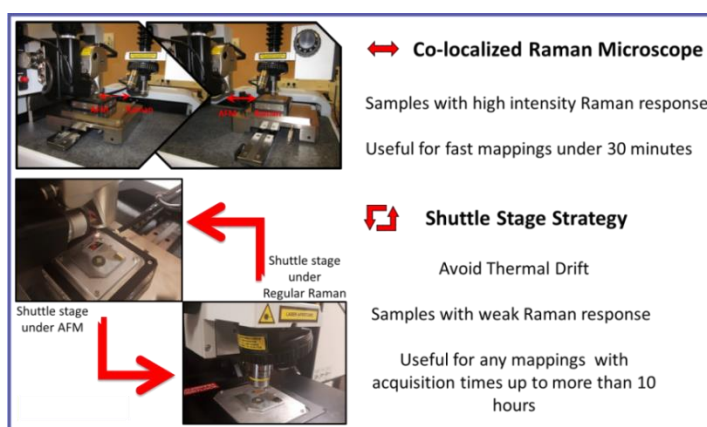
Des améliorations substantielles ont dû être effectuées pour permettre la co-localisation des informations AFM/Raman:

- Une table piézoélectrique active spécialement conçue a été installée sous l'AFM pour supprimer le bruit des vibrations mécaniques et du fonctionnement du spectromètre Raman;
- Pour limiter les effets de la dérive thermique causée par les variations de température dans la pièce, nous avons remplacé les pieds du spectromètre Raman.

Finalemment, deux stratégies différentes ont été développées pour la co-localisation (utilisant chacun des deux microscopes Raman) en fonction de l'intensité de réponse Raman de l'échantillon. Pour les échantillons qui répondent intensément au Raman, la platine motorisée AFM est simplement utilisée pour déplacer l'échantillon de l'AFM vers le microscope Raman co-localisé, et réciproquement. Pour les polymères, qui répondent faiblement au Raman, le temps d'acquisition des mappings peut atteindre jusqu'à plus de 10

heures (avec des dimensions de  $10 \times 10 \mu\text{m}^2$  correspondant à 441 points). Dans ce cas, une dérive thermique latérale aussi faible que quelques  $\mu\text{m}$  sur plusieurs heures, rend la cartographie impossible en raison de distorsions au cours de l'analyse. Ceci est problématique lors de l'utilisation du Microscope Raman Co-localisé, puisque l'échantillon est placé sur la platine AFM et est donc soumis aux dérives thermiques existant entre les deux instruments. Par conséquent,

une stratégie spécifique a été développée à l'aide d'une navette qui permet de transférer l'échantillon entre l'AFM et le Microscope Raman classique, permettant des mappings avec des temps d'acquisition illimités. Pour limiter le déplacement de repositionnement (en X, Y et aussi en direction Z), nous avons gravé des cibles sur la surface des supports d'échantillons, ce qui a amélioré la précision de la co-localisation (erreur inférieure à  $3 \mu\text{m}$  dans les directions x et y). Une erreur aussi faible peut alors être corrigée lors de la superposition d'images AFM et Raman.



L'optimisation de la configuration du système était essentielle, mais pas suffisante pour une caractérisation co-localisée efficace. Une préparation d'échantillon appropriée était nécessaire pour atteindre les performances ultimes de chaque instrument en termes de sensibilité et de résolution spatiale. La préparation d'échantillons devait aussi respecter les exigences de qualité de l'échantillon pour une caractérisation propre telles que: l'accès à la section transversale complète du matériau (de la surface au cœur) et aucune modification mécanique, thermique, chimique, structurelle ou morphologique lors de la préparation. La Cryo-ultramicrotomie sans enrobage a été choisie comme la meilleure méthode de préparation d'échantillon pour notre stratégie, fournissant un échantillon approprié pour les analyses AFM et Raman (faible rugosité et surface parallèle au support d'échantillon), en préservant les propriétés intrinsèques de l'échantillon. Par ailleurs, la technique ouvre la possibilité de multiples analyses complémentaires par microscopie électronique (SEM, TEM et STEM) ou par  $\mu$ -ATR-FTIR par exemple.

Plusieurs limitations techniques ont dû être dépassées afin de rendre possible la préparation d'échantillon par Cryo-Ultramicrotomy. Parmi celles-ci, nous soulignons:

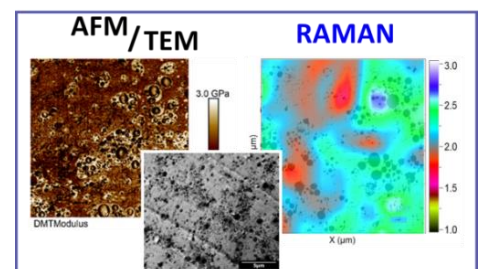
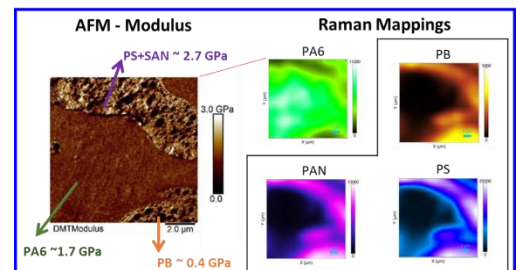
- L'adaptation d'un support d'échantillon spécifique pour permettre la préparation de membranes minces sans enrobage, en supprimant toute modification chimique (réaction/diffusion de la résine d'enrobage);
- Pour les échantillons sensibles à l'eau, une stratégie a été développée pour la suppression du dépôt de givre sur la surface de l'échantillon lors du réchauffement jusqu'à la température ambiante afin d'éviter toute modification morphologique due au gonflement ou à la solubilisation de l'échantillon;
- L'utilisation de renforts mécaniques inertes (polymères) pour obtenir une analyse  $\mu$ -ATR-FTIR de la coupe transversale de membranes minces.

La stratégie développée a été appliquée à trois systèmes polymères différents: 1) des mélanges polyamide 6 (PA6) / acrylonitrile-butadiène-styrène (ABS), compatibilisés avec un styrène-acrylonitrile greffé anhydride maléique (SAN-MA); 2) de membranes hybrides constituées d'une matrice polymère de type polyétheréthercétone sulfoné (sPEEK) et d'une phase inorganique chimiquement active préparée par chimie Sol-Gel (SG); 3) des copolymères à bloc de type PS-PEO-PS utilisés comme électrolytes pour les batteries lithium.

### 1) Compatibilisation des mélanges de polymères à base de PA6 /ABS

La première étude, présentée au chapitre 4, a porté sur l'impact du compatibilisant et des protocoles de mélange sur la morphologie d'un mélange PA6/ABS non miscible. Les principaux résultats sont les suivants:

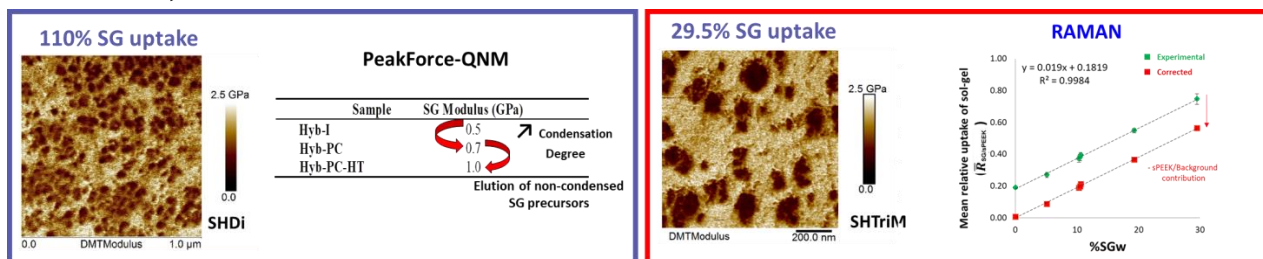
- L'association des propriétés nanomécaniques obtenues par AFM et l'analyse chimique Raman a pu fournir une identification sans ambiguïté des composants du système étudié. L'analyse nanomécanique du mélange PA6/ABS immiscible était en accord avec la littérature ;
- L'ajout du copolymère SAN-MA à différentes étapes du mélange peut développer différentes morphologies finales (particules dans matrice ou presque co-continues), ce qui affecte la rhéologie des mélanges fondus et donc la dispersion et la distribution des sous-phases de l'ABS à l'échelle nanométrique ;
- La présence du compatibilisant favorise la formation de la phase cristalline  $\gamma$ , dont la quantité et la distribution dépendent des protocoles de mélange.



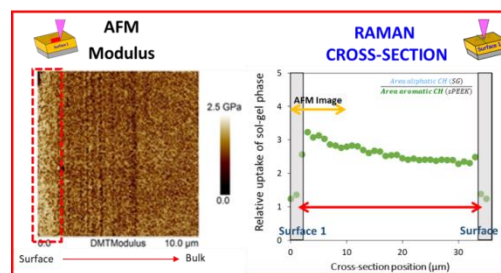
## 2) Membranes hybrides pour pile à combustible

La deuxième étude, présentée au chapitre 5, a porté sur la fabrication de membranes hybrides pour pile à combustible à base de deux précurseurs sol-gel différents. L'objectif principal de cette étude était de qualifier l'impact de chaque étape du processus de fabrication (imprégnation/condensation et traitements thermiques) sur les propriétés physiques, nanomécaniques et chimiques des membranes, ainsi que leur stabilité au fil du temps, en utilisant la co-localisation AFM/Raman et des analyses complémentaires.

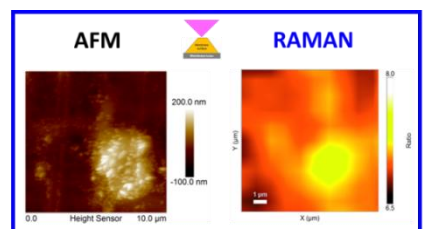
- La morphologie des différentes membranes a été révélée par les propriétés mécaniques des différentes phases. Des analyses nanomécaniques et chimiques quantitatives ont été réalisées;



- La formation d'une couche appauvrie (concentration SG inférieure) d'environ un micromètre d'épaisseur des deux côtés des membranes a été observée, alors que la concentration en phase SG était presque constante dans le reste de l'épaisseur de la membrane;

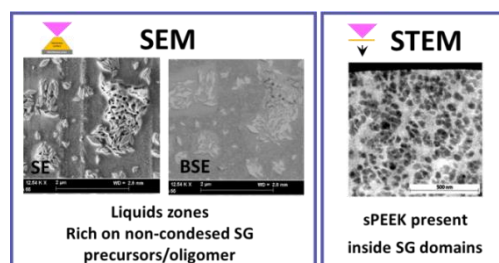


- Des membranes après les premières étapes de fabrication ont montré sur la surface de leur coupe transversale la diffusion et la cristallisation d'espèces hydrosolubles de la phase SG dans l'eau condensée après la coupe de l'échantillon.



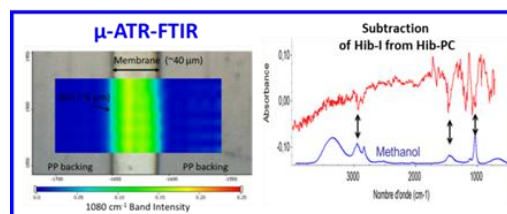
Non-condensed SG precursors/oligomers

Des analyses complémentaires de microscopie électronique par SEM et STEM sur les surfaces cryo-ultramicrotomées et les sections ultra-fines collectées ont également fourni des informations précieuses pour la compréhension du processus de diffusion et cristallisation des précurseurs/oligomères SG non condensés, et de la morphologie des membranes en général.



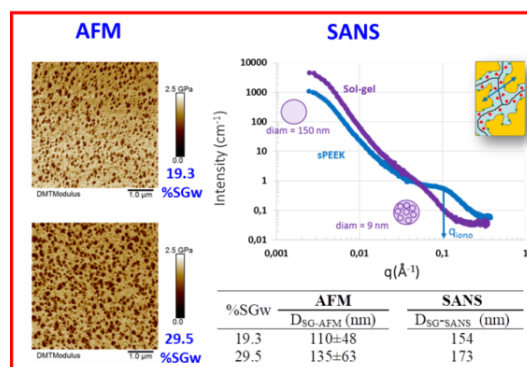
Nous avons également adapté la cryo-ultramicrotomie pour l'imagerie  $\mu$ -ATR-FTIR de la coupe transversale des membranes hybrides:

- Le traitement de post-condensation augmente le degré de condensation de la phase SG. Cela a été mis en évidence par l'élimination du méthanol au cours de cette étape de fabrication.



Finalement, nous avons allié l'analyse morphologique par AFM avec une autre technique complémentaire, la diffusion des neutrons à petit angle (SANS), pour aller plus loin dans la compréhension de la structure du matériau. La morphologie observée par AFM a orienté le choix du modèle utilisé pour l'ajustement des données SANS, qui ont montré que:

- La phase SG présente un système hiérarchiquement organisé, composé de particules élémentaires qui s'accumulent dans des domaines de formes arrondis;
- Le diamètre moyen des agrégats SG mesurés par AFM ( $D_{SG-AFM}$ ) et par SANS ( $D_{SG-SANS}$ ) est raisonnablement concordant, en considérant les différentes procédures de calcul de la moyenne. Les deux analyses confirment le diamètre croissant des domaines SG avec la teneur en SG.



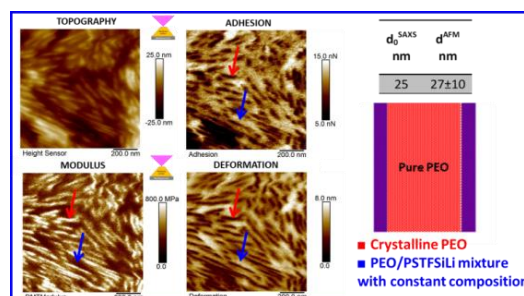
### 3) Électrolytes copolymères à bloc pour batteries lithium

La troisième étude, présentée au chapitre 6, a porté sur l'étude morphologique d'une série de copolymères tribloc, utilisés comme électrolytes polymères dans des batteries lithium (LMP). L'addition de sel de lithium au copolymère augmente considérablement sa conductivité ionique mais aussi son hydrophilie, ce qui rend difficile la préparation de l'échantillon par cryo-ultramicrotomie pour une observation directe. Les principaux développements ont été les suivants:

- Une stratégie innovante a été développée pour la procédure de cryo-ultramicrotomie en raison de la haute sensibilité du matériau à l'eau, permettant d'obtenir des échantillons appropriés pour l'analyse AFM (sur la surface cryo-ultramicrotomée de la membrane) et aussi des sections ultra-fines pour l'analyse complémentaire en microscopie électronique (TEM/STEM) évitant leur solubilisation dans l'eau.

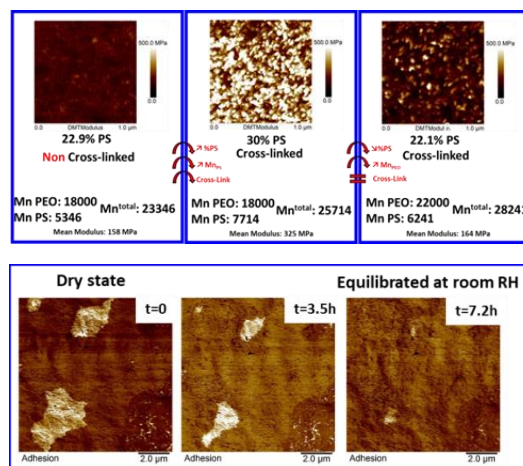
Les trois systèmes étudiés étaient basés sur des copolymères PS-PEO-PS avec du sel de lithium ou sous forme "single-ion". L'étude a porté sur l'analyse nanomécanique et morphologique par AFM et sa corrélation avec les mesures SAXS. Les principales conclusions sont les suivantes:

- Les différences nanomécaniques entre les phases ont permis l'analyse morphologique des copolymères et la mesure des distances entre domaines. Une bonne corrélation avec les mesures précédentes de SAXS a été obtenue;





- Des mesures nanomécaniques quantitatives ont permis de suivre l'évolution des matériaux selon leur structure chimique: effet de réticulation et augmentation de la longueur des blocs PS et PEO;
- L'évolution des propriétés nanomécaniques de surface de l'état sec jusqu'à l'équilibre avec l'humidité relative de la pièce a été mise en évidence.



### Les apports de la Stratégie de Co-localisation pour l'étude de systèmes multiphasés

Pour chacune des trois études présentées dans cette thèse, la co-localisation AFM/Raman et la stratégie multi-technique développée ont été utiles pour l'acquisition d'informations précieuses qui n'aurait pas pu être accessibles par d'autres moyens. Cette stratégie peut être appliquée à l'étude d'une variété de matériaux différents et peut fournir les informations suivantes:

#### 1) Identification des phases

L'association des propriétés nanomécaniques AFM et l'analyse chimique de Raman peuvent fournir une identification sans ambiguïté des composants du système étudié.

#### 2) Distribution des phases (et des additifs)

L'analyse de la distribution des phases dans le matériau peut être effectuée par l'association directe de l'AFM avec les microscopies électroniques (SEM/STEM/TEM). Cette information peut être corrélée aux processus de fabrication, à la présence d'additifs et à des traitements thermiques. La spectroscopie Raman peut fournir des informations supplémentaires en sondant la signature chimique des phases polymorphes ou des additifs dans le matériau, ce qui ne peut pas toujours être sondés directement par contraste nanomécanique ou chimique (staining).

#### 3) De la morphologie à l'analyse structurale

Les différences nanomécaniques entre les phases permettent une observation directe de la nanostructure, la mesure des distances entre domaines et la corrélation avec l'analyse par des techniques complémentaires telles que SAXS et SANS, afin d'approfondir la compréhension de la structure du matériau. Les techniques de diffusion des rayons X et des neutrons peuvent fournir des informations supplémentaires non sondées par les différences nanomécaniques mises en évidence par AFM. L'association de ces techniques permet la compréhension morphologique/structurale complète du matériau de l'échelle nano à l'échelle macroscopique, comme en témoigne la caractérisation des copolymères "single-ion", pour lesquels les études SAXS précédentes ont permis une interprétation correcte des images AFM.

#### 4) Analyses nanomécanique et chimique quantitative pour suivre l'évolution du matériau

La stratégie développée permet l'analyse chimique de la coupe transversale du matériau afin de qualifier l'impact de chaque étape de fabrication sur ses propriétés physiques, nanomécaniques et chimiques, ainsi que leur stabilité au fil du temps. Les mesures nanomécaniques obtenues par AFM et l'analyse chimique quantitative par Raman peuvent être utilisées qualitativement et quantitativement sur l'étude de tout changement lié à l'évolution de la structure, à l'oxydation ou aux pertes des composants par des traitements thermiques et le vieillissement des matériaux polymères. L'analyse par  $\mu$ -ATR-FTIR sur la coupe transversale de membranes polymères peut également fournir des informations complémentaires à la spectroscopie Raman, révélant les effets de l'oxydation indésirable et l'évolution chimique après des traitements chimiques/thermiques. L'association des deux techniques peut être utile pour optimiser les processus et identifier les mécanismes de dégradation pour atténuer les effets du vieillissement.

#### 5) Étude des processus dynamiques

Les changements morphologiques et des propriétés nanomécaniques et chimiques des échantillons peuvent être suivis en temps réel pour différents stimuli, tels que les variations d'humidité, l'ajout d'additifs, variation de la température ou des processus tels que la cristallisation. Dans ce cas, la cinétique du phénomène à suivre au fil du temps doit être compatible avec la vitesse d'imagerie de l'AFM. Le même type d'expériences peut être effectué sous le spectromètre Raman en suivant des bandes spécifiques liées à des groupes fonctionnalisés, des polymorphes ou une cristallinité globale dans des conditions contrôlées, par exemple d'une humidité allant de 0 (sous flux d'azote sec) à 100% d'humidité relative. La spectroscopie Raman est capable d'acquérir des spectres en moins d'une seconde afin de sonder les changements en temps réel, en étant limité par la gamme d'analyse et principalement par l'intensité de la réponse Raman de l'échantillon.

## Perspectives

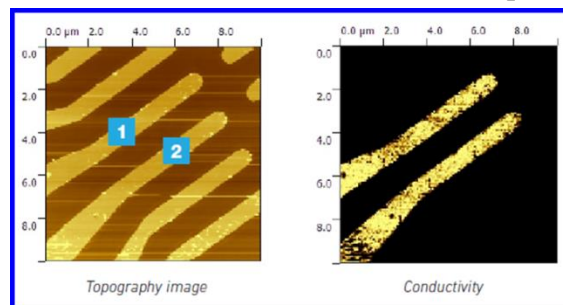
Le potentiel d'amélioration de la quantité d'informations auxquelles on peut accéder en utilisant la stratégie co-localisée AFM-Raman repose sur les capacités des différents modes de fonctionnement AFM et des techniques complémentaires. Les principales perspectives du travail sont les suivantes:

#### 1) Utilisation des modes AFM complémentaires

La Microscopie de Force Atomique peut sonder une variété de propriétés de matériaux selon les méthodes d'opération. Les propriétés telles que le courant, la conductance, le potentiel de surface et la capacité sont de plus en plus importantes dans un certain nombre d'applications, y compris la recherche sur les semi-conducteurs, les cellules solaires et les batteries, les polymères conducteurs et la nanoélectronique. L'analyse thermique localisée peut également être utile pour étudier les effets du vieillissement dans les matériaux. Parmi les modes de fonctionnement pertinents, nous mettons en évidence trois modes qui peuvent être utilisés en plus du PeakForce QNM afin d'aider à la compréhension des relations « mise en œuvre-structure-propriétés-durabilité » et élargir la gamme de matériaux étudiés:

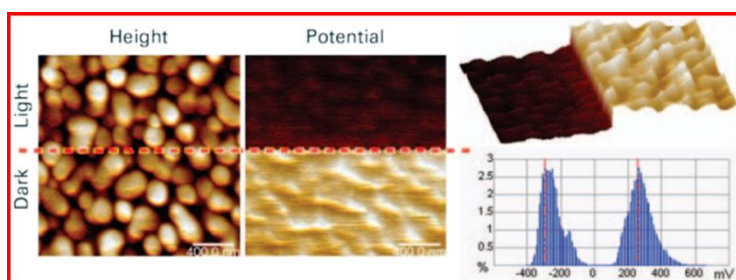
- **Conductive AFM (C-AFM):**

Dans ce mode, une tension de polarisation est appliquée entre la pointe et l'échantillon, ce qui permet de mesurer simultanément la topographie du matériau et le flux de courant électrique au point de contact de la pointe avec la surface de l'échantillon. Cette technique peut être utile pour identifier et caractériser les chemins de conduction dans les composites polymères et les électrolytes (conductivité ionique des membranes hybrides pour PEMFC, des copolymères utilisés comme électrolytes pour les batteries lithium, ainsi que les nanocomposites contenant des nanotubes de carbone et des matériaux piézoélectriques).<sup>284-288</sup>



- **Microscopie à sonde de Kelvin (KPFM):**

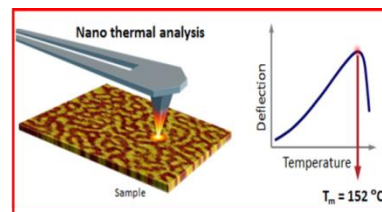
Ce mode représente la répartition du potentiel de surface d'un échantillon sans contact direct de la pointe avec l'échantillon. Les applications comprennent l'imagerie du potentiel de Kelvin ou la fonction de travail d'une surface et la mesure des différences de tension appliquées



entre les conducteurs. Ce mode peut être associé au Peak Force (PeakForce KPFM™) afin d'acquérir simultanément la topographie à l'échelle nanométrique et la cartographie des propriétés électriques et mécaniques pour une large gamme d'échantillons, tels que des matériaux organiques semi-conducteurs pour transistors à couche mince, mélanges organiques pour le photovoltaïque et les matériaux d'électrode, qui peuvent présenter des variations de potentiel de surface dans des conditions de lumière/obscurité attribuées à des changements dans les propriétés physiques et chimiques, y compris la taille des particules, la phase de la couche superficielle et les dépôts nanocristallins.<sup>289,290</sup>

- **Nano analyse thermique (Nano-TA):**

Ce mode permet une caractérisation thermique à haute résolution avec une résolution spatiale d'environ 100 nm pour corréliser l'information morphologique aux propriétés thermiques locales d'un matériau. Plutôt qu'une réponse moyenne de l'échantillon donnée par des méthodes thermiques conventionnelles, telles que la calorimétrie différentielle à balayage (DSC), l'analyse thermomécanique (TMA) et l'analyse mécanique dynamique (DMA), la Nano-TA peut fournir des informations locales sur les composants/défauts et les profils de propriétés thermiques sur la coupe transversale de revêtements, films et membranes.<sup>291-295</sup>



L'association de ces différents modes de fonctionnement avec les propriétés nanomécaniques fournies par le mode PeakForce QNM et l'analyse chimique par Raman peuvent donc permettre l'étude d'une large gamme de matériaux polymères.

## 2) Modes de microscopie électronique et caractérisation d'échantillons sensibles à l'eau

Les techniques de microscopie électronique telles que SEM, TEM et STEM ouvrent une large gamme de possibilités en termes de caractérisation complémentaire à la stratégie de co-localisation AFM-Raman. La spectroscopie de rayons X à dispersion d'énergie (EDS) et la spectroscopie de perte d'énergie (EELS) sont des techniques utiles pour l'analyse élémentaire (numéro atomique  $Z > 10$ ) et peuvent être intéressantes pour l'analyse de l'interface des nano charges chimiquement modifiés dans les nanocomposites et les matériaux hybrides.

Les développements réalisés au cours de l'étude des électrolytes polymères pour les batteries lithium ouvrent de nouvelles possibilités pour la caractérisation des échantillons sensibles à l'eau. Les études morphologiques par TEM/STEM sur des sections minces collectées par cryo-ultramicrotomie restent à faire et imposeront des défis sur le contrôle des paramètres d'imagerie pour éviter l'endommagement des échantillons par le faisceau d'électrons.

## 3) Études du vieillissement des matériaux

La stratégie développée alliant la caractérisation nanomécanique par AFM avec une caractérisation chimique qualitative et quantitative par spectroscopie Raman et l'imagerie  $\mu$ -ATR-FTIR est un outil puissant pour l'étude des matériaux vieillis et des processus de dégradation. Pour les membranes hybrides pour PEMFC, notre prochain objectif est d'utiliser cette stratégie d'analyse pour quantifier les modifications physiques et chimiques induites dans les membranes hybrides SG/sPEEK après leur test (vieillissement) sur un banc de pile. La même stratégie peut être appliquée à l'étude des copolymères pour les batteries au lithium après le cyclage afin de comprendre d'abord les changements chimiques/structurels induits par le vieillissement, puis d'optimiser la structure et de concevoir des stratégies de stabilisation.

## 4) Corrélation de l'analyse microstructurale avec les propriétés fonctionnelles

Enfin, d'autres recherches doivent être effectuées pour corrélérer les connaissances microstructurales fondamentales des matériaux et leurs propriétés fonctionnelles. Dans le cas des mélanges compatibilisés PA6/ABS, par exemple, l'effet des différentes morphologies et de la distribution des phases devrait avoir une incidence sur la résistance mécanique, la résistance aux chocs et la température de distorsion thermique des mélanges, ce qui doit encore être étudié. Dans le même contexte, les effets de différents précurseurs de SG, leur quantité et leur distribution dans les membranes hybrides doivent être corrélés à leur conductivité protonique, au comportement de gonflement et aux propriétés mécaniques afin d'ajuster le processus de fabrication pour obtenir des membranes présentant des performances optimales.



# ANNEXES

---

## Annex 1. - Annexes of Chapter 4: Compatibilization of compatibilized blends based on PA6/ABS

### Annex 1.1 - Blending procedure

The polymeric blends were prepared at the Federal University of São Carlos (UFSCar, Brazil), in a co-rotating twin screw extruder manufactured by B&P Process Equipment and Systems (L/D= 25, D= 19 mm), with temperature profile of 200/220/220/220/230 °C operating at screw speed of 160 RPM. The twin-screw profile used during melt blending process is shown on Figure A.1. All polyamide formulations were dried in a vacuum oven at 80°C for at least 16 h before extrusion.

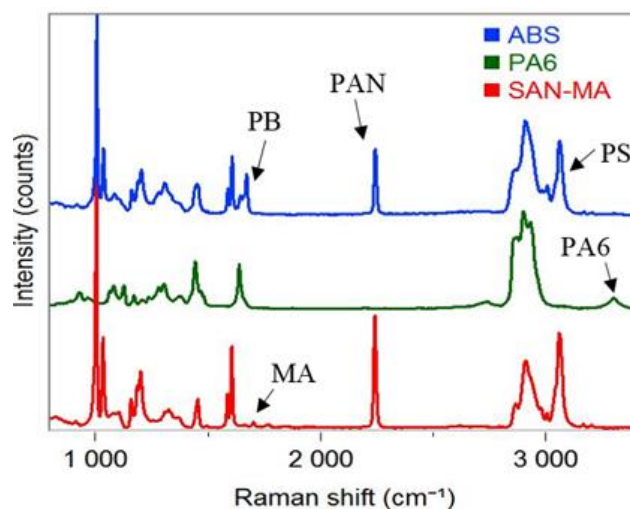


Figure A.1. Employed twin-screw profile

The composition of the binary reference blend and the compatibilized blends was fixed at PA6+ABS (60/40 wt %) and PA6/ABS/SAN-MA (57.5/37.5/5 wt %), respectively. The materials obtained by extrusion were quenched in water, granulated, dried and injection molded at 245 °C, into standard specimens for mechanical and thermomechanical analysis, using an Arburg Allrounder 270V machine with a mold temperature of 50°C.

### Annex 1.2 - Raman band assignment of the blend components

The chemical Raman signatures of PA6, ABS and SAN-MA were recorded separately, in order to properly assign the contributions of each phase. Figure A.2 shows the characteristic spectra of each component and Table A.1 summarizes the main Raman bands of PA6, ABS and the maleic anhydride group of SAN-MA. For the proper identification and quantification of each phase, characteristic bands were chosen to avoid superposition. For the PA6 the characteristic band chosen was centered at 3300  $\text{cm}^{-1}$ , assigned to the NH vibrations. For the components of the ABS phase: C=C vibration of Polybutadiene at  $\sim 1660 \text{ cm}^{-1}$ , CN vibration of polyacrylonitrile at  $\sim 2240 \text{ cm}^{-1}$  and aromatic CH vibration of Polystyrene at  $\sim 3055 \text{ cm}^{-1}$ . The maleic anhydride of SAN-MA presents some characteristic bands at 1775  $\text{cm}^{-1}$  (C=C) and 1846  $\text{cm}^{-1}$  (C=O) however very weak.



**Figure A.2.** Raman spectra of ABS, PA6, and SAN-MA and identified with an arrow the characteristic bands used for identification. PA6 at 3300cm<sup>-1</sup> (NH), PB at 1660 cm<sup>-1</sup> (C=C), PAN at 2240 cm<sup>-1</sup> (CN), PS at 3055 cm<sup>-1</sup> (aromatic CH) and MA at 1775 cm<sup>-1</sup> (C=O)

**Table A.1** Raman spectra of the components and assignment of the Raman bands <sup>160,199,296-298</sup>

PA6	ABS			MA	Assignment
	PAN	PB	PS		
928 <sub>m</sub>			1000 <sub>vs</sub> 1030 <sub>m</sub>		CO-NH Aromatic ring Aromatic ring
1060-1225 <sub>m</sub>				1065 <sub>m</sub>	ν(C-O) ν(C-C)
1440 <sub>s</sub>	1440 <sub>m</sub>	1440 <sub>m</sub>	1440 <sub>m</sub> 1580 <sub>w</sub> 1600 <sub>m</sub>	1264 <sub>m</sub>	ν(C-O), ν(C-COO) CH2 bending Aromatic Ring Aromatic Ring
1635 <sub>s</sub>		1650 <sub>sh</sub> 1667 <sub>m</sub>		1775 <sub>vw</sub> 1846 <sub>vw</sub>	Amide-I ν(C=C) cis ν(C=C) trans ν(C=O) ν(C=O)
	2238 <sub>s</sub>				Nitrile
2882 <sub>vs</sub>		2880 <sub>m</sub>	2880 <sub>m</sub>		ν(CH2)
2901 <sub>vs</sub>		2900 <sub>s</sub>	2900 <sub>s</sub>		ν(CH2)
2958 <sub>vs</sub>					ν(CH2)
			3055 <sub>s</sub>		Aromatic ring
3300 <sub>m</sub>					ν(N-H)

vs: very strong; s: strong; m: medium; w: weak; vw: very weak; sh: shoulder; ν: stretching



### Annex 1.3 - Rheological Measurements

Viscoelastic behaviors of polymeric blends were evaluated on a parallel-plate Advanced Rheometric Expansion System (ARES) rheometer (DEMa, São Carlos, Brazil). Samples were compression molded into 1 mm thickness disk-shape specimens at 245°C. Frequency sweep tests from 500 to 0.1 rad were carried out in oscillatory shear and strain of 5% at 245°C under dry nitrogen atmosphere. Each rheological measurement was performed within the materials' linear viscoelastic region.

### Annex 1.4 - Differential Scanning Calorimetry (DSC)

Melting and crystallization temperatures and the corresponding enthalpies of the PA6/ABS blends were determined by differential scanning calorimetry (DSC) using a TA Instruments Q20 apparatus. These analyses were performed on samples cut from the center part of the injection molded specimens. Prior to analysis, samples were dried 24 hours under a nitrogen flux in order to avoid any moisture artifacts on the thermograms.<sup>299</sup> A heat-cool-heat program was used from 30 to 250°C with a heating/cooling rate of 10°C.min<sup>-1</sup>. Crystallization temperatures ( $T_c$ ) and enthalpies ( $\Delta H_c$ ) were obtained from the cooling cycle; melting temperatures ( $T_m$ ) and enthalpies ( $\Delta H_f$ ) were obtained from the first and second heating cycle and the degree of crystallization ( $X_c$ ) was calculated according to Eq. A.1:

$$X_c = \frac{\Delta H_f}{\Delta H_f^0(PA6)} \times \frac{1}{w_{PA6}} \times 100 \quad A.1$$

Where  $\Delta H_f$  is the enthalpy of fusion obtained by DSC;  $\Delta H_f^0(PA6) = 240 \text{ Jg}^{-1}$  is the enthalpy of fusion of 100% crystalline PA6 and  $w_{PA6}$  is the weight fraction of PA6 in the blends.<sup>300</sup>

The enthalpy of fusion of  $\alpha$  and  $\gamma$  phases was determined by Karl-Heinz Illers<sup>300</sup> as 241  $\text{Jg}^{-1}$  for the  $\alpha$ -phase and 239  $\text{Jg}^{-1}$  for  $\gamma$ -phase. Since the difference is small, the mean value of 240  $\text{Jg}^{-1}$  was used for quantification of both phases by deconvolution of the melting peak. The determination of the baseline used to calculate the crystallinity index of each sample was done using the procedure described in the literature<sup>299</sup>, in order to take into account any effects of residual moisture (dried samples under a nitrogen flux), silent crystallization and stress relaxations.

### Annex 1.5 - Fabrication and analysis of the reference PA6 polymorphs

In order to obtain raw data on the polymorphs' Raman chemical signature, PA6 samples in different crystallographic forms were prepared: an amorphous sample was obtained by quenching in liquid nitrogen a PA6 sample from the melt (250°C), and crystalline samples exhibiting  $\alpha$  and  $\gamma$  phases were obtained by isothermal crystallization (from the melt at 250°C) at 180°C and 80°C respectively. X-Ray Diffraction analysis of the references samples was performed for the identification of PA6 samples presenting a single polymorph ( $\alpha$ ,  $\gamma$  or amorphous) in order to allow the assignment of the Raman spectra to each PA6 polymorph. The X-Ray diffraction patterns in Figure A.3(a) show that each of the reference samples presents only one single polymorph of PA6 crystal, as described in the literature.<sup>243,301,302</sup> DSC analysis showed that the  $\gamma$  sample presented less than 5% of crystallinity and two  $\alpha$  samples presented 33 and 19% of crystallinity (labelled 33%C and 19%C). The determination of the crystallinity index by DSC requires special care for polyamides (due to moisture absorption, silent crystallization and stress relaxation) and it becomes more difficult for low crystallinity samples.<sup>299</sup> Raman spectra were then acquired on preferential zones

where the crystallinity was higher, detected by polarized optical microscopy (for  $\gamma$  sample). Figure A.3(b)) presents the characteristic Raman spectra of the  $\alpha$ ,  $\gamma$  and amorphous phases. The C-C stretching region of the PA6 Raman spectra is composed of three primary peaks at 1060, 1080, and 1125  $\text{cm}^{-1}$ . The peaks at 1060 and 1125  $\text{cm}^{-1}$  are characteristic of the C-C symmetric vibrations for trans conformation of the backbone, the signature of the monoclinic  $\alpha$ -phase of PA6, while the 1080  $\text{cm}^{-1}$  peak is attributed to the C-C vibration of gauche conformation, signature of the hexagonal  $\gamma$ -phase.<sup>198–200</sup> One can see that the  $\gamma$ -phase has also a characteristic peak that appears at 960  $\text{cm}^{-1}$  and which, although not very intense, could be used for phase identification. The amorphous phase presents both 1080 and 1125  $\text{cm}^{-1}$ , characteristic of gauche and trans conformations, globally with low intensity and no preferable conformation. The increase of crystallinity in each of the crystalline forms engenders the prevalence of one band relative to the other. Thus, it is possible to quantify the presence of each phase by the characteristic intensity ratio of the bands at 1080 and 1125  $\text{cm}^{-1}$  ( $I_{1080}/I_{1125}$ ).

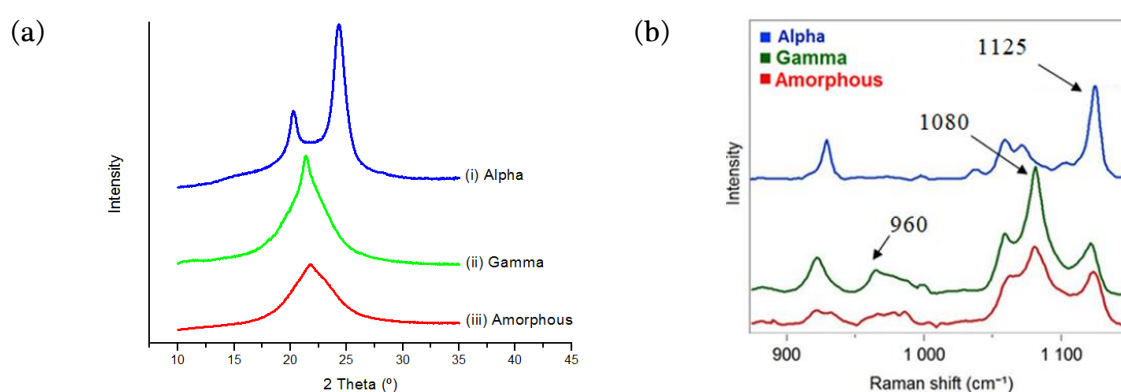


**Figure A.3.** (a) X-Ray Diffraction of Polyamide 6 in different forms. (i) Alpha form, (ii) Gamma and (iii) Amorphous; and (b) respective Raman spectra of each phase

Table A.2 reports the  $I_{1080}/I_{1125}$  Raman ratio from the literature and experimentally calculated from at least 10 different spectra, as well as samples' crystallinity index estimated by DSC. The amorphous samples presented an  $I_{1080}/I_{1125}$  ratio of  $1.41 \pm 0.05$ . Increasing the amount of  $\alpha$ -phase (19%C) decreased the  $I_{1080}/I_{1125}$  ratio down to  $0.43 \pm 0.04$  and an increase on its crystallinity (33%C) decreased even more the ratio down to  $0.33 \pm 0.01$ . The low standard variations of the measurements confirm the homogeneity of these samples. Contrarily, the  $I_{1080}/I_{1125}$  ratio increased to  $2.0 \pm 0.4$  with the increase of  $\gamma$ -phase. Despite efforts, a gamma sample with higher crystallinity could not be obtained by isothermal crystallization. Nevertheless, one can expect that the  $I_{1080}/I_{1125}$  ratio will increase with  $\gamma$ -phase's crystallinity. In conclusion, the higher the crystallinity of  $\gamma$ -phase detected, the higher the  $I_{1080}/I_{1125}$  ratio. Inversely, the ratio decreases with the increasing crystallinity of  $\alpha$ -phase. Since the Raman intensity characteristic of one phase is proportional to its content in the material, the differences between the experimentally calculated values and the literature are related to different samples' crystallinities (no information on the crystallinity index available from literature data).

**Table A.2.** Characteristic band intensity ratios from literature and calculated experimentally from at least 10 Raman spectra in an area of  $10 \times 10 \mu\text{m}^2$ . The overall crystallinity index on the sample is presented in brackets

	$I_{1080}/I_{1125}$		
	Amorphous	Alpha ( $\alpha$ )	Gamma ( $\gamma$ )
Literature <sup>201</sup>	-	0.42	2.5
Experimental	1.41±0.05 [ $< 5\%C$ ]	0.33±0.01 [ $33\%C$ ] 0.43±0.04 [ $19\%C$ ]	2.0±0.4 [ $< 5\%C$ ]*

\* Raman spectra acquired where the crystallinity was higher, detected by polarized optical microscopy

### Annex 1.6 - Co-localized AFM-Raman analyses of the compatibilized blends

Co-localized AFM-Raman analyses were done in order to evaluate the impact of the blending protocol on the compatibilization (phases' distribution, structure) and the co-localization precision. Raman mappings presented in Figure A.4 are relative to the chemical distribution of each component in the blends co-localized with AFM images in a  $10 \times 10 \mu\text{m}^2$  area (Figure A.4 (a)-1 to 3) corresponding to 1-(PA6/ABS/SAN-MA), 2-(ABS/SAN-MA)+PA6 and 3-(PA6/SAN-MA)+ABS). Figure A.4(b)-1 to (b)-3 present the PA6 matrix signal, which appears homogeneous on the mapped area of the three samples contrary to what was observed for the reference PA6+ABS sample (Figure 4.8). Figure A.4 (c)-1 to (c)-3 are relative to the Polybutadiene. Due to the micrometric resolution of the Raman, the PB spheres included in the ABS phase cannot be individually distinguished, but zones with higher concentration of PB spheres are clearly visible on the Raman mappings. Based on these mappings, the areas corresponding to higher concentration of PB domains were highlighted by a red border and superposed on a binarization of the AFM modulus images as shown on Figure A.4 (f)-1 to (f)-3. The binary AFM modulus images show the PB spheres in black to be used as guides for the co-localization. The AFM/Raman co-localization efficiency is confirmed by the good correlation between the PB Raman mappings and the PB clusters highlighted by AFM. The Raman maps showing the distribution of the PS and PAN phases (Figure A.4 (d) and (e), respectively) reveal the presence of these components all over the samples, whatever the blending protocol, i.e., the signal is never zero (scale limits were chosen in order to enhance contrast for correlation with the ABS clusters). In contrast, the reference sample PA6+ABS (Figure A.4 (d) and (e)), exhibited a clear phase separation between PA6 and PS/PAN (the signal relative to PS and PAN is zero inside Polyamide areas). This fact also evidences the improvement on the PA6/ABS miscibility due to the addition of a SAN-MA compatibilizer. The mapped area of the sample (ABS/SAN-MA)+PA6 presented higher Raman signal of PB, PAN and PS than the other samples (brighter zones on the image). This is related to the bigger size and thickness of the ABS domains and its almost co-continuous morphology, in accordance the previous AFM and TEM images of Figure 4.11.

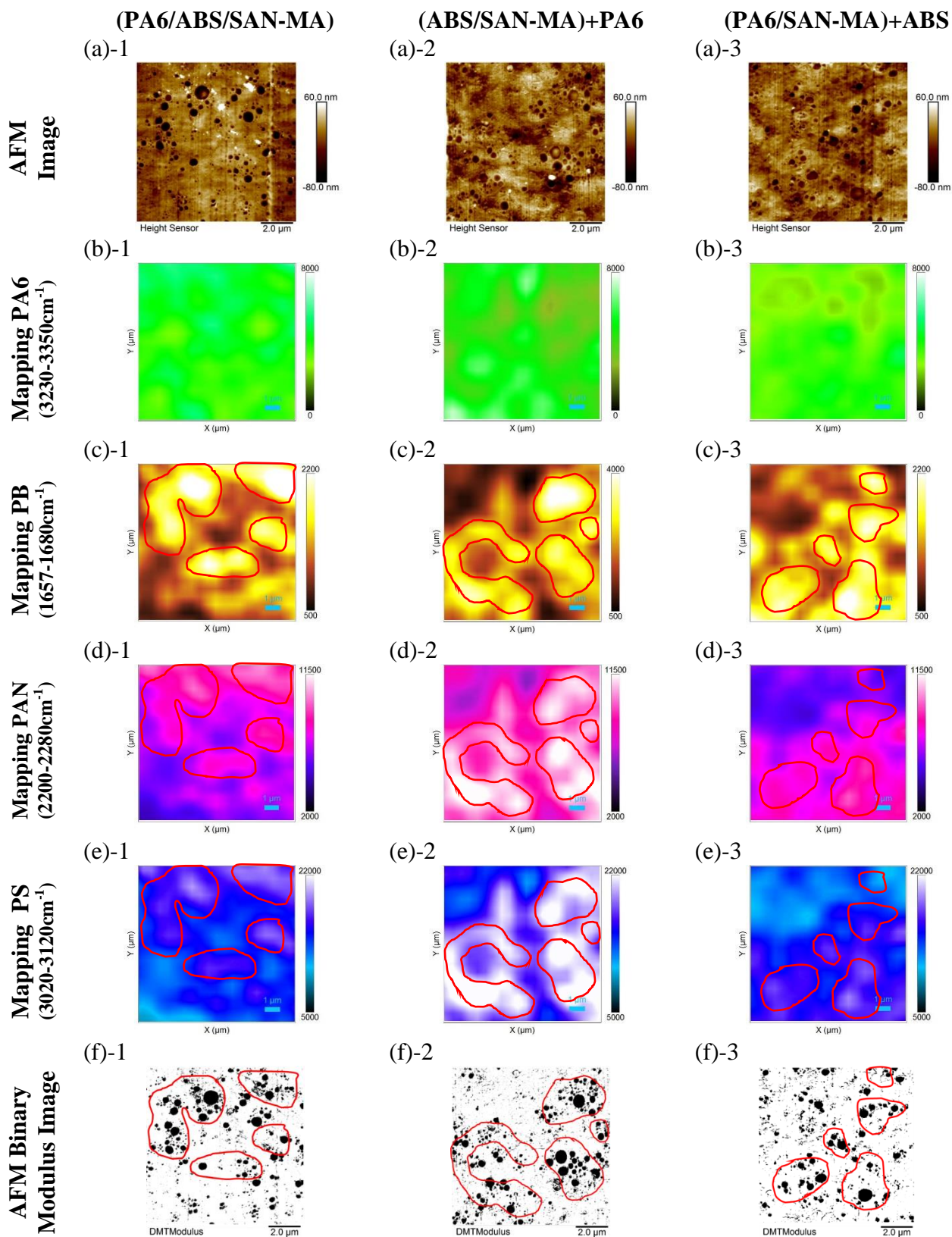


**Figure A.4.** AFM-Raman co-localized analysis of samples 1- (PA6/ABS/SAN-MA), 2- (ABS/SAN-MA)+PA6 and 3-(PA6/SAN-MA)+PA6. (a) AFM Image; Raman mapping area relative to: (b) Polyamide 6 (c) Polybutadiene (d) Acrylonitrile and (e) Polystyrene; (f) AFM Binary Modulus image. PB domains were highlighted by a red border on the images (c) to (f).

### Annex 1.7 - Raman analysis of characteristic PA6 $\gamma$ -phase band at 960 $\text{cm}^{-1}$

An attempt to distinguish between the  $\alpha$  and the amorphous phases was performed using the  $\gamma$ -phase characteristic peak at 960  $\text{cm}^{-1}$  and the peak at 920  $\text{cm}^{-1}$  (CO-NH), to calculate a new ratio  $I_{920}/I_{960}$  capable of revealing the contribution of the  $\alpha$ -phase. The higher the crystallinity of  $\alpha$ -phase detected, the higher the  $I_{920}/I_{960}$  ratio ( $I_{920}/I_{960} \rightarrow \infty$ ). Inversely, the ratio decreases with the increasing amount of amorphous phase ( $I_{920}/I_{960} \sim 1$ ). This means that if one compare this ratio with the  $I_{1080}/I_{1125}$  ratio it would be possible to distinguish if the zones of lower  $I_{1080}/I_{1125}$  ratio ( $\sim 1.5$ ) are mixtures of  $\alpha+\gamma$  or amorphous zones. However, a clear conclusion was difficult to provide for these blends, due to the low intensity of this peak and the presence of high intensity peaks related to the PS phase at 1000 and 1030  $\text{cm}^{-1}$ , as one can observe on Figure A.5(a). This increases the uncertainty on the deconvolution of the peak at 960  $\text{cm}^{-1}$  for further analysis. Figure A.5(b) shows the result of a subtraction of a spectrum with low  $I_{1080}/I_{1125}$  ratio from one with a high ratio. One can see that the remaining peaks are all relative to the Polyamide 6 in  $\gamma$ -phase, which confirms that areas with high  $I_{1080}/I_{1125}$  ratio present more  $\gamma$ -phase than the low ratio zones. However, it is not possible to affirm if these low ratio zones are composed of mixtures of  $\alpha+\gamma$  or amorphous zones.

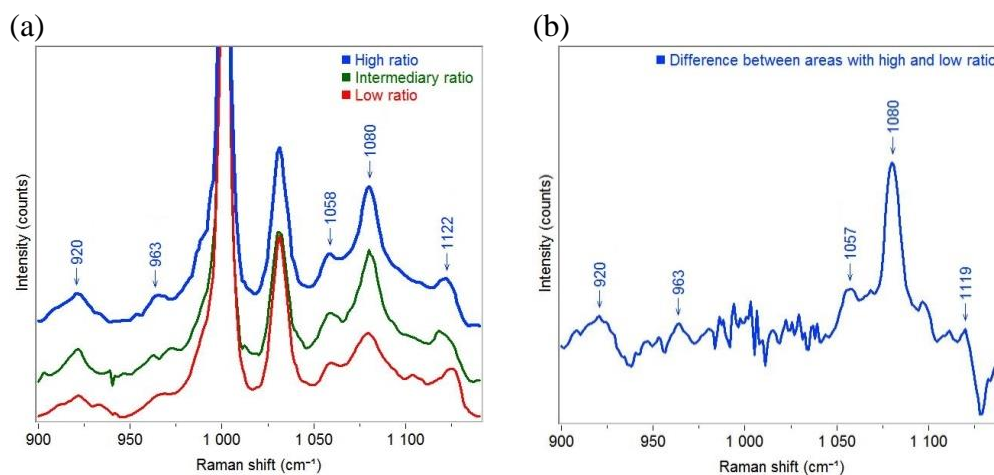


**Figure A.5.** (a) Typical spectra of areas with high, intermediary and low ratio  $I_{1080}/I_{1125}$ ; (b) Spectra of the subtraction of the low  $I_{1080}/I_{1125}$  ratio spectrum from the a high ratio  $I_{1080}/I_{1125}$  spectrum

## Annex 2. - Annexes of Chapter 5: Hybrid Membranes for Fuel Cell

### Annex 2.1 - Fabrication process of the hybrid membranes based on SHDi precursor

The fabrication of the hybrid membranes based on SHDi precursor was done as part of the Ph.D. thesis of Isabel Zamanillo López at the laboratory SyMMES/Grenoble. The steps were done as follows:

#### Step 1: From a pristine to a host sPEEK membrane

Prior to the impregnation of the host sPEEK membrane with the SG precursor, the host membrane was prepared as followed. The pristine sPEEK membranes were re-acidified in a 1M sulfuric acid solution at room temperature for 4 hours and triple rinsed with pure water. Then a hydrothermal treatment (liquid water at 80°C for 72h) was applied on the re-acidified membrane in order to improve the nano-phase separation between hydrophilic and hydrophobic domains. This hydrothermal treatment allows improving the membrane's proton conductivity to make it comparable with the benchmark Nafion.<sup>303</sup> Finally this host sPEEK membrane was conditioned in 50-

50vol% methanol-water mixture, the solvent composition used for the SG impregnation/condensation step.

**Step 2:** Sol-Gel impregnation/condensation into a host sPEEK membrane

A 0.2 M SG precursor solution in a 50/50 water/ethanol mixture at pH 4.5 (addition of acetic acid) was prepared. 2 hours were needed to obtain a homogenous solution, after what the host sPEEK membrane was immersed into this solution during 4 days (at room temperature). Then the membrane was removed, rinsed with pure water to avoid the formation of a SG coating on the outer surface (potential loss of proton conductivity and problems of compatibility with the electrodes in fuel cell), and then dried under vacuum conditions at room temperature.

**Step 3:** Post-Condensation (PC) of the SG phase to improve its extent of condensation

The hybrid membrane was thermally post-condensed at 74°C and 6.3%RH for 72 hours.

**Step 4:** A HydroThermal (HT) treatment to improve the proton conductivity of the hybrid membrane

A hydrothermal treatment (liquid water at 80°C for 72 hours) was applied to the hybrid membrane in order to improve its proton conductivity, and eventually remove any uncondensed SG precursors or entrapped oligomers.

**Annex 2.2 - Thermogravimetric Analysis (TGA) of hybrid membranes based on SHDi precursors**

The SG uptake of the hybrid membrane was determined by thermogravimetric analysis (TGA 92-12 from Setaram Instrumentation, with a resolution of 1 µg). Samples were heated at 10°C/min from room temperature up to 700°C under O<sub>2</sub> flow to ensure a complete degradation of the organic phase. The SG uptake was determined according to Equation A.2 taking into account the SiO<sub>2</sub> weight residue at 700°C and the weight of dry hybrid membrane at 200°C (a temperature corresponding to the complete water desorption).

$$\%SG = \frac{\frac{m \text{ SiO}_2 \text{ residue at } 700^\circ\text{C}}{M\text{SiO}_2} \times MSG}{m \text{ hybrid membrane at } 200^\circ\text{C} - \left( \frac{m \text{ SiO}_2 \text{ residue at } 700^\circ\text{C}}{M\text{SiO}_2} \times MSG \right)} \times 100\%$$

A.2

Where  $M \text{ SiO}_2 = 60.08 \text{ g/mol}$  and  $MSG = \text{Molar Mass of the SG repeat unit of the condensed SG phase from SHDi precursor} = 134.32 \text{ g/mol}$ .

**Annex 2.3 - Raman assignment of the sPEEK and SG phase chemical signatures**

The chemical Raman signatures of each component of the hybrid membranes were recorded separately, in order to properly assign the contributions of each phase. Figure A.6 below shows the typical spectra of the host sPEEK membrane and a hydrolyzed and condensed precursor, here called polySHDi, from 400 to 3250 cm<sup>-1</sup>. The assignment of each peak is listed on Table A.3. The differentiation of both phases can be easily done from 2400 to 3250 cm<sup>-1</sup> once the peak centered at ~3070 cm<sup>-1</sup> is assigned as to the contribution of the CH units of the aromatic ring presented on the sPEEK structure, and the peak centered at ~2900 cm<sup>-1</sup> refers to the -CH<sub>2</sub> /-CH<sub>3</sub> vibrations presented on the Sol-Gel structure, as well as the peak at ~2580 cm<sup>-1</sup> which is related to the thiol (-SH)

functions. The presence of a peak at  $\sim 507\text{ cm}^{-1}$  can indicate the presence of di-sulfide (-S-S-) functions issued from an oxidation of thiol units.

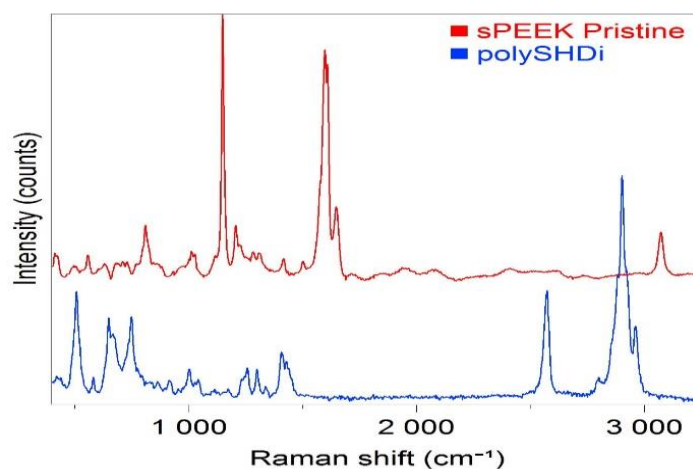


**Figure A.6.** Raman spectra of pure sPEEK and condensed SG precursor (polySHDi)

**Table A.3.** Observed Raman shifts (cm-1), band intensities and assignments for the polymers<sup>244,304-306</sup>

sPEEK	polySHDi	Assignment
	507 m	$\nu(\text{S-S})$
	648 m	$\nu(\text{S-C})$
	746 m	$\nu(\text{S-C})$
810 m		$\omega(\text{CH})$
	863 w	$\text{CH}_2$ rock trans
	1002 w	$\nu(\text{C-C})$ trans
1010 w		Ring stretching mode or $\delta\text{C-H}$
	1039 w	$\text{CH}_2$ rock trans
1147 vs		$\delta(\text{C-CO-C})$ stretching mode
	1233 w	$\text{CH}_2$ twist
1206 w		$\nu\phi\text{-O}$
	1254 w	$\text{CH}_2$ twist
1280 w		Ring mode
	1301 w	$\text{CH}_2$ twist
1308 w		Ring mode
	1337 w	$\text{CH}_2$ twist
	1409 m	$\delta(\text{CH}_2)/\delta(\text{CH}_3)$
1414 w		$\nu\text{-CO-} / \nu\text{C-O-C}$
	1429 m	$\delta(\text{CH}_2)/\delta(\text{CH}_3)$
1499 w		$\nu\text{C=C}$ Ring stretches
1596 vs		$\nu\text{C=C}$ Ring stretches
1606 vs		$\nu\text{C=C}$ Ring stretches
1645 m		$\nu\text{C=O}$
	2571 s	$\nu\text{S-H}$
	2798 w	$\nu(\text{CH}_2)$
	2882 sh	$\nu(\text{CH}_2)$
	2901 s	$\nu(\text{CH}_2)$
	2958 m	$\nu(\text{CH}_3)/\nu(\text{CH}_2)$
3070 m		$\nu\text{C-H}$ aromatic ring

vs: very strong; s: strong; m: medium; w: weak; sh: shoulder;  $\nu$ : stretching;  $\delta$ : bending;  $\omega$ : wagging

### Annex 2.4 - Fabrication process of the hybrid membranes based on SHTriM precursor

The fabrication of the membranes was done as part of Ph.D. thesis of Natacha Huynh at the laboratory SyMMES. The steps were done as follows:

#### Step 1: From a pristine to a host sPEEK membrane

Prior to the impregnation of the host sPEEK membrane with the SG precursor, the host membrane was prepared following the previous procedure described at Annex 2.1.

#### Step 2: Sol-Gel impregnation/condensation into a host sPEEK membrane

A 0.1 M SG precursor solution in a 64/36 water/ethanol mixture at pH 4 (addition of acetic acid) was prepared. After a complete SG precursor's dissolution (2 hours), the host sPEEK membranes were immersed in different volumes of this solution, in order to vary the SG uptake, for 40 hours at 30°C. Then the membranes were removed and dried under nitrogen flux at room temperature.

#### Step 3: Post-Condensation (PC) of the SG phase to improve its extent of condensation

The hybrid membrane was thermally cured at 80°C and 10%RH for 24 hours to increase the hydrolysis/condensation of the SG precursors/oligomers into the host membrane.

**Step 4:** HydroThermal (HT) treatment to improve the proton conductivity of the hybrid membrane.

A hydrothermal treatment (liquid water at 80°C for 72 hours) was applied to the hybrid membrane in order to improve its proton conductivity, and eventually remove any uncondensed SG precursors or entrapped oligomers.

### Annex 2.5 - Effect of trapped water on the surface of Polyethylene terephthalate (PET) membranes

Polyethylene terephthalate (PET) membranes were provided by an industrial partner. In order to produce porous membranes, samples were irradiated using the track-etching technique. The structure of PET is presented in Figure A.7 and a summary of the studied samples is presented in Table A. 4. Samples of PET membranes with a thickness of about 30  $\mu\text{m}$  were trimmed and cryo-ultramicrotomed using the procedure described on Chapter 3.

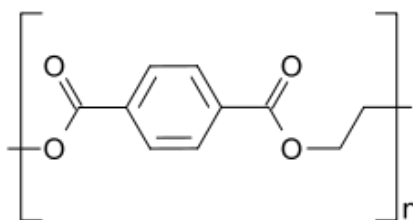


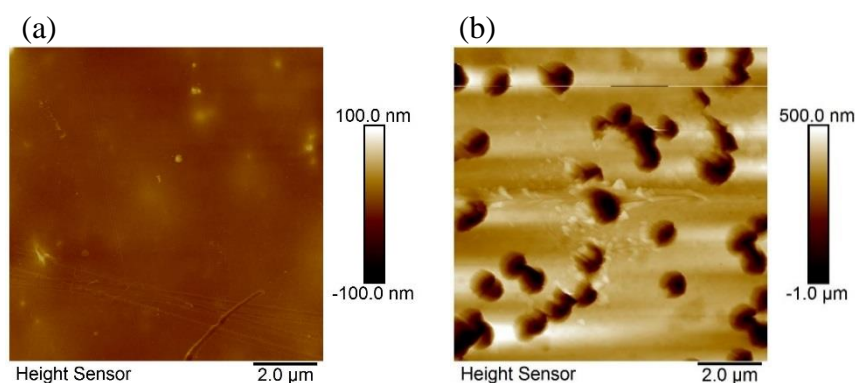
Figure A.7. PET structure

Table A. 4. PET samples and fabrication step

Sample	Step of fabrication
PET-Pristine	Pristine PET membrane
PET-Porous	Porous PET membrane after irradiation

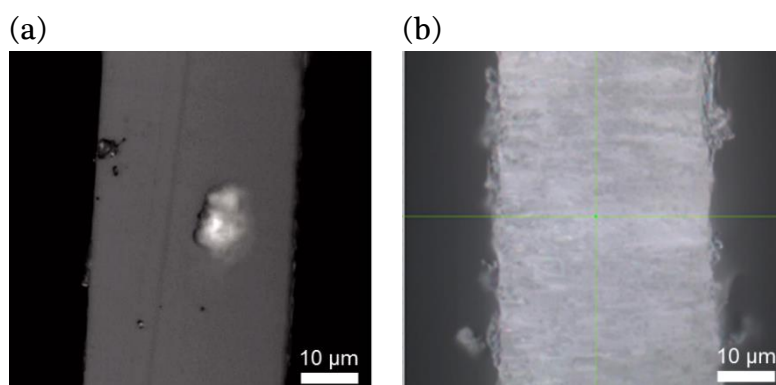


Figure A.8 shows topographic images ( $10 \times 10 \mu\text{m}^2$ ) collected on the PET membrane surface (non cryo-ultramicrotomed). Sample PET-Pristine shows a rather flat surface while the holes with a diameter of about  $1 \mu\text{m}$  formed by irradiation are clearly visible on the PET-Porous membrane.



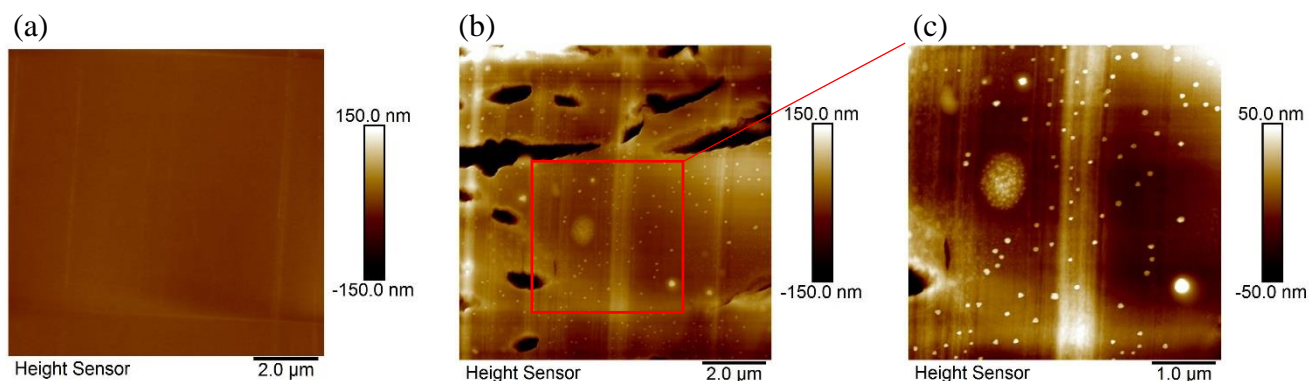
**Figure A.8.** AFM topographic images of a  $10 \times 10 \mu\text{m}^2$  area of the external surface (non ultramicrotomed) of samples (a) PET-Pristine and (b) PET-Porous

Figure A.9 shows optical images of the cryo-ultramicrotomed surfaces of samples. PET-Pristine presents a very flat surface, despite some vertical lines caused by scratches on the knife and some dust on the surface. PET-Porous, however, presents a very rough surface after cryo-ultramicrotomy due to the presence of the pores, which makes difficult AFM imaging of large areas and hampers the access to the complete cross-section of the membrane. Nevertheless, there are still suitable limited areas for analysis.



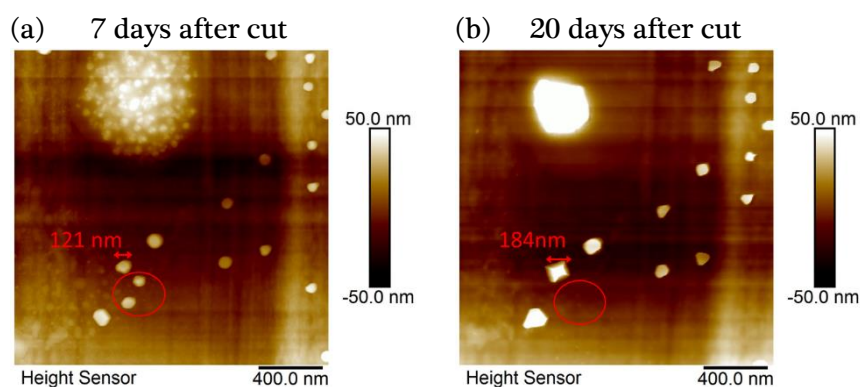
**Figure A.9.** Optical image of samples (a) PET-Pristine and (b) PET-Porous after cryo-ultramicrotomy

Figure A.10 shows the AFM topographic images of the cryo-ultramicrotomed surface of the samples. One can see on sample PET-Porous Figure A.10(b) that the cryo-ultramicrotomy procedure evenly cuts the pores, which appear as elongated features with very low topography (black on the image). On the center of the image (Figure A.10(c)), we observed the presence of small objects appearing with higher topography, some of them concentrated in a round shaped zone. As the objects should have been cut by the diamond knife during ultramicrotomy, these objects necessarily appeared after the sample preparation procedure, probably due to water trapped on the surface after warming to the room temperature (at this time, no specific procedure was developed to avoid the deposition of ice crystal on the sample surface at the end of the cryo-ultramicrotomy step). Sample PET-Pristine, however, did not present any objects or signs of water trapped on its surface (Figure A.10 (a)).



**Figure A.10.** AFM topography images of a  $10 \times 10 \mu\text{m}^2$  area of samples (a) PET-Pristine and (b) PET-Porous. (c) Inset relative to a  $5 \times 5 \mu\text{m}^2$  area showing objects on the surface of sample PET-Porous

As for the hybrid membranes, we have followed the evolution of these objects on the surface over time. Figure A.11 shows the topography of the samples 7 and 20 days after cutting. We could see that the high topography round shape shrank after 20 days and at the same time showed a decrease on adhesion (not shown). The objects inside it get unified at the center of the zone. Some of the objects have also grown in size, from 121 to 184 nm (as indicated by the red arrows on the image), and others with a small size disappeared (red circle on the image). The disappearance of the high topography zones with time is an evidence of water evaporation. The disappearance of the small size objects and the growth of others may indicate that the small ones have been consumed by the growth of the bigger ones, forming crystals with polygonal shapes. Due to the nanodimensions of the crystals, it was not possible to do direct Raman analysis (volume resolution of about  $1 \mu\text{m}^3$ ). We have tried to use the AFM to pile up the nano-crystals to achieve a compatible size with the Raman resolution, as we have done with the hybrid membranes based on SHDi SG phase. However, the very rough surface of the porous sample made it difficult to move a reasonable amount of crystals from a large surface for analysis.



**Figure A.11.** AFM topography images of a  $2 \times 2 \mu\text{m}^2$  area of sample PET-Porous (a) after cryo-ultramicrotomy and (b) 20 days after the procedure

Therefore, SEM analyses at the same area of sample PET-Porous probed by AFM have been performed to collect additional information (Figure A.12). SEM was used in two different modes of operation collecting respectively the “Secondary Electrons” (SE) and the “Back-Scattered Electrons” (BSE). Figure A.12 (b) shows the SE-SEM image of the surface. One can see the crystals almost systematically close to a small hole on the surface, probably small channels that allowed the migration of low molecular weight molecules, which fed the growth of the crystals until the evaporation of water. However, these small holes are not seen by AFM, maybe hidden by the crystals above it, or remaining water. It is possible that when the sample was put in the SEM microscope, the

water trapped in these channels was expelled during the equilibration of the sample in vacuum, dislocating the crystal from the top of the hole. On the BSE image (Figure A.12 (c)) corresponding to the same area shown on Figure A.12 (b), one can observe three different contrasts: the membrane's surface (gray areas), the crystals (brighter areas) and darker area corresponding to the pores with a deeper topography (BSE is not sensitive to low topography variations). The brighter BSE signal of the crystals indicates that they scatter more electrons than the surrounding materials, maybe because of their higher crystallinity density.

We can hypothesize that the irradiation used to make the membrane porous induces chain scissions and the formation of PET oligomers. PET oligomers are probably hydro-soluble due to the formation of oxidized groups. In the presence of water, they can solubilize and migrate to the surface. The water evaporation is slowed by the presence of the dissolved oligomers, favoring the migration of other species to the surface. Once the concentration of these oligomers attains a critical point, crystallization can occur.

As expected, SEM analysis of sample PET-Pristine (Figure A.13) showed no crystals on the surface, even several days after cryo-ultramicrotomy. It is clear that the irradiation is responsible for the creation of water-soluble low molecular weight species that can diffuse from the membrane when in contact with water.

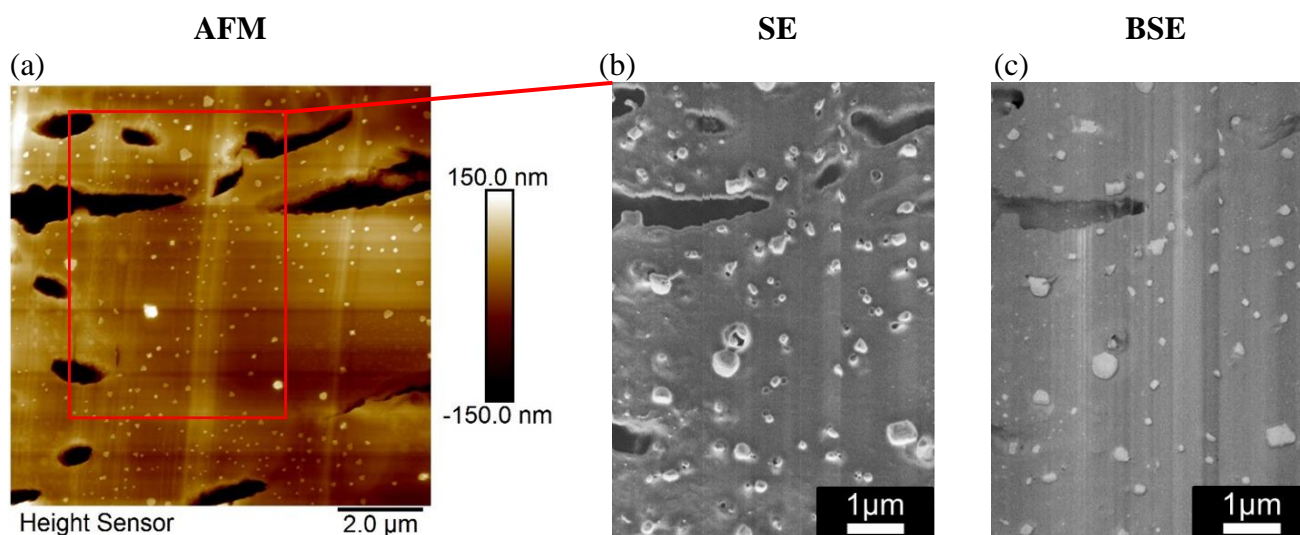


**Figure A.12.** Co-localized AFM/SEM analysis of sample PET-Porous: (a) AFM topography image of a  $10 \times 10 \mu\text{m}^2$  area; (b) SEM-SE image of the area delimited by the red line and (c) correspondent SEM-BSE image of the same area.

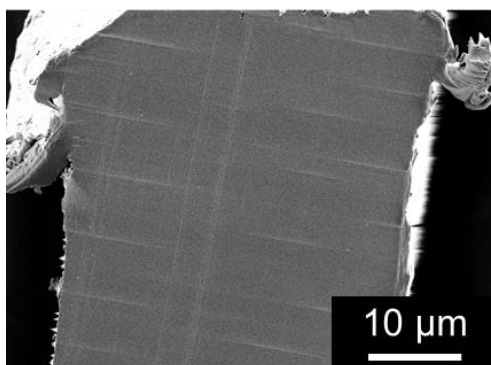


**Figure A.13.** SEM-SE image of sample PET-Pristine showing no crystal on the surface after cryo-ultramicrotomy

In order to provide chemical evidence of the elution of these species on water, samples of PET-Pristine and PET-Porous were soaked in water from 1 month and the soaking waters issued from these natural ageing were analyzed by Raman spectroscopy. Figure A.14 shows the Raman spectra from the water collected from sample PET-Porous and PET-Pristine, and the chemical signature of the Polyethylene bag containing the water. Although no difference can be seen from the PE bag and the water issued from sample PET-Pristine, one can see the apparition of new Raman bands at 875, 1000, 1610 and 3067  $\text{cm}^{-1}$  in the water used for sample PET-Porous. These bands can be related to the elution of PET oligomers from the irradiated sample.

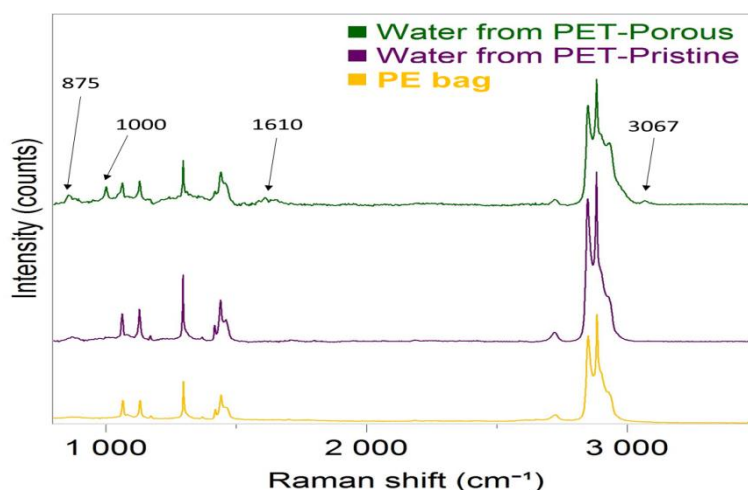


**Figure A.14.** Raman spectra of samples PET-Pristine, PET-Porous and the PE bag showing the apparition of new Raman bands at 875, 1000, 1610 and 3067  $\text{cm}^{-1}$  in the water used for sample PET-Porous.

Even though the direct identification and chemical assignment of the crystals by Raman spectroscopy could not have been done, their presence and growth is one more evidence that water trapped on the surface of cryo-ultramicrotomed samples (if a specific methodology is not applied to avoid frost deposition) can engender the elution of water soluble molecules from the bulk to the opened surface. Their further crystallization after water evaporation is possible, depending on their chemical structure.

# List of Tables

---

Table 1.1. Tensile and Impact strength of the PP composites <sup>23</sup>	7
Table 2.1. Comparison of PU and PS modulus measured with different techniques and nanomechanical models <sup>98</sup>	27
Table 2.2. Summary table of advantages and limitations of the sample preparation methods	41
Table 2.3. Summary table of techniques used for morphological and chemical characterization of polymers	51
Table 3.1. Cryo-ultramicrotomy parameters used for sample trimming and sectioning	59
Table 4.1. Mechanical and thermal properties of each component of the blend <sup>184,185</sup>	85
Table 4.2. Effect of SAN-MA Incorporation and Blending Sequence on the Melting and Crystallization Parameters of PA6, PA6+ABS and Ternary Blends on the first heating cycle	90
Table 4.3. Effect of SAN-MA Incorporation and Blending Sequence on the Melting and Crystallization Parameters of PA6, PA6+ABS and Ternary Blends on the cooling and second heating cycle.	91
Table 4.4. Characteristic band intensity ratios from literature and calculated experimentally.	92
Table 5.1 Sample and fabrication step	108
Table 5.2 Modulus of each phase of the hybrid membranes (AFM measurement) and SG phase uptake (TGA)	112
Table 5.3 Samples, step of fabrication and SG content determined by weighting	123
Table 5.4 Modulus of each phase of the hybrid membranes (AFM) and percentage of SG phase (TGA)	125
Table 5.5 AFM and SANS measurements of the hybrid membranes	128
Table 6.1. Composition and thermal properties of the copolymers studied. <sup>262,264</sup>	145
Table 6.2. Theoretical morphology, SAXS and AFM results for sample SPEOS and SPEOS+LiTFSI <sup>262</sup>	149
Table 6.3. AFM PeakForce QNM analysis of samples SPC <sub>18</sub> S, SPC <sub>18</sub> S_X and SPC <sub>22</sub> S_X	151
Table 6.4. SAXS results for samples SPC <sub>18</sub> S, SPC <sub>18</sub> S_X and SPC <sub>22</sub> S_X <sup>264</sup>	152
Table 6.5. Composition of the PSTFSILi-PEO-PSTFSILi copolymer	152
Table 6.6. SAXS results for the “single-ion” sample and inter-lamellar distance measured by AFM	154

# List of Figures

Figure 1.1. TEM micrograph of an immiscible PPE/SAN 60/40 wt% blend and table of mechanical properties of PPE, SAN and 60/40 PPE/SAN blend. <sup>3,4</sup>	2
Figure 1.2. TEM micrographs showing different morphologies developed for increasing amount of SBM compatibilizer into PPE/SAN blends. The table presents the corresponding mechanical properties. <sup>3,4</sup>	3
Figure 1.3. Example of multilayer polymer material composed of an outer layer of nylon, a gas barrier layer of EVOH and the contact layer of LDPE intercalated with adhesive layers	4
Figure 1.4. Different properties of PLLA films as function of the degree of crystallinity: (a) Young's modulus, (b) elongation at break and (c) permeability to water vapor (WVP). The crystal polymorphs are indicated for each degree of crystallinity. <sup>16</sup>	5
Figure 1.5. Scheme of reaction of hydrolysis and condensation of a silane coupling agent for surface modification of fibers. R: vinyl groups, epoxy, amino, mercapto; X: methyl or ethyl groups.	6
Figure 1.6. SEM micrographs representing the interfacial adhesion between GF and PP matrix for PP/GFc (a, a1), PP/GFf (b, b1), PP/2MPP/GFf (c, c1), PP/3MPP/GFf (d, d1) PP/10MPP/GFf (e, e1). (a1), (b1), (c1), (d1) and (e1) are enlarged areas marked by the dashed yellow squares in (a), (b), (c), (d) and (e) respectively. <sup>24</sup>	7
Figure 1.7. (a) Polarized optical micrographs during an isothermal PP crystallization at 135°C around a single fiber (GFc or GFf) (b) SEM micrograph of the etched fracture surface for PP/2%MPP/GFf injection molded sample. Adapted from <sup>24</sup>	8
Figure 1.8. SEM image characteristic of nanoclay morphology in a 95/5 wt% Polyamide6-Montmorillonite nanocomposite: (a) agglomerated and (b) exfoliated. <sup>29</sup>	9
Figure 1.9. PLM photographs of (a) neat PTT and (b) PTT nanocomposite with 10wt% of clay. Adapted from <sup>45</sup>	10
Figure 1.10. Example of copolymer morphologies: (a) lamellae (b) hexagonal packed cylinders (c) bicontinuous gyroids and (d) cubic packed spheres. Adapted from <sup>52-54</sup>	10
Figure 1.11. AFM topographic images on the membrane's surface of (a) PS, (b) PS96/PB4, (c) PS45/PB55, (d) PS30/PB70 and (e) PB. Adapted from <sup>55</sup>	11
Figure 1.12. Morphology profile through the material thickness detected by optical microscopy (central micrograph) and by AFM height maps. The positions where the analyses were performed are indicated by arrows pointing on the cross section optical micrograph. <sup>57</sup>	12
Figure 1.13. Schematic representation of the different properties to be characterized on the surface and the bulk of membranes	16
Figure 2.1. Basic setup for AFM analysis showing the reflection of the laser on the cantilever surface towards the photodetector. Adapted from <sup>73</sup>	20
Figure 2.2. (a) Schematic representation of the tip-sample interaction dynamics <sup>79</sup> (b) Force-distance curve obtained from the tip-surface contact with the approach in blue and the retraction in red. Different mechanical properties are extracted from the curves: Modulus from the slope of the linear part, Adhesion from the minimum force of the retraction curve, Deformation calculated from the distance in separation from the point of contact to the maximum load on the approach curve, and Dissipation of energy as the area between the approach and retraction curves (yellow area).	22
Figure 2.3. 5x5 $\mu\text{m}^2$ AFM PF-QNM images of (a) topography, (b) Young's modulus and (c) adhesion force presented with their corresponding profiles, along the dashed line indicated in the corresponding image. Adapted from <sup>80</sup>	23
Figure 2.4. AFM modulus images of (a) uncompatibilized POE/PA6 and (b) reactive compatibilized POE-g-MA/PA6 blends. Interfacial roughening observed with nanomechanical mapping: (c) POE/PA6 and (d) POE-g-MA/PA6 blends.	23
Figure 2.5. (a) SEM micrographs showing the direct measurement of the cantilever and tip dimensions (b) Blind tip reconstruction for evaluation of tip shape. <sup>90,92</sup>	25

- Figure 2.6. Schematic representation of two different kinds of indenters and the mechanical models used to describe the tip-sample interaction.  $F$  is the applied force (from force curve),  $E$  is the Young's modulus (fit parameter),  $\nu$  is Poisson's ratio (typically 0.2-0.5 for polymer materials),  $R$  is the radius of curvature of the indenter (tip),  $\delta$  is indentation depth,  $\gamma$  the work of adhesion and  $\alpha$  is the half angle of the indenter.<sup>96,97</sup> 26
- Figure 2.7. Energy level diagram showing the states involved in Raman signal 28
- Figure 2.8. (a) Raman spectrum of Polystyrene (b) schematic representation of different chemical and structural information issued from the interpretation of Raman spectra. 28
- Figure 2.9. Schematic representation of a Confocal Raman spectrometer. Adapted from<sup>104,105</sup> 29
- Figure 2.10. Raman mapping images of (b) PLA/PCL binary blend and (b) PLA50/TPS30/PCL20 ternary blend plotted from the combination of intensity maps of the bands centered at  $1768\text{ cm}^{-1}$  (PLA) and  $1723\text{ cm}^{-1}$  (PCL).<sup>106</sup> 30
- Figure 2.11. (a) Schematic representation of the confocal aperture used for depth profiling (b) Confocal depth profiling scan through a  $15\text{ }\mu\text{m}$  coating of PE on PET. Adapted from<sup>107,108</sup> 30
- Figure 2.12. (a) Lateral scan on the cross-section of PET/PE laminate showing spectra at each distance from the PET/PE interface (b) schematic representation of the effect of the excited waveguide modes which increase the observed PET signals outside the sample.<sup>108</sup> 31
- Figure 2.13. (a) Bruker/Horiba Jobin Yvon AFM-Raman setup composed of (1) AFM Dimension Icon; (2) Modified Raman LabRam HR; (3) Motorized stage from Icon equipped with a second piezoelectric stage controlled by LabRam for Raman mapping. Co-localization strategy is shown by images (b) with the sample below the AFM head and (c) with the sample below the Raman objective.<sup>126</sup> 33
- Figure 2.14. (a) Witec setup allying AFM-Raman in a single instrument. (b) AFM head installed on the objective turret (c) Co-localization strategy based on the turning of the objective turret to switch between AFM and Raman analyses. 33
- Figure 2.15. Schematic representation of Tip-Enhanced Raman Spectroscopy in two configurations: (a) transmission for transparent samples and (b) reflection for opaque samples. Adapted from<sup>127</sup> 34
- Figure 2.16. Schematic representation of the cryo-fracture procedure on a polymer membrane 35
- Figure 2.17. (a) Schematic representation of tip convolution when probing a rough sample and the differences on the contact point (b) AFM Topography image of a PMMA sample and (c) correspondent AFM Modulus image of the sample showing modulus heterogeneities artifacts induced by sample roughness. Adapted from<sup>129</sup> 36
- Figure 2.18. Schematic representation of Cryo-Ultramicrotomy operation showing: (a) motion of the sample holder during sectioning and (b) the collection of thin sections on a copper grid.<sup>131</sup> (c) Optical microscopy image of a 200 mesh grid with thin transparent samples highlighted by the red circles.<sup>67</sup> 37
- Figure 2.19. (a) Comparison of the surface roughness of an area of  $5\times 5\text{ }\mu\text{m}^2$  obtained by cryo-fracture and cryo-ultramicrotomy of a polyurethane sample. Example of an area of  $2\times 2\text{ }\mu\text{m}^2$  a (b) non-optimized and an (c) optimized (cutting temperature and speed) surface of a cryo-ultramicrotomed sample of a heterophasic polypropylene copolymer sample. Adapted from<sup>80,132</sup> 38
- Figure 2.20. Schematic representation of the embedding procedure for sectioning of thin materials 38
- Figure 2.21. Schematic representation of a FIB instrument composed by an electron and an ionic beam. (a) Sample is perpendicular to the electron beam for imaging and (b) the sample is tilted for milling with the ionic beam. Adapted from<sup>135</sup> 39
- Figure 2.22. (a) FIB milling of the cross-section of a DPNR-graft-PS copolymer (b) Inset showing details of the microstructure, PS appearing in bright domains and DPNR in dark. 40
- Figure 2.23. XANES spectra showing the effect of electron and ion beam on the chemical structure of a polyacrylamide. Adapted from<sup>137</sup> 40
- Figure 2.24. (a) Schematic representation of the interaction volume of the primary beam with the material showing the regions where the different signals come from. 44
- Figure 2.25. Example of damage caused by a 20keV electron beam on a polymer sample. Images from (1) to (7) are relative to different etching times applied on the sample to gradually remove the irradiated material and to reveal the damage. Adapted from<sup>145</sup> 46

- Figure 2.26. SEM micrographs of a PP/UHMWPE blend: (a) skin layer showing shish-kebab structures; (b) subskin layer showing  $\beta$ -cylindrulites and (c) core layer showing bundle-like  $\beta$  crystals. The yellow arrow represents the flow direction.<sup>147</sup> 46
- Figure 2.27. SEM-BSE images of elastomer phases in PP matrix with different weight compositions: (a) EPDM<sub>40</sub>/EOC<sub>10</sub>/PP<sub>50</sub>, (b) EPDM<sub>30</sub>/EOC<sub>20</sub>/PP<sub>50</sub>, (c) EPDM<sub>20</sub>/EOC<sub>30</sub>/PP<sub>50</sub>, (d) EPDM<sub>10</sub>/EOC<sub>40</sub>/PP<sub>50</sub>.<sup>148</sup> 47
- Figure 2.28. TEM micrographs of PPO/PA6 nanocomposites at low magnification (a) showing small domains of PPO phase (light gray) in PA6 phase (dark gray) and at higher magnification (b) showing dark lines inside the PA6 phase relative to the organoclay.<sup>149</sup> 48
- Figure 2.29. (a) STEM image of silica reinforced polybenzimidazole membranes with elemental maps for the elements C, O and Si displayed as insets. (b) EDS scan line of a silica particle showing the corresponding elemental distribution.<sup>151</sup> 49
- Figure 2.30. Schematic representation of the IR spectroscopy in ATR mode 50
- Figure 2.31. Micro ATR-FTIR mappings with dimension of 300x300 $\mu\text{m}^2$  representing the distribution of R-PA6 in different UHMWPE/R-PA6 blends. (a) uncompatibilized blend and (b) compatibilized blend with HDPE-g-MAH. Maps were obtained using a FTIR spectrum of R-PA6 as uniquely representative FTIR imaging recognition results.<sup>157</sup> 50
- Figure 2.32. Characterization strategy 52
- Figure 3.1. (a) Ultramicrotome LEICA EM UC7 (RT setup) and (b) cryo-chamber installed for cryo-ultramicrotomy 57
- Figure 3.2. Sample holder used to cut thick membranes (a) classical and (b) modified to minimize the risk of collision when cutting thin membranes close to the surface of the holder. 58
- Figure 3.3. (a) Schematic representation of sample preparation from standard injection molded specimens (b) Optical micrograph of the trapezoidal shape trimmed at the top of the triangular section, before cryosectionning. 58
- Figure 3.4. Trimmed membrane sandwiched in aluminum foil 59
- Figure 3.5. (a) Schematic representation of the cryo-ultramicrotomy procedure of a polymeric membrane (b) Optical micrograph of the cryo-ultramicrotomy cutting of a thick membrane without embedding 60
- Figure 3.6. Co-localized AFM/Raman setup installed at the laboratory SyMMES 61
- Figure 3.7. a) Schematic representation of the tip trajectory and deflection signal in function of time. In this representation, the Sync Distance parameter represents the time correspondent to the maximum deflection (Peak Force). (b) Images of the proper adjustment of the Sync Distance. 1) Sync too early; 2) Correct Sync Distance and 3) Sync too late. 64
- Figure 3.8. Deflection-distance curve on the sapphire sample showing the limits for deflection sensitivity determination. 65
- Figure 3.9. (a) AFM Log Modulus image of PS-LDPE standard sample. PS appearing in white yellow and LDPE in dark brown. (b) Log Modulus section corresponding to the line on the image showing a log difference of about 1.4 between both phases. 65
- Figure 3.10. Algorithm of the calibration procedure 66
- Figure 3.11. Offset shift correction of the Zero Order 67
- Figure 3.12. (a) Calibration of the sinus bar position by the correction of the Si peak at 520  $\text{cm}^{-1}$  (b) Evaluation of the confocality by the ratio of intensities measured with a hole of 200 and 1000  $\mu\text{m}$ , here a ratio of 51.8% was found. 68
- Figure 3.13. Co-localized AFM/Raman setup. The red arrows show the Co-localized Raman Microscope installed in front of the AFM and the Regular Raman Microscope positioned with direct access in front of the user 68
- Figure 3.14. (a) Stage below AFM head for topographic/nanomechanical analysis and (b) below the co-localized Raman microscope for chemical analysis 69
- Figure 3.15. ((a) Shuttle stage design showing the dock to be installed on both AFM and Raman and the shuttle stage itself with both targets and the sample area. (b) Illustration of the shuttle stage strategy. 70
- Figure 3.16. (a) SEM image of the Micro-Targets milled by FIB on the surface of the sample holder (b) Detail of one micro-target. 70



Figure 3.17. (a) Polymeric membrane sample sandwiched between aluminum foil and PP sheets on side view (b) Top view of the sandwiched sample	72
Figure 3.18. Schematic representation of $\mu$ -ATR-FTIR imaging. (a) Field of view of the detector and contact area of the crystal. (b) Germanium conical tip on sample. (c) Mapping of a large area of the sample with multiple steps	72
Figure 4.1. Polyamide 6 structure	78
Figure 4.2. Impact strength (notched izod) of different polymeric materials <sup>163</sup>	79
Figure 4.3. (a) Structures of the ABS components: Polyacrylonitrile, polybutadiene and polystyrene. (b) TEM image showing the morphology of a ABS (SAN65.9/PB-g-SAN34.1 w/w with 44%wt PB content in PB-g-SAN). The rubber particles (PB) appear in dark and the SAN matrix in white, which is also present in sub-inclusions inside the rubber particles. The scale bar represents 200 nm. Adapted from <sup>169</sup>	79
Figure 4.4. Schematic representations of particle break down under a shearing stress field and coalescence. Adapted from <sup>170</sup>	80
Figure 4.5. Scheme of the effect of physical compatibilizers on the morphology of initially immiscible blends showing fine and smaller particles dispersed in the matrix	81
Figure 4.6. Scheme of the imidization reaction between Maleic Anhydride and PA6.	81
Figure 4.7. Chemical structures of (a) PA6 and (b) components of ABS copolymer and (c) components of SAN-MA copolymer	82
Figure 4.8. AFM-Raman co-localized analysis of sample PA6+ABS (a) AFM Image; Colocalized Raman mapping relative to: (b) Polyamide 6 (3230-3350 $\text{cm}^{-1}$ ) (c) Polybutadiene (1657-1680 $\text{cm}^{-1}$ ) (d) Acrylonitrile (2200-2280 $\text{cm}^{-1}$ ) and (e) Polystyrene (3020-3120 $\text{cm}^{-1}$ )	84
Figure 4.9. Complementary AFM 5x5 $\mu\text{m}^2$ images of a PA6+ABS blend: (a) Topography (b) Modulus (c) Deformation (d) Adhesion	84
Figure 4.10. AFM 15x15 $\mu\text{m}^2$ Modulus images of (a) reference sample PA6+ABS and (b) compatibilized sample (PA6/ABS/SAN-MA)	86
Figure 4.11. (a) AFM 10x10 $\mu\text{m}^2$ Modulus images, (b) TEM images. Samples: 1-(PA6/ABS/SAN-MA); 2-(ABS/SAN-MA)+PA6 and 3-(PA6/SAN-MA)+ABS;	87
Figure 4.12. Rheological behavior of (PA6/ABS) and ternary blends. (a) Complex viscosity; (b) Storage modulus ( $G'$ ) and (c) Loss modulus ( $G''$ ).	88
Figure 4.13. Schematic representation of the AFM/TEM analyses and results.	89
Figure 4.14. DSC thermograms obtained during the first heating cycle of samples (i) PA6; (ii) PA6+ABS; (iii) (PA6/ABS/SAN-MA); (iv) (ABS/SAN-MA)+PA6 and (v) (PA6/SAN-MA)+ABS	90
Figure 4.15. DSC thermograms obtained during the second heating cycle of samples (i) PA6; (ii) PA6+ABS; (iii) (PA6/ABS/SAN-MA); (iv) (ABS/SAN-MA)+PA6 and (v) (PA6/SAN-MA)+ABS	91
Figure 4.16. Typical Raman spectra of Polyamide alpha, gamma and amorphous phases.	92
Figure 4.17. (a) Superposition of PB Raman mapping (band integration between 1657-1680 $\text{cm}^{-1}$ ) on the binary AFM Modulus image, showing the PB phase in black. The higher the amount of PB, the brighter is the pixel. (b) Ratio of the peak intensities $I_{1080}/I_{1125}$ for : 1-(PA6/ABS/SAN-MA); 2- (ABS/SAN-MA)+PA6 and 3-(PA6/SAN-MA)+ABS.	93
Figure 4.18. Schematic representation of the analyses and results.	95
Figure 5.1. Operating principle of a fuel cell. Adapted from <sup>205</sup>	102
Figure 5.2. Nafion <sup>®</sup> structure	104
Figure 5.3. (a) sPEEK structure (X=0.4)	104
Figure 5.4. Representation of hydrolysis and condensation of a generic precursor molecule	106
Figure 5.5. Sol-Gel phase formation by hydrolysis and condensation of SG precursor	107
Figure 5.6. Schema of the different steps of fabrication of the hybrid membranes	108
Figure 5.7. (a) Optical Image of the cryo-ultramicrotomed surface of sample Hyb-PC-HT; (b) AFM modulus image of the first 10 $\mu\text{m}$ of the cross-section from the left of the outer surface (corresponding to the red square drawn over (a)); (c) Co-localized Raman analysis of the membrane's skin (blue cross) and bulk (green cross).	109
Figure 5.8. (a) Membrane's skin and bulk normalized spectra (normalization relative to the CH-band intensity of sPEEK at 3080 $\text{cm}^{-1}$ ) (b) Relative SG phase uptake inside the Hyb-PC-HT membrane's cross-section	

- (area ratio between the band between 2785 and 3015 $\text{cm}^{-1}$  and the band between 3020 and 3120 $\text{cm}^{-1}$ ; membrane thickness: 35  $\mu\text{m}$ ) 110
- Figure 5.9. Hybrid membranes' structure at different stages of the fabrication process revealed by AFM and STEM. Sample Hyb-I: (a - AFM Height; b - AFM Modulus and c- STEM); Sample Hyb-PC: (d - AFM Height; e - AFM Modulus and f - STEM); and sample Hyb-PC-HT: (g - AFM Height; h - AFM Modulus and i - STEM). 111
- Figure 5.10. Optical microphotographs evidencing both the quality of the cryo-ultramicrotomed membranes cross-sections of hybrid membrane at each step of the fabrication process: (a) after impregnation/condensation (Hyb-I membrane); (b) after post-condensation step (Hyb-PC membrane) and (c) after hydrothermal treatment (Hyb-PC-HT membrane), and the presence of water droplets for (a) and (b). 113
- Figure 5.11. AFM images confirm the presence of water droplets on the cross-section of sample Hyb-I from (a) to (d); and a zone swollen by water on sample Hyb-PC from (e) to (h) 114
- Figure 5.12. AFM Height and Adhesion images of the cryo-ultramicrotomed surface of Hyb-I membrane taken just after cutting (a), 15 days after cutting (b), 30 days after cutting (c) and 90 days after cutting (d). The red arrows highlight the growth of non-adhesive objects inside de water droplets. The zoomed inset on image (d) evidences the regular shape of the growing objects. 115
- Figure 5.13. AFM Height images of the cryo-ultramicrotomed Hyb-I membrane before (a) and after nano-sweeping the growing objects (b). 115
- Figure 5.14. AFM images of the pack of particles (a) Topography, (b) Modulus, (c) Deformation and (d) Adhesion 116
- Figure 5.15. (a) Pack of growing objects piled-up by the AFM tip on sample Hyb-I (b) Raman mapping of the ratio SG/sPEEK 117
- Figure 5.16. SEM images taken 90 days after cryo-ultramicrotomy of the cross-section of sample Hyb-I (a - SE mode; b - BSE mode) and of sample Hyb-PC (c - SE mode; d - BSE mode). 118
- Figure 5.17. (a) Example of  $\mu$ -ATR-FTIR imaging of sample Hyb-I (30  $\mu\text{m}$ ) sandwiched between two PP sheets (~200  $\mu\text{m}$  each). The mapping is relative to the peak at 1080  $\text{cm}^{-1}$  (Si-O-Si), red meaning high intensity of the band and blue zero intensity. (b) FTIR spectrum of sample Hyb-I (after impregnation/condensation) in the middle of membrane's cross-section. 120
- Figure 5.18. Subtraction of Hyb-I from Hyb-PC spectra (red line) showing the decrease of the bands at 2900, 1460 and 1025  $\text{cm}^{-1}$  and reference methanol spectrum (blue). 121
- Figure 5.19. SHTriM sol-gel precursor structure before and after a first step of hydrolysis and condensation 123
- Figure 5.20. Composition of three AFM modulus images of the first 10  $\mu\text{m}$  of the left side of the membranes' cross-sections. 124
- Figure 5.21. AFM modulus images of samples (a) Hybrid\_10\_PC\_HT (b) Hybrid\_20\_PC\_HT and (c) Hybrid\_30\_PC\_HT 125
- Figure 5.22. (a) Schematic setup of SANS experiments. (b) Principle of scattering and definition of scattering vector  $q$ . Interferences between two spherical waves scattered by two atoms separated by  $r$  in real space.<sup>236</sup> 126
- Figure 5.23. Contrast matching principle 127
- Figure 5.24. SANS spectra of the sPEEK (blue, obtained for 83.5%-16.5%  $\text{H}_2\text{O}-\text{D}_2\text{O}$ ) and Sol-Gel (purple, obtained for 50%-50%  $\text{H}_2\text{O}-\text{D}_2\text{O}$ ) phases obtained by selective phase matching with contrast variation method. The incoming wavelength was  $\lambda=6 \text{ \AA}$ . Sample-detector distances of 2.8 m and 17.6 m were used to cover the extended range of momentum transfer  $0.003 < Q < 0.4 \text{ \AA}^{-1}$ , allowing to probe sizes and correlations in the range of 2-300 nm. 127
- Figure 5.25. (a) Relative amount of SG phase through the membranes' cross-sections (area ratio between the bands between 2800 and 3020  $\text{cm}^{-1}$  and the band between 3020 and 3130 $\text{cm}^{-1}$ ) for samples presenting different SG uptakes. Membranes' thicknesses were normalized. (b) to (d) present AFM modulus images of the first 10  $\mu\text{m}$  of the left side of the membranes' cross-sections (a) Hybrid\_10\_PC\_HT (b) Hybrid\_20\_PC\_HT and (c) Hybrid\_30\_PC\_HT. Red dashed lines surround the SG depleted zone at the outer surface. 129

- Figure 5.26. (a) Example of spectra on the cross-section of sPEEK and hybrid membranes with %SGw varying from 5 to 30% (b) Mean relative uptake of SG phase ( $RSGsPEEK$ ) as a function of the SG uptake measured by weighting (%SGw). Experimental points are shown in green and the corrected points from the subtraction of the sPEEK spectra are shown in red. 130
- Figure 6.1. Principle of operation of a lithium metal battery. During the discharging process, lithium ions migrate through the electrolyte system, ion-conducting medium, and separator membrane, from anode to cathode (left image), while the transport direction is reversed during the charging process (right image).<sup>246</sup> 138
- Figure 6.2. SEM image of Lithium dendrites at the Lithium Metal Electrode's surface.<sup>250</sup> 139
- Figure 6.3. Polyethylene oxide (PEO) structure 139
- Figure 6.4. Theoretical phase diagram of a triblock copolymer. Schematic examples of morphologies are given. L: lamellar, C: cylindrical, S: spheres and G: gyroids. N is the degree of polymerization of the diblocks formed by snipping the triblocks in half. Adapted from <sup>255</sup> 140
- Figure 6.5. Conductivity of different morphologies and measurement directions. Adapted from <sup>257</sup> 141
- Figure 6.6. Examples of Lithium salts for lithium batteries: (a) lithium trifluoromethanesulfonate (LiTf "Triflate") (b) lithium bis(fluorosulfonyl)imide (LiFSI) (c) lithium bis(fluoromalonato)borate (LiDFOB). Adapted from <sup>258,259</sup> 141
- Figure 6.7. Examples of single-ion copolymers. (a) Li [PSTFSILi-g-MPEGA] (b) PS-b-P(MALi-co-OEGMA) and (c) poly(LiMTFSI)-b-PEO-b-poly(LiMTFSI). More details in <sup>261-263</sup> 142
- Figure 6.8. Example of SAXS spectrum of a PS-PEO diblock copolymer. Mn PS= 9200 g.mol<sup>-1</sup> and Mn PEO= 8700g.mol<sup>-1</sup>.<sup>265</sup> 142
- Figure 6.9. (a) TEM image (2x2 μm<sup>2</sup>) and (b) AFM phase image (1x1 μm<sup>2</sup>) of a PS-PEO-PS copolymer with composition  $f_{PEO} = 0.27$ .<sup>266</sup> 143
- Figure 6.10. Structures of (a) PS-PEO-PS, (b) PS-PCi-PS (i=18 or 22) and (c) lithium bis(trifluorosulfone)imide (LiTFSI) 144
- Figure 6.11. Schematic cross-linking reaction of PS-PCi-PS (i=18 or 22) 144
- Figure 6.12. Optical photographs of the membrane's surface and thin sections on copper grid in different conditions: (a) affected surface and solubilized thin section after cryo-ultramicrotomy without control of frost deposition and (b) intact surface and thin section collected after optimized cryo-ultramicrotomy with water-control. 146
- Figure 6.13. AFM images relative to sample SPEOS (a) Height and (b) Modulus images of a 10x10 μm<sup>2</sup> area. 147
- Figure 6.14. AFM images of a 3x3 μm<sup>2</sup> area of sample SPEOS. (a) Height, (b) Modulus and (c) Topography section of the blue line on figure (b). 147
- Figure 6.15. Copolymer SPEOS+LiTFSI morphology revealed by Height and Modulus AFM images. (a) Height and (b) Modulus of a 3x3 μm<sup>2</sup> area; (c) represents the section of the red line on figure (b). (d) Height and (e) Modulus of a 1x1 μm<sup>2</sup> area; (f) represents the section of the blue line on figure (e). 148
- Figure 6.16. Schematic representation of the measured distances: the PS domain thickness, the distance between PS domains ( $d_{PS}$ ) and the distance between PEO lamellae ( $d_{PEO}$ ). 149
- Figure 6.17. AFM Height (a) and Modulus (b) images of a 10x10 μm<sup>2</sup> area of the sample SPEOS+LiTFSI from the surface to the bulk showing highly oriented lamellae perpendicular to the membrane's surface (left). The zoomed inset on (b) shows the lamellae on an area of 3x3 μm<sup>2</sup>. 150
- Figure 6.18. AFM Height of the copolymer systems: (a) SPC<sub>18</sub>S, (b) SPC<sub>18</sub>S\_X and (c) SPC<sub>22</sub>S\_X and the corresponding Modulus images (d) (e) and (f). Images are 1x1 μm<sup>2</sup>. 151
- Figure 6.19. Structure of the PSTFSILI-PEO-PSTFSILI copolymer 152
- Figure 6.20. AFM (a) Height and (b) Modulus images of a 1x1 μm<sup>2</sup> area of sample PSTFSILI-PEO-PSTFSILI. 153
- Figure 6.21. Schematic representation of the evolution of the morphology with the composition of single-ion copolymers at room temperature. Adapted from <sup>268</sup> 153
- Figure 6.22. AFM images of a 1x1 μm<sup>2</sup> area of sample PSTFSILI-PEO-PSTFSILI. (a) Height, (b) Modulus, (c) Adhesion and (d) Deformation. Red arrow points on a crystalline PEO lamella and blue arrow on the amorphous phase composed of amorphous PEO blended with PSTFSILI. 154

- Figure 6.23. (a) Tensile test at 40°C of a PSTFSILi-PEO-PSTFSILi and a PS-PEO-PS copolymer. (b) Evolution of conductivity of PSTFSILi-PEO-PSTFSILi copolymer as a function of temperature. <sup>260</sup> 155
- Figure 6.24. AFM images of a 3x3  $\mu\text{m}^2$  area of the sample TF1514. (a) Height, (b) and (c) Error Channel. The dashed red lines added on image (c) highlight the grain boundaries. 155
- Figure 6.25. Schematic representation of the effect of domain orientation on the ionic transport for a lamellar morphology. The red domain representing the non-conductive phase and the blue domain the conductive phase. <sup>246</sup> 156
- Figure 6.26. (a) Schematic representation of an electrolyte based on a block copolymer showing the discontinuity of the domains. Non-conductive domains are in red, the conductive domains in blue and grain boundaries in black. (b) Decrease in conductivity due to the presence of channel bending. (c) Absence of conduction due to the perpendicular orientation of two grains. <sup>275</sup> 156
- Figure 6.27. AFM images of a 3x3  $\mu\text{m}^2$  area of the “single-ion” sample PSTFSILi-PEO-PSTFSILi. (a) Height, (b) Modulus, (c) Adhesion and (d) Deformation. The red dashed line delimits a grain with different behavior compared to the others. 157
- Figure 6.28. AFM deformation image of a 3x3  $\mu\text{m}^2$  area of the “single-ion” sample PSTFSILi-PEO-PSTFSILi. Red arrows indicate the mean values of deformation of the lamellae inside the domain and on the adjacent grains. Blue arrows indicate the mean values of the mixture PEO+PSTFSILi inside the domain and on the adjacent grains. 158
- Figure 6.29. AFM adhesion images of a 10x10  $\mu\text{m}$  area showing the evolution of the high adhesion grains with time. (a) Initial state, t=0; (b) after 3.5 hours and (c) after 7.2 hours. 158
- Figure 6.30. Schematic representation of the surface properties of the “single-ion” sample PSTFSILi-PEO-PSTFSILi. (a) Side view and (b) Top view 159
- Figure 6.31. Schematic representation of the effect of hydration on the surface properties of the “single-ion” sample PSTFSILi-PEO-PSTFSILi. (a) Excluded PSTFSILi blocks from the crystalline PEO at the surface. (b) Water from the relative humidity breaks the crystallinity of the PEO chains at the edge of the grain boundary. (c) The PSTFSILi blocks solubilize in the amorphous PEO gradually from the edge to the interior. (d) Complete solubilization of the PSTFSILi blocks in the amorphous PEO makes the modulus, adhesion and deformation signals drop. (e) Top view of the schematic representation showing the dry state and after RH equilibrium. 160



# BIBLIOGRAPHY

---

- (1) Parameswaranpillai, J.; Thomas, S.; Grohens, Y. Polymer Blends: State of the Art, New Challenges, and Opportunities. In *Characterization of Polymer Blends: Miscibility, Morphology and Interfaces*; Thomas, S., Grohens, Y., Jyotishkumar, P., Eds.; Wiley-VCH Verlag GmbH & Co. KGaA, 2015; pp 1–6.
- (2) Coleman, M. M.; Graf, J. F.; Painter, P. Specific Interactions and the Miscibility of Polymer Blends. *Technomic* **1991**, 20.
- (3) Ruckda, H.; Abetz, V.; Mu, A. H. E. Toughening of Immiscible PPE/SAN Blends by Triblock Terpolymers. *Polymer (Guildf)*. **2007**, 48, 2700–2719 DOI: 10.1016/j.polymer.2007.03.005.
- (4) Sandler, J. K. W.; Altsta, V.; Schmalz, H.; Abetz, V.; Mu, A. H. E. Compatibilisation of PPE / SAN Blends by Triblock Terpolymers : Correlation between Block Terpolymer Composition , Morphology and Properties. **2006**, 47, 2772–2790 DOI: 10.1016/j.polymer.2006.02.064.
- (5) Dixon, J. *Packaging Materials 9. Multilayer Packaging for Food and Beverages*; 2011.
- (6) Kim, J. K.; Thomas, S.; Saha, P. *Multicomponent Polymeric Materials*; Kim, J. K., Thomas, S., Saha, P., Eds.; Springer, 2016.
- (7) Gherardi, R.; Becerril, R.; Nerin, C.; Bosetti, O. Development of a Multilayer Antimicrobial Packaging Material for Tomato Puree Using an Innovative Technology. *LWT - Food Sci. Technol.* **2016**, 72, 361–367 DOI: 10.1016/j.lwt.2016.04.063.
- (8) Sidwell, J. A. *Food Contact Polymeric Materials*; iSmithers Rapra Publishing, 1992.
- (9) Langhe, D.; Ponting, M. *Manufacturing and Novel Applications of Multilayer Polymer Films*; William Andrew, 2016.
- (10) Ren, X.; Ren, J.; Deng, M. Poly ( Amide-6-B-Ethylene Oxide ) Membranes for Sour Gas Separation. *Sep. Purif. Technol.* **2012**, 89, 1–8 DOI: 10.1016/j.seppur.2012.01.004.
- (11) Shieh, J.; Shung, T. Cellulose Nitrate-Based Multilayer Composite Membranes for Gas Separation. **2000**, 166, 259–269.
- (12) Peter, J.; Peinemann, K. Multilayer Composite Membranes for Gas Separation Based on Crosslinked PTMSP Gutter Layer and Partially Crosslinked Matrimid<sup>®</sup> 5218 Selective Layer. **2009**, 340, 62–72 DOI: 10.1016/j.memsci.2009.05.009.
- (13) Bazzarelli, F.; Bernardo, P.; Tasselli, F.; Clarizia, G.; Dzyubenko, V. G.; Vdovin, P.; Jansen, J. C. Multilayer Composite SBS Membranes for Pervaporation and Gas Separation. *Sep. Purif. Technol.* **2011**, 80 (3), 635–642 DOI: 10.1016/j.seppur.2011.06.025.
- (14) Gezgin, Z.; Lee, T. C.; Huang, Q. Nanoscale Properties of Biopolymer Multilayers. *Food Hydrocoll.* **2017**, 63, 209–218 DOI: 10.1016/j.foodhyd.2016.08.040.
- (15) Cavallo, D.; Goossens, H.; Meijer, H. E. H. Co-Extruded Multilayer Polymer Films for Photonic Applications. In *Organic and Hybrid Photonic Crystals*; Comoretto, Da., Ed.; Springer International Publishing Switzerland, 2015; pp 145–166.
- (16) Cocca, M.; Laura, M.; Lorenzo, D.; Malinconico, M.; Frezza, V. Influence of Crystal Polymorphism on Mechanical and Barrier Properties of Poly (L-Lactic Acid). *Eur. Polym. J.* **2011**, 47 (5), 1073–1080 DOI: 10.1016/j.eurpolymj.2011.02.009.
- (17) Wunderlich, B.; Grebowicz, J. Thermotropic Mesophases and Mesophase Transitions of Linear, Flexible Macromolecules. *Adv. Polym. Sci.* **1984**, 60/61, 1–59 DOI: 10.1007/3-540-12994-4\_1.
- (18) Kaw, A. K. *Mechanics of Composite Materials*; CRC Taylor and Francis Group, 2006.
- (19) Zheng, N.; He, J.; Zhao, D.; Huang, Y.; Gao, J.; Mai, Y. Improvement of Atomic Oxygen Erosion Resistance of Carbon Fiber and Carbon Fiber / Epoxy Composite Interface with a Silane Coupling Agent. *JMADE* **2016**, 109, 171–178 DOI: 10.1016/j.matdes.2016.07.004.
- (20) Xie, Y.; Hill, C. a. S.; Xiao, Z.; Militz, H.; Mai, C. Silane Coupling Agents Used for Natural Fiber/polymer Composites: A Review. *Compos. Part A Appl. Sci. Manuf.* **2010**, 41 (7), 806–819 DOI: 10.1016/j.compositesa.2010.03.005.
- (21) Cui, H.; Kessler, M. R. Pultruded Glass Fiber / Bio-Based Polymer : Interface Tailoring with Silane Coupling Agent. *Compos. Part A* **2014**, 65, 83–90 DOI: 10.1016/j.compositesa.2014.05.021.
- (22) Abdelmouleh, M.; Boufi, S.; Belgacem, M.; Dufresne, a. Short Natural-Fibre Reinforced Polyethylene and Natural Rubber Composites: Effect of Silane Coupling Agents and Fibres Loading. *Compos. Sci. Technol.* **2007**, 67 (7–8), 1627–1639 DOI: 10.1016/j.compscitech.2006.07.003.
- (23) Castellano, M.; Gandini, A.; Fabbri, P.; Belgacem, M. N. Modification of Cellulose Fibres with Organosilanes : Under What Conditions Does Coupling Occur ? **2004**, 273, 505–511 DOI: 10.1016/j.jcis.2003.09.044.
- (24) Luo, G.; Li, W.; Liang, W.; Liu, G.; Ma, Y.; Niu, Y. Coupling Effects of Glass Fiber Treatment and Matrix Modification on the Interfacial Microstructures and the Enhanced Mechanical Properties of Glass Fiber/polypropylene Composites. *Compos. Part B* **2017**, 111, 190–199 DOI: 10.1016/j.compositesb.2016.12.016.
- (25) El-Sabbagh, A. Effect of Coupling Agent on Natural Fibre in Natural Fibre/polypropylene Composites on

- Mechanical and Thermal Behaviour. *Compos. Part B* **2014**, *57*, 126–135 DOI: 10.1016/j.compositesb.2013.09.047.
- (26) Liu, Y.; Zhang, X.; Song, C.; Zhang, Y.; Fang, Y.; Yang, B.; Wang, X. An Effective Surface Modification of Carbon Fiber for Improving the Interfacial Adhesion of Polypropylene Composites. *Mater. Des.* **2015**, *88*, 810–819 DOI: 10.1016/j.matdes.2015.09.100.
- (27) Chawla, K. K. *Composite Materials*.
- (28) Ra, A.; Merah, N.; Boukhili, R.; Al-qadhi, M. Impact Resistance of Hybrid Glass Fiber Reinforced Epoxy/nanoclay Composite. *Polym. Test.* **2017**, *57*, 1–11 DOI: 10.1016/j.polymertesting.2016.11.005.
- (29) Tjong, S. C. Structural and Mechanical Properties of Polymer Nanocomposites. *Mater. Sci. Eng. R* **2006**, *53* (August), 73–197 DOI: 10.1016/j.mser.2006.06.001.
- (30) Chan, M.; Lau, K.; Wong, T.; Ho, M.; Hui, D. Mechanism of Reinforcement in a Nanoclay/polymer Composite. *Compos. Part B* **2011**, *42*, 1708–1712 DOI: 10.1016/j.compositesb.2011.03.011.
- (31) Sancaktar, E.; Kuznicki, J. Nanocomposite Adhesives: Mechanical Behavior with Nanoclay. *Int. J. Adhes. Adhes.* **2011**, *31* (5), 286–300 DOI: 10.1016/j.ijadhadh.2010.09.006.
- (32) Opelt, C. V.; Becker, D.; Lepienski, C. M.; Coelho, L. A. F. Reinforcement and Toughening Mechanisms in Polymer Nanocomposites E Carbon Nanotubes and Aluminum Oxide. *Compos. Part B* **2015**, *75*, 119–126 DOI: 10.1016/j.compositesb.2015.01.019.
- (33) Chen, J.; Yan, N. Mechanical Properties and Dimensional Stability of Organo-Nanoclay Modified Biofiber Polymer Composites. *Compos. Part B* **2013**, *47*, 248–254 DOI: 10.1016/j.compositesb.2012.11.015.
- (34) Liu, D.; Pourrahimi, A. M.; Olsson, R. T.; Hedenqvist, M. S.; Gedde, U. W. Influence of Nanoparticle Surface Treatment on Particle Dispersion and Interfacial Adhesion in Low-Density Polyethylene/aluminium Oxide Nanocomposites. *Eur. Polym. J.* **2015**, *66*, 67–77 DOI: 10.1016/j.eurpolymj.2015.01.046.
- (35) Chan, M.; Lau, K.; Wong, T. T.; Cardona, F. Interfacial Bonding Characteristic of Nanoclay/polymer Composites. *Appl. Surf. Sci.* **2011**, *258* (2), 860–864 DOI: 10.1016/j.apsusc.2011.09.016.
- (36) Ammar, A.; Elzatahry, A.; Al-maadeed, M.; Alenizi, A. M.; Huq, A. F.; Karim, A. Nanoclay Compatibilization of Phase Separated Polysulfone/polyimide Films for Oxygen Barrier. *Appl. Clay Sci.* **2017**, *137*, 123–134 DOI: 10.1016/j.clay.2016.12.012.
- (37) Müller, C. M. O.; Borges, J.; Yamashita, F. Composites of Thermoplastic Starch and Nanoclays Produced by Extrusion and Thermopressing. *Carbohydr. Polym.* **2012**, *89* (2), 504–510 DOI: 10.1016/j.carbpol.2012.03.035.
- (38) Pramoda, K. P.; Liu, T.; Liu, Z.; He, C.; Sue, H. Thermal Degradation Behavior of Polyamide 6/clay Nanocomposites. *Polym. Degrad. Stab.* **2003**, *81*, 47–56 DOI: 10.1016/S0141-3910(03)00061-2.
- (39) Lebaron, P. C.; Wang, Z.; Pinnavaia, T. J. Polymer-Layered Silicate Nanocomposites: An Overview. *Appl. Clay Sci.* **1999**, *15*, 11–29.
- (40) Tan, B.; Thomas, N. L. A Review of the Water Barrier Properties of Polymer/clay and Polymer/graphene Nanocomposites. *J. Memb. Sci.* **2016**, *514*, 595–612 DOI: 10.1016/j.memsci.2016.05.026.
- (41) Wu, Q.; Li, M.; Gu, Y.; Li, Y.; Zhang, Z. Nano-Analysis on the Structure and Chemical Composition of the Interphase Region in Carbon Fiber Composite. *Compos. Part A* **2014**, *56*, 143–149 DOI: 10.1016/j.compositesa.2013.10.003.
- (42) Wang, M.; Wang, Z.; Li, N.; Liao, J.; Zhao, S.; Wang, J.; Wang, S. Relationship between Polymer-Filler Interfaces in Separation Layers and Gas Transport Properties of Mixed Matrix Composite Membranes. *J. Memb. Sci.* **2015**, *495*, 252–268 DOI: 10.1016/j.memsci.2015.08.019.
- (43) Jeddi, J.; Yousefzade, O.; Babaei, A.; Ghanbar, S.; Rostami, A. Morphology, Microstructure and Rheological Properties of SAN (Styrene-Acrylonitrile)/ EPDM (Ethylene-Propylene-Diene Monomer) Nanocomposites: Investigating the Role of Organoclay Type and Order of Mixing. *Mater. Chem. Phys.* **2017**, *187*, 191–202 DOI: 10.1016/j.matchemphys.2016.12.001.
- (44) Musse Branco, C.; Sharma, S.; Madalena, M.; Forte, D. C.; Steinberger-wilckens, R. New Approaches towards Novel Composite and Multilayer Membranes for Intermediate Temperature-Polymer Electrolyte Fuel Cells and Direct Methanol Fuel Cells. *J. Power Sources* **2016**, *316* (x), 139–159 DOI: 10.1016/j.jpowsour.2016.03.052.
- (45) Smith, L.; Vasanthan, N. Effect of Clay on Melt Crystallization, Crystallization Kinetics and Spherulitic Morphology of Poly(trimethylene Terephthalate) Nanocomposites. *Thermochim. Acta* **2015**, *617*, 152–162 DOI: 10.1016/j.tca.2015.08.035.
- (46) Cuthbert, O.; Sinha, S.; Bandyopadhyay, J.; Wesley-smith, J.; Mohammad, N. Morphology, Thermal Properties and Crystallization Kinetics of Ternary Blends of the Polylactide and Starch Biopolymers and Nanoclay: The Role of Nanoclay Hydrophobicity. *Polymer (Guildf)* **2015**, *71*, 82–92 DOI: 10.1016/j.polymer.2015.06.058.
- (47) As, L.; Hassan, S.; Ali, H.; Häußler, L.; Wagenknecht, U.; Heinrich, G. Non-Isotermal Crystallization Behavior of PLA/LLDPE/nanoclay Hybrid: Synergistic Role of LLDPE and Clay. *Thermochim. Acta* **2013**, *565*, 102–113 DOI: 10.1016/j.tca.2013.04.016.
- (48) Lai, S.; Li, H.-C.; Liao, Y.-C. Properties and Preparation of Compatibilized Nylon 6 nanocomposites/ABS Blends: Part II - Physical and Thermal Properties. *Eur. Polym. J.* **2007**, *43*, 1660–1671 DOI: 10.1016/j.eurpolymj.2007.02.009.



- (49) Pramoda, K. P.; Mohamed, A.; Phang, I. Y.; Liu, T. Crystal Transformation and Thermomechanical Properties of Poly(vinylidene Fluoride)/clay Nanocomposites. *Polym. Int.* **2005**, *54* (November 2004), 226–232 DOI: 10.1002/pi.1692.
- (50) Phang, I. Y.; Pramoda, K. P.; Liu, T.; He, C. Crystallization and Melting Behavior of Polyester/clay Nanocomposites. *Polym. Int.* **2004**, *53* (November 2003), 1282–1289 DOI: 10.1002/pi.1513.
- (51) Liu, T. X.; Liu, Z. H.; Ma, K. X.; Shen, L.; Zeng, K. Y.; He, C. B. Morphology, Thermal and Mechanical Behavior of Polyamide 6/layered-Silicate Nanocomposites. *Compos. Sci. Technol.* **2003**, *63*, 331–337.
- (52) Lodge, T. P. Block Copolymers: Past Successes and Future Challenges. *Macromol. Chem. Phys.* **2003**, *204*, 265–273.
- (53) Abetz, V.; Simon, P. F. W. Phase Behaviour and Morphologies of Block Copolymers. In *Block Copolymers I*; Abetz, V., Ed.; Springer Berlin Heidelberg, 2005; pp 125–212.
- (54) Ruzette, A.-V.; Leibler, L. Block Copolymers in Tomorrow's Plastics. *Nat. Mater.* **2005**, *4*, 19–31.
- (55) Zhuang, G.; Wey, M.; Tseng, H. Effect of Copolymer Microphase-Separated Structures on the Gas Separation Performance and Aging Properties of SBC-Derived Membranes. *J. Memb. Sci.* **2017**, *529*, 63–71 DOI: 10.1016/j.memsci.2017.01.060.
- (56) Pantani, R.; Coccorullo, I.; Speranza, V.; Titomanlio, G. Modeling of Morphology Evolution in the Injection Molding Process of Thermoplastic Polymers. *Prog. Polym. Sci.* **2005**, *30*, 1185–1222 DOI: 10.1016/j.progpolymsci.2005.09.001.
- (57) Liparoti, S.; Sorrentino, A.; Speranza, V.; Titomanlio, G. Multiscale Mechanical Characterization of iPP Injection Molded Samples. *Eur. Polym. J.* **2017**, *90* (March), 79–91 DOI: 10.1016/j.eurpolymj.2017.03.010.
- (58) Karimi, H.; Bajestani, M. B.; Mousavi, S. A.; Garakani, R. M. Polyamide Membrane Surface and Bulk Modification Using Humid Environment as a New Heat Curing Medium. *J. Memb. Sci.* **2017**, *523* (September 2016), 129–137 DOI: 10.1016/j.memsci.2016.09.042.
- (59) Ameli, A.; Kazemi, Y.; Wang, S.; Park, C. B.; Pötschke, P. Process-Microstructure-Electrical Conductivity Relationships in Injection-Molded Polypropylene/carbon Nanotube Nanocomposite Foams. *Compos. Part A* **2017**, *96*, 28–36 DOI: 10.1016/j.compositesa.2017.02.012.
- (60) Ghosh, S.; Viana, J. C.; Reis, R. L.; Mano, J. F. Oriented Morphology and Enhanced Mechanical Properties of Poly (L-Lactic Acid) from Shear Controlled Orientation in Injection Molding. *Mater. Sci. Eng. A* **2008**, *490*, 81–89 DOI: 10.1016/j.msea.2008.01.003.
- (61) Fujiyama, M. Morphology-Mechanical Property Relationships in Injection Molding. In *Polypropylene An A-Z reference*; Karger-Kocsis, J., Ed.; Springer Netherlands, 1999; pp 519–526.
- (62) Li, Q.; Pan, X.; Hou, C.; Jin, Y.; Dai, H.; Wang, H. Exploring the Dependence of Bulk Properties on Surface Chemistries and Microstructures of Commercially Composite RO Membranes by Novel Characterization Approaches. *Desalination* **2012**, *292*, 9–18 DOI: 10.1016/j.desal.2012.02.005.
- (63) Zhang, W.; Yu, Z.; Qian, Q.; Zhang, Z.; Wang, X. Improving the Pervaporation Performance of the Glutaraldehyde Crosslinked Chitosan Membrane by Simultaneously Changing Its Surface and Bulk Structure. *J. Memb. Sci.* **2010**, *348*, 213–223 DOI: 10.1016/j.memsci.2009.11.003.
- (64) Paci, B.; Generosi, A.; Bailo, D.; Albertini, V. R.; Bettignies, R. De. Discriminating Bulk, Surface and Interface Aging Effects in Polymer-Based Active Materials for Efficient Photovoltaic Devices. *Chem. Phys. Lett.* **2010**, *494* (1–3), 69–74 DOI: 10.1016/j.cplett.2010.05.076.
- (65) Eibl, S. Comparison of Surface and Bulk Analytical Techniques for the Distinct Quantification of a Moderate Thermal Pre-Load on a Carbon Fibre Reinforced Plastic Material. *Polym. Degrad. Stab.* **2017**, *135*, 31–42.
- (66) Techniques for Membrane Surface Characterization. In *Surface Engineering of Polymer Membranes*; Springer Berlin Heidelberg, 2009; pp 5–63.
- (67) Corazza, M.; Simonsen, S. B.; Gnaegi, H.; Thydén, K. T. S.; Krebs, F. C.; Gevorgyan, S. A. Comparison of Ultramicrotomy and Focused-Ion-Beam for the Preparation of TEM and STEM Cross Section of Organic Solar Cells. *Appl. Surf. Sci.* **2016**, *389*, 462–468 DOI: 10.1016/j.apsusc.2016.07.096.
- (68) Shi, H.; Shi, D.; Wang, X.; Yin, L.; Yin, J.; Mai, Y. A Facile Route for Preparing Stable Co-Continuous Morphology of LLDPE/PA6 Blends with Low PA6 Content. *Polymer (Guildf.)* **2010**, *51*, 4958–4968 DOI: 10.1016/j.polymer.2010.08.023.
- (69) Munroe, P. R. The Application of Focused Ion Beam Microscopy in the Material Sciences. *Mater. Charact.* **2009**, *60* (1), 2–13 DOI: 10.1016/j.matchar.2008.11.014.
- (70) Schmitz, P.; Janocha, S. Films. In *Ullmann's Polymers and Plastics: Products and Processes*; Wiley-VCH Verlag GmbH & Co. KGaA, 2012; pp 650–676.
- (71) Sawyer, L. C.; Grubb, D. T. *Polymer Microscopy*, 2nd editio.; Springer-Science+Business Media, B.V., 1996.
- (72) Bernstein, R.; Kaufman, Y.; Freger, V. Membrane Characterization. In *Encyclopedia of Membrane Science and Technology*; Hoek, E. M. V., Tarabara, V. V., Eds.; John Wiley & Sons, Inc., 2013; pp 1–41.
- (73) Kaemmer, S. B. Introduction to Bruker's ScanAsyst and PeakForce Tapping AFM Technology. In *Application note #133*; Bruker Nano Surfaces Division, 2011; pp 1–12.

- (74) Binnig, G.; Quate, C. F. Atomic Force Microscope. *Phys. Rev. Lett.* **1986**, *56*, 930–933 DOI: 10.1103/PhysRevLett.56.930.
- (75) Rivoal, J.; Frétygny, C. Microscopie À Force Atomique (AFM). *Techniques de l'Ingénieur*. 2005, p 22.
- (76) Coulon, G. Imagerie de Surface de Polymères: Microscopie À Force Atomique. *Doss. Tech. l'Ingénieur* **2012**.
- (77) Chatterjee, S.; Gadad, S. S.; Kundu, T. K. Atomic Force Microscopy A Tool to Unveil the Mystery of Biological Systems. *Resonance* **2010**, No. July, 622–642.
- (78) Vancso, J.; Schon, P.; Duvigneau, J. What's New in Atomic Force Microscopy of Polymers? An Update. *Microsc. Anal.* **2009**, *23*, 5–11.
- (79) Pittenger, B.; Erina, N.; Su, C. Quantitative Mechanical Property Mapping at the Nanoscale with PeakForce QNM. In *App. Note* **128**, 2012; p 12.
- (80) Martinez-Tong, D. E.; Najar, A. S.; Soccio, M.; Nogales, A.; Bitinis, N.; Lopez-Manchado, M. A.; Ezquerro, T. A. Quantitative Mapping of Mechanical Properties in Poly(lactic Acid)/natural Rubber/organoclay Bionanocomposites as Revealed by Nanoindentation with Atomic Force Microscopy. *Compos. Sci. Technol.* **2014**, *104*, 34–39 DOI: DOI 10.1016/j.compscitech.2014.08.030.
- (81) Wang, D.; Fujinami, S.; Liu, H.; Nakajima, K.; Nishi, T. Investigation of Reactive Polymer - Polymer Interface Using Nanomechanical Mapping. *Macromolecules* **2010**, *7*, 5521–5523 DOI: 10.1021/ma100799s.
- (82) Megevand, B.; Pruvost, S.; Lins, L. C.; Livi, S.; Gerard, J.-F.; Duchet-Rumeau, J. Probing Nanomechanical Properties with AFM to Understand the Structure and Behavior of Polymer Blends Compatibilized with Ionic Liquids. *RSC Adv.* **2016**, *6*, 96421–96430 DOI: 10.1039/C6RA18492H.
- (83) Smolyakov, G.; Pruvost, S.; Cardoso, L.; Alonso, B.; Belamie, E.; Duchet-Rumeau, J. AFM PeakForce QNM Mode: Evidencing Nanometre-Scale Mechanical Properties of Chitin-Silica Hybrid Nanocomposites. *Carbohydr. Polym.* **2016**, *151*, 373–380 DOI: 10.1016/j.carbpol.2016.05.042.
- (84) Smolyakov, G.; Pruvost, S.; Cardoso, L.; Alonso, B.; Belamie, E.; Duchet-Rumeau, J. PeakForce QNM AFM Study of Chitin-Silica Hybrid Films. *Carbohydr. Polym.* **2017**, *166*, 139–145 DOI: 10.1016/j.carbpol.2017.02.075.
- (85) te Riet, J.; Katan, A. J.; Rankl, C.; Stahl, S. W.; van Buul, A. M.; Phang, I. Y.; Gomez-Casado, A.; Schön, P.; Gerritsen, J. W.; Cambi, A.; Rowan, A. E.; Vancso, G. J.; Jonkheijm, P.; Huskens, J.; Oosterkamp, T. H.; Gaub, H.; Hinterdorfer, P.; Figdor, C. G.; Speller, S. Interlaboratory Round Robin on Cantilever Calibration for AFM Force Spectroscopy. *Ultramicroscopy* **2011**, *111*, 1659–1669 DOI: 10.1016/j.ultramic.2011.09.012.
- (86) Emerson, R. J.; Camesano, T. a. On the Importance of Precise Calibration Techniques for an Atomic Force Microscope. *Ultramicroscopy* **2006**, *106*(4–5), 413–422 DOI: 10.1016/j.ultramic.2005.11.008.
- (87) Kim, M. S.; Choi, J. H.; Kim, J. H.; Park, Y. K. Accurate Determination of Spring Constant of Atomic Force Microscope Cantilevers and Comparison with Other Methods. *Measurement* **2010**, *43*, 520–526 DOI: 10.1016/j.measurement.2009.12.020.
- (88) Georgakaki, D.; Mitridis, S.; Sapalidis, A. A.; Mathioulakis, E.; Polatoglou, H. M. Calibration of Tapping AFM Cantilevers and Uncertainty Estimation: Comparison between Different Methods. *Meas. J. Int. Meas. Confed.* **2013** DOI: 10.1016/j.measurement.2013.08.010.
- (89) Ohler, B. Practical Advice on the Determination of Cantilever Spring Constants. Veeco Instruments Inc 2007, pp 1–12.
- (90) Flater, E. E.; Zacharakis-Jutz, G. E.; Dumba, B. G.; White, I. A.; Clifford, C. A. Towards Easy and Reliable AFM Tip Shape Determination Using Blind Tip Reconstruction. *Ultramicroscopy* **2014**, *146*, 130–143 DOI: 10.1016/j.ultramic.2013.06.022.
- (91) Kopycinska-Müller, M.; Geiss, R. H.; Hurley, D. C. Contact Mechanics and Tip Shape in AFM-Based Nanomechanical Measurements. *Ultramicroscopy* **2006** DOI: 10.1016/j.ultramic.2005.12.006.
- (92) Sikora, A. Quantitative Normal Force Measurements by Means of Atomic Force Microscopy Towards the Accurate and Easy Spring Constant Determination. *Nanosci. Nanometrology* **2016**, *2* (1), 8–29 DOI: 10.11648/j.nsnm.20160201.12.
- (93) Lin, D. C.; Horkay, F. Nanomechanics of Polymer Gels and Biological Tissues: A Critical Review of Analytical Approaches in the Hertzian Regime and beyond. *Soft Matter* **2008**, *4*(4), 669 DOI: 10.1039/b714637j.
- (94) Derjaguin, B. V.; Muller, V. M.; Toporov, Y. U. P. Effect of Contact Deformation on the Adhesion of Particles. *J. Colloid Interface Sci.* **1975**, *52*(3), 105–108 DOI: 10.1016/0021-9797(75)90018-1.
- (95) Sweers, K. K. M.; Bennink, M. L.; Subramaniam, V. Nanomechanical Properties of Single Amyloid Fibrils. *J. Phys. Condens. Matter* **2012**, *24*, 12 DOI: 10.1088/0953-8984/24/24/243101.
- (96) Cappella, B. *Mechanical Properties of Polymers Measured through AFM Force-Distance Curves*; Alig, I., Pasch, H., Schönherr, H., Eds.; Springer International Publishing Switzerland, 2016.
- (97) Young, T. J.; Monclus, M. A.; Burnett, T. L.; Broughton, W. R.; Ogini, S. L.; Smith, P. A. The Use of the PeakForce Quantitative Nanomechanical Mapping AFM-Based Method for High-Resolution Young's Modulus Measurement of Polymers. *Meas. Sci. Technol.* **2011**, *22*(12), 125703 DOI: 10.1088/0957-0233/22/12/125703.
- (98) Schön, P.; Bagdi, K.; Molnár, K.; Markus, P.; Pukánszky, B.; Julius Vancso, G. Quantitative Mapping of Elastic

- Moduli at the Nanoscale in Phase Separated Polyurethanes by AFM. *Eur. Polym. J.* **2011**, *47* (4), 692–698 DOI: 10.1016/j.eurpolymj.2010.09.029.
- (99) Dokukin, M. E.; Sokolov, I. Quantitative Mapping of the Elastic Modulus of Soft Materials with HarmoniX and Peak Force QNM AFM Modes. *Langmuir* **2012**, *28* (46), 16060–16071 DOI: 10.1021/la302706b.
- (100) Hunt, B. J.; James, M. I. *Polymer Characterization*; Springer Netherlands, 1993.
- (101) Kennedy, J. P. *Introduction to Polymer Spectroscopy*; Springer Berlin Heidelberg, 1984.
- (102) Stuart, B. H. Polymer Crystallinity Studied Using Raman Spectroscopy. *Vib. Spectrosc.* **1996**, *10*, 79–87.
- (103) Schmidt, U.; Hild, S.; Ibach, W.; Hollricher, O. Characterization of Thin Polymer Films on the Nanometer Scale with Confocal Raman AFM. *Macromol. Symp.* **2005**, *230*, 133–143 DOI: 10.1002/masy.200551152.
- (104) Ferraro, J. R.; Nakamoto, K.; Brown, C. W. *Introductory Raman Spectroscopy*; Elsevier, 2003.
- (105) Fenn, M. B.; Xanthopoulos, P.; Pyrgiotakis, G.; Grobmyer, S. R.; Pardalos, P. M.; Hench, L. L. Raman Spectroscopy for Clinical Oncology. *Adv. Opt. Technol.* **2011**, *20* DOI: 10.1155/2011/213783.
- (106) Luckachan, G. E.; Mittal, V. Evaluation of Crystallinity Variation and Phase Dispersion in Polymer Blends and Nanocomposites by Raman Mapping. *J. Polym. Res.* **2015**, *22*, 1–12 DOI: 10.1007/s10965-015-0878-0.
- (107) Everall, N. The Influence of out-of-Focus Sample Regions on the Surface Specificity of Confocal Raman Microscopy. *Applied spectroscopy*. 2008, pp 591–598.
- (108) Everall, N. J. Confocal Raman Microscopy: Common Errors and Artefacts. *Analyst* **2010**, *135* (10), 2512–2522 DOI: 10.1039/c0an00371a.
- (109) Everall, N. J. Confocal Raman Microscopy: Why the Depth Resolution and Spatial Accuracy Can Be Much Worse than You Think. *Applied Spectroscopy*. 2000, pp 1515–1520.
- (110) Washer, G.; Brooks, T.; Saulsberry, R. Characterization of Kevlar Using Raman Spectroscopy. *J. Mater. Civ. Eng.* **2009**, *21*, 226–234 DOI: 10.1061/(ASCE)0899-1561(2009)21:5(226).
- (111) Scipioni, R.; Gazzoli, D.; Teocoli, F.; Palumbo, O.; Paolone, A.; Ibris, N.; Brutti, S.; Navarra, M. A. Preparation and Characterization of Nanocomposite Polymer Membranes Containing Functionalized SnO<sub>2</sub> Additives. *Membranes (Basel)* **2014**, *4*, 123–142 DOI: 10.3390/membranes4010123.
- (112) Das, R. S.; Agrawal, Y. K. Raman Spectroscopy: Recent Advancements, Techniques and Applications. *Vib. Spectrosc.* **2011**, *57*, 163–176 DOI: 10.1016/j.vibspec.2011.08.003.
- (113) López-García, U.; Antaño-López, R.; Orozco, G.; Chapman, T.; Castaneda, F. Characterization of Electrodialysis Membranes by Electrochemical Impedance Spectroscopy at Low Polarization and by Raman Spectroscopy. *Sep. Purif. Technology* **2009**, *68*, 375–381 DOI: 10.1016/j.seppur.2009.06.012.
- (114) Radice, S.; Oldani, C.; Merlo, L.; Rocchia, M. Aquivion PerfluoroSulfonic Acid Ionomer Membranes : A Micro-Raman Spectroscopic Study of Ageing. *Polym. Degrad. Stab.* **2013**, *98* (6), 1138–1143 DOI: 10.1016/j.polymdegradstab.2013.03.015.
- (115) Mattsson, B.; Ericson, H.; Torell, L. M.; Sundholm, F. Degradation of a Fuel Cell Membrane as Revealed by Micro-Raman Spectroscopy. *Electrochim. Acta* **2000**, *45*, 1405–1408.
- (116) Peike, C.; Kaltenbach, T.; Weiss, K. A.; Koehl, M. Indoor vs. Outdoor Aging - Polymer Degradation in PV Modules Investigated by Raman Spectroscopy. In *Proceedings of SPIE*; Dhere, N. G., Wohlgemuth, J. H., Eds.; Spie-Int Soc Optical Engineering: Bellingham, 2012; Vol. 8472.
- (117) X. S. Liu; A. S. Vaughan; G. Chen. A Raman Spectroscopy Study of Bulk and Surface Ageing Phenomena in Polyethylene. *Annu. Rep. Conf. Electr. Insul. Dielectr. Phenom.* **2003**, 145–148.
- (118) Foster, B. New Atomic Force Microscopy (AFM) Approaches Life Sciences Gently, Quantitatively, and Correlatively. *Am. Lab.* **2012**, *44* (4), 24–28.
- (119) Wang, M.; Peng, Z. Investigation of the Nano-Mechanical Properties and Surface Topographies of Wear Particles and Human Knee Cartilages. *Wear* **2015**, *324–325*, 74–79 DOI: 10.1016/j.triboint.2013.05.005.
- (120) Panaitescu, D. M.; Frone, A. N.; Nicolae, C. Micro- and Nano-Mechanical Characterization of Polyamide 11 and Its Composites Containing Cellulose Nanofibers. *Eur. Polym. J.* **2013**, *49* (12), 3857–3866 DOI: 10.1016/j.eurpolymj.2013.09.031.
- (121) Panaitescu, D. M.; Vuluga, Z.; Radovici, C.; Nicolae, C. Morphological Investigation of PP/nanosilica Composites Containing SEBS. *Polym. Test.* **2012**, *31* (2), 355–365 DOI: 10.1016/j.polymertesting.2011.12.010.
- (122) Johnson, D.; Hilal, N. Characterisation and Quantification of Membrane Surface Properties Using Atomic Force Microscopy: A Comprehensive Review. *Desalination* **2015**, *356*, 149–164 DOI: 10.1016/j.desal.2014.08.019.
- (123) Panaitescu, D. M.; Frone, A. N.; Spataru, I. C. Effect of Nanosilica on the Morphology of Polyethylene Investigated by AFM. *Compos. Sci. Technol.* **2013**, *74*, 131–138 DOI: 10.1016/j.compscitech.2012.10.001.
- (124) Khulbe, K. C.; Matsuura, T. Characterization of Synthetic Membranes by Raman Spectroscopy, Electron Spin Resonance, and Atomic Force Microscopy; a Review. *Polymer (Guildf)* **2000**, *41*, 1917–1935.
- (125) Roigé, A.; Campoy-quiles, M.; Ossó, J. O.; Alonso, M. I.; Vega, L. F.; Garriga, M. Surface vs Bulk Phase Transitions in Semiconducting Polymer Films for OPV and OLED Applications. *Synth. Met.* **2012**, *161* (23–24), 2570–2574 DOI: 10.1016/j.synthmet.2011.09.031.

- (126) Kaemmer, S. Advances in Combined Atomic Force and Raman Microscopy. In *Application Note #136*; Bruker Nano Surfaces Division, 2012; p 10.
- (127) Hayazawa, N.; Tarun, A.; Taguchi, A.; Furusawa, K. Tip-Enhanced Raman Spectroscopy. In *Raman Spectroscopy for Nanomaterials Characterization*; Kumar, C. S. S. R., Ed.; Springer Berlin Heidelberg, 2012; pp 445–476.
- (128) Gołek, F.; Mazur, P.; Ryszka, Z.; Zuber, S. AFM Image Artifacts. *Appl. Surf. Sci.* **2014**, *304*, 11–19 DOI: 10.1016/j.apsusc.2014.01.149.
- (129) Haba, D.; Kaufmann, J.; Brunner, A. J.; Resch, K.; Teichert, C. Observation of Elastic Modulus Inhomogeneities in Thermosetting Epoxies Using AFM - Discerning Facts and Artifacts. *Polymer (Guildf)*. **2014**, *55*, 4032–4040 DOI: 10.1016/j.polymer.2014.06.030.
- (130) Ayache, J.; Beaunier, L.; Boumendil, J.; Ehret, G.; Laub, D. *Sample Preparation Handbook for Transmission Electron Microscopy Techniques*; Springer-Verlag New York, 2010.
- (131) Michler, G. H. *Electron Microscopy of Polymers*; Springer-Verlag Berlin Heidelberg, 2008; Vol. 1.
- (132) Tanem, B. S.; Kamfjord, T.; Augestad, M.; Lovgren, T. B.; Lundquist, M. Sample Preparation and AFM Analysis of Heterophase Polypropylene Systems. *Polymer (Guildf)*. **2003**, *44*, 4283–4291 DOI: 10.1016/S0032-3861(03)00392-6.
- (133) Li, J. The Focused-Ion-Beam Microscope - More than a Precision Ion Milling. *JOM* **2006**, *58* (3), 27–31 DOI: 10.1007/s11837-006-0156-z.
- (134) Raffa, V.; Castrataro, P.; Menciasci, A.; Dario, P. Focused Ion Beam as a Scanning Probe: Methods and Applications. In *Applied Scanning Probe Methods II*; Bhushan, B., Fuchs, H., Eds.; Springer Berlin Heidelberg, 2006; pp 361–412.
- (135) Bailey, R. J.; Geurts, R.; Stokes, D. J.; de Jong, F.; Barber, A. H. Evaluating Focused Ion Beam Induced Damage in Soft Materials. *Micron* **2013**, *50*, 51–56 DOI: 10.1016/j.micron.2013.04.005.
- (136) Fukuhara, L.; Kosugi, K.; Yamamoto, Y.; Jinnai, H.; Nishioka, H.; Ishii, H.; Kawahara, S. FIB Processing for Natural Rubber with Nanomatrix Structure. *Polymer (Guildf)*. **2015**, *57*, 143–149 DOI: 10.1016/j.polymer.2014.11.020.
- (137) Bassim, N. D.; De Gregorio, B. T.; Kilcoyne, a. L. D.; Scott, K.; Chou, T.; Wirick, S.; Cody, G.; Stroud, R. M. Minimizing Damage during FIB Sample Preparation of Soft Materials. *J. Microsc.* **2012**, *245* (3), 288–301 DOI: 10.1111/j.1365-2818.2011.03570.x.
- (138) Xie, S.; Harkin-jones, E.; Shen, Y.; Hornsby, P.; Mcafee, M.; McNally, T.; Patel, R.; Benkreira, H.; Coates, P. Quantitative Characterization of Clay Dispersion in Polypropylene-Clay Nanocomposites by Combined Transmission Electron Microscopy and Optical Microscopy. *Mater. Lett.* **2010**, *64* (2), 185–188 DOI: 10.1016/j.matlet.2009.10.042.
- (139) Pereira, A. G. B.; Gouveia, R. F.; Carvalho, G. M. De; Rubira, A. F.; Muniz, E. C. Polymer Blends Based on PEO and Starch: Miscibility and Spherulite Growth Rate Evaluated through DSC and Optical Microscopy. *Mater. Sci. Eng. C* **2009**, *29*(2), 499–504 DOI: 10.1016/j.msec.2008.09.009.
- (140) Lin, J.; Woo, E. M. Correlation between Interactions, Miscibility, and Spherulite Growth in Crystalline/crystalline Blends of Poly (Ethylene Oxide ) and Polyesters. *Polymer (Guildf)*. **2006**, *47*, 6826–6835 DOI: 10.1016/j.polymer.2006.07.039.
- (141) Morozov, I. A.; Solodko, V. N.; Kurakin, A. Y. Quantitative Study of Filled Rubber Microstructure by Optical and Atomic Force Microscopy. *Polym. Test.* **2015**, *44*, 197–207 DOI: 10.1016/j.polymertesting.2015.04.007.
- (142) Pereira, A. G. B.; Paulino, A. T.; Nakamura, C. V.; Britta, E. A.; Rubira, A. F.; Muniz, E. C. Effect of Starch Type on Miscibility in Poly (Ethylene Oxide) (PEO)/ Starch Blends and Cytotoxicity Assays. *Mater. Sci. Eng. C* **2011**, *31* (2), 443–451 DOI: 10.1016/j.msec.2010.11.004.
- (143) Choi, B. Optical Microscopy Study on the Crystallization in PEO-Salt Polymer Electrolytes. *Solid State Ionics* **2004**, *168*, 123–129 DOI: 10.1016/j.ssi.2004.01.026.
- (144) Olympus. Opto-digital Microscope DSX500 overview <http://www.olympus-ims.com/en/microscope/dsx500/> (accessed Jul 1, 2017).
- (145) Sawyer, L. C.; Grubb, D. T.; Meyers, G. F. Fundamentals of Microscopy. In *Polymer Microscopy*; Springer New York, 2008; pp 27–66.
- (146) Gedde, U. W. Microscopy of Polymers. In *Polymer Physics*; Springer Netherlands, 1999; pp 239–257.
- (147) Jin, M.; Jin, B.; Xu, X.; Li, X.; Wang, T.; Zhang, J. Effects of Ultrahigh Molecular Weight Polyethylene and Mould Temperature on Morphological Evolution of Isotactic Polypropylene at Micro-Injection Moulding Condition. *Polym. Test.* **2015**, *46*, 41–49 DOI: 10.1016/j.polymertesting.2015.06.018.
- (148) Uthaiyan, N.; Jarnthong, M.; Peng, Z.; Junhasavasdikul, B. Micro-Scale Morphologies of EPDM/EOC/PP Ternary Blends: Relating Experiments to Predictive Theories of Dispersion in Melt Mixing. *Mater. Des.* **2016**, *100*, 19–29 DOI: <http://dx.doi.org/10.1016/j.matdes.2016.03.099>.
- (149) Li, Y.; Shimizu, H. Novel Morphologies of Poly ( Phenylene Oxide ) ( PPO )/ Polyamide 6 ( PA6 ) Blend Nanocomposites. **2004**, *45*, 7381–7388 DOI: 10.1016/j.polymer.2004.09.018.
- (150) Ansell, P.; Dixon, M. Why STEM Not TEM ? [http://www.spectral.se/spectral.nsf/fl164f3e9b82f0feb1256dccc004611c1/d4a98a973f4e0290c12571e300376e06/\\$FILE/208 Why STEM Not TEM.pdf](http://www.spectral.se/spectral.nsf/fl164f3e9b82f0feb1256dccc004611c1/d4a98a973f4e0290c12571e300376e06/$FILE/208%20Why%20STEM%20Not%20TEM.pdf) (accessed Jul 20, 2007).

- (151) Heinzl, C.; Ossiander, T.; Gleich, S.; Scheu, C. Transmission Electron Microscopy Study of Silica Reinforced Polybenzimidazole Membranes. *J. Memb. Sci.* **2015**, *478*, 65–74 DOI: 10.1016/j.memsci.2014.12.051.
- (152) Koenig, J. L. Fourier Transform Infrared Spectroscopy of Polymers. In *Spectroscopy: NMR, Fluorescence, FT-IR. Advances in Polymer Science*; Springer Berlin Heidelberg, 1993; pp 87–154.
- (153) Chan, K. L. A.; Govada, L.; Bill, R. M.; Chayen, N. E.; Kazarian, S. G. Attenuated Total Reflection-FT-IR Spectroscopic Imaging of Protein Crystallization. *Anal. Chem.* **2009**, *81* (10), 3769–3775 DOI: 10.1021/ac900455y.
- (154) Chan, K. L. A.; Hammond, S. V.; Kazarian, S. G. Applications of Attenuated Total Reflection Infrared Spectroscopic Imaging to Pharmaceutical Formulations. *Anal. Chem.* **2003**, *75* (9), 2140–2146 DOI: 10.1021/ac026456b.
- (155) Glassford, S. E.; Govada, L.; Chayen, N. E.; Byrne, B.; Kazarian, S. G.; Crystal, G. Micro ATR FTIR Imaging of Hanging Drop Protein Crystallisation. *Vib. Spectrosc.* **2012**, *63*, 492–498 DOI: 10.1016/j.vibspec.2012.07.011.
- (156) Kazarian, S. G.; Chan, K. L. A. FTIR Imaging of Polymeric Materials under High-Pressure Carbon Dioxide. *Macromolecules* **2004**, *37*, 579–584 DOI: 10.1021/ma035420y.
- (157) Cheng, J.; Yang, X.; Dong, L.; Yuan, Z.; Wang, W.; Wu, S.; Chen, S.; Zheng, G.; Zhang, W.; Zhang, D.; Wang, H. Effective Nondestructive Evaluations on UHMWPE / Recycled-PA6 Blends Using FTIR Imaging and Dynamic Mechanical Analysis. *Polym. Test.* **2017**, *59*, 371–376 DOI: 10.1016/j.polymertesting.2017.02.021.
- (158) Nagle, D. J.; George, G. A.; Rintoul, L.; Fredericks, P. M. Use of Micro-ATR/FTIR Imaging to Study Heterogeneous Polymer Oxidation by Direct Solvent Casting onto the ATR IRE. *Vib. Spectrosc.* **2010**, *53*, 24–27 DOI: 10.1016/j.vibspec.2010.01.018.
- (159) Fernandes, J. P. C.; Mareau, V. H.; Gonon, L. AFM-Raman Co-Localization Setup: Advanced Characterization Technique for Polymers. *Int. J. Polym. Anal. Charact.* **2017**, 1–7 DOI: 10.1080/1023666X.2017.1391740.
- (160) Lobo, H.; Bonilla, J. W. *Handbook of Plastic Analysis*; Marcel Dekker, Inc., 2003.
- (161) Bashford, D. *Thermoplastics*; Springer Netherlands, 1997.
- (162) Gallego, R.; García-Lopez, D.; Merino, J. C.; Pastor, J. M. The Effect of Montmorillonite and Compatibilizer Quantities on Stiffness and Toughness of Polyamide Nanoblends a JC Merino a , B and JM Pastor a , B. *Polym. Int.* **2010**, *59*, 472–478 DOI: 10.1002/pi.2724.
- (163) PolymerTechnology & Services LLC. Brochure. 2013, p 12.
- (164) Tanrattanakul, V.; Sungthong, N.; Raksa, P. Rubber Toughening of Nylon 6 with Epoxidized Natural Rubber. *Polym. Test.* **2008**, *27*, 794–800 DOI: 10.1016/j.polymertesting.2008.05.013.
- (165) Burgish, G.; Paternoster, M.; Peduto, N.; Saraceno, A. Toughness Enhancement of Polyamide 6 Modified with Different Type of Rubber:the Influence of Internal Rubber Cavitation. *J. Appl. Polym. Sci.* **1997**, *66*, 777–787.
- (166) Wang, C.; Su, J. X.; Li, J.; Yang, H.; Zhang, Q.; Du, R. N.; Fu, Q. Phase Morphology and Toughening Mechanism of Polyamide 6/EPDM-G-MA Blends Obtained via Dynamic Packing Injection Molding. *Polymer (Guildf)*. **2006**, *47*, 3197–3206.
- (167) Jr., E. C.; Kopacak, U.; Goncalves, M. C.; S.P. Nunes. In Situ Compatibilization of Polyamide 6/natural Rubber Blends with Maleic Anhydride. *Polymer (Guildf)*. **2000**, *41*, 5929–5935.
- (168) Whelan, T.; Goff, J. *Injection Molding of Thermoplastics Materials*; Whelan, T., Goff, J., Eds.; Van Nostrand Reinhold, 1990.
- (169) Zhang, N.; Bao, X. X.; Tan, Z. Y.; Sun, S. L.; Zhou, C.; Yang, H. D.; Zhang, H. X. Morphology and Mechanical Properties of ABS Blends Prepared from Emulsion-Polymerized PB-G-SAN Impact Modifier with AIBN as Initiator. *J. Appl. Polym. Sci.* **2007**, *105*, 1237–1243 DOI: 10.1002/app.
- (170) Kryszeński, M.; Galeski, A.; Martuscelli, E. *Polymer Blends Processing, Morphology and Properties. Vol 2*; Kryszeński, M., Galeski, A., Martuscelli, E., Eds.; Springer Science+Business Media, LLC, 1984.
- (171) Utracki, L. A.; Shi, H. Development of Polymer Blend Morphology During Compounding in a Twin-Screw Extruder. Part I: Droplet Dispersion and Coalescence-A Review. *Polym. Eng. Sci.* **1992**, *32* (24), 1824–1833.
- (172) Singh, H.; Gupta, N. K. Evolution of Properties in ABS/PA6 Blends Compatibilized by Fixed Weight Ratio SAGMA Copolymer. *J. Polym. Res.* **2011**, *18* (6), 1365–1377.
- (173) Jafari, S. H.; Ptschke, P.; Stephan, M.; Pompe, G.; Warth, H.; Alberts, H. Thermal Behavior and Morphology of Polyamide 6 Based Multicomponent Blends. *J. Appl. Polym. Sci.* **2002**, *84* (14), 2753–2759 DOI: 10.1002/app.10570.
- (174) Kudva, R. A.; Keskkula, H.; Paul, D. R. Compatibilization of Nylon 6/ABS Blends using Glycidyl Methacrylate/methyl Methacrylate Copolymers. *Polymer (Guildf)*. **1998**, *39* (12), 2447–2460 DOI: 10.1016/S0032-3861(97)00583-1.
- (175) As'habi, L.; Jafari, S. H.; Khonakdar, H. A.; Baghaei, B. Morphological, Rheological and Thermal Studies in Melt Processed Compatibilized PA6/ABS/clay Nanocomposites. *J. Polym. Res.* **2011**, *18*, 197–205.
- (176) Sundararajs, U.; Macosko, C. W. Drop Breakup and Coalescence in Polymer Blends : The Effects of Concentration and Compatibilization. *Macromolecules* **1995**, *28*, 2647–2657.
- (177) Al-Malaika, S. *Reactive Modifiers for Polymers*, 1st ed.; Al-Malaika, S., Ed.; Blackie Academic & Professional, 1997.
- (178) Zhou, X.; Zhang, P.; Jiang, X.; Rao, G. Influence of Maleic Anhydride Grafted Polypropylene on the Miscibility of Polypropylene / Polyamide-6 Blends Using ATR-FTIR Mapping. *Vib. Spectrosc.* **2009**, *49*, 17–21 DOI:

- 10.1016/j.vibspec.2008.04.004.
- (179) Majumdar, B.; Keskkula, H.; Pault, D. R. Effect of the Nature of the Polyamide on the Properties and Morphology of Compatibilized Nylon/acrylonitrile-Butadiene-Styrene Blends. *Polymer (Guildf)*. **1994**, *35* (25), 5468–5477.
- (180) Ishak, Z. A. M.; Chow, W. S.; Takeichi, T. Influence of SEBS-G-MA on Morphology, Mechanical, and Thermal Properties of PA6/PP/organoclay Nanocomposites. *Eur. Polym. J.* **2008**, *44*, 1023–1039 DOI: 10.1016/j.eurpolymj.2008.01.019.
- (181) Chiang, C.; Chang, F. Polymer Blends of Polyamide-6 (PA6) and Poly (Phenylene Oxide) (PPO) Compatibilized by Styrene-Maleic Anhydride (SMA) Copolymer. *Polymer (Guildf)*. **1997**, *38* (19), 4807–4817.
- (182) Visakh, P. M.; Thomas, S.; Chandra, A. K.; Mathew, A. P. *Advances in Elastomers I - Blends and Interpenetrating Networks*; Visakh, P. M., Thomas, S., Chandra, A. K., Mathew, A. P., Eds.; Springer, 2013.
- (183) Evans, A. G.; Ahmad, Z. B.; Gilbert, D. G.; Beaumont, P. W. R. Mechanisms of Toughening in Rubber Toughened Polymers. *Acta Metall.* **1986**, *34* (1), 79–87.
- (184) Quaresimin, M.; Schulte, K.; Zappalorto, M.; Chandrasekaran, S. Toughening Mechanisms in Polymer Nanocomposites: From Experiments to Modelling. *Compos. Sci. Technol.* **2016**, *123*, 187–204 DOI: 10.1016/j.compscitech.2015.11.027.
- (185) Argon, A. S.; Cohen, R. E. Toughenability of Polymers. *Polymer (Guildf)*. **2003**, *44*, 6013–6032 DOI: 10.1016/S0032-3861(03)00546-9.
- (186) Contents, S.; Class, P. *Polymer Data Handbook*; Oxford University Press, 1999.
- (187) Shen, L.; Yee, I.; Liu, T. Nanoindentation Studies on Polymorphism of Nylon 6. *Polym. Test.* **2006**, *25*, 249–253 DOI: 10.1016/j.polymertesting.2005.09.019.
- (188) Wildes, G.; Keskkula, H.; Paul, D. R. Morphology of PC/SAN Blends: Effect of Reactive Compatibilization, SAN Concentration, Processing, and Viscosity Ratio. *J. Polym. Sci. Part B Polym. Phys.* **1999**, *37*, 71–82.
- (189) Lyu, S. P.; Jones, T. D.; Bates, F. S.; Macosko, C. W. Role of Block Copolymers on Suppression of Droplet Coalescence. *Macromolecules* **2002**, *35*, 7845–7855 DOI: 10.1021/ma020754t.
- (190) Boudenne, A.; Ibos, L.; Candau, Y.; Thomas, S. *Handbook of Multiphase Polymer Systems*; John Wiley & Sons, 2011.
- (191) Jafari, S. H.; Stephan, M.; Warth, H.; Alberts, H. Multicomponent Blends Based on Polyamide 6 and Styrenic Polymers: Morphology and Melt Rheology. *Polymer (Guildf)*. **2002**, *43*, 6985–6992.
- (192) Mojarrad, A.; Jahani, Y.; Barikani, M. Investigation on the Correlation Between Rheology and Morphology of PA6 / ABS Blends Using Ethylene Acrylate Terpolymer as Compatibilizer. *J. Appl. Polym. Sci.* **2011**, *120*, 2173–2182 DOI: 10.1002/app.
- (193) Solomon, M. J.; Almusallam, A. S.; Seefeldt, K. F.; Somwangthanaroj, A.; Varadan, P. Rheology of Polypropylene/Clay Hybrid Materials. *Macromolecules* **2001**, *34*, 1864–1872.
- (194) Castro, L. D. ; Oliveira, A. D.; Kersch, M.; Altstädt, V.; Pessan, L. A. Effects of Mixing Protocol on Morphology and Properties of PA6 / ABS Blends Compatibilized with MMA-MA. *J. Appl. Polym. Sci.* **2016**, *43612*, 1–8 DOI: 10.1002/app.43612.
- (195) Kim, B. K.; Lee, Y. M.; Jeong, H. M. Physical Properties of ABS/SMA/nylon-6 Ternary Blends: Effect of Blending Sequence. *Polymer (Guildf)*. **1993**, *34* (10), 2075–2080.
- (196) Paul, D. R.; Barlow, J. W. Polymer Blends (or Alloys). *J. Macromolecular Sci. Part C* **1980**, *18* (1), 109–168 DOI: dx.doi.org/10.1080/00222358008080917 PLEASE.
- (197) Pötschke, P.; Paul, D. R. Formation of Co-Continuous Structures in Melt-Mixed Immiscible Polymer Blends. *J. Macromol. Sci. Part C* **2003**, *43* (1), 87–141 DOI: 10.1081/MC-120018022.
- (198) Fornes, T. D.; Paul, D. R. Crystallization Behavior of Nylon 6 Nanocomposites. *Polymer (Guildf)*. **2003**, *44*, 3945–3961 DOI: 10.1016/S0032-3861(03)00344-6.
- (199) Liu, S.; Zhang, C.; Proniewicz, E.; Proniewicz, L. M.; Kim, Y.; Liu, J.; Zhao, Y.; Xu, Y.; Wu, J. Crystalline Transition and Morphology Variation of Polyamide 6/CaCl<sub>2</sub> Composite during the Decomplexation Process. *Spectrochim. Acta Part A Mol. Biomol. Spectrosc.* **2013**, *115*, 783–788 DOI: 10.1016/j.saa.2013.06.056.
- (200) Stephans, J. S.; Chase, D. B.; Rabolt, J. F. Effect of the Electrospinning Process on Polymer Crystallization Chain Conformation in Nylon-6 and Nylon-12. *Macromolecules* **2004**, *37*, 877–881.
- (201) Ferreira, V.; Depecker, C.; Laureyns, J.; Coulon, G. Structures and Morphologies of Cast and Plastically Strained Polyamide 6 Films as Evidenced by Confocal Raman Microspectroscopy and Atomic Force Microscopy. *Polymer (Guildf)*. **2004**, *45*, 6013–6026 DOI: 10.1016/j.polymer.2004.06.018.
- (202) Zhong, L.; Ren, X.; Yang, S.; Chen, E.; Sun, C.; Stroeks, A.; Yang, T. Lamellar Orientation of Polyamide 6 Thin Film Crystallization on Solid Substrates. *Polymer (Guildf)*. **2014**, *55*, 4332–4340.
- (203) Kolesov, I.; Mileva, D.; Androsch, R.; Schick, C. Structure Formation of Polyamide 6 from the Glassy State by Fast Scanning Chip Calorimetry. *Polymer (Guildf)*. **2011**, *52*, 5156–5165 DOI: 10.1016/j.polymer.2011.09.007.
- (204) Roeder, J.; Oliveira, R. V. B.; Gonc, M. C.; Soldi, V.; Pires, A. T. N. Polypropylene/polyamide-6 Blends: Influence of Compatibilizing Agent on Interface Domains. *Polym. Test.* **2002**, *21*, 815–821.
- (205) Heinzl, A. Fuel Cells and Hydrogen Technology. In *Technology Guide*; Bullinger, H.-J., Ed.; Springer, Berlin,

- Heidelberg, 2009; pp 368–373.
- (206) Lamy, C.; Jones, D. J.; Coutanceau, C.; Brault, P.; Martemianov, S. Do Not Forget the Electrochemical Characteristics of the Membrane Electrode Assembly When Designing a Proton Exchange Membrane Fuel Cell Stack. *Electrochim. Acta* **2011**, *56* (28), 10406–10423 DOI: 10.1016/j.electacta.2011.05.098.
- (207) Zhang, J.; Xie, Z.; Zhang, J.; Tang, Y.; Song, C.; Navessin, T.; Shi, Z.; Song, D.; Wang, H.; Wilkinson, D. P.; Liu, Z.-S.; Holdcroft, S. High Temperature PEM Fuel Cells. *J. Power Sources* **2006**, *160* (2), 872–891 DOI: <https://doi.org/10.1016/j.jpowsour.2006.05.034>.
- (208) Schmidt, T. J.; Gasteigerand, H. A.; Behm, R. J. Rotating Disk Electrode Measurements on the CO Tolerance of a High-Surface Area Pt/Vulcan Carbon Fuel Cell Catalyst. *J. Electrochem. Soc.* **1999**, *146* (4), 1296–1304 DOI: DOI: 10.1149/1.1391761.
- (209) Sood, R.; Cavaliere, S.; Jones, D. J.; Rozière, J. Electrospun Nanofibre Composite Polymer Electrolyte Fuel Cell and Electrolysis Membranes. *Nano Energy* **2016**, *26*, 729–745 DOI: 10.1016/j.nanoen.2016.06.027.
- (210) Subianto, S.; Pica, M.; Casciola, M.; Cojocaru, P.; Merlo, L.; Hards, G.; Jones, D. J. Physical and Chemical Modification Routes Leading to Improved Mechanical Properties of Perfluorosulfonic Acid Membranes for PEM Fuel Cells. *J. Power Sources* **2013**, *233*, 216–230 DOI: 10.1016/j.jpowsour.2012.12.121.
- (211) Jones, D. J.; Rozière, J. Advances in the Development of Inorganic – Organic Membranes for Fuel Cell Applications. *Adv. Polym. Sci.* **2008**, *215* (July), 219–264 DOI: 10.1007/12\_2008\_150.
- (212) *2015 ANNUAL REPORT of The Hydrogen and Fuel Cell Technical Advisory Committee*; 2016.
- (213) Adjemian, K. T.; Dominey, R.; Krishnan, L.; Ota, H.; Majsztrik, P.; Zhang, T.; Mann, J.; Kirby, B.; Gatto, L.; Velo-Simpson, M.; Leahy, J.; Srinivasan, S.; Benziger, J. B.; Bocarsly, and Andrew B. Function and Characterization of Metal Oxide-Nafion Composite Membranes for Elevated-Temperature H<sub>2</sub>/O<sub>2</sub> PEM Fuel Cells. *Chem. Mater.* **2006**, *18* (9), 2238–2248 DOI: 10.1021/cm051781b.
- (214) Chandan, A.; Hattenberger, M.; El-kharouf, A.; Du, S.; Dhir, A.; Self, V.; Pollet, B. G.; Ingram, A.; Bujalski, W. High Temperature (HT) Polymer Electrolyte Membrane Fuel Cells (PEMFC) - A Review. *J. Power Sources* **2013**, *231*, 264–278 DOI: 10.1016/j.jpowsour.2012.11.126.
- (215) Wu, J.; Yuan, X. Z.; Martin, J. J.; Wang, H.; Zhang, J.; Shen, J.; Wu, S.; Merida, W. A Review of PEM Fuel Cell Durability: Degradation Mechanisms and Mitigation Strategies. *J. Power Sources* **2008**, *184*, 104–119 DOI: 10.1016/j.jpowsour.2008.06.006.
- (216) Borup, R.; Meyers, J.; Pivovar, B.; Kim, Y. S.; Mukundan, R.; Garland, N.; Myers, D.; Wilson, M.; Garzon, F.; Wood, D.; Zelenay, P.; More, K.; Stroh, K.; Zawodzinski, T.; Boncella, J.; McGrath, J. E.; Inaba, M.; Miyatake, K.; Hori, M.; Ota, K.; Ogumi, Z.; Miyata, S.; Nishikata, A.; Siroma, Z.; Uchimoto, Y.; Yasuda, K.; Kimijima, K.-I.; Iwashita, N. Scientific Aspects of Polymer Electrolyte Fuel Cell Durability and Degradation. *Chem. Rev.* **2007**, *107* (10), 3904–3951 DOI: 10.1021/cr050182l.
- (217) Kreuer, K. D.; Schuster, M.; Obliers, B.; Diat, O.; Traub, U.; Fuchs, A.; Klock, U.; Paddison, S. J.; Maier, J. Short-Side-Chain Proton Conducting Perfluorosulfonic Acid Ionomers: Why They Perform Better in PEM Fuel Cells. *J. Power Sources* **2008**, *178* (2), 499–509 DOI: <https://doi.org/10.1016/j.jpowsour.2007.11.011>.
- (218) Kreuer, K. D. On the Development of Proton Conducting Polymer Membranes for Hydrogen and Methanol Fuel Cells. **2001**, *185*, 29–39.
- (219) Mendil-Jakani, H.; López, I. Z.; Mareau, V. H.; Gonon, L. Optimization of Hydrophilic/hydrophobic Phase Separation in sPEEK Membranes by Hydrothermal Treatments. *Phys. Chem. Chem. Phys.* **2017**, *19*, 16013–16022 DOI: 10.1039/C7CP00087A.
- (220) Portale, G.; Carbone, A.; Martinelli, A.; Passalacqua, E. Microstructure, State of Water and Proton Conductivity of Sulfonated Poly(ether Ether Ketone). *Solid State Ionics* **2013**, *252* (0), 62–67 DOI: <https://doi.org/10.1016/j.ssi.2013.08.031>.
- (221) Delhorbe, V.; Cailleateau, C.; Chikh, L.; Guillermo, A.; Gebel, G.; Morin, A.; Fichet, O. Influence of the Membrane Treatment on Structure and Properties of Sulfonated Poly(ether ether ketone) Semi-Interpenetrating Polymer Network. *J. Memb. Sci.* **2013**, *427*, 283–292 DOI: 10.1016/j.memsci.2012.10.001.
- (222) Chikh, L.; Delhorbe, V.; Fichet, O. (Semi-)Interpenetrating Polymer Networks as Fuel Cell Membranes. *J. Memb. Sci.* **2011**, *368* (1–2), 1–17 DOI: 10.1016/j.memsci.2010.11.020.
- (223) Jones, D. J.; Rozière, J. V.3: Fuel Cell Technology and Applications. In *Handbook of Fuel Cells–Fundamentals, Technology and Applications*; Vielstich, W., Lamm, A., Gasteiger, H., Eds.; Wiley, 2003; p 447.
- (224) Rozière, J.; Jones, D. J. No Title. In *Proceedings of the 1st European PEFC Forum*; Büchi, F., Scherer, G., Wokaun, A., Eds.; Lucerne, 2001; p 145.
- (225) Alberti, G.; Casciola, M. Composite Membranes for Medium-Temperature PEM Fuel Cells. *Annu. Rev. Mater. Res.* **2003**, *33*, 129–154 DOI: <https://doi.org/10.1146/annurev.matsci.33.022702.154702>.
- (226) Savadogo, O. Emerging Membranes for Electrochemical Systems Part II. High Temperature Composite Membranes Forpolymer Electrolyte Fuel Cell (PEFC) Applications. *J. Power Sources* **2004**, *127* (1–2), 135–161 DOI: 10.1016/j.jpowsour.2003.09.043.

- (227) Aparicio, M.; Lecoq, E.; Castro, Y.; Duran, A. Proton Conducting Organic/Inorganic Sol-Gel Membranes Produced from Phenyltriethoxysilane and 3-Methacryloxypropyl Trimethoxysilane. *J. Sol-Gel Sci. Technol.* **2005**, *34*, 233–239.
- (228) Deng, Q.; Moore, R. B.; Mauritz, K. A. Novel Nafion/ORMOSIL Hybrids via in Situ Sol-Gel Reactions. 1. Probe of ORMOSIL Phase Nanostructures by Infrared Spectroscopy. *Chem. Mater.* **1995**, *7*, 2259–2268.
- (229) Mauritz, K. A.; Hassan, M. K. Nanophase Separated Perfluorinated Ionomers as Sol-Gel Polymerization Templates for Functional Inorganic Oxide Nanoparticles. *Polym. Rev.* **2007**, *47*, 543–565 DOI: 10.1080/15583720701638393.
- (230) Colicchio, I.; Demco, D. E.; Baias, M.; Keul, H.; Moeller, M. Influence of the Silica Content in SPEEK-Silica Membranes Prepared from the Sol-Gel Process of Polyethoxysiloxane : Morphology and Proton Mobility. *J. Memb. Sci.* **2009**, *337*, 125–135 DOI: 10.1016/j.memsci.2009.03.037.
- (231) Mauritz, K. A. Organic-Inorganic Hybrid Materials: Perfluorinated Ionomers as Sol-Gel Polymerization Templates for Inorganic Alkoxides. *Mater. Sci. Eng. C* **1998**, *6*, 121–133.
- (232) Schubert, U. Chemistry and Fundamentals of the Sol-Gel Process. In *The Sol-Gel Handbook: Synthesis, Characterization and Applications. Volume 2*; Levy, D., Zayat, M., Eds.; John Wiley & Sons, 2015; p 1616.
- (233) Brinker, C. J.; Scherer, G. W. *Sol-Gel Science: The Physics and Chemistry of Sol-Gel Processing*; Academic Press, Inc, 1990.
- (234) Hüsing, N.; Hartmann, S. Inorganic-Organic Hybrid Porous Materials. In *Organic-Inorganic Hybrid Nanomaterials*; Kalia, S., Haldorai, Y., Eds.; Springer International Publishing, 2015; pp 143–185.
- (235) Delhorbe, V.; Cailleteau, C.; Chikh, L.; Guillermo, A.; Gebel, G.; Morin, A.; Fichet, O. Influence of the Membrane Treatment on Structure and Properties of Sulfonated Poly (Etheretherketone) Semi-Interpenetrating Polymer Network. *J. Memb. Sci.* **2013**, *427*, 283–292 DOI: 10.1016/j.memsci.2012.10.001.
- (236) Cousin, F. Small Angle Neutron Scattering. *EPJ Web Conf.* **2015**, *104*, 1–49 DOI: <https://doi.org/10.1051/epjconf/201510401004>.
- (237) Zemb, T.; Lindner, P. *Neutron, X-Rays and Light. Scattering Methods Applied to Soft Condensed Matter*, 1st ed.; Zemb, T., Lindner, P., Eds.; North Holland, 2002.
- (238) Online, V. A.; Lopez, I. Z.; Legrand, P. M.; Mareau, V. H.; Gonon, L. A New Interpretation of SAXS Peaks in Sulfonated Poly(ether Ether Ketone) (sPEEK) Membranes for Fuel Cells †. **2014**, 11228–11235 DOI: 10.1039/c4cp00710g.
- (239) Gebel, G. Structure of Membranes for Fuel Cells: SANS and SAXS Analyses of Sulfonated PEEK Membranes and Solutions. *Macromolecules* **2013**, *46*, 6057–6066.
- (240) Mauritz, K. A.; Stefanithis, D.; Davis, S. V.; Scheetz, R. W.; Pope, R. K.; Wilkes, G. L.; Huang, H.-H. Microstructural Evolution of a Silicon Oxide Phase in a Perfluorosulfonic Acid Lonomer by an In Situ Sol-Gel Reaction. *J. Appl. Polym. Sci.* **1995**, *55*, 181–190.
- (241) Beaucage, G. Combined Small-Angle Scattering for Characterization of Hierarchically Structured Polymer Systems over Nano-to-Micron Meter: Part II Theory. *Polym. Sci. A Compr. Ref.* **2012**, *2*, 399–409 DOI: 10.1016/B978-0-444-53349-4.00032-7.
- (242) Stuart, B. H. A Fourier Transform Raman Spectroscopy Study of the Crystallisation Behaviour of a Poly (Ether Ether Ketone)/ Poly (Ether Sulphone) Blend. *Spectrochim. Acta Part A* **1997**, *53*(1997), 107–110.
- (243) Everall, N. J.; Chalmers, J. M.; Ferwerda, R.; van der Maas, J. H.; Hendra, P. J. Measurement of Poly (Aryl Ether Ether Ketone) Crystallinity in Isotropic and Uniaxial Samples Using Fourier Transform-Raman Spectroscopy: A Comparison of Univariate and Partial Least-Squares Calibrations. *J. Raman Spectrosc.* **1994**, *25* (June 1993), 43–51.
- (244) Ellis, G.; Naffakh, M.; Marco, C.; Hendra, P. J. Fourier Transform Raman Spectroscopy in the Study of Technological Polymers Part 1: Poly (Aryl Ether Ketones ), Their Composites and Blends. **1997**, *1425*(97).
- (245) Maddams, W. F. A Review of Fourier-Transform Raman Spectroscopic Studies on Polymers. *Spectrochim. Acta* **1994**, *50A*, 1967–1986.
- (246) Young, W.-S.; Kuan, W.-F.; Epps, T. H. Block Copolymer Electrolytes for Rechargeable Lithium Batteries. *J. Polym. Sci. Part B Polym. Phys.* **2014**, *52*(1), 1–16.
- (247) I. Yoshimatsu, T. Hirai, J. Y. Lithium Electrode Morphology during Cycling in Lithium Cells. *J. Electrochem. Soc.* **1988**, *135*, 2422–2427.
- (248) Koch, V. R.; Young, J. H. The Stability of the Secondary Lithium Electrode in Tetrahydrofuran-Based Electrolytes. *J. Electrochem. Soc.* **1979**, *125*, 1371–1377.
- (249) M. Rosso, C. Brissot, A. Teyssot, M. Dollé, L. Sannier, J.M. Tarascon, R. Bouchet, S. L. Dendrite Short-Circuit and Fuse Effect on Li/polymer/Li Cells. *Electrochim. Acta* **2006**, *51* (25), 5334–5340.
- (250) Dollé, M.; Sannier, L.; Beaudoin, B.; Trentin, M.; Tarascon, J. M. Live Scanning Electron Microscope Observations of Dendritic Growth in Lithium/polymer Cells. *Electrochem. Solid - State Lett.* **2002**, *5*, 286–289.
- (251) F. Croce, G.B. Appetecchi, L. Persi, B. S. Nanocomposite Polymer Electrolytes for Lithium Batteries. *Nature* **1998**, *394*, 456–458.
- (252) Monroe, C.; Newman, J. The Impact of Elastic Deformation on Deposition Kinetics at Lithium/Polymer Interfaces. *J. Electrochem. Soc.* **2005**, *152*, 396–404.



- (253) Johansson, P. First Principles Modelling of Amorphous Polymer Electrolytes: Li<sup>+</sup>-PEO, Li<sup>+</sup>-PEI, and Li<sup>+</sup>-PES Complexes. *Polym.* **2001**, *42*, 4367–4373.
- (254) D. Devaux, R. Bouchet, D. Glé, R. D. Mechanism of Ion Transport in PEO/LiTFSI Complexes: Effect of Temperature, Molecular Weight and End Groups. *Solid State Ionics* **2012**, *227*, 119–127.
- (255) Matsen, M. W. Effect of Architecture on the Phase Behavior of AB-Type Block Copolymer Melts. *Macromolecules* **2012**, *45* (4), 2161–2165 DOI: 10.1021/ma202782s.
- (256) S.B. Darling. Directing the Self-Assembly of Block Copolymers. *Prog. Polym. Sci.* **2007**, *32*, 1152–1204.
- (257) Young, W.-S.; Epps, T. H. Ionic Conductivities of Block Copolymer Electrolytes with Various Conducting Pathways: Sample Preparation and Processing Considerations. *Macromolecules* **2012**, *45*, 4689–4697.
- (258) Younesi, R.; Veith, G. M.; Johansson, P.; Edström, K.; Vegge, T. Lithium Salts for Advanced Lithium Batteries: Li-metal, Li-O<sub>2</sub>, and Li-S. *Energy Environ. Sci.* **2015**, *8* (7), 1905–1922 DOI: 10.1039/C5EE01215E.
- (259) Burjanadze, M.; Karatas, Y.; Kaskhedikar, N.; Kogel, L. M.; Kloss, S.; Gentshev, A.-C.; Hiller, M. M.; Müller, R. a.; Stolina, R.; Vettikuzha, P.; Wiemhöfer, H.-D. Salt-in-Polymer Electrolytes for Lithium Ion Batteries Based on Organo-Functionalized Polyphosphazenes and Polysiloxanes. *Zeitschrift für Phys. Chemie* **2010**, *224* (10–12), 1439–1473 DOI: 10.1524/zpch.2010.0046.
- (260) Bouchet, R.; Maria, S.; Meziane, R.; Aboulaich, A.; Lienafa, L.; Bonnet, J.; Phan, T. N. T.; Bertin, D.; Gigmès, D.; Devaux, D.; Denoyel, R.; Armand, M. Efficient Electrolytes for Lithium-Metal Batteries. *Nat. Mater.* **2013**, *12*, 1–6.
- (261) Feng, S.; Shi, D.; Liu, F.; Zheng, L.; Nie, J.; Feng, W. Single Lithium-Ion Conducting Polymer Electrolytes Based on Poly [(4-Styrenesulfonyl)(trifluoromethanesulfonyl ) Imide ] Anions. *Electrochim. Acta* **2013**, *93*, 254–263 DOI: 10.1016/j.electacta.2013.01.119.
- (262) Rolland, J.; Poggi, E.; Vlad, A.; Gohy, J.-F. Single-Ion Diblock Copolymers for Solid-State Polymer Electrolytes. *Polymer (Guildf)* **2015**, *68*, 344–352 DOI: 10.1016/j.polymer.2015.04.056.
- (263) Porcarelli, L.; Aboudzadeh, M. A.; Rubatat, L.; Nair, J. R.; Shaplov, A. S.; Gerbaldi, C.; Mecerreyes, D. Single-Ion Triblock Copolymer Electrolytes Based on Poly(ethylene Oxide) and Methacrylic Sulfonamide Blocks for Lithium Metal Batteries. *J. Power Sources* **2017**, *364*, 191–199 DOI: 10.1016/j.jpowsour.2017.08.023.
- (264) Glatter, O.; Kratky, O. *Small Angle X-Ray Scattering*; London: Academic Press Inc. Ltd., 1982.
- (265) Zhu, L.; Cheng, S. Z. D.; Calhoun, B.; Ge, Q.; Quirk, R. P.; Thomas, E. L.; Hsiao, B. S.; Yeh, F.; Lotz, B. Phase Structures and Morphologies Determined by Self-Organization, Vitrification, and Crystallization: Confined Crystallization in an Ordered Lamellar Phase of PEO-B-PS Diblock Copolymer. *Polymer (Guildf)* **2001**, *42*, 5829–5839.
- (266) Pelletier, B. Caractérisation Approfondie de Copolymères Triblocs PS-B-POE-B-PS Utilisés En Tant qu'Electrolytes Polymères Solides Pour Les Batteries Lithium-Métal-Polymère, 2015.
- (267) Yang, P.; Yu, X.; Han, Y. Transition between Crystallization and Microphase Separation in PS-B-PEO Thin Film Influenced by Solvent Vapor Selectivity. *Polymer (Guildf)* **2010**, *51* (21), 4948–4957 DOI: 10.1016/j.polymer.2010.08.025.
- (268) Lassagne, A. Synthèse et Caractérisation de Nouveaux Électrolytes Copolymères Pour Batteries Lithium Métal Polymère, 2017.
- (269) Bouchet, R.; Phan, T. N. T.; Beaudoin, E.; Devaux, D.; Davidson, P.; Bertin, D.; Denoyel, R. Charge Transport in Nanostructured PS-PEO-PS Triblock Copolymer Electrolytes. *Macromolecules* **2014**, *47*, 2659–2665.
- (270) Claudy, P.; Létoffé, J. M.; Camberlain, Y.; Pascault, J. P. Glass Transition of Polystyrene versus Molecular Weight. *Polym. Bull.* **1983**, *9* (4–5), 208–215 DOI: 10.1007/BF00283709.
- (271) Frenck, L. Study of a Buffer Layer Based on Block Copolymer Electrolytes , between the Lithium Metal and a Ceramic Electrolyte for Aqueous Lithium-Air Battery Study of a Buffer Layer Based on Block Copolymer Electrolytes , between the Lithium Metal and a Ceramic Ele, 2017.
- (272) Singh, M.; Odusanya, G.; Wilmes, G. M.; Eitouni, H. B.; Gomez, E. D.; Patel, A. J.; Chen, V. L.; Park, M. J.; Fragouli, P.; Iatrou, H.; Hadjichristidis, N.; Cookson, D.; Balsara, N. P. Effect of Molecular Weight on the Mechanical and Electrical Properties of Block Copolymer Electrolytes. *Macromolecules* **2007**, *40* (13), 4578–4585 DOI: doi:10.1021/ma0629541.
- (273) Sax, J.; Ottino, J. M. Modeling of Transport of Small Molecules in Polymer Blends: Application of Effective Medium Theory. *Polym. Eng. Sci.* **1983**, *23* (3), 165–176.
- (274) Jinnai, H.; Yasuda, K.; Nishi, T. Three-Dimensional Observations of Grain Boundary Morphologies in a Cylinder-Forming Block Copolymer. *Macromol. Symp.* **2006**, *245–246* (1), 170–174.
- (275) Chintapalli, M.; Chen, X. C.; Thelen, J. L.; Teran, A. A.; Wang, X.; Garetz, B. A.; Balsara, N. P. Effect of Grain Size on the Ionic Conductivity of a Block Copolymer Electrolyte. *Macromolecules* **2014**.
- (276) Noort, S. J. T. Van; Werf, K. Van Der; Groot, B. G. De; Hulst, N. F. Van; Greve, J. Height Anomalies in Tapping Mode Atomic Force Microscopy in Air Caused by Adhesion. *Ultramicroscopy* **1997**, *69*, 117–127.
- (277) Dubourg, F.; Aime, J. P. Role of the Adhesion between a Nanotip and a Soft Material in Tapping Mode AFM. *Surf. Sci.* **2000**, *466*, 137–143.

- (278) Carrillo, F.; Gupta, S.; Balooch, M.; Marshall, S. J.; Marshall, G. W.; Pruitt, L.; Puttlitz, C. M. Nanoindentation of Polydimethylsiloxane Elastomers: Effect of Crosslinking, Work of Adhesion, and Fluid Environment on Elastic Modulus. *J. Mater. Res.* **2017**, *20* (10), 2820–2830 DOI: 10.1557/JMR.2005.0354.
- (279) Kaufman, J. D.; Klapperich, C. M. Surface Detection Errors Cause Overestimation of the Modulus in Nanoindentation on Soft Materials. *J. Mech. Behav. Biomed. Mater.* **2009**, *2* (4), 312–317 DOI: 10.1016/j.jmbbm.2008.08.004.
- (280) Gupta, S.; Carrillo, F.; Li, C.; Pruitt, L.; Puttlitz, C. Adhesive Forces Significantly Affect Elastic Modulus Determination of Soft Polymeric Materials in Nanoindentation. *Mater. Lett.* **2007**, *61*, 448–451 DOI: 10.1016/j.matlet.2006.04.078.
- (281) Dinte, B. P.; Watson, G. S.; Dobson, J. F.; Myhra, S. Artefacts in Non-Contact Mode Force Microscopy: The Role of Adsorbed Moisture. *Ultramicroscopy* **1996**, *63*, 115–124.
- (282) Ebenstein, D. M.; Wahl, K. J. A Comparison of JKR-Based Methods to Analyze Quasi-Static and Dynamic Indentation Force Curves. *J. Colloid Interface Sci.* **2006**, *298*, 652–662 DOI: 10.1016/j.jcis.2005.12.062.
- (283) Houston, J. E.; Doelling, C. M.; Vanderlick, T. K.; Hu, Y.; Scoles, G.; Wenzl, I.; Lee, T. R. Comparative Study of the Adhesion, Friction, and Mechanical Properties of CF<sub>3</sub>- and CH<sub>3</sub>-Terminated Alkanethiol Monolayers. *Langmuir* **2005**, *21* (9), 3926–3932 DOI: 10.1021/la046901t.
- (284) Hiesgen, R.; Helmly, S.; Morawietz, T.; Yuan, X.-Z.; Wang, H.; Friedrich, K. A. Atomic Force Microscopy Studies of Conductive Nanostructures in Solid Polymer Electrolytes. *Electrochim. Acta* **2013**, *110*, 292–305 DOI: 10.1016/j.electacta.2013.04.147.
- (285) Morawietz, T.; Handl, M.; Oldani, C.; Friedrich, K. A.; Hiesgen, R. Quantitative in Situ Analysis of Ionomer Structure in Fuel Cell Catalytic Layers. *ACS Appl. Mater. Interfaces* **2016**, *8* (40), 27044–27054 DOI: 10.1021/acsami.6b07188.
- (286) Kiss-Pataki, B.; Tiusanen, J.; Dobrik, G.; Vértesy, Z.; Horváth, Z. E. Visualization of the Conductive Paths in Injection Moulded MWNT/polycarbonate Nanocomposites by Conductive AFM. *Composites Science and Technology*. 2014, pp 102–109.
- (287) Hiesgen, R.; Aleksandrova, E.; Meichsner, G.; Wehl, I.; Roduner, E.; Friedrich, K. A. High-Resolution Imaging of Ion Conductivity of Nafion® Membranes with Electrochemical Atomic Force Microscopy. *Electrochim. Acta* **2009**, *55* (2), 423–429 DOI: 10.1016/j.electacta.2009.05.049.
- (288) Takimoto, N.; Takamuku, S.; Abe, M.; Ohira, A.; Lee, H.-S.; McGrath, J. E. Conductive Area Ratio of Multiblock Copolymer Electrolyte Membranes Evaluated by E-AFM and Its Impact on Fuel Cell Performance. *J. Power Sources* **2009**, *194* (2), 662–667 DOI: 10.1016/j.jpowsour.2009.06.045.
- (289) Nagpure, S. C.; Bhushan, B.; Babu, S. S. Surface Potential Measurement of Aged Li-Ion Batteries Using Kelvin Probe Microscopy. *J. Power Sources* **2011**, *196* (3), 1508–1512 DOI: 10.1016/j.jpowsour.2010.08.031.
- (290) Musumeci, C.; Liscio, A.; Palermo, V.; Samorì, P. Electronic Characterization of Supramolecular Materials at the Nanoscale by Conductive Atomic Force and Kelvin Probe Force Microscopies. *Mater. Today* **2014**, *17* (10), 504–517 DOI: 10.1016/j.mattod.2014.05.010.
- (291) Timofeeva, M.; Bolshakov, A.; Tovee, P. D.; Zeze, D. A.; Dubrovskii, V. G.; Kolosov, O. V. Scanning Thermal Microscopy with Heat Conductive Nanowire Probes. *Ultramicroscopy* **2016**, *162*, 42–51 DOI: 10.1016/j.ultramicro.2015.12.006.
- (292) Juszczak, J.; Kaźmierczak-Balata, A.; Firek, P.; Bodzenta, J. Measuring Thermal Conductivity of Thin Films by Scanning Thermal Microscopy Combined with Thermal Spreading Resistance Analysis. *Ultramicroscopy* **2017**, *175*, 81–86 DOI: 10.1016/j.ultramicro.2017.01.012.
- (293) Dai, X.; Moffat, J. G.; Wood, J.; Reading, M. Thermal Scanning Probe Microscopy in the Development of Pharmaceuticals. *Adv. Drug Deliv. Rev.* **2012**, *64* (5), 449–460 DOI: 10.1016/j.addr.2011.07.008.
- (294) Nakamoto, K.; Urasaki, T.; Hondo, S.; Murahashi, N.; Yonemochi, E.; Terada, K. Evaluation of the Crystalline and Amorphous States of Drug Products by Nanothermal Analysis and Raman Imaging. *J. Pharm. Biomed. Anal.* **2013**, *75*, 105–111 DOI: 10.1016/j.jpba.2012.11.020.
- (295) Dawson, A.; Rides, M.; Maxwell, A. S.; Cuenat, A.; Samano, A. R. Scanning Thermal Microscopy Techniques for Polymeric Thin Films Using Temperature Contrast Mode to Measure Thermal Diffusivity and a Novel Approach in Conductivity Contrast Mode to the Mapping of Thermally Conductive Particles. *Polym. Test.* **2015**, *41* (1), 198–208 DOI: 10.1016/j.polymertesting.2014.11.008.
- (296) Guilment, J.; Bokobza, L. Determination of Polybutadiene Microstructures and Styrene-Butadiene Copolymers Composition by Vibrational Techniques Combined with Chemometric Treatment. *Vib. Spectrosc.* **2001**, *26*, 133–149.
- (297) Stuart, B. H. A Fourier Transform Raman Study of Water Sorption by Nylon 6. *Polym. Bull.* **1994**, *33*, 681–686.
- (298) Menchaca, C.; Manoun, B.; Martínez-Barrera, G.; Castaño, V. M.; López-Valdivia, H. In Situ High-Temperature Raman Study of Crystalline Nylon 6,12 Fibers Gamma-Irradiated in Argon Atmosphere. *J. Phys. Chem. Solids* **2006**, *67*, 2111–2118 DOI: 10.1016/j.jpcs.2006.05.017.

- (299) Khanna, Y. P.; Kuhn, W. P. Measurement of Crystalline Index in Nylons by DSC: Complexities and Recommendations. *J. Polym. Sci. Part B Polym. Phys.* **1997**, *35*, 2219–2231.
- (300) Illers, K.-H. Polymorphie, Kristallinitat Und Schmelzwarme von Poly(c-Caprolactam), 2\*). *Makromol. Chem.* **1978**, *179*, 497–507.
- (301) Kolesov, I.; Androsch, R. The Rigid Amorphous Fraction of Cold-Crystallized Polyamide 6. *Polymer (Guildf)*. **2012**, *53* (21), 4770–4777 DOI: 10.1016/j.polymer.2012.08.017.
- (302) Heuvel, H. M.; Huisman, R.; Lind, K. C. J. B. Quantitative Information from X-Ray Diffraction of Nylon-6 Yarns . I . Development of a Model for the Analytical Description of Equatorial X-Ray Profiles. *J. Polym. Sci.* **1976**, *14*, 921–940.
- (303) Mendil-Jakani, H.; Zamanillo Lopez, I.; Legrand, P. M.; Mareau, V. H.; Gonon, L. A New Interpretation of SAXS Peaks in Sulfonated Poly(ether Ether Ketone) (sPEEK) Membranes for Fuel Cells. *Phys. Chem. Chem. Phys.* **2014**, *16*, 11228–11235 DOI: 10.1039/c4cp00710g.
- (304) Thompson, W. R.; Cai, M.; Ho, M.; Pemberton, J. E. Hydrolysis and Condensation of Self-Assembled Monolayers of (3-Mercaptopropyl) Trimethoxysilane on Ag and Au Surfaces. *Langmuir* **1997**, *13* (8), 2291–2302.
- (305) Smith, E.; Dent, G. *Modern Raman Spectroscopy – A Practical Approach*; Wiley, 2005.
- (306) Products, R.; Note, T. Characteristic Raman Vibrational Frequencies of Organic Groups. **1991**, No. 1103, 1–2.

## Summary

*The comprehension of the intrinsic characteristics and interactions found in complex polymeric systems is important and challenging for the development of new engineering solutions. In order to elucidate the process-structure-properties interplays, the co-localization of different information becomes essential, to obtain reliable answers. The characterization of both the surface and the bulk of materials is also of prime importance, especially for thin polymeric materials (<100  $\mu\text{m}$ ) such as membranes, which can present contrasted properties profiles throughout their thickness. To do so, the material must be properly opened with no structural, chemical and morphological modifications. Therefore, the main objective of this thesis was to develop an experimental methodology of characterization allying the co-localization of morphological, nanomechanical and chemical information using a special setup combining Atomic Force Microscopy and Confocal Raman Microspectroscopy to study cross-sections of cryo-ultramicrotomed samples.*

*We applied the developed strategy to three different polymer systems: 1) blends of Polyamide 6 (PA6) and Acrylonitrile-Butadiene-Styrene (ABS), compatibilized with a Styrene-Acrylonitrile grafted with Maleic Anhydride (SAN-MA); 2) hybrid membranes of sulfonated polyether-etherketone (sPEEK) with active networks prepared by Sol-Gel (SG) chemistry; 3) block copolymers based on PS-PEO-PS used as polymer electrolyte membranes. The first study was focused on the impact of the compatibilizer and the mixing protocols on the morphology of an immiscible PA6/ABS blend. Co-localized AFM/Raman established that the addition of the SAN-MA copolymer, at different steps of the blending, favors the formation of the PA6  $\gamma$  polymorph with amounts and distribution depending on the blending protocols. The different resulting morphologies were found to impact the blends' rheological properties. The second study focused on the fabrication of hybrid sPEEK/SG membranes for Fuel Cell based on two different SG precursors. The main goal of this study was to qualify the impact of each step of fabrication on the membranes' physical, nanomechanical and chemical properties, as well as their stability over time. Quantitative nano-mechanical (AFM) and chemical analysis (Raman) of the SG phase revealed its evolution throughout the fabrication process, confirming the efficiency of the applied thermal treatments. For membranes based on (3-mercaptopropyl)-trimethoxysilane SG precursor, it has been shown that the SG phase presents a hierarchically organized system, composed of elementary particles which aggregate into the round shape domains. The presence of SG phase inside the membrane (AFM/Raman) conserves the hydrophobic/hydrophilic nanophase separation of the host sPEEK, but the increasing SG uptake limits the swelling of the host membrane, which can affect its proton conductivity. Finally, the third study was focused on the morphological analysis of a series of triblock copolymers, used as polymer electrolytes in batteries. Their nanomechanical heterogeneities allowed the measurement of the inter-domain distances between the PS and PEO phases directly from the AFM images which were correlated to Small Angle X-Ray Scattering (SAXS) measurements. It has been shown that the material's surface nanomechanical properties evolve from the dry state to the equilibrium with the room relative humidity.*

*To summarize, the development of the characterization methodology allying co-localized AFM/Raman with multiple complementary techniques allowed for the study of different complex polymeric systems for a variety of applications. In each of the three studies of this thesis, the co-localization and multi-technique strategy provided valuable information that could not be accessed by other means. This could only be possible by the adaptation of cryo-ultramicrotomy for sample preparation, especially for thin polymer membranes and water sensitive samples.*

Keywords: AFM, Raman, co-localization, cryo-ultramicrotomy, polymer membrane, Electron Microscopy,

## Résumé

*L'étude avancée de systèmes polymères complexes (mélanges compatibilisés, nanocomposites, copolymères à bloc, etc) est cruciale pour le développement de nouvelles solutions d'ingénierie. Afin d'élucider les relations mise en œuvre-structure-propriétés-durabilité de ces systèmes, la co-localisation d'informations chimique, physique et morphologique devient essentielle pour obtenir des réponses fiables. La caractérisation de la surface et de l'intérieur des matériaux est également d'une importance primordiale, en particulier pour les matériaux polymères minces (<100  $\mu\text{m}$ ) tels que les membranes, qui peuvent présenter des profils de propriétés contrastés entre les surfaces et le coeur. Ces profils de propriétés peuvent être induits par le procédé de mise en œuvre, la chimie du matériau ou son vieillissement. Pour cela, le matériau doit être correctement ouvert sans modification structurelle, chimique ou morphologique. Par conséquent, l'objectif principal de cette thèse a été de développer une méthodologie expérimentale de caractérisation alliant la co-localisation des informations morphologiques, nanomécaniques et chimiques obtenues par le couplage de la Microscopie de Force Atomique (AFM) et la Microspectroscopie Confocale Raman et d'une technique de préparation des coupes transversales par cryo-ultramicrotomie.*

*La stratégie développée a été appliquée à trois systèmes polymères différents: 1) des mélanges polyamide 6 (PA6) / acrylonitrile-butadiène-styrène (ABS), compatibilisés avec un styrène-acrylonitrile greffé anhydride maléique (SAN-MA); 2) de membranes hybrides constituées d'une matrice polymère de type polyétheréthercétone sulfoné (sPEEK) et d'une phase inorganique chimiquement active préparée par chimie Sol-Gel (SG); 3) des copolymères à bloc de type PS-PEO-PS utilisés comme électrolytes pour les batteries lithium. L'étude morphologique du mélange PA/ABS a montré que l'addition d'un copolymère SAN-MA améliore significativement la dispersion de la phase ABS dans la matrice PA et, en fonction du protocole appliqué, modifie la morphologie du mélange et la structure cristalline de la phase PA (teneur/distribution des phases  $\alpha$ - $\gamma$ ). Les modifications morphologiques observées ont ensuite été corrélées aux propriétés rhéologiques des mélanges. L'étude des membranes hybrides sPEEK/SG avait pour objectif de comprendre l'impact des étapes clés d'élaboration de ces membranes sur la morphologie des mélanges, la distribution de la phase SG dans la matrice sPEEK et sa densité de réticulation et le précurseur utilisé: (3-mercaptopropyl)-methyl-diméthoxysilane (SHDi) et (3-mercaptopropyl)-triméthoxysilane (SHTriM). L'efficacité des traitements thermiques appliqués aux différentes étapes du processus de fabrication des membranes SHDi a été démontrée. Pour les membranes basées sur le précurseur SHTriM, il a été démontré que la phase SG présente un système hiérarchiquement organisé, avec des domaines sphériques composés de particules élémentaires plus petites. L'inclusion d'une phase SG à l'intérieur de la membrane sPEEK ne perturbe pas la nanoséparation hydrophobe/hydrophile de la matrice, mais limite son gonflement. Enfin, une analyse morphologique a été réalisée sur une série de copolymères à bloc utilisés comme électrolytes polymères dans les batteries lithium. Le contraste nanomécanique des différentes phases a permis de mesurer les distances inter-domaine entre les phases PS et PEO par AFM et une bonne corrélation a été obtenue avec des résultats de diffusion de rayons X aux petits angles (SAXS). Il a été démontré que les propriétés nanomécaniques de surface du matériau évoluent avec son hydratation (humidité relative de la pièce).*

*Dans chacune des trois études présentées dans cette thèse, la stratégie de co-localisation et a fourni des informations précieuses inaccessibles autrement. Cela ne fut possible qu'après une mise en œuvre spécifique de la cryo-ultramicrotomie pour la coupe de membranes fines et d'échantillons sensibles à l'eau.*

Mots-clés: AFM, Raman, co-localisation, cryo-ultramicrotomie, membrane, microscopie électronique,

